ZESZYTY HISTORYCZNE POLITECHNIKI WARSZAWSKIEJ
16/2014 ISSN 1427-308X

# ROK JANA CZOCHRALSKIEGO
# T. 2
# Pamięci Profesora Jana Czochralskiego

## Wybór publikacji

**prof. Mirosław Władysław Nader – współautor i redaktor naukowy**

Warszawa 2014

Zeszyt zaopiniowany pozytywnie przez Senacką Komisję ds. Historii i Tradycji

Recenzenci

*prof. dr hab. Janusz Cisek*
*em. prof. nzw. dr hab. Jacek Czajewski*

Współautor
Redaktor naukowy

*prof. Mirosław Władysław Nader*

Opracowanie redakcyjne i graficzne

*Eliza Królak*

Korekta

*Oficyny Wydawniczej Politechniki Warszawskiej*

Projekt okładki i skład

*Andrzej Kowalczyk*



Wydawnictwo dofinansowane ze środków Ministerstwa Nauki i Szkolnictwa Wyższego

**ISSN 1427-380X**

Druk i oprawa: Drukarnia Oficyny Wydawniczej Politechniki Warszawskiej. tel. 22 234-55-93

# Spis treści

**Prof. Jan Czochralski w gabinecie na Politechnice Warszawskiej**

# Wybór prac

*Ewa Talik*

# Badanie struktury elektronowej i własności magnetycznych monokryształów związków międzymetalicznych R-T (R – pierwiastek ziem rzadkich, T – metal przejściowy 3d, 4d, 5d)

Dynamiczny rozwój technologii stał się możliwy dzięki rozwojowi fizyki ciała stałego. Poznanie budowy materii umożliwiło postęp w wytwarzaniu i kształtowaniu materiałów, dziś już nawet z precyzją atomową. Stało się możliwe jednak dopiero po odkryciu w 1885 r. promieni rentgenowskich. Zastosowano to promieniowanie do badań struktury ciał stałych. Dlatego też w setną rocznicę zapoczątkowania tych badań, rok 2014 został ustanowiony Międzynarodowym Rokiem Krystalografii IYCr. Kryształy stanowią obiekt badań krystalografii.

Profesor Jan Czochralski, twórca jednej z najbardziej wykorzystywanych metod otrzymywania monokryształów, urodził się i żył w czasach intensywnego rozwoju nauki i techniki.

Dzisiaj nazwisko profesora wiąże się z metodą otrzymywania monokryształów, którą zapoczątkował w 1916 r., kiedy prowadził badania nad krystalizacją metali. Badał szybkość krystalizacji metali przez zanurzanie kapilary w tyglu z roztopionym metalem i powolne jej przesuwanie ku górze. W wyniku tego procesu wyciągania cieczy z tygla i jej chłodzenia otrzymywał wykrystalizowany metal w postaci pręcika o średnicy ok. 1 mm i o długości kilkanastu centymetrów.

Ten pomysł po wielu latach, w 1950 r., wykorzystali amerykańscy uczeni G.K. Teal i J.B. Little z Bell Labs do wyciągania monokryształów germanu. Potem została ona zastosowana do krzemu, a następnie do otrzymywania wielu innych monokryształów związków i roztworów stałych, stosowanych szeroko do dzisiaj w mikroelektronice.

Badania prowadzone w Instytucie Fizyki Uniwersytetu Śląskiego, są kontynuacją badań twórcy metody nad właściwościami metali, ich stopów i związków międzymetalicznych. Zastosowane modyfikacje takie, jak atmosfera gazu obojętnego w procesie wzrostu kryształu, cewka lewitacyjnej, zautomatyzowany mechanizm wyciągania itp. pozwoliły rozszerzyć klasę krystalizowanych materiałów o związki zawierające reaktywne pierwiastki ziem rzadkich czy aktynowce. Celem prowadzonych badań jest poznanie wpływu metalu przejściowego na własności magnetyczne związków R-T oraz zbadanie roli procesów hybrydyzacyjnych w kształtowaniu się oddziaływań. Badania prowadzone na monokryształach dostarczają informacji o anizotropii własności, umożliwiają badania struktury elektronowej powierzchni niezakłóconych zanieczyszczeniami z granic międzyziarnowych, jakie często występują w polikrystalicznych próbkach. Prowadzone badania mają charakter badań podstawowych, lecz dotyczą materiałów o potencjalnych zastosowaniach w chłodnictwie magnetycznym, w elektronice spinowej, w magazynowaniu wodoru, w implantologii medycznej itp.

Monokryształy opisane poniżej otrzymywane są metodą Czochralskiego z lewitującego wsadu o małej jego masie ~1.5 g. Metoda ta zapewnia hodowlę bez kontaktu

z tyglem i zabezpiecza wsad od zanieczyszczeń materiałem tygla. Metoda ta pozwoliła otrzymywać monokryształy również materiałów trudnotopliwych.

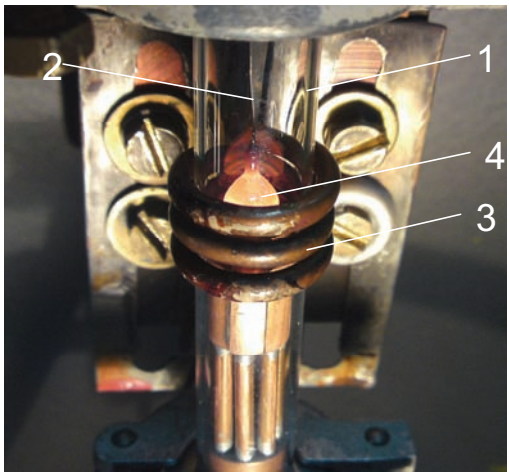

Fot. 1. Aparatury Czochralskiego: 1 rurka kwarcowa, 2 ostrze do wyciągania kryształu, 3 cewka, 4 próbka

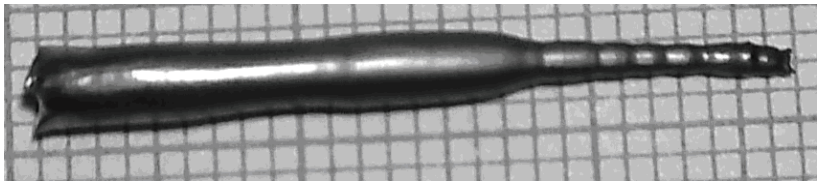
Fot. 2. Przykładowe zdjęcie monokryształu związku $Ho_5Pd_2$

## 1. Związki $R_3T$

W latach dziewięćdziesiątych ubiegłego wieku zainteresowanie badaczy kończyło się na związkach $RT_2$. Istniał pogląd, że dla związków z większą zawartością pierwiastka ziem rzadkich, magnetyzm metalu przejściowego jest nieistotny. Przeprowadzone badania wykazały, że metal przejściowy poprzez fluktuacje spinowe modyfikuje oddziaływania nawet w związkach $R_3T$, czyli z dużą zawartością metalu ziem rzadkich. Pomiary wykonywano na szeregu bardzo dobrej jakości monokryształów tych związków, co umożliwiło nie tylko badania anizotropii własności fizycznych, ale przede wszystkim zapewniło dokładne pomiary struktury elektronowej metodą spektroskopii fotoelektronów (XPS).

Pojęto prace nad powiązaniem wyników badań struktury elektronowej i własności magnetycznych związków międzymetalicznych. Dla związków $Y_3Ni$ oraz $Gd_3Ni$ wykonane badania struktury elektronowej wykazały, że stany 3d niklu tworzą bardzo wąskie pasmo o szerokości połówkowej 1 eV położone 1.7 eV poniżej poziomu Fermiego. Wierzchołek tego wypełnionego pasma hybrydyzuje z dnem prawie pustego pasma 4d itru. Daje to możliwość dynamicznych fluktuacji spinowych, co potwierdził,

np. anomalny przebieg oporu elektrycznego, charakterystyczny dla takich fluktuujących układów (silna ujemna krzywizna i efekt nasycenia). Szczególnie interesujący jest przebieg oporu elektrycznego uzyskano dla związków $Gd_3T$. W wyniku złożenia dwóch wkładów do oporu elektrycznego, mianowicie wkładu związanego z porządkowaniem się magnetycznej podsieci gadolinu oraz wkładu związanego z fluktuacjami spinowymi w metalu przejściowym w postaci silnej ujemnej krzywizny, temperaturowy przebieg oporu elektrycznego wykazuje powyżej temperatury uporządkowania całkowite nasycenie ($d\rho/dT \approx 0$).

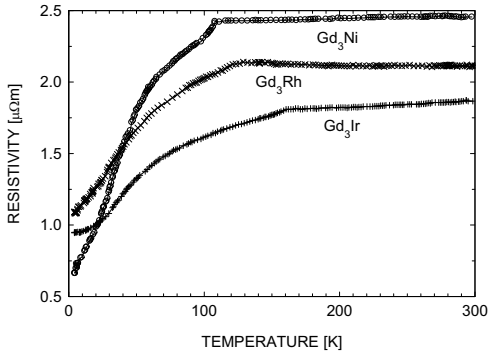


Rys. 1. Przebiegi temperaturowe oporności elektrycznej związków $Gd_3T$ (T=Ni, Rh, Ir)

Pomiary namagnesowania w silnych polach magnetycznych ujawniły dużą anizotropię badanych związków. Wysokotemperaturowe badania podatności magnetycznej wykazały, że największe zawyżenie efektywnego momentu magnetycznego, liczone na jon pierwiastka ziem rzadkich, występuje dla związków $Gd_3T$, stopniowo maleje dla podobnych związków z terbem i holmem oraz osiąga zero dla związków z erbem. Może to świadczyć o polaryzującej roli pola molekularnego działającego na atomy metalu T umieszczonego wewnątrz graniastosłupa utworzonego przez jony pierwiastka ziem rzadkich w strukturze $Fe_3C$, w której badane związki krystalizują. Temperaturowe badania parametrów sieciowych związków $Gd_3T$ (T = Ni, Rh, Ir) ujawniły, że największe efekty magnetoobjętościowe występują dla związku z niklem (T-3d) a najmniejsze dla związku z irydem (T-5d). Dla analogicznego szeregu $Er_3T$ efekty magnetoobjętościowe nie występują, podobnie jak zawyżenie efektywnego momentu magnetycznego liczonego na jon pierwiastka ziem rzadkich. Dla związków z terbem, holmem i dysprozem efekty te są pośrednie. Badania oporności elektrycznej wykazały istnienie dwóch wkładów: wkładu związanego z porządkowaniem się podsieci metalu ziem rzadkich z widoczną temperaturą uporządkowania oraz wkładu od fluktuacji spinowych metalu T. Złożenie tych dwóch przyczynków było odpowiedzialne za efekty nasycenia oporu elektrycznego w podwyższonych temperaturach. Badania struktury elektronowej pokazały, że fluktuacje spinowe są efektem hybrydyzacji wypełnionego pasma d metalu T z prawie pustym pasmem d metalu ziem rzadkich. Polaryzującą rola pola molekularnego działającego wytwarzanego przez atomy R na jon metalu T i efekty hybrydyzacyjne odpowiedzialne za fluktuacje spinowe determinują na własności związków $R_3T$.

Dla związku $Tb_3Rh$ stwierdzono gigantyczny efekt magnetokaloryczny (GMCE) w okolicach magnetycznego uporządkowania 88 K. Zmiany entropii obliczone z pomiarów izoterm magnetycznych przy zastosowaniu równania Maxwella w polach 2T, 5T i 7T wynoszą -11.6 J/Kkg, 17.9 J/Kkgoraz 21 J/Kkg odpowiednio. GMCE jest związany z przejściem pierwszego rodzaju ze stanu para- do ferromagnetycznego poprzez zarodkowanie faz Griffitha począwszy od $T_G > T_c$. W temperaturach poniżej 20 K obserwuje się przejścia metamagnetyczne i efekty termomagnetyczne (ZFC i FC). Praca ta pokazała, że nie tylko przemiana strukturalna ale również zarodki nowego porządku w fazie paramagnetycznej mogą prowadzić do przemiany fazowej I rodzaju i związanej zwykle z taką przemianą dużą zmianą entropii, co prowadzi do dużej wartości zjawiska magnetokalorycznego.

Fot. 3. Topografia rengenowska Berga-Barretta monokryształu $Tb_3Rh$

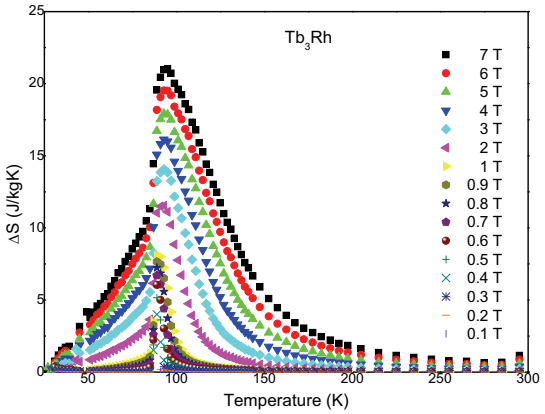


Rys. 2. Zmiana entropii magnetycznej w zakresie pól 0.1 – 7 T w związku $Tb_3Rh$ [24]

Wyniki prac zostały opublikowane w wymienionych poniżej czasopismach o zasięgu międzynarodowym.

1. E. Talik, J. Szade, J. Heimann, A. Winiarska, A. Winiarski and A. Chełkowski "X-ray examination, electrical resistivity and magnetic properties of $R_3Co$ single crystals (R = Y, Gd, Dy and Ho)" J.Less-Common Met. 138 (1988) 129–136.

2. E. Talik, J. Heimann, J. Szade and A. Chełkowski “Temperature dependence of magnetic susceptibility and electrical resistivity of $La_3Co$ and $Lu_3Co$” J. Less-Common Met. 155 (1989) 241–246.
3. E. Talik, A. Winiarska and A. Winiarski “Crystal growth of $R_3Ni$ intermetallic compounds by Czochralski method from a levitated melt (R = Y, Gd, Tb, Dy, Ho and Er)” J. Crystal Growth 126 (1993) 718–720.
4. E. Talik and M. Neumann “XPS investigation of $Y_3Ni$ and $Gd_3Ni$ single crystals” Physica B 193 (1994) 207–212.
5. E. Talik “Magnetic and transport properties of $R_3Ni$ system (R = Y, Gd, Tb, Dy, Ho and Er)” Physica B 193 (1994) 213–220.
6. E. Talik and T. Mydlarz “Metamagnetic transition in $Y_3Ni$ single crystal” J. Alloys and Compounds 215 (1994) L7–L8.
7. E. Talik and M. Neumann “Spin fluctuations in $R_3T$ compounds ( R = Gd, T = Rh, Ir)” J. Magn. Magn. Mat. 140-144 (1995) 795–796.
8. E. Talik and A. Ślebarski “Properties of $Gd_3T$ compounds (T = Rh, Ir, Pd) J. Alloys and Compounds 223 (1995) 87–90.
9. E. Talik, M. Neumann, A. Ślebarski and A. Winiarski “Properties of $Y_3Rh$ and $Y_3Ir$ single crystals” Physica B 212 (1995) 25–32.
10. E. Talik, T. Mydlarz and A. Gilewski “Magnetization of $Dy_3Ni$ single crystal” J. Alloys and Compounds 233 (1996) 136–139.
11. E. Talik, T. Mydlarz and A. Gilewski “Magnetization of $Er_3Ni$ single crystal” J. Magn. Magn. Mater. 157/158 (1996) 405–406.
11. E. Talik and A. Ślebarski International Centre for Diffraction Data, Powder Diffraction File - Release 1998 X ray diffraction data of $Y_3Ni$ (48-1559), $Gd_3Ni$ (48–1557) and $Tb_3Ni$ (48–1558).
12. E.Talik, M. Neumann, J. Kusz, H. Böhm, T. Mydlarz, A. Winiarski and J. Heimann “Properties of $Er_3Rh$ single crystals” J. Magn. Magn. Mat. 186 (1998) 33–40.
13. E.Talik, M.Neumann and T. Mydlarz “Properties of $Dy_3Rh$ single crystal” Proceedings of International Syposium Condesed Matter Physics (Uni-Service 1997) 137–141.
14. E. Talik, M. Neumann and T. Mydlarz “Photoemission study and magnetization of $Gd_3Pd$ intermetallic compound” J. Magn. Magn. Mater. 189 (1998) 183–188.
15. E. Talik, J. Kusz, H. Böhm, T. Mydlarz „Magnetic properties of $Ho_3Rh$ single crystals” J. Alloys and Compounds 336 (2002) 29–35.
16. E. Talik, W. Witas, J. Kusz, A. Winiarski, T. Mydlarz, M. Neumann, H. Böhm „Magnetic properties of $Tb_3Rh$ single crystals” Physica B 293 (2000) 75–83.
17. J. Kusz. H. Böhm and E. Talik “X-ray investigation and discussion of the magnetostriction of $Gd_3T$ (T= Ni, Rh, Ir) single crystals” J. Applied Crystallography 33 (2000) 213– 217.
18. E. Talik, J. Kusz, H. Bohm and T. Mydlarz „Electronic structure and magnetic properties of $Er_3Ir$ single crystal” J. Magn. Magn. Mater. 324 (2001) 459–468.
19. E.Talik, M. Klimczak “Giant macgnetocaloric effect in $Tb_3Rh$. J. Alloys and Compounds 486 (2009) L30–L33.

## 2. Związki $Fe_{1-x}V_xAl$

Związki międzymetaliczne $Fe_{1-x}V_xAl$ w zależności od stężenia wanadu i termicznej lub mechanicznej obróbki, mogą wykazywać atomowo uporządkowaną strukturę regularną $DO_3$ (fcc), $L2_1$ (fcc), B2 (sc) lub atomowo nieuporządkowaną strukturę typu A2 (bcc). Z badań układu $Fe_{1-x}V_xAl$ można stwierdzić, że właściwości struktury krystalicznej, magnetyczne i niezwykłe własności transportowe są związane z silnym procesem hybrydyzacji stanów 3d żelaza i wanadu. Ta hybrydyzacja powoduje poszerzenie stanów i ich przesunięcie do wyższej energii wiązania. W konsekwencji tego porządek dalekiego zasięgu zanika i jest utworzona wąska przerwa energetyczna w pobliżu poziomu Fermiego, co pokazały badania w zakresie pasma walencyjnego XPS. Ponadto zastąpienie atomów Fe wanadem powoduje znaczny wzrost oporności resztkowej i pojawienie się anomalnych przebiegów zależności temperaturowej oporności właściwej osiągając maksimum dla x=1.

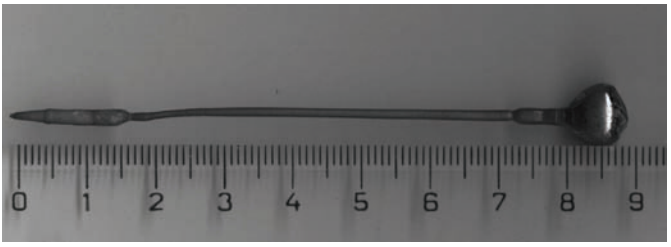


Fot. 4. Przykładowe zdjęcie monokryształu związku $Fe_{2.25}V_{0.75}Al$

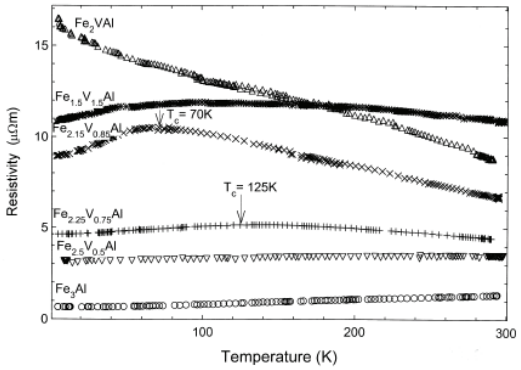


Rys. 3. Temperaturowe zależności oporności elektrycznej szeregu


1. E. Talik, J. Szade, J. Heimann, A. Winiarski, A. Winiarska, K. Majewska and A. Chełkowski "Growth of $Fe_{3-x}V_xAl$" J. Crystal Growth 102 (1990) 187–190.
2. W. Zarek, E. Talik, J. Heimann, M. Kulpa, A. Winiarska, M. Neumann, "Electronic structure, magnetic and electrical properties of $Fe_{1-x}V_xAl$ compounds" J. Alloys and Comp. 297(1999) 53–58.

## 3. Związki $RFe_4Al_8$

Związki $RFe_4Al_8$ krystalizujące w strukturze $ThMn_{12}$ do dziś cieszą się zainteresowaniem ze względu na silną anizotropię i ciekawe własności magnetyczne. Badania oporności elektrycznej i podatności magnetycznej $YFe_4Al_8$ wykazały istnienie antyferromagnetycznego uporządkowania w 195 K oraz słaby ferromagnetyzm poniżej 100 K. Dla $DyFe_4Al_8$ i $HoFe_4Al_8$ podsieć żelaza porządkuje antyferromagnetycznie w 185 K a dla $ErFe_4Al_8$ w 150 K. Dla wszystkich tych związków stwierdzono występowanie efektów termomagnetycznych poniżej 30 K. Badania neutronowe przeprowadzone na monokryształach wykazały, że podsieć żelaza i pierwiastka ziem rzadkich tworzą długozasięgowe uporządkowanie. Zachowanie podobne do szkła spinowego poniżej 30 K można wytłumaczyć cykloidalnym uporządkowaniem momentów magnetycznych oraz czułością modulowanej magnetycznej struktury na obecność nawet słabych pól magnetycznych.

Jednym z badanych zagadnień były prace nad związkami uranu i toru stanowiąc kontynuację badań związków $RFe_4Al_8$. Otrzymano monokryształy $UFe_4Al_8$, $ThFe_4Al_8$, $ScFe_4Al_8$ i $YFe_4Al_8$. Dla powyższych związków istotne jest wykonanie pomiarów struktury elektronowej na monokryształach ze względu na wysoką reaktywność tych związków. Linie pochodzące od utlenionego materiału zdecydowanie zakłócają pasmo walencyjne i linie rdzeniowe nie pozwalając na właściwą interpretację zwłaszcza satelitarnych linii stanów 4f.

Elektrony 5f posiadają znacznie większą rozciągłość przestrzenną w porównaniu ze stanami 4f w lantanowcach oraz stanami elektronów wędrownych w metalach 3d. Kiedy odległość pomiędzy atomami uranu jest większa niż 3.6Å (limit Hilla), powinny wykazywać magnetyzm. To kryterium jest jednak nie wystarczające ze względu na procesy hybrydyzacji stanów 5f ze stanami s, p, d pasma przewodnictwa. Istnie możliwość występowania kilku stanów 5f takich, jak $5f^2$, $5f^3$, $5f^4$ jako stany końcowe w procesie fotoemisji. Najbardziej zewnętrzne stany przekrywają się z pasmem przewodnictwa przy poziomie Fermiego, powodując asymetrię linii ze względu na możliwość silnego rozpraszania elektron-dziura.

W strukturze elektronowej uranu linia XPS U4f jest rozszczepiona, nie tylko ze względu na oddziaływanie spin-orbita, na dwie linie $U4f_{7/2}$ oraz $U4f_{5/2}$. Dodatkowe rozszczepienie linii może pochodzić ze sprzężenia dziury powstałej po fotoemisji w stanach U4f (*l=3; s=±1/2; j=7/2, 5/2)* ze stanami U5f.

Podobne zjawisko obserwuje się dla stanów Gd4d i nazywa się procesem super Costera-Kroninga. Rzeczywiście trzy linie są zwykle obecne są w widmie stanów U4f. Czasami pierwsza linia satelitarna może być przekryta linią pochodzącą od tlenku uranu lub niewidoczna z powodu dużej asymetrii całkowitej linii U4f. Stopień asymetrii, natężenie oraz szerokość linii jest związana z poszerzeniem związanym z czasem życia najbardziej zewnętrznych stanów U5f, które mogą rozciągać się do pasma przewodnictwa i mieć w związku z tym krótki czas życia. Linie satelitarne bardziej symetryczne sugerują silniejszą lokalizację i stąd dłuższy czas życia. Pierwsza linia satelitarna (3 eV poniżej linii głównej) jest dobrze widoczna, gdy stany 5f uranu tworzą wąskie pasmo. Druga linia satelitarna (7 eV poniżej linii głównej) jest zawsze widoczna z powodu najsilniejszego ekranowania. Pole spinowe obecne w związku może mieć wpływ na czas życia stanów w podpowłokach. To zjawisko może być bardziej skom-

plikowane z powodu mieszania międzypasmowego. Dla związków $UNiSb_2$ i $U_3Ge_5$, pokazujących dwie pary satelitów U4f (3 eV i 7 eV) tylko uran posiada moment magnetyczny. Ponadto wartość momentu magnetycznego jest większa niż dla $UFe_4Al_8$ (satelita 7eV). Te dwa fakty sugerują pasmowy charakter stanów U5f w ostatnim związku.

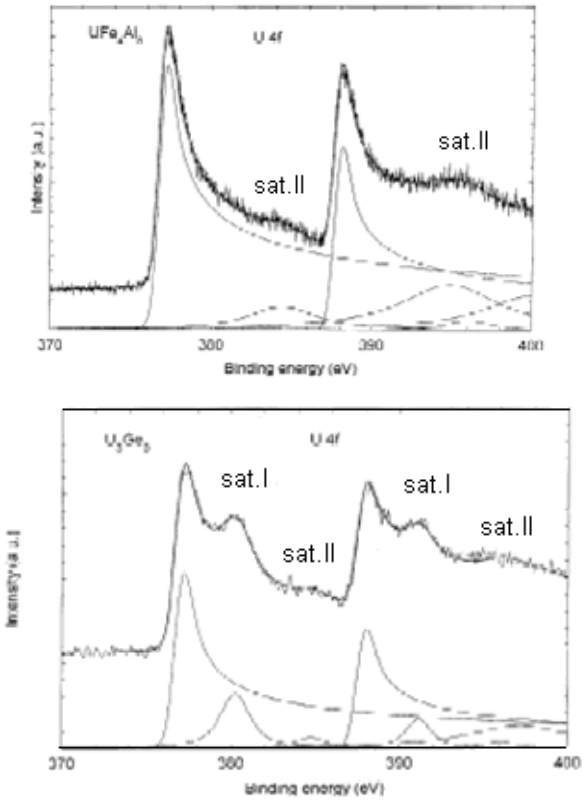


Rys. 4. Struktura multipletowa linii XPS U4f w związku $UFe_4Al_8$ i $U_3Ge_5$[41]

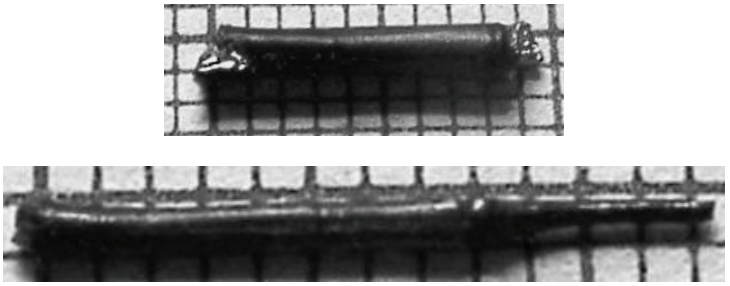

Fot. 5. Zdjęcia monokryształów związku $ScFe_4Al_8$

Poniżej podany jest wykaz publikacji z badań nad tą grupą związków:


1. A. Chełkowski, E. Talik, J. Szade, J. Heimann, A. Winiarska and A. Winiarski "Crystal structure, magnetic and electrical properties of $YFe_4Al_8$ single crystals" Physica B 168 (1991) 149–152.
2. E. Talik, J. Szade and J. Heimann "Spin glass behaviour and magnetic anisotropy in $DyFe_4Al_8$ single crystal" Physica B 190 (1993) 361–365.
3. Z. Drzazga, E. Talik, J. Heimann and J. Szade "Magnetocrystalline anisotropy of $RFe_4Al_8$ single crystals investigated by torque magnetometry" IEEE Transactions on Magnetics 30 (1994)1006–1008.
4. E. Talik, J. Szade, J. Heimann and T. Mydlarz "Resistivity anomaly and magnetic properties of $HoFe_4Al_8$" Physica B 205 (1994) 127–132.
5. T. Mydlarz, E. Talik, J. Szade and J. Heimann "High field magnetization of $DyFe_4Al_8$ single crystal" J. Alloys and Compounds 219 (1995) 225–227.
6. J. Heimann, J. Szade, E. Talik and T. Mydlarz "Magnetic anisotropy of $ErFe_4Al_8$ single crystal" J. Magn. Magn. Mat. 140-144 (1995) 1033–1034.
7. J.A. Paixao, S. Landridge, S. Aa. Sorensen, B. Lebech, A.P. Goncalves, G.H. Lander, J.P. Brown, P. Burlet and E. Talik "Unusual sublattice interactions in compounds with $ThMn_{12}$ structure" Physica B 234–236 (1997) 614– 616.
8. E.Talik, M. Neumann, T. Mydlarz, J. Kusz, H. Böhm, A. Winiarski and A. Gilewski "Magnetism of manganese in $RMn_2$ and $RMn_4Al_8$ (R=Y, Gd, Er) intermetallics" J. Condensed Matter 10 (1998) 581–592.
9. S. Langridge, J.A. Paixao, N. Bernhoeft, C. Vettier, G. H. Lander, Doon Gibbs, S.Aa. Sorensen, A. Stunault, D. Wermeille, E. Talik "Changes in 5d-band polarization in rare earth compounds" Phys. Rev. Letters 82 (1999) 2187–2190.
10. J.A. Paixäo, M. Ramos Silva, A. Aa. Sorensen, H. Lebech, G.H. Lander, P.J. Brown, S. Langridge, E. Talik, A.P. Goncalves "Neutron - scattering study of the magnetic structure of $DyFe_4AL_8$ and $HoFe_4Al_8$ Phys. Rev. B 61 (2000) 6176–6188.
11. E. Talik. A. Winiarski, B. Kotur, W. Suski, "Growth and Characterization of $ScFe_4Al_8$ Single Crystal" Crystal Research and Technology 36 (2001) 119–1122.
12. H. Misiorek, J. Stępień – Damm, W. Suski, E. Talik, B. Y. Kotur, V. M. Dmitriev "Lattice parameters, magnetic susceptibility and thermal conductivity of $ScFe_4Al_8$ and $YFe_4Al_8$" J. Alloys and Compounds 363 (2004) 78–84.
13. V.M. Dmitriew, J. Stępień-Damm, W. Suski, E. Talik N. N. Prentslau „Possible coexistence of antiferromagnetism, spin-glass and superconductivity in $ScFe_4Al_8$ and single crystals" Phys. Stat. Sol.(c) 1 (2004) 1824–1827.
14. V.M. Dmitriew, N.N. Prentslau, I.V. Zalochevskii, L.A. Ishchenko, B.Y. Kotur, W. Suski, E. Talik "Superconductivity, negative magnetoresistance and electrical conduction anisotropy in $YFe_4Al_8$ and $ScFe_4Al_8$ single crystals in the frequency range $0\text{-}10^8$ Hz" Low Temperature Physics 29 (2003) 901–909.
15. E. Talik, Marie – Emilie Lucas, W. Suski, R. Troć „XPS spectra of the $AFe_4Al_8$ compounds with A = Y, Sc, U and Th" J. Alloys and Comppounds 350 (2003) 72–76.
16. K. Rećko, L. Dobrzyński, A. Goukassov, M. Biernacka, M. Brancewicz, A. Makal, K. Woźniak, J. Waliszewski, E. Talik, B. Kotur, W. Suski „Magnetic

phase transition in $ScFe_4Al_8$ by powder and single crystal neutron diffraction" Phase Transitions, 80 (2007) 575–586.
17. K. Rećko, L. Dobrzyński, M.-H. Lemee-Cailleau, J. Waliszewski, E. Talik, W. Suski, P. Courtois „On the crystal and magnetic behaviour of $ScFe_4Al_8$ single crystals" Acta Physica Polonica A 115 (2009) 206–208.
18. V.M. Dmitriev, A.V.Terekhov, W. Suski, L.A. Ishchenko, J. Ćwik, T. Palewski, B. Ya. Kotur, E. Talik "Negative magnetoresistivity of the $RM_4Al_8$ (R=Sc, Y, Ce, Yb, Lu; M=Cr, Mn, Fe) ternaries with $ThMn_2$ – type crystal structure" J. Alloys and Compounds 452 (2008) 217–224.

## 4. Związki $RMn_2$

Związki te są ciekawe ze względu na niestabilność momentu magnetycznego manganu wynikającą z przekraczania krytycznej odległości Mn-Mn z powodu kontrakcji lantanowców. Wykonane zostały po raz pierwszy badania struktury elektronowej na monokryształach $RMn_2$ oraz pomiary szeregu własności fizycznych monokryształów wzdłuż głównych kierunków krystalograficznych. Metoda Czochralskiego z lewitującego roztopu pozwoliła uzyskać bardzo dobrej jakości monokryształy, bez domieszek fazy ferromagnetycznej, od której nie były wolne kryształy hodowane metodą Bridgmana i szereg próbek polikrystalicznych. Świadczą o tym publikowane wcześniej wyniki pomiarów magnetycznych. Szczególne znaczenie miały badania struktury elektronowej, możliwe do wykonania praktycznie tylko na monokryształach, ze względu na wysoką reaktywność tych związków. Tylko dobrej jakości monokryształ złamany w warunkach wysokiej próżni pozwolił uzyskać widmo XPS pozbawione zanieczyszczeń tlenem, który zakłóca szczególnie pasmo walencyjne dla próbek polikrystalicznych, ze względu na wysoką reaktywność badanego materiału. Dla $YMn_2$ stwierdzono rozszczepienie pasma 3d manganu rzędu 2 eV, co odpowiadało dokładnie obliczeniom struktury elektronowej wykonanym przez Yamadę oraz wartości momentu magnetycznego wyznaczonego przy pomocy spolaryzowanych neutronów. Kształt pasma walencyjnego, malejąca gęstość stanów przy poziomie Fermiego zmienia się w zależności od pierwiastka ziem rzadkich. Odpowiada to malejącej na skutek kontrakcji lantanowców odległości pomiędzy atomami manganu i zmianom momentu magnetycznego. Pomiary magnetyczne ujawniły silna anizotropię występującą w tych związkach. Otrzymano po raz pierwszy monokryształy $ScMn_2$ w celu wykonania pomiarów struktury elektronowej i porównania jej ze strukturą elektronową $YMn_2$ oraz obliczeniami teoretycznymi Yamady i Shimizu. Stwierdzono, że pasmo 3d manganu dominujące w przy poziomie Fermiego dla $YMn_2$ jest rozszczepione podobnie jak dla $YMn_2$, jednakże gęstość stanów przy poziomie Fermiego jest mniejsza dla związku ze skandem. Tłumaczy to własności $ScMn_2$ jako jedynie spinowego fluktuatora, podczas gdy $YMn_2$ posiada zlokalizowany moment magnetyczny na manganie. Dla $ScMn_2$ odległość Mn-Mn jest najmniejsza spośród związków $RMn_2$. Model odległości krytycznej przewiduje brak zlokalizowanego momentu magnetycznego dla $ScMn_2$. Pomiary struktury elektronowej potwierdziły słuszność modelu struktury elektronowej Yamady i Shimizu.

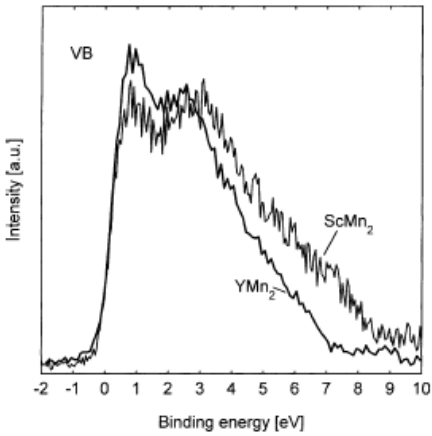


Rys.5. Porównanie XPS pasm walencyjnych $ScMn_2$ i $YMn_2$

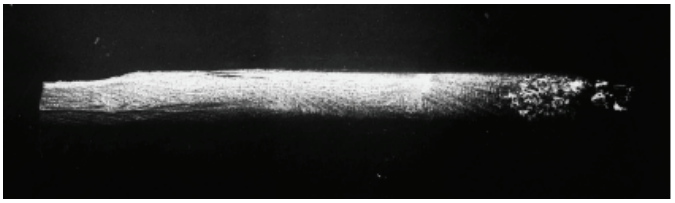

Fot. 6. Topografia rentgenowska Berga- Barretta związku $HoMn_2$

Wyniki prac opublikowano w następujących czasopismach:


1. E. Talik and M.Kulpa "Electronic structure of $TbMn_2$ and $DyMn_2$ single crystals" J. Alloys and Compounds 286 (1999) 158–161.
2. M.Kulpa and E. Talik "Crystal growth and characterization of $RMn_2$ (R=Gd, Tb, Dy, Er) intemetallics" Crystal Research and Technology 34 (1999) 621–625.
3. E. Talik, M. Kulpa, T. Mydlarz, J. Kusz, H. Böhm, A. Winiarski "Magnetic properties of the $TbMn_2$ single crystals" Physica B 271 (1999) 265–272.
4. E. Talik, M. Kulpa, T. Mydlarz, J. Kusz, H. Bohm „Magnetic properties of $DyMn_2$ single crystals" J. Alloys and Compounds 308 (2000) 30–37.
5. E. Talik, M. Kulpa, A. Winiarski, T. Mydlarz and M . Neumann „Electronic structure and magnetic properties of $HoMn_2$ single crystals" J. Alloys and Compounds 316 (2001) 51–57.
6. M. Kulpa and E. Talik Powder Diffraction File Release 2001, 51–1398, 51–1399, 51-1400 X ray diffraction data of $GdMn_2$, $TbMn_2$ and $DyMn_2$
7. M. Kulpa . E. Talik, A. Winiarski, T. Mydlarz, A. Gilewski, J. Kusz, H. Böhm, W. Suski „Electronic structure and magnetic properties of $ScMn_2$ single crystal" J. Alloys and Compounds 386 (2005) 82–86.
8. E. Talik, M. Kulpa, T. Mydlarz, J. Kusz, H. Böhm "Magnetic properties of $ErMn_2$ single crystals" J. Alloys and Compounds 348 (2003) 12–17.

## 5. Związki RPdAl

Badania struktury elektronowej i właściwości magnetycznych monokryształów GdTAl, gdzie T = Pd i Rh oraz GdPdX (X = Al, Si, Ga, Ge, In, Sn) oraz RPdAl (R = Tb, Dy, Ho, Er).

Badania dotyczą procesów hybrydyzacji pasma d metalu ziemi rzadkiej i przejściowego z pasmami sp metalu X oraz wpływu tych procesów na własności magnetyczne wymienionych wyżej związków międzymetalicznych. Niezwykle interesujące własności ujawniły badania monokryształu GdNiAl i GdPdAl. Otrzymane metodą Czochralskiego monokryształy tych związków krystalizują w strukturze heksagonalnej typu ZrNiAl, podczas gdy próbki topione w metodą łukową krystalizują w strukturze rombowej typu TiNiSi. Pomiary temperaturowej zależności parametrów sieciowych, oporu elektrycznego, podatności magnetycznej dc wykazały występowanie przejścia izostrukturalnego pierwszego rodzaju z wysokotemperaturowej modyfikacji HTM I do niskotemperaturowej modyfikacji HTM II w temperaturze 220 K dla GdNiAl i w 80 K dla GdPdAl. Skok parametrów sieciowych związany z tym przejściem powoduje np. dla GdPdAl zmniejszenie parametru *a* o 0.7% i wzrost parametru *c* o 1.3%. Przejście magnetyczne związane z porządkowaniem się podsieci gadolinu występuje w temperaturze 48 K i reorientacja momentów magnetycznych w 20 K. Z pomiarów namagnesowania wynika niekolinearność struktury magnetycznej dla obu związków. Pomiary podatności magnetycznej ujawniły, że efektywny moment magnetyczny w fazie HTM I jest taki jak dla gadolinu pierwiastkowego a w fazie HTM II jest zawyżony. Badania struktury elektronowej wykazały, że poziom Fermiego leży w obszarze hybrydyzowanych stanów. Stany 4d palladu dominują, są jednak odsunięte bezpośrednio od poziomu Fermiego. Mogą jednak występować fluktuacje spinowe na skutek przekrywania wypełnionego pasma palladu 4d z pustymi prawie pasmami 5d gadolinu i 3s3p aluminium. Temperaturowe pomiary struktury elektronowej GdPdAl ujawniły zmiany pasma walencyjnego w temperaturze przejścia izostrukturalnego. Takie przejście obserwuje się jeszcze dla TbPdAl. Począwszy od DyPdAl przejścia izostrukturalne nie występują. Może to świadczyć o roli pola molekularnego wytworzonego przez momenty magnetyczne pierwiastka ziem rzadkich w podmagnesowaniu podsieci palladu.

Badania kontynuowane były dla monokryształów GdRhAl, DyPdAl, HoPdAl, GdPdSi, GdPdSn, GdPdGe, GdPdIn. Z przeprowadzonych badań wynika, że właściwości związków potrójnych RTX są wynikiem złożonych zjawisk fizycznych, począwszy od frustacji magnetycznej, poprzez efekty hybrydyzacyjne do indukowanego magnetyzmu palladu. Nie tylko liczba elektronów, ale także ich rozkład przestrzenny odgrywają ważną rolę w procesach hybrydyzacyjnych, wpływają na strukturę krystaliczną i magnetyczne właściwości badanych związków. Potrójne związki GdPdX krystalizowały w stabilnych strukturach rombowych. Ich temperatury uporządkowania były bliskie stosunkowo niskie rzędu 30 K. Jednakże pomiary oporu elektrycznego pokazały systematyczne zmiany nachylenia, na skutek zmieniającego się czynnika fononowego. Pokazano eksponencjalną zależność nachylenia $d\rho_{ph}/dT$ od gęstości d=nM/v (n – liczba molekuł w komórce elementarnej, M-masa cząsteczkowa, V – objętość komórki elementarnej). Zaobserwowano regularną zmianę szerokości połówkowej linii 4d palladu w zależności od metalu X, związaną ze stopniem przekrywania się orbitali i ich rozciągłością przestrzenną oraz ilością elektronów typu p. Jedynie

związek z indem wykazywał względnie wysoką temperaturę porządkowania (około 100 K). Charakteryzowała go jednocześnie największa gęstość d, stąd najmniejsze $d\rho_{ph}/dT$ oraz najwęższa linia Pd 4d. Wskazuje to na najsilniejszą lokalizację palladu w tej grupie związków i większą rolę oddziaływania RKKY w tym związku.

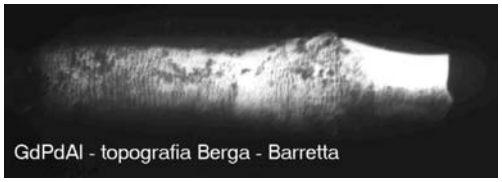


Fot. 6. Tografia rentgenowska Berga-Barretta monokryształu związku GdPdAl

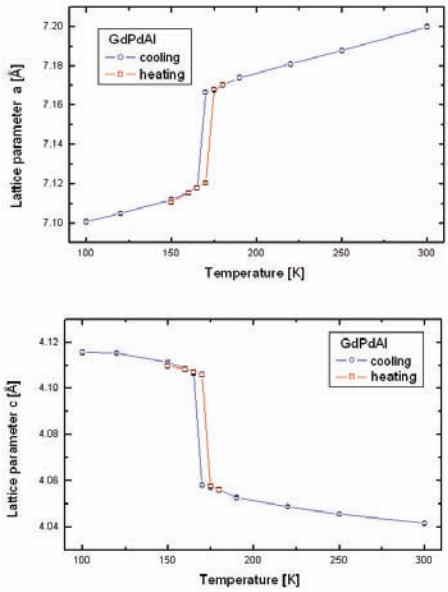


Rys. 6. Temperaturowe zmiany parametrów sieciowych związku GdPdAl związane z przemianą izostrukturalną HTM I i HTM II [56]

Wyniki badań opublikowano:

1. E. Talik, M. Skutecka, J. Kusz, H. Böhm, J. Jarosz, T. Mydlarz, A. Winiarski „Magnetic properties of GdPdAl single crystals" J. Alloys and Compounds 325 (2001) 42–49.
2. J. Jarosz, E. Talik, T. Mydlarz, J. Kusz, H. Böhm and A. Winiarski "Crystallographic and electronic structure, magnetic and electrical properties of GdNiAl single crystal" J. Mag. Magn. Mater 208 (1999) 169–170.
3. E. Talik, M. Skutecka, J. Kusz, H. H. Böhm "Magnetic properties of DyPdAl" J. Magn. Magn. Mater. 272-276 (2004) 767–768.
4. J. Kusz, H. Böhm, E. Talik, M. Skutecka, J. Deniszczyk "Isostructural phase transition in the GdPdAl single crystals" J. Alloys and Compounds 348 (2003) 65–71.

5. E. Talik, M. Skutecka, T. Mydlarz, J. Kusz, H. Böhm „Role of hybridization in magnetic properties of DyPdAl single crystals" J. Alloys and Compounds 391 (2005) 1–7.
6. E. Talik, M. Skutecka, J. Kusz, H. Böhm, T. Mydlarz "Electronic structure and magnetic properties of HoPdAl single crystal" J. Alloys and Compounds 359 (2003) 103–108.
7. E. Talik, M. Skutecka, J. Kusz, H. Böhm, T. Mydlarz, J. Jarosz "Electronic structure sand magnetic properties of GdRhAl single crystals" J. Alloys and Compounds 363 (2004) 52–59.

## 6. Związki $Gd_7Pd_3$, $Gd_{7-x}Y_xPd_3$ (x = 0÷6), $Gd_7Rh_3$, $GdPd_{3-x}Ni_x$

Na monokryształach serii związków $Gd_{7-x}Y_xPd_3$ (x = 0÷6) przeprowadzono badania struktury krystalicznej i elektronowej. Wykonano kierunkowe pomiary podatności magnetycznej stało- i zmiennopolowej oraz wyliczono, na podstawie pomiarów magnetycznych, wielkość zmian entropii (efekt magnetokaloryczny). Monokryształy otrzymane zostały metodą Czochralskiego z lewitującego wsadu. Badania topografii rentgenowskiej metodą Berga-Barretta potwierdziły dobrą jakość uzyskanych monokryształów. Przeprowadzone badania struktury krystalicznej szeregu $Gd_{7-x}Y_xPd_3$ (x = 0÷6) wykazały, że wszystkie związki wykrystalizowały w strukturze heksagonalnej typu $Th_7Fe_3$. Dla wszystkich próbek badanego szeregu obserwuje się anomalne przebiegi temperaturowych zależności zmian parametrów komórki elementarnej. Wykazują one odchylenie od teoretycznej krzywej wyliczonej na podstawie teorii Grüneisen'a - Debye'a ($\Theta_D$ = 160 K) oraz efekt magnetoobjętościowy poniżej temperatury uporządkowania magnetycznego w poszczególnych związkach. Dla wszystkich przebadanych związków krzywe oporu elektrycznego $\rho$(T) charakteryzują następujące cechy i) duża ujemna krzywizna poniżej temperatury uporządkowania magnetycznego, $T_C$, ii) brak wyraźnej anomalii w $T_C$, iii) względnie małe wartości *RRR* oraz iv) silna anizotropia. Jony Gd w swojej podsieci posiadają duży i zlokalizowany moment magnetyczny. Zatem za ferromagnetyczny porządek magnetyczny w badanym układzie odpowiedzialne jest pośrednie oddziaływanie wymienne typu *RKKY*. Stopniowe obniżanie temperatury uporządkowania magnetycznego wraz ze zmniejszaniem zawartości magnetycznych jonów Gd związane jest ze słabnącym oddziaływaniem *RKKY*. Temperatury Curie dla związków $Gd_7Pd_3$, $GdY_6Pd_3$, $Gd_5Y_2Pd_3$, $Gd_4Y_3Pd_3$, $Gd_3Y_4Pd_3$, $Gd_2Y_5Pd_3$, $GdY_6Pd_3$, wynoszą odpowiednio: 334 K, 299 K, 263 K, 240 K, 197 K, 150 K oraz 75 K. Zatem, podstawiając związek wyjściowy, $Gd_7Pd_3$, różną ilością atomów Y możemy płynnie regulować temperaturę Curie. Wyznaczone wartości magnetycznych momentów nasycenia dla większości badanych związków są zawyżone w stosunku do teoretycznej wartości dla swobodnych jonów $Gd^{3+}$. Takie zachowanie można przypisać wkładowi pochodzącemu od hybrydyzowanych pasm elektronów 4*d* jonów Pd, 4*d* jonów Y oraz 5*d* jonów Gd.

Przy zastosowaniu zmodyfikowanej metody Czochralskiego z lewitującego wsadu otrzymano nową serię związków międzymetalicznych $Gd_7Ni_xPd_{3-x}$ (x = 1, 2, 3). Przeprowadzone badania struktury krystalicznej szeregu wykazały, że wszystkie związki wykrystalizowały w strukturze heksagonalnej typu $Th_7Fe_3$. Na otrzymanych monokryształach wykonano również wstępne badania własności magnetycznych, które

wykazały, że wszystkie otrzymane monokryształy porządkują się ferromagnetycznie. Związek $Gd_7NiPd_2$ porządkuje się w 298 K. $Gd_7Ni_2Pd$ porządkuje się w temperaturze 225 K, podczas gdy $Gd_7Ni_3$ w temperaturze 145 K. Stwierdzono także zachowanie wartości zmian entropii magnetycznej mimo podstawień palladu niklem.

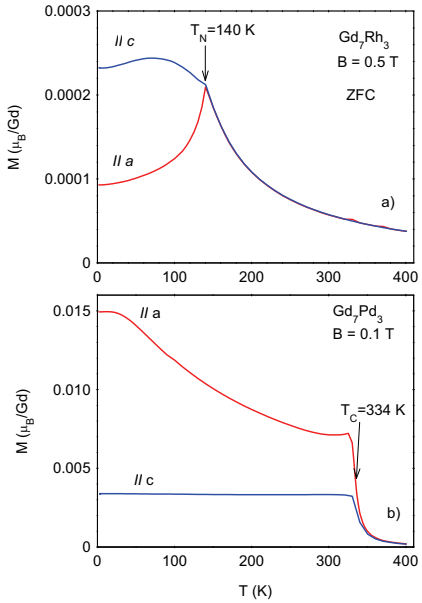


Rys. Anizotropia przebiegu oporności elektrycznej związków $Gd_7T_3$, gdzie T=Pd, Rh

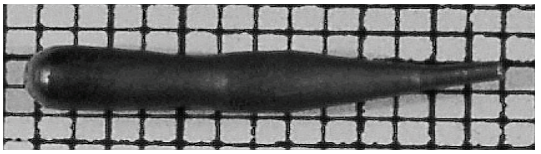

Fot. 8. Zdjęcie monokryształu nowego związku międzymetalicznego $GdY_6Pd_3$

Wyniki prac opublikowano między innymi w czasopismach:


1. E. Talik, M. Klimczak, A. Winiarski and R. Troć "$Gd_7T_3$ (T = Rh, Pd) intermetallics crystal growth" J. Crystal Growth 283 (2005) 547–552.
2. E. Talik, M. Klimczak, R. Troć, J. Kusz, W. Hofmeister, A. Damm „Comparison of the magnetic properties of $Gd_7T_3$ (T=Pd, Rh) single crystals" J. Alloys and Compounds 427 (2007) 30–36.
3. E. Talik „90th anniversary of Czochralski method" J. Alloys and Compounds 442 (2007) 70–73.
4. M. Klimczak, E. Talik, R. Troć, K. Gofryk, D. Badurski Magnetoresistance behaviour and thermoelectric transport properties of $Gd_7T_3$ (T = Pd, Rh) single crystals J. Alloys and Compounds 442 (2007) 172–175.
5. E. Talik, M. Klimczak, A. Winiarski, R. Troć „Crystal growth of $Gd_{7-x}Y_xPd_3$ intermetallics" J. Crystal Growth 310 (2008) 1886−1890.

6. E.Talik, M. Klimczak, R. Troć, J. Kusz, W. Hofmeister, A. Winiarski „Comparison od magnetic and transport properties of $Gd_6YPd_3$ and $Gd_7Pd_3$ single crystals" J. Alloys and Compounds 460 (2008) 1−7.
7. M. Klimczak, E. Talik and V.H. Tran "Infuence of Yttrium Substitution on the Electronic Structure and Magnetic Moment of $Gd_{7-x}Y_xPd_3$ (x = 0, 1, 2, 3, 4)" Acta Physica Polonica A 115 (2009) 200–202.
8. E Talik, M Klimczak, V H Tran, J Kusz, W Hofmeister, A Winiarski and R Troć "Coexistence of localized magnetism and itinerant ferromagnetism in a $Gd_5Y_2Pd_3$ single crystal" Intermetallics 18 (2010) 27–35.
9. M. Oboz, E. Talik, J. Kusz, W. Hofmeister, „Magnetic and transport properties of $Gd_3Y_4Pd_3$ single crystal" J. Alloys and Comp. 492 (2010) 13–18.
10. E. Talik, M. Oboz, V. H. Tran, J. Kusz, W. Hofmeister, A. Winiarski "Magnetic properties of $Gd_4Y_3Pd_3$ single crystal" J. Crystal Growth 312 (2010) 1651–1658
11. M. Oboz, E. Talik, J. Kusz, W. Hofmeister, „Magnetic and transport properties of $Gd_3Y_4Pd_3$ single crystal" J. Alloys and Comp. 492 (2010) 13–18.
12. E. Talik, M. Oboz, V. H. Tran, J. Kusz, W. Hofmeister, A. Winiarski "Magnetic properties of $Gd_4Y_3Pd_3$ single crystal" J. Crystal Growth 312 (2010) 1651–1658.
13. M. Oboz E. Talik, J. Kusz and A. Winiarski „Physical properties of $Gd_7NiPd_2$ single crystal" J. Alloys and Compounds 509 (2011) 4478–4483.
14. M. Oboz, E. Talik, and A. Winiarski "Magnetocaloric effect in GdCu intermetallic compound" Cryst. Res. Technol. 47, No. 3, (2012) 341–346.
15. E. Talik, M. Oboz "Czochralski Method for Crystal Growth of Reactive Intermetallics" Acta Physica Polonica A 124 (2013) 340–343.
16. E. Talik, M. Oboz, J. Kusz, A. Winiarski, W. Hofmeister "Magnetic and transport properties of $Gd_{7-x}Y_xPd_3$ (x = 0÷6) system" J. Alloys and Compounds 582 (2014) 718–729.

## Zakończenie

Metoda wyciągania kryształów Czochralskiego jest stale modyfikowana na potrzeby technologii coraz to bardziej skomplikowanych materiałów. W dotychczas zbadanych materiałach otrzymanych na bazie pierwiastków ziem rzadkich i metali przejściowych stwierdzono wiele struktur krystalicznych, przejść krystalograficznych oraz bogactwo zachowań magnetycznych, których natura nie jest dotąd dostatecznie poznana. Istotną rolę odgrywa anizotropia oraz struktura elektronowa. Własności fizyczne, zwłaszcza anizotropia mogą być jednoznacznie określone dopiero przy dysponowaniu monokryształami dobrej jakości. Istotne jest przeprowadzenie na nich kompleksowych badań. Wyniki z różnych metod badawczych, uzyskane na tych samych próbkach, cechuje większa spójność. Unika się, spotykanych w literaturze, rozbieżności wyników występujących dla pomiarów na różnie otrzymanych próbkach. Ułatwiona jest wiarygodna, całościowa interpretacja. W tych warunkach można wykrywać i opisywać różnorodne powiązania występujące między strukturami krystaliczną i elektronową, własnościami magnetycznymi oraz oporem elektrycznym. Szczegółowe wyniki dotychczas przeprowadzonych badań zawarte są między innymi w wymienionej w poszczególnych działach bibliografii

ELSEVIER

Journal of Non-Crystalline Solids 287 (2001) 145–161

JOURNAL OF NON-CRYSTALLINE SOLIDS

www.elsevier.com/locate/jnoncrysol

Section 3. Stability and crystallization

# Nanocrystallization of metallic glasses

Tadeusz Kulik *

*Faculty of Materials Science and Engineering, Warsaw University of Technology, Wołoska 141, 02-507 Warsaw, Poland*

**Abstract**

The paper summarizes briefly the current status of research in the field of nanocrystallization of metallic glasses especially highlighting the influence of glass composition and conditions of devitrification process on size, morphology and composition of crystallization products. Conventional crystallization creates a nanocrystalline structure only in glasses with particular compositions. Any metallic glass, decomposing in a primary crystallization process, can be converted into partially nanocrystalline material using non-conventional methods of heat treatment, e.g. high-temperature or low-temperature nanocrystallization. Temperature of devitrification process influences sizes and compositions of crystallization products for any volume fraction of crystalline phase. The change of crystallites sizes can change their morphologies. The change of a crystallite composition usually affects the lattice parameter but also can result in a change of crystallographic structure of the same phase or in formation of another phase. Composition of primary crystallites is dependent on temperature as well as on time of devitrification process. The lower the annealing temperature and the shorter the annealing time (smaller crystallites) the more the crystallites composition differs from the equilibrium state. 

*PACS:* 81.05.Kf; 81.07.Bc; 81.40.Ef; 64.70.Kb

## 1. Introduction

Polycrystalline solids with grain size less than 100 nm are called nanocrystalline materials and can be produced using various methods and different starting phase: vapour (inert gas condensation, sputtering, plasma processing, vapour deposition), liquid (electrodeposition, rapid solidification) or solid (mechanical alloying, severe plastic deformation, spark erosion) [1–3]. Most of the methods offer two possibilities for creation of nanocrystalline structure: directly in one process or indirectly through an amorphous precursor. Nanocrystallization of metallic glasses is an example of the second procedure. In this case, nanocrystalline material is produced in two steps: (1) formation of amorphous state by quenching of liquid alloy, and (2) partial or complete crystallization of the amorphous alloy by annealing. Three important groups of nanocrystalline materials produced from metallic glasses can be distinguished: constructional Al-based alloys [4–11], magnetically soft [12–17] and magnetically hard [18–25] Fe-based alloys. Examples of the alloys compositions and main aspects of their structure are presented in Table 1. There are two basic parameters characterizing structure of these materials: crystallite diameter, $D$, and volume fraction, $V_{cr}$, of nanocrystals. The optimum amount of nanocrystalline phase differs for each group. In the case of magnetically hard nanocrystalline materials, full [20,25] or almost full [22,23] crystallization

* Tel.: +48-22 660 8399; fax: +48-22 660 8514.
*E-mail address:* tkulik@inmat.pw.edu.pl (T. Kulik).

0022-3093/01/$ - see front matter 
PII: S0022-3093(01)00627-5

Table 1
General characteristics of the three main groups of nanocrystalline materials produced by devitrification of metallic glasses ($V_{cr}$ – volume fraction of crystalline phase, $D$ – diameter of nanocrystals, $\lambda_s$ – saturation magnetostriction constant, $\langle K \rangle$ – averaged magnetocrystalline anisotropy, $\sigma_f$ – fracture strength)

| Nanocrystalline materials | Magnetically soft (Fe-based) | Constructional (Al-based) | Magnetically hard (Fe-based) |
|---|---|---|---|
| Alloys | Finemet® ($Fe_{73.5}Cu_1Nb_3Si_{13.5}B_9$) | Al–RE–TM (RE = Y, Ce, Nd, Sm; TM = Ni, Co, Fe, Cu) | Fe–RE–B |
| | Nanoperm® ($Fe_{84}Zr_{3.5}Nb_{3.5}B_8Cu_1$) | | e.g. $Fe_{82.3}Nd_{11.8}B_{5.9}$ $Fe_{88}Nb_2\,Pr_5\,B_5$ |
| | Hitperm ($Fe_{44}Co_{44}Zr_7B_4Cu_1$) | GIGAS® | |
| Structure | Nanocrystals (bcc-Fe) + Amorphous matrix | Amorphous matrix + Nanocrystals (fcc-Al) | Nanocrystals $Fe_{14}Nd_2B$ (+ $Fe_3B$, bcc-Fe, Am) |
| Sructural parameters | | | |
| $V_{cr}$ | 70–75% $\Rightarrow$ $\lambda_s \approx 0$ | $\leqslant$40% $\Rightarrow$ ductility | $\leqslant$100% |
| $D$ | $\leqslant$15 nm $\Rightarrow$ $\langle K \rangle \approx 0$ | $V_{cr} \uparrow$, $D \downarrow \Rightarrow$ $\sigma_f \uparrow$ | <25 nm |
| Properties | High permeability, low magnetic losses | High specific strength at high temperatures | High coercivity, high remanence |

is required. For constructional and magnetically soft nanocrystalline materials the optimum mechanical and magnetic properties, respectively, are obtained after partial crystallization of their amorphous precursors [4,12], which means that they are two-phase materials composed of nanocrystals and an amorphous matrix. To preserve ductility in Al-based nanocrystalline alloys, $V_{cr}$ should not exceed 20% in ternary (Al–Y–Ni) [4] and 40% in quaternary (Al–Y–Ni–Cu) [9] alloys. Mechanical properties of these materials can be explained and predicted using mixture model based on the volume fractions of amorphous matrix and nanocrystals, proposed by Kim et al. [11]. GIGAS is a commercial name of Al-based nanocrystalline alloys with strength up to 1 GPa [26].

The most structure sensitive are properties of magnetically soft Fe-based nanocrystalline alloys. The volume fraction of nanocrystals should be the fraction which compensates their negative magnetostriction contribution by positive magnetostriction contribution of the amorphous matrix. A non-magnetostrictive Fe-based nanocrystalline material can be obtained for $V_{cr} = 70$–75%, depending on an alloy composition [27]. On the other hand, the diameter of nanocrystals, $D$, should be smaller than the magnetic exchange length in the crystalline phase to substantially reduce the contribution of magnetocrystalline anisotropy of this phase to the total magnetic anisotropy of a material [28]. According to random anisotropy model, developed by Herzer [28], the $D$ should not exceed about 15 nm in the case of α-Fe(Si) and α-Fe nanocrystals, present in Finemet [12] and Nanoperm [13] alloys, respectively.

Metallic glasses can be considered as materials which are kinetically metastable and thermodynamically unstable. Most of them are stable at temperatures close to room temperature and can be transformed to crystalline state at temperatures greater than room temperature. The onset temperature of the crystallization process, $T_x$, is called crystallization temperature and is usually determined during continuous heating with typical heating rates (10 to 20 K/min). The crystallization temperature as well as the mode of crystallization (primary, eutectic or polymorphous) are mainly dependent on an alloy composition [29]. The transformation from amorphous to fully crystalline state can proceed in one step (polymorphous and eutectic crystallization) or in several steps (primary crystallization). Crystallization of metallic glasses usually involves nucleation and growth processes [30]. To obtain nanoscale structure the crystallization process should proceed with the largest nucleation rate and the slowest crystal growth. Such conditions can be obtained for alloys with some compositions or by applying particular

methods of heat treatment. It was shown theoretically by Crespo et al. [31] and experimentally by Köster et al. [32] that metallic glasses with primary crystallization and with time-dependent long-range diffusion controlled growth rates are the most suitable candidates for nanocrystallization. Nevertheless, nanocrystalline structure was observed also for eutectically ($Pd_{60}Ti_{20}Si_{20}$ [33,34] and $Cu_{50}Ti_{40}Al_{10}$ [35]) and polymorphously ($Cu_{50}Ti_{40}Ni_{10}$ [35] and $Zr_{50}Co_{50}$ [36]) crystallizing glasses.

The subject of nanocrystallization of amorphous solids was summarized in 1996 by Lu [37]. More recently McHenry et al. [38] extensively reviewed the recent developments in the synthesis, structural characterization, properties and applications in the fields of amorphous and nanocrystalline magnetically soft materials.

The aim of this paper is to summarize briefly the current status of research in the field of nanocrystallization of metallic glasses, especially emphasizing the influence of glass composition and conditions of devitrification process on size, morphology and composition of crystallization products.

## 2. The role of glass composition in nanocrystallization process

Magnetically soft alloy with composition $Fe_{73.5}Cu_1Nb_3Si_{13.5}B_9$ and commercial name Finemet® [12] was the first nanocrystalline material obtained by crystallization of a metallic glass, with magnetic properties better than those found for the amorphous counterpart and therefore interesting from an applications point of view. Similar alloy with composition $Fe_{73.5}Cu_1Nb_3Si_{15.5}B_7$ is known as Vitroperm®. Nanoperm® is the next commercially available magnetically soft nanocrystalline alloy obtained using the same method. It was developed by Suzuki et al. [13], initially as Fe–Zr–B alloy. Finally, the best soft magnetic properties were found for the composition $Fe_{84}Zr_{3.5}Nb_{3.5}B_8Cu_1$ [16]. More recently (Fe,Co)–M–B–Cu (M = Zr, Nb or Hf) nanocrystalline alloys, called Hitperm, have been shown to have saturation magnetizations >1.6 T and Curie temperatures >1240 K [17,38,39]. Hitperm alloys are candidates for high-temperature soft-magnetic applications [17,39]. All these alloys can be transformed from amorphous to partially nanocrystalline state applying conventional annealing at temperatures close to crystallization temperatures. These alloys have a primary crystallization and are multicomponent. Each element has a particular effect. Silicon and boron are so called glass-forming elements, which facilitate forming the amorphous state of the alloys and increase thermal stability of amorphous phase. Iron and cobalt are the elements with magnetic moments and are the basic constituents of magnetic alloys. It is desirable to keep their content as large as possible to maximize magnetization of an alloy. Cobalt replacing iron increases magnetizations and Curie temperatures of both amorphous matrix and nanocrystals in Nanoperm-like (Fe–Zr–B–Cu) alloys [17,40,41]. In Finemet-like (Fe–Cu–Nb–Si–B) alloys only Curie temperature of nanocrystals increases whereas magnetizations of both phases decrease with the increase of cobalt content [41]. Copper, niobium and zirconium, despite their smaller concentrations in these alloys, affect the crystallization process and are responsible for nanocrystalline structure. Structures of Finemet® and Finemet-like alloys with missing copper and/or niobium, after conventional annealing for 1 h [42], are shown in Fig. 1. Nanocrystalline structure, with average grain diameter ~11 nm, is detected only in the alloys containing pairs of alloying elements (copper and niobium or copper and tantalum). The remaining alloys have larger crystallites. In the ternary Fe–Si–B alloy the crystals form dendrites with arm spans up to 300 nm. These results illustrate that under conventional conditions of annealing only metallic glasses with some compositions can be transformed into nanocrystalline material.

Copper, due to its very limited solubility in iron, forms small clusters, which can serve as sites for heterogeneous nucleation of Fe-based crystallites and increase their number by orders of magnitude. Hono et al. [43,44] have shown, using atom probe field ion microscopy (APFIM), that copper enriched clusters are formed prior to the onset of the crystallization process of Finemet. Ayers et al. [45]

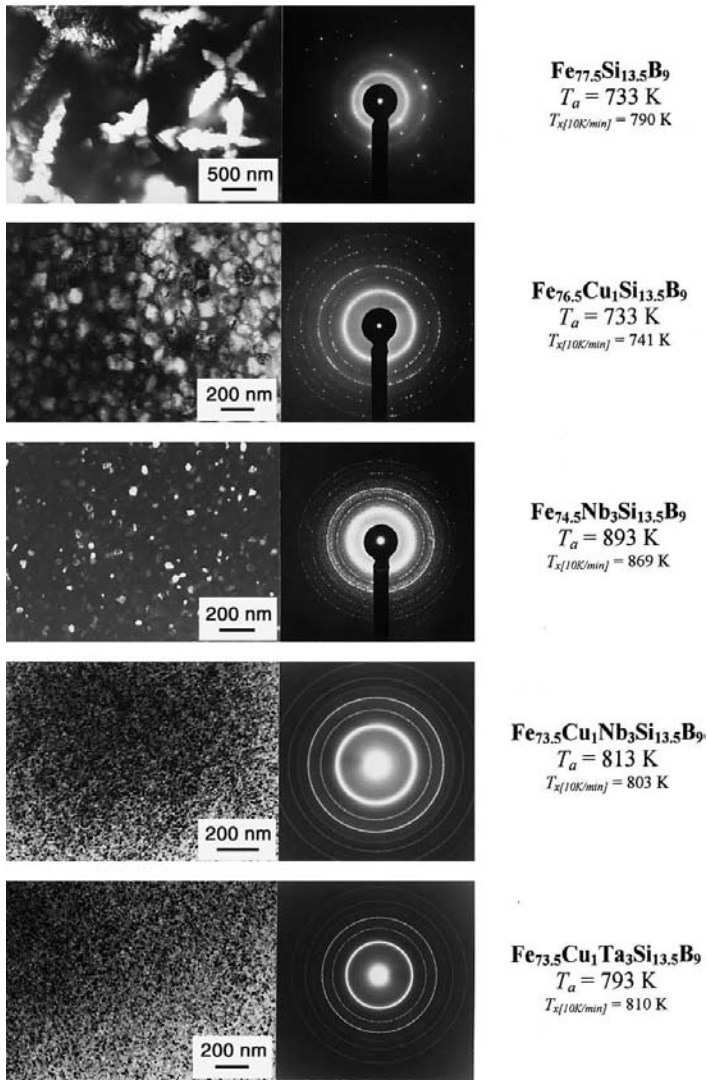


Fig. 1. Transmission electron micrographs and electron diffraction patterns of initially amorphous alloys after the first stage of crystallization obtained by conventional annealing at $T_a$ for 1 h [42]. ($T_x$ – crystallization onset temperature determined during continuous heating.)

reporting results of extended X-ray absorption fine structure (EXAFS) measurements also have shown that copper rich clusters with a near fcc structure form early in the precipitation process in $Fe_{73.5}Cu_1Nb_3Si_{13.5}B_9$ and $Fe_{76.5}Cu_1Si_{13.5}B_9$ glasses. Small angle neutron scattering (SANS) experiments allowed Ohnuma et al. [46] to estimate the average diameter and interparticle distance of copper enriched clusters in Finemet to be 1.8 and 6 nm, respectively. Copper clustering prior to the crystallization process was also observed (APFIM) by Zhang et al. [47] in Nanoperm alloys. Kataoka et al. [48] reported improvement of magnetic properties by addition of gold to Fe–Si–B–Nb alloy and concluded that grain refinement might have occurred. Duhaj et al. [49] have confirmed, using transmission electron microscopy (TEM), that gold has similar effect as copper on structure of Finemet-like alloys. Therefore, it can be stated that elements insoluble in iron, such as copper and gold, alter rate of heterogeneous nucleation and thus facilitate nanocrystallization of metallic glasses. However, recent report of Zhang and Zhu [50] shows that gold addition has no effect on nanocrystallization of Fe–Zr–B glasses. Different behaviour of gold in Fe–Si–B–Nb [48,49] and Fe–Zr–B [50] glasses can be attributed to much stronger attractive interactions between gold and zirconium then gold and niobium atoms. Predicted by Bakker [51] values of the interfacial enthalpy for gold solved in zirconium and niobium are $-294$ and $-134$ J/mol, respectively. Consequently, gold atoms do not cluster before the primary crystallization but co-segregation of gold and zirconium occurs during the growth of α-Fe crystallites without any influence on their nucleation and growth process [50].

On the other hand, elements such as niobium, tantalum and zirconium, which are rejected from a crystallization front to the amorphous matrix, decrease crystal growth because of relatively smaller diffusivity of big atoms of these elements in an amorphous phase [52]. According to Yavari and Drbohlav [53], the rejected atoms generate diffusion double-layers with larger concentration gradients. The layers also explain measured differences in Curie temperatures of the amorphous matrix in partially nanocrystalline alloy and fully amorphous alloy of the same composition as the matrix [53]. Results of EXAFS studies of nanocrystalline $Fe_{85}Zr_7B_6Cu_2$ alloy (Nanoperm®) indicate that the boundaries between α-Fe nanocrystallites and amorphous matrix are in the form of Fe-free interfaces with thickness of about 0.3 nm [54]. Recently reported results of SANS measurements of nanocrystalline $Fe_{73.5}Cu_1Nb_3Si_{15.5}B_7$ alloy (Vitroperm®) give experimental evidence for the accumulation of niobium atoms at the surface of α-Fe(Si) nanocrystallites [55]. These observations support the inhibitor concept of nanocrystallization of metallic glasses. Concentration of the elements controlling the growth rate of primary crystallites (e.g. Zr, Nb, Ta) in Nanoperm-type alloys is much larger (∼7 at.%) than in Finemet-type alloys (∼3 at.%). Probably, this difference is the reason that nanocrystalline structure can be obtained, using simple conventional annealing, in Cu-free Nanoperm-type alloys and cannot in Cu-free Finemet-type alloys. However, even in Nanoperm-type alloys the size of nanocrystallites can be reduced by copper addition and its influence increases with boron concentration, as was shown by Kopcewicz et al. [56]. Average diameter of α-Fe(Si) nanocrystallites in Finemet-type alloys does not exceed 15 nm after annealing (for 1 h) at temperatures up to ∼900 K and then increases [57,58] independently of boron and silicon concentrations in an alloy [57]. Evidently, the niobium addition in these alloys is responsible for the observed thermal stability of size of the nanocrystallites.

In Al-based alloys slowly diffusing elements with larger atomic radii in the amorphous matrix, that are insoluble in primary nanocrystals (α-Al), are rare earth elements [59–64] such as yttrium [8–11,62–64], cerium [59,62], neodymium [7,59,62], samarium [61] or ytterbium [65]. Nevertheless, their effectiveness in blocking growth of primary nanocrystals differs, e.g. Calin and Köster [63] have reported that partially nanocrystallized Nd-containing alloy ($Al_{90}Ni_6Nd_4$) is more stable against crystal coarsening than Y-containing alloy ($Al_{85}Ni_5Y_{10}$). The largest heterogeneous nucleation rates and number densities of nuclei observed during crystallization of Al–Ni–(Y, Ce, Nd) glasses [61] can be attributed to preferred

associations formed during melt spinning between component atoms (clusters) which serve as nucleants [59,62,64].

Hono and Ping recently reported results of APFIM studies of magnetically hard nanocrystalline $Fe_{73}Nd_{4.5}B_{18.5}Co_3Ga_1$ alloy and showed that cobalt and gallium atoms are rejected from $Fe_3B$ primary crystallites and control their growth by reducing the mobility at the crystal/amorphous interface [66].

Multicomponent alloys rich in zirconium have better glass-forming ability and can be produced in the amorphous state in a bulk form directly from the liquid, e.g. in Zr–Al–Cu–Ni [67], Zr–Ni–Cu–Ti [68] and Zr–Ni–Cu–Ti–Be [69] metallic systems. Greater strength bulk nanocrystalline materials can be produced by partial devitrification of bulk Zr-based glasses [70–72]. As was reported by Köster et al. [73] and Murty et al. [74], oxygen influences the crystallization process of Zr-based glasses. Presence of oxygen in $(Zr_{50}Co_{50})_{96}O_4$ glass incereases the formation of nanocrystalline structure by reduction of crystal growth rate and increase of nucleation rate by several orders of magnitude [73]. Results of APFIM studies of bulk amorphous $Zr_{65}Cr_{15}Al_{10}Pd_{10}$ alloy conducted by Chen et al. [75] showed that oxygen is uniformly distributed in the amorphous phase and its redistribution occurs during annealing. Impurity oxygen promotes crystallization and changes the crystallization mode by forming metastable phases containing oxygen. Increase of oxygen content above 0.4 at.% in $Zr_{65-x}Cu_{27.5}Al_{7.5}O_x$ glass results in formation of primary nano-quasicrystals instead of big polymorphic crystals of $Zr_2(Cu,Al)$ [74]. Chen et al. [76] recently showed that an icosahedral quasicrystalline phase with size $\sim$20 nm can be obtained during primary crystallization of bulk $Zr_{65}Al_{7.5}Ni_{10}Cu_{7.5}Ag_{10}$ glass. Löffler et al. [77] proposed model for nanocrystallization of undercooled bulk $Zr_{41.5}Ti_{13.8}Ni_{10}Cu_{12.5}Be_{22.5}$ glass. According to the model the glass first decomposes on the nanometer scale into two amorphous phases, increasing the nucleation probability, and later nanocrystallization occurs in one of the amorphous phases. A thermodynamic model for nanocrystallization in bulk metallic glasses was recently published by Desre [78].

## 3. The effects of annealing conditions on crystallization products

Fe-based Finemet®, Nanoperm® and their modifications, e.g. Vitroperm® and Hitperm as well as Al-based Gigas®, are nanocrystallizing metallic glasses and do not require any special heat treatment to be converted into nanocrystalline material [12,16,17,79]. They used to be transformed from amorphous to partially nanocrystalline state during simple isothermal annealing at temperature close to crystallization temperature in a time of, usually, 1 h. This kind of treatment can be called conventional nanocrystallization and is widely used by many researchers [80–90]. To determine susceptibility to nanocrystallization, especially of new alloys, it is useful to correlate microstructure and physical properties (magnetic or mechanical) with thermal properties of the glass. For this reason, heat treatment in a calorimeter applying continuous heating with a constant heating rate to a determined temperature, $T_{max}$, followed by cooling at a constant cooling rate is convenient. In this case $T_{max}$ is usually higher than the temperature of the end of the first crystallization step and less than the onset temperature of the second step of crystallization of the glass [79].

Both techniques of conventional nanocrystallization are effective only for those glasses which nanocrystallize more easily. It was found [91–94] that application of particular heat treatments makes possible nanocrystallization of any primarily crystallizing metallic glasses. Two different temperature regimes have been found to be useful for nanocrystallization of these metallic glasses: high-temperature [91,92] and low-temperature [93]. As already reported, by applying high temperature and very short time of annealing it is possible to create nanocrystalline structure even in ternary (Fe–Si–B [91] and Co–Si–B [92]) and binary (Fe–B [94,95]) glasses. Köster et al. [36] obtained nanocrystalline structure using high-temperature annealing also in polymorphously crystallizing $Zr_{50}Co_{50}$ glass. High-temperature nanocrystallization can be realized by flash annealing of amorphous ribbons using Joule heating [92,94]. Figs. 2 and 3 show the structures of par-

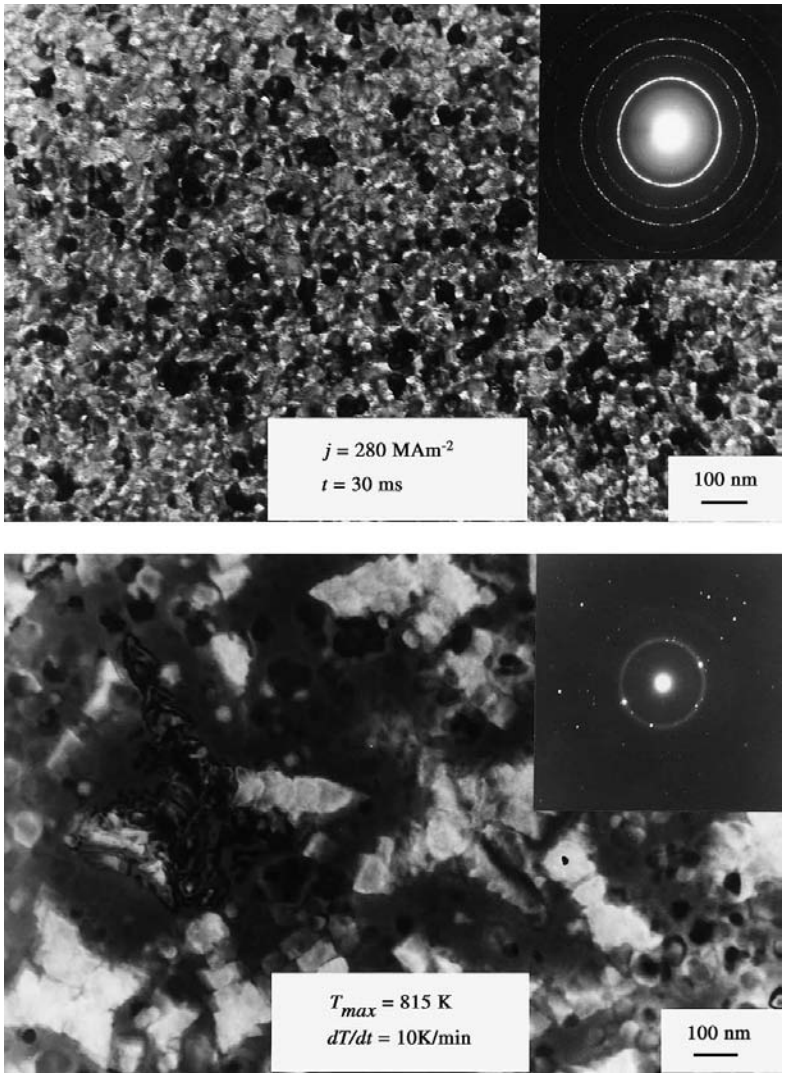


Fig. 2. Transmission electron micrographs and electron diffraction patterns of initially amorphous $Fe_{77.5}Si_{13.5}B_9$ alloy after the first stage of crystallization obtained by: conventional annealing during continuous heating from room temperature up to 815 K [79] and high-temperature flash annealing with current density $j = 280$ MA/m$^2$ and pulse time $t = 30$ ms [91].

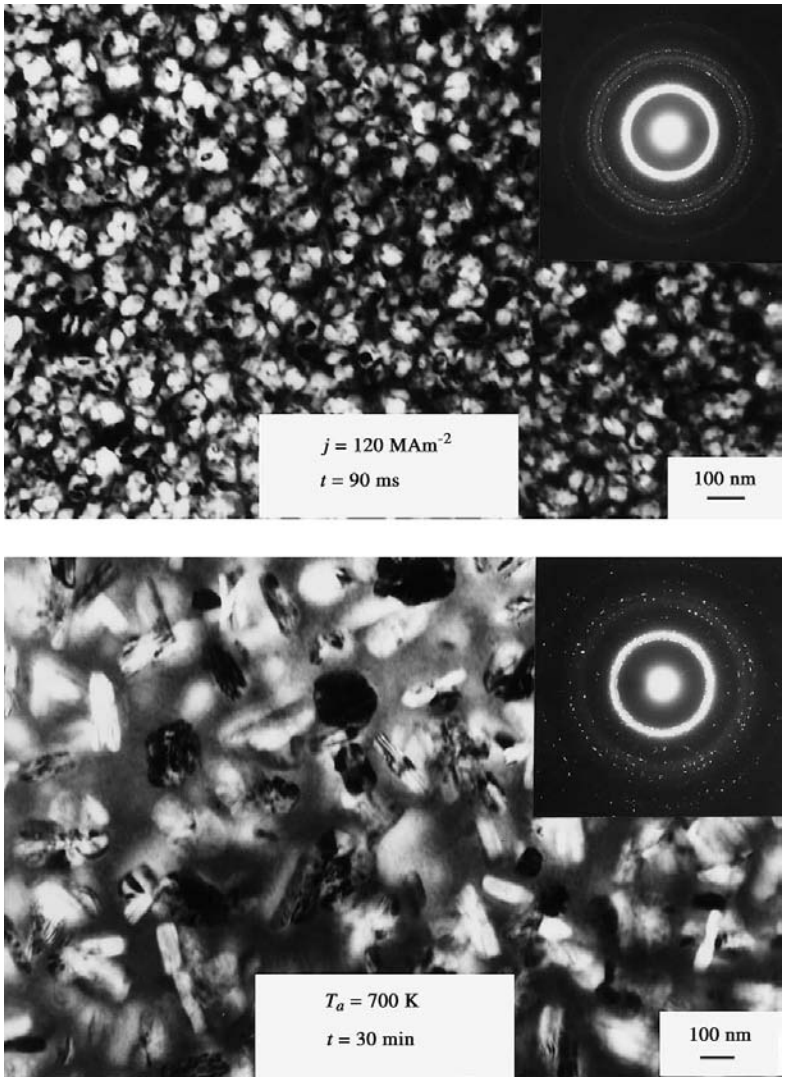


Fig. 3. Transmission electron micrographs and electron diffraction patterns of initially amorphous $Co_{78}Si_{11}B_{11}$ alloy after the first stage of crystallization obtained by: conventional isothermal annealing at 815 K for 30 min or high-temperature flash annealing with current density $j = 120$ MA/m$^2$ and pulse time $t = 90$ ms [92].

tially crystallized $Fe_{76.5}Si_{13.5}B_9$ and $Co_{78}Si_{11}B_{11}$ glasses, respectively, after conventional and flash annealing. It is evident from these figures that application of high-temperature annealing resulted in nanocrystalline structure for both alloys, whereas large crystals were observed after conventional annealing.

On the other hand, it was found [93,96–98] that application of relatively low temperature and longer annealing times also makes possible creation of nanocrystalline structure in ternary or even binary alloys. The influence of annealing temperature on size and morphology of α-Fe crystals in $Fe_{83}B_{17}$ glass after partial crystallization is presented in Fig. 4. The decrease of annealing temperature by 100 K resulted in much smaller crystals and a change in morphology of the crystals. Instead of dendrites with arms span ~100 nm, spherical crystals with average diameter ~35 nm are observed after annealing at the lower temperature.

Studies of metallic glasses after crystallization in a temperature range from 550 to 900 K revealed that size, morphology and composition of crystallization products depend on the annealing temperature [96]. Fig. 5 shows a wide spectrum of structures obtained in the same glass after annealing at different temperatures. The diffraction patterns confirm that in all the cases shown in Fig. 5, $Fe_{76.5}Cu_1Si_{13.5}B_9$ alloy is composed of bcc iron-based crystals and an amorphous matrix. Nevertheless, morphology and size of the crystals depend on the annealing temperature as shown in Fig. 5. The structure obtained after annealing at $T_a = 743$ K is typical for conventional crystallization of this alloy. Crystallization at higher $T_a$ results in smaller crystals. The top micrograph in Fig. 5 shows nanocrystalline structure obtained by high-temperature flash annealing. On the other hand, crystallization at lower $T_a$ results in larger crystals. When the annealing temperature is low enough the crystals become of such big size that they develop dendrites [93]. It was found that this change of morphology from spherulites to dendrites appears when the crystals exceed a critical size. The critical size depends on alloy composition and was observed to be ~130 and ~50 nm for $Fe_{76.5}Cu_1Si_{13.5}B_9$ and $Fe_{83}B_{17}$, respectively.

As seen in the bottom micrograph in Fig. 5, when the annealing temperature is below a critical temperature (~600 K for $Fe_{76.5}Cu_1Si_{13.5}B_9$ glass) again nanocrystalline structure can be obtained. The first results of prolonged (~300 h) annealing of metallic glasses at low temperatures (500–650 K) were published by Masumoto et al. [97], who obtained ultrafine structure for $Pd_{80}Si_{20}$, $Fe_{80}P_{13}C_7$, $Fe_{78}Si_{10}B_{12}$, $Co_{75}Si_{15}B_{10}$ and $Ni_{75}Si_8B_{17}$ alloys. Similar results were obtained by Thorpe et al. [98] for $Fe_{80}Ni_{40}P_{14}B_6$ alloy after annealing at 400 K for 1400 h and by Kulik et al. [93] for $Fe_{77.5}Si_{13.5}B_9$ after annealing at 573 K for 300 h. This effect can be explained assuming the existence in metallic glasses of small quenched-in clusters with short-range order close to a crystalline phase, which can serve as nuclei or sites for heterogeneous nucleation of crystals. It can be assumed that the clusters have a distribution in size in the range from $D_{min}$ up to $D_{max}$. As shown schematically in Fig. 6, if the annealing temperature $T_a$ is higher than $T_{a1}$ then all clusters are smaller than the critical cluster and, hence, all clusters are unstable and dissolve in an amorphous phase. When temperatures of conventional annealing exceed $T_{a1}$ quenched-in clusters do not participate in the crystallization process of metallic glasses. On the other hand, for $T_a < T_{a2}$ all clusters are bigger than the critical size and are stable and can serve as nuclei or nucleation sites. Therefore, the low-temperature nanocrystallization can be a result of existence of such clusters, which are nuclei and start to grow or are heterogeneous nucleation sites of new crystals.

Special method of low-temperature nanocrystallization of Fe–Si–B glasses, using high-current–density electropulsing, was proposed by Teng et al. [100] and Lai et al. [101]. Electropulsing of $Fe_{78}Si_9B_{13}$ glass for 30 min at average temperature ~673 K, which is substantially below the crystallization temperature ($T_{x\ (20\ K/min)} \approx 800$ K [102]), resulted in formation of primary α-Fe(Si) crystallites with average diameter of 23 nm [100]. However, the physical mechanism of electro-nanocrystallization is not yet understood [101]. On the other hand, by application of high pressure during crystallization of $Zr_{41}Ti_{14}Ni_9Cu_{12.5}Be_{22.5}C_1$ bulk glass Wang et al. [103] obtained very fine

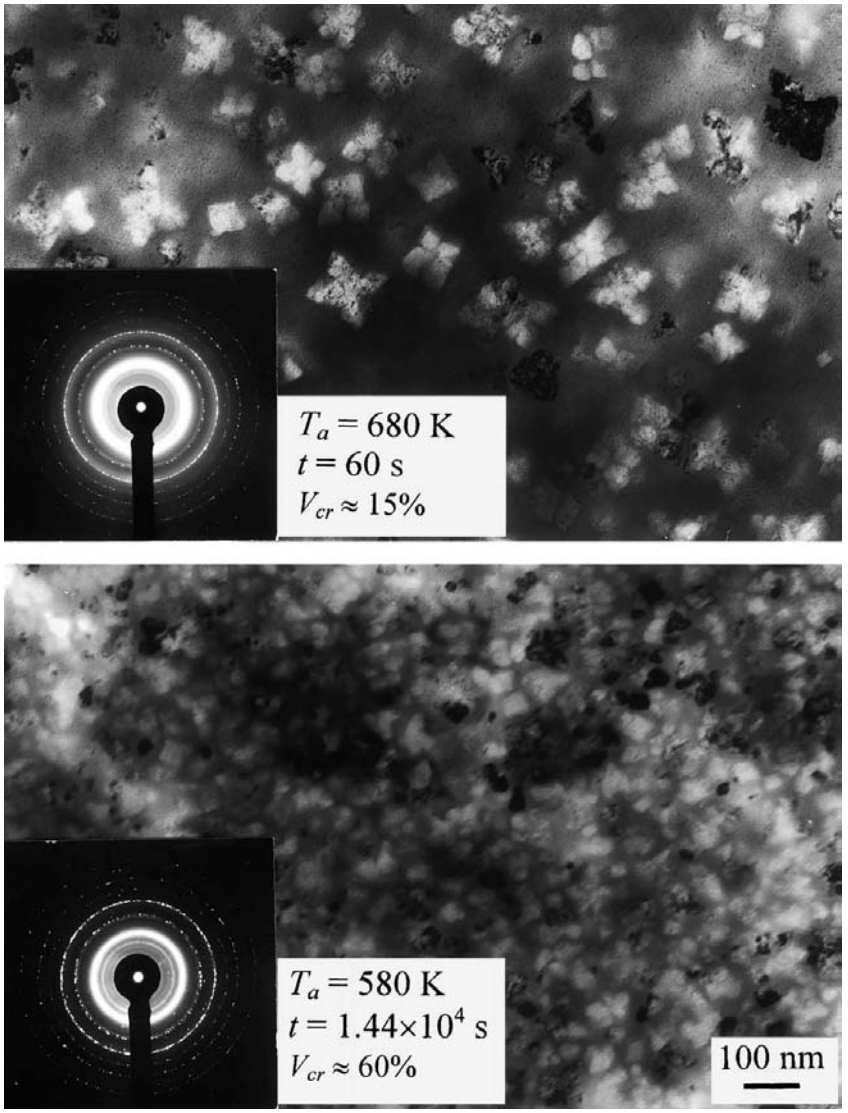


Fig. 4. Transmission electron micrographs and electron diffraction patterns of initially amorphous $Fe_{83}B_{17}$ alloy after conventional isothermal annealing at 680 K for 1 min or low-temperature annealing at 580 K for 4 h [99].

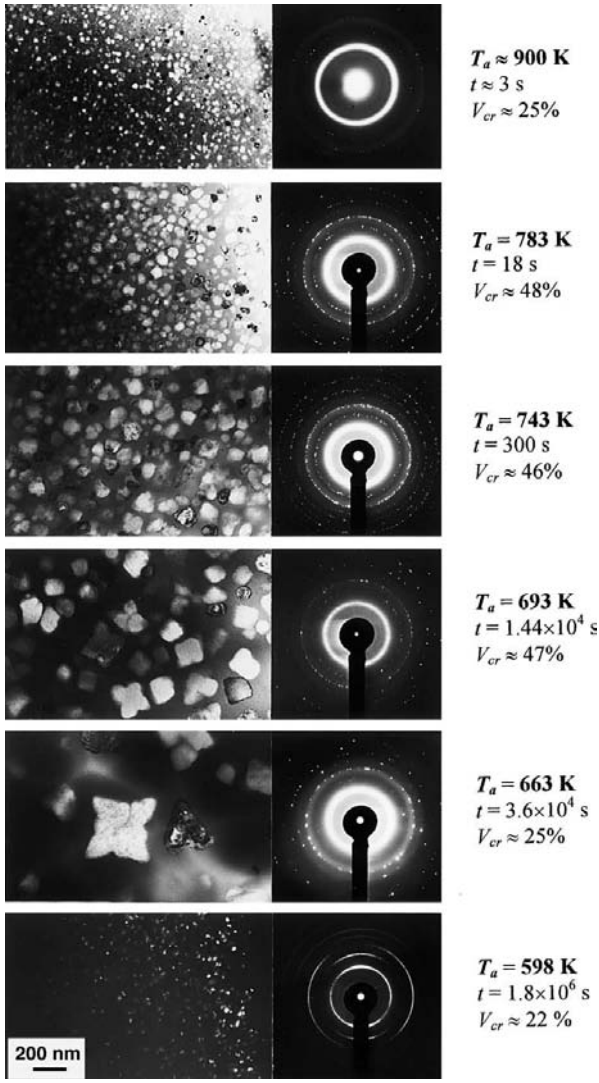


Fig. 5. Transmission electron micrographs and electron diffraction patterns of initially amorphous $Fe_{76.5}Cu_1Si_{13.5}B_9$ alloy after annealing at different temperatures $T_a$ for time $t$ [96].

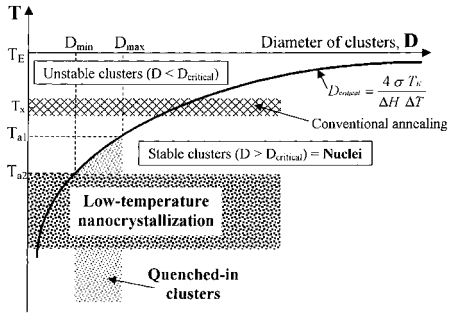


Fig. 6. Schematic diagram of temperature dependence of nucleus critical diameter $D_{critical}$ ($\sigma$-glass/crystal interfacial energy, $T_E$-equilibrium (melting) temperature, $T_a$-annealing temperature, $\Delta H$-crystallization enthalpy, $\Delta T = T_E - T_a$-undercooling).

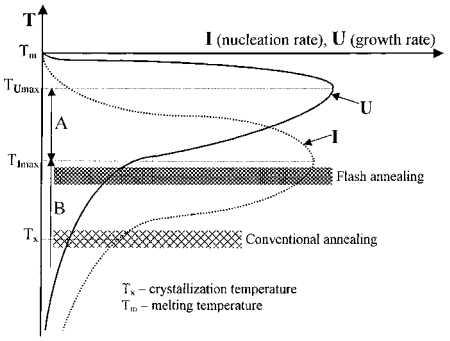


Fig. 7. Schematic diagram of temperature dependence of nucleation rate $I$ and growth rate $U$.

structure with primary crystallites less than 5 nm in diameter. The origin of the nanocrystallization phenomenon was attributed to the copious nucleation and slow crystal growth rate induced by high-pressure annealing. Moreover, it was observed [103] that the pressure reduced the crystallization temperature (by ~16 K/GPa) and determined the phase during the crystallization of the glass.

A possible explanation of the effect of high-temperature annealing on size of crystals appearing during crystallization of metallic glasses is presented in Fig. 7. As is known [104,105], the temperature of maximum growth rate, $T_{U\max}$, is less than the melting temperature, $T_m$, and the temperature of maximum nucleation rate, $T_{I\max}$, is much less than $T_m$. Solidification of liquid alloys usually takes place at $T > T_{I\max}$ (temperature range named **A** in Fig. 7) and crystallization of metallic glasses proceeds at $T_a < T_{I\max}$ (the range **B**). According to Fig. 7, an increase of annealing temperature, $T_a$, should be associated with much greater increase of nucleation rate, $I$, than growth rate, $U$. As a result of this difference, much finer structure will be present after high-temperature crystallization (flash-annealing) than after conventional crystallization.

Substantial reduction of crystal sizes, due to application of high-temperature annealing instead of conventional treatment, was observed also by Załuska et al. [94] in $Fe_{80}B_{20}$ and by Abrosimova et al. [95] in $Fe_{85}B_{15}$ and [106] $Fe_{82.5}B_{17.5}$ glasses. On the other hand, in the case of nanocrystallizing Finemet-type alloys [107,108] and Nanoperm-type alloys [109] both high-temperature annealing as well as conventional annealing led to similar nanocrystalline structure. Nevertheless, the mean size of nanocrystallites was slightly smaller after high-temperature crystallization [107–109].

High-temperature crystallization is most often realized using Joule heating and is called flash or current annealing. A model of Joule heating in amorphous metallic ribbons was developed by Allia et al. [110]. High-temperature nanocrystallization of metallic glasses using Joule heating was applied by many researchers to modify structure and improve properties of nanocrystalline materials. Allia et al. [111] have found that $Fe_{73.5}Cu_1Nb_3Si_{13.5}B_9$ after high-temperature nanocrystallization had a smaller brittleness (by ~30%) and larger initial permeability (by ~50%) than after conventional nanocrystallization. Larger initial permeability was also observed for $Fe_{83}Nb_7B_9Cu_1$ by Park et al. [112], who ascribed this effect to finer structure of the alloy after high-temperature nanocrystallization. Gorria et al. [113] reported much less brittleness of $Fe_{73.5}Cu_1Nb_3Si_{13.5}B_9$ and $Fe_{86}Cu_1Zr_7B_6$ alloys, supporting ten times greater tensile stress after flash annealing than after conventional annealing. Gupta et al. [108] attributed this effect to lower concentration of boron at the

amorphous/crystal interphase because a part of boron is retained inside the nanocrystals if they are formed during current annealing. Altoé et al. [114] reported that magnetically hard $Fe_{78}Nd_4B_{18}$ alloy after high-temperature nanocrystallization had larger remanence (by 12%) and coercivity (by 20%) than the same alloy crystallized conventionally. Kojima et al. [115] performed high-temperature crystallization of amorphous Fe–Co–Nb–(Nd, Pr)–B alloys using rapid heating (with rates up to 3 K/s) in an infrared furnace. Such treatment caused refinement of both primary α-Fe phase and also $Nd_2Fe_{14}B$ phase which precipitates subsequently around the former phase. Consequently the improvement of hard magnetic properties of these Fe-rich nanocomposite materials was achieved [115].

The size, morphology of crystallites and the mechanism of crystallization and crystallization products themselves can depend on the temperature of devitrification of a metallic glass. Recently, Illekova and Duhaj [116] reported for $Fe_{53.5}Ni_{20}Cu_1Nb_3Si_{13.5}B_9$ glass a change of crystallization mode from primary to eutectic, when the heating rate was increasing above 20 K/min, which was a consequence of the shift of crystallization process to higher temperatures. Załuska and Matyja [117] have found that applying high-temperature (flash) annealing a change of crystallization mode from polymorphous (γ phase) to eutectic (α + γ phases) can be obtained in $Fe_{45}Ni_{35}Si_{10}B_{10}$ and $Fe_{40}Ni_{40}Si_{10}B_{10}$ glasses. Abrosimova et al. [106] have observed a change of space-group of $Fe_3B$ tetragonal lattice from $\bar{I}4$ to $P4_2/n$ with the increase of annealing temperature using Joule heating.

The annealing temperature also influences the composition of crystallization products. This effect is indirectly dectected by changing lattice parameter, $a$, of the crystalline phase with change of annealing temperature, as shown in Fig. 8. Annealing of $Fe_{76.5}Cu_1Si_{13.5}B_9$ glass at temperatures higher than 650 K results in formation of α-Fe(Si) (bcc solid solution of silicon in iron) with lattice parameter considerably less than that (0.2866 nm) [118] for pure α-Fe. This effect is commonly known of smaller size of silicon atoms (than iron atoms) forming with iron a substitutional solid solution. From the experimentally determined relation between $a$ and silicon concentration in α-Fe(Si) [118] I estimate that crystals formed in $Fe_{76.5}Cu_1Si_{13.5}B_9$ glass at $T_a > 650$ K contain 14–17 at.% of silicon, depending on their volume fraction. Thus the concentration of silicon in primary crystals is close to its relative (in relation to iron) concentration in the alloy, for which $C_{Si}/(C_{Si} + C_{Fe}) = 0.15$. As seen in Fig. 8, a decrease of $T_a$ results in an increase of $a$ indicating that α-Fe(Si) crystallites become progressively depleted in silicon, which is correlated to decreasing solubility of silicon in iron. Similar effect was observed for Fe–Si–B glasses by Mattern et al. [119] and Ueda et al. [120] and for Finemet-type Fe–Cu–Nb–Si–B alloys by Battezzati and Baricco [121] and Borrego et al. [122].

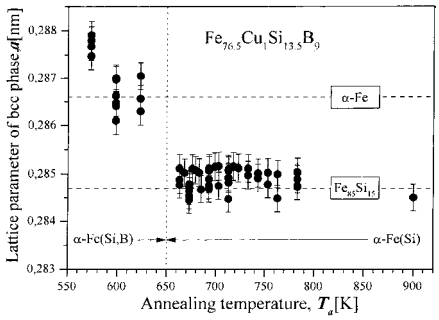


Fig. 8. Influence of devitrification temperature $T_a$ on lattice parameter $a$ of primary crystals in initially amorphous $Fe_{76.5}Cu_1Si_{13.5}B_9$ alloy [96].

As seen in Fig. 8, for $T_a \leqslant 650$ K the lattice parameter of the bcc phase exceeds that for pure α-Fe. This effect is explained by assuming that the crystalline phase is not only a substitutional solid solution of silicon in iron but also an interstitial solid solution of boron in iron. Formation of supersaturated solid solution of boron in α-Fe was observed by Duhaj and Hanic [123] during crystallization of $Fe_{86}B_{14}$ and $Fe_{84}B_{16}$ glasses. Therefore, the observed increase of $a$ with the decrease of $T_a$ can be explained by a decrease of silicon content or/and an increase of boron content in α-Fe(Si,B) phase. In the case of Finemet-type alloys the dependence of $a$ on $T_a$ can be additionally related to niobium atoms entrapped in α-Fe(Si,B) nanocrystals. Similar effect of entrapping atoms of

insoluble element in a basic constituent (solvent) of an alloy, related to crystallization of a metallic glass at relatively low temperatures, was observed also in $Al_{90}Y_{10}$ and $Al_{80}Y_5Ni_{15}$ alloys [124]. For example, in $Al_{90}Y_{10}$ glass heated continuously to the temperature of the maximum of the first calorimetric peak, the lattice parameter $a$ of fcc α-Al(Y) phase increased from 0.4065 to 0.4078 nm with the decrease of maximum annealing temperature from 540 to 440 K (when heating rate was decreased from 200 to 2 K/min). Both $a$s for α-Al(Y) are greater than that (0.4049 nm) [125] for pure α-Al. This effect is associated with the bigger size of yttrium atoms (0.181 nm in diameter) than aluminium atoms (0.142 nm). Larger $a$ indicates greater content of yttrium in α-Al(Y) after crystallization at lower temperature. I conclude that composition of primary crystals is dependent on temperature of devitrification process and the lower the annealing temperature the more the crystals composition differs from the equilibrium state.

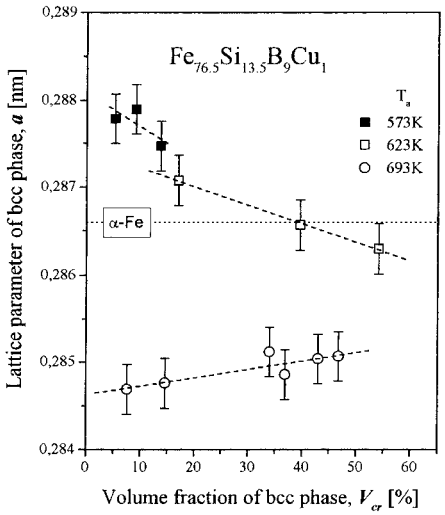


Fig. 9. Dependence of lattice parameter $a$ of primary crystals on their volume fraction $V_{cr}$ (annealing time) in initially amorphous $Fe_{76.5}Cu_1Si_{13.5}B_9$ alloy after isothermal annealing at different temperatures $T_a$ [99].

The composition of primary crystals changes also with annealing time. Fig. 9 shows the dependence of $a$ on volume fraction, $V_{cr}$, of bcc phase in $Fe_{76.5}Cu_1Si_{13.5}B_9$ alloy after isothermal annealing at different temperatures. These results can be explained assuming that concentrations of the solute elements (silicon and boron) decrease with increase of $V_{cr}$ or in other words with increase of annealing time. At high temperatures (693 K) mainly silicon is dissolved in iron and a decrease of its concentration in α-Fe(Si) with annealing time should result in the observed increase of $a$. On the other hand, at low temperatures (573 and 623 K) boron in α-Fe(Si,B) can be expected by me and the decrease of its content with annealing time should result in the observed decrease of $a$ of this phase. Remarkable decrease of $a$ of primary phase with the annealing time was observed also for Finemet-type Fe–Cu–Nb–Si–B alloys [36,121,122,126]. On the other hand, Curie temperature $T_c$ of the nanocrystalline phase in Finemet® increases with the annealing time [127]. These changes of $a$ and $T_c$ indicate a significant change in the composition with increasing size of primary nanocrystals. It is very probable that small Fe-based nanocrystallites are supersaturated by all alloying elements and tend to the equilibrium state during crystallization process. Barquín et al. [126] observed that composition stabilization of Fe(Si) nanocrystals during crystallization process of $Fe_{73.5}Cu_1Nb_3Si_{13.5}B_9$ glass was achieved after 1 h annealing at 773 K. Therefore, it can be concluded that the increase of annealing time of a metallic glass results not only in a larger volume fraction of crystalline phase and size of crystallites but also in a composition of the phase closer to the equilibrium state.

## 4. Conclusions

The possibility of nanocrystalline phase creation by crystallization of metallic glasses depends mainly on the alloy composition and temperature of the process. Conventional crystallization enables the creation of nanocrystalline structure only in glasses with a specific composition. Two non-conventional methods of nanocrystallization of metallic glasses can be applied: (1) high-temperature

nanocrystallization using flash annealing followed by fast cooling, and (2) low-temperature nanocrystallization, by prolonged annealing at temperatures below the critical temperature. With these methods it is possible to form nanocrystalline structure in any metallic glass having a primary crystallization process.

Temperature of devitrification process influences sizes and compositions of crystallization products for any volume fraction of crystalline phase. The change of crystallites sizes can lead to a change in their morphology, e.g. from spherulites to dendrites, when the crystallites exceed a critical size (~50 and ~130 nm for $Fe_{83}B_{17}$ and $Fe_{76.5}Cu_1$ $Si_{13.5}B_9$ alloys, respectively). The change of a crystallite composition usually affects the lattice parameter but also can result in a change of crystallographic structure of the same phase or in formation of another phase. Annealing temperature sometimes determines the type of crystallization process (primary, eutectic or polymorphous).

Composition of primary crystallites is dependent on temperature as well as on time of devitrification process. The lower the annealing temperature and the shorter the annealing time (smaller crystallites) the more the crystallites composition differs from the equilibrium state.

## References


[1] C. Suryanarayana, Int. Mater. Rev. 40 (1995) 41.
[2] B. Cantor, Mater. Sci. Forum 307 (1999) 143.
[3] A.L. Greer, Mater. Sci. Forum 269–272 (1998) 3.
[4] A. Inoue, K. Ohtera, A.-P. Tsai, T. Masumoto, Jpn. J. Appl. Phys. 27 (1988) L280.
[5] Y.H. Kim, A. Inoue, T. Masumoto, Trans. JIM 31 (1990) 747.
[6] H. Chen, Y. He, G.J. Shiflet, S.J. Poon, Scr. Metall. 25 (1991) 1421.
[7] J.H. Paik, F.W.J. Botta, A.R. Yavari, Mater. Sci. Forum 225–227 (1996) 305.
[8] Z.C. Zhong, X.Y. Jiang, A.L. Greer, Mater. Sci. Eng. A 226–228 (1997) 531.
[9] J. Latuch, A. Kokoszkiewicz, H. Matyja, Mater. Sci. Eng. A 226–228 (1997) 809.
[10] Z.C. Zhong, X.Y. Jiang, A.L. Greer, Philos. Mag. 76 (1997) 505.
[11] H.S. Kim, P.J. Warren, B. Cantor, H.R. Lee, Nanostr. Mater. 11 (1999) 241.
[12] Y. Yoshizawa, S. Oguma, K. Yamauchi, J. Appl. Phys. 64 (1988) 6044.
[13] K. Suzuki, N. Kataoka, A. Inoue, T. Masumoto, Mater. Trans. JIM 31 (1990) 743.
[14] K. Suzuki, A. Makino, A. Inoue, T. Masumoto, J. Appl. Phys. 74 (1993) 3316.
[15] H.K. Lachowicz, A. Ślawska-Waniewska, J. Magn. Magn. Mater. 133 (1994) 238.
[16] A. Makino, T. Bitoh, A. Inoue, T. Masumoto, J. Appl. Phys. 81 (1997) 2736.
[17] M.A. Willard, D.E. Laughlin, M.E. McHenry, D. Thoma, K. Sickafus, J.O. Cross, V.G. Harris, J. Appl. Phys. 84 (1998) 6773.
[18] R. Coehoorm, D.B. De Mooiji, J.P.W.B. Duchateau, K.H.J. Buschow, J. Phys. 49 (1988) 699.
[19] E.F. Kneller, R. Hawing, IEEE Trans. Magn. 27 (1991) 3588.
[20] A. Manaf, R.A. Buckly, H.A. Davies, J. Magn. Magn. Mater. 128 (1993) 302.
[21] L. Withanawasam, A.S. Murphy, G.C. Hadjipanayis, R.F. Krause, J. Appl. Phys. 78 (1994) 7065.
[22] A. Inoue, A. Takeuchi, A. Makino, T. Masumoto, Mater. Trans. JIM 36 (1995) 676.
[23] A. Inoue, A. Takeuchi, A. Makino, T. Masumoto, Mater. Trans. JIM 36 (1995) 962.
[24] T. Hopfinger, A.R. Yavari, D. Negri, J. Alonso, A. Hernando, J. Magn. Magn. Mater. 164 (1996) L7.
[25] A. Takeuchi, A. Inoue, A. Makino, Mater. Sci. Eng. A 226–228 (1997) 636.
[26] A. Inoue, H. Kimura, Mater. Sci. Eng. A 286 (2000) 1.
[27] T. Kulik, G. Vlasák, R. Żuberek, Mater. Sci. Eng. A 226–228 (1997) 701.
[28] G. Herzer, IEEE Trans. Magn. MAG-25 (1989) 3327.
[29] U. Herold, U. Köster, in: B. Cantor (Ed.), Proceedings of the Third International Conference Rapidly Quenched Metals, vol. I, Metals Society, London, 1978, p. 281.
[30] U. Köster, U. Herold, in: H.J. Güntherodt, H. Beck (Eds.), Glassy Metals I, Topics in Applied Physics, vol. 46, Springer, Berlin, 1981, p. 225.
[31] D. Crespo, T. Pradell, N. Clavaguera, M.T. Clavaguera-Mora, Mater. Sci. Eng. A 238 (1997) 160.
[32] U. Köster, U. Schünemann, M. Blank-Bewersdorff, S. Brauer, M. Sutton, G.B. Stephenson, Mater. Sci. Eng. A 133 (1991) 611.
[33] L. Battezzati, C. Antonione, G. Riontino, F. Marino, H.R. Sinning, Acta Metall. Mater. 39 (1991) 2107.
[34] M. Baricco, L. Battezzati, Mater. Sci. Forum 179–181 (1995) 597.
[35] W.N. Myung, L. Battezzati, M. Baricco, K. Oaki, A. Inoue, T. Masumoto, Mater. Sci. Eng. A 179&180 (1994) 371.
[36] U. Köster, J. Meinhardt, Mater. Sci. Eng. A 178 (1994) 271.
[37] K. Lu, Mater. Sci. Eng. R 16 (1996) 161.
[38] M.E. McHenry, M.A. Willard, D.E. Laughlin, Prog. Mater. Sci. 44 (1999) 291.
[39] H. Iwanabe, B. Lu, M.E. McHenry, D.E. Laughlin, J. Appl. Phys. 85 (1999) 4424.

[40] S. He, K. He, B. Shen, H. Zhang, S. Zhang, H. Guo, J. Appl. Phys. 86 (1999) 6301.
[41] M. Müller, H. Grahl, N. Mattern, U. Kühn, B. Schnell, J. Magn. Magn. Mater. 160 (1996) 284.
[42] T. Kulik, Magnetically Soft Nanocrystalline Materials Obtained by the Crystallization of Metallic Glasses, Publishing House of Warsaw University of Technology, Warsaw, 1998, p. 38 (in Polish).
[43] K. Hono, K. Hiraga, Q. Wang, A. Inoue, T. Sakurai, Acta Metall. Mater. 40 (1992) 2137.
[44] K. Hono, J.-L. Li, Y. Ueki, A. Inoue, T. Sakurai, Appl. Surf. Sci. 67 (1993) 398.
[45] J.D. Ayers, V.G. Harris, J.A. Sprague, W.T. Elam, H.N. Jones, Acta Mater. 46 (1998) 1861.
[46] M. Ohnuma, K. Hono, H. Onodera, J.S. Pedersen, S. Linderoth, Nanostr. Mater. 12 (1999) 693.
[47] Y. Zhang, K. Hono, A. Inoue, T. Sakurai, Scr. Mater. 34 (1996) 1705.
[48] N. Kataoka, T. Matsunaga, A. Inoue, T. Masumoto, Mater. Trans. JIM 30 (1989) 947.
[49] P. Duhaj, P. Švec, D. Janičkovič, I. Mat'ko, Mater. Sci. Eng. A 133 (1991) 398.
[50] Y. Zhang, F. Zhu, J. Mater. Res. 15 (2000) 1271.
[51] H. Bakker, in: M. Magini, H. Wöhlbier (Eds.), Materials Science Foundations vol. 1: Enthalpies in Alloys, TransTech, Aedermannsdorf, 1998, p. 69.
[52] R.W. Cahn, in: R.W. Cahn, P. Haasen, E.J. Kramer (Eds.), Materials Science and Technology, vol. 9: Glassses and Amorphous Materials, VCH, Weinheim, 1991, p. 493.
[53] A.R. Yavari, O. Drbohlav, Mater. Trans. JIM 36 (1995) 896.
[54] Y. Swilem, E. Sobczak, R. Nietubyć, P. Dłużewski, A. Ślawska-Waniewska, J. Alloys Comp. 286 (1999) 103.
[55] H. Hermann, A. Heinemann, N. Mattern, A. Wiedenmann, Europhys. Lett. 51 (2000) 127.
[56] M. Kopcewicz, A. Grabias, D.L. Williamson, J. Appl. Phys. 82 (1997) 1747.
[57] T. Kulik, A. Hernando, Mater. Sci. Forum 179–181 (1995) 587.
[58] S.D. Kaloshkin, Mater. Sci. Forum 307 (1999) 119.
[59] A.R. Yavari, O. Drbohlav, Mater. Sci. Forum 225–227 (1996) 295.
[60] J.C. Foley, D.R. Allen, J.H. Perepezko, Mater. Sci. Eng. A 226–228 (1997) 569.
[61] T. Gloriant, A.L. Greer, Nanostr. Mater. 10 (1998) 389.
[62] M. Calin, A. Rüdiger, U. Köster, Mater. Sci. Forum 343–346 (2000) 359.
[63] M. Calin, U. Köster, Mater. Sci. Forum 269–272 (1998) 749.
[64] S. Saini, A. Zaluska, Z. Altounian, J. Non-Cryst. Solids 250–252 (1999) 714.
[65] G.E. Abrosimova, A.S. Aronin, Yu.V. Kir'janov, T.F. Gloriant, A.L. Greer, Nanostr. Mater. 12 (1999) 617.
[66] K. Hono, D.H. Ping, Mater. Sci. Forum 307 (1999) 69.
[67] A. Inoue, T. Zhang, T. Masumoto, Mater. Trans. JIM 31 (1990) 177.
[68] V.V. Molokanov, V.N. Chebotnikov, Key Eng. Mater. 41&42 (1990) 319.
[69] A. Pecker, W.L. Johnson, Appl. Phys. Lett. 63 (1993) 2342.
[70] A. Inoue, C. Fan, Nanostr. Mater. 12 (1999) 741.
[71] A. Inoue, C. Fan, A. Takeuchi, J. Non-Cryst. Solids 250–252 (1999) 724.
[72] A. Inoue, Intermetallics 8 (2000) 455.
[73] U. Köster, A. Rüdiger, J. Meinhardt, Mater. Sci. Forum 307 (1999) 9.
[74] B.S. Murty, D.H. Ping, K. Hono, A. Inoue, Acta Mater. 48 (2000) 3985.
[75] M.W. Chen, A. Inoue, T. Sakurai, D.H. Ping, K. Hono, Appl. Phys. Lett. 74 (1999) 812.
[76] M.W. Chen, A. Inoue, T. Zhang, A. Sakai, T. Sakurai, Intermetalics 8 (2000) 493.
[77] J. Löffler, W.L. Johnson, Appl. Phys. Lett. 76 (2000) 3394.
[78] P.J. Desre, Philos. Mag. 80 (2000) 401.
[79] T. Kulik, Mater. Sci. Eng. A 159 (1992) 95.
[80] G. Herzer, IEEE Trans. Magn. MAG-26 (1990) 1397.
[81] T.H. Noh, M.B. Lee, H.J. Kim, I.K. Kang, J. Appl. Phys. 67 (1990) 5568.
[82] M. Müller, N. Mattern, L. Illgen, Z. Metallkd. 82 (1991) 895.
[83] M. Vázquez, P. Marín, J. González, A. Hernando, E. Pulido, in: A. Conde, C.F. Conde, M. Millán (Eds.), Trends in Non-Crystalline Solids, World Scientific, Singapore, 1992, p. 157.
[84] C. Polak, R. Grössinger, H. Sassik, G. Herzer, J. Magn. Magn. Mater. 104–107 (1992) 100.
[85] I. Škorvánek, R. Gerling, J. Appl. Phys. 72 (1992) 3417.
[86] C. Wittwer, W. Riehemann, W. Heye, J. Magn. Magn. Mater. 133 (1994) 287.
[87] J. Bigot, N. Lecaude, J.C. Perron, C. Milan, C. Ramiarinjaona, J.F. Rialland, J. Magn. Magn. Mater. 133 (1994) 299.
[88] Z. Wang, K. He, S. He, Y. Zhang, Y. Fu, L. Zhang, J. Magn. Magn. Mater. 171 (1997) 300.
[89] V. Franco, C.F. Conde, A. Conde, J. Appl. Phys. 84 (1998) 5108.
[90] M. Miglierini, M. Kopcewicz, B. Idzikowski, Z.E. Horváth, A. Grabias, I. Škorvánek, P. Duźewski, Cs.S. Daróczi, J. Appl. Phys. 85 (1999) 1014.
[91] T. Kulik, T. Horubała, H. Matyja, Mater. Sci. Eng. A 157 (1992) 107.
[92] T. Kulik, D. Bucka, H. Matyja, J. Mater. Sci. Lett. 12 (1993) 76.
[93] T. Kulik, J. Ferenc, H. Matyja, Mater. Sci. Forum 235–238 (1997) 421.
[94] A. Załuska, L. Załuski, A. Witek, Mater. Sci. Eng. 89 (1989) 11.
[95] G.E. Abrosimova, A.S. Aronin, V.A. Stelmuh, Solid State Phys. 33 (1991) 3570 (in Russian).
[96] T. Kulik, Mater. Sci. Forum 269–272 (1998) 707.
[97] T. Masumoto, H. Kimura, A. Inoue, Y. Waseda, Mater. Sci. Eng. 23 (1976) 141.
[98] S.J. Thorpe, B. Ramaswami, K.T. Aust, Acta Metall. 36 (1988) 795.
[99] T. Kulik, unpublished data.

[100] G.Q. Teng, Y.S. Chao, Y. Geng, L. Dong, Z.H. Lai, Jpn. J. Appl. Phys. 35 (1996) 5320.
[101] Z.H. Lai, H. Conrad, G.Q. Teng, Y.S. Chao, Mater. Sci. Eng. A 287 (2000) 238.
[102] N. DeCristofaro, A. Freilich, G. Fish, J. Mater. Sci. 17 (1982) 2365.
[103] W.H. Wang, D.W. He, D.Q. Zhao, Y.S. Yao, M. He, Appl. Phys. Lett. 75 (1999) 2770.
[104] U. Köster, J. Meinhardt, H. Alves, Mater. Sci. Forum 179–181 (1995) 533.
[105] A.L. Greer, Metall. Mater. Trans. 27A (1996) 549.
[106] G.E. Abrosimova, A.S. Aronin, A.V. Bezrukov, S.P. Pankratov, A.V. Serebriakov, Metallofizika 4 (1982) 69 (in Russian).
[107] R. Houssa, V. Franco, A. Conde, J. Magn. Magn. Mater. 203 (1999) 199.
[108] A. Gupta, N. Bhagat, G. Principi, A. Maddalena, N. Malhotra, B.A. Dasannacharya, P.S. Goel, H. Amenitsch, S. Bernstorff, Intermetallics 8 (2000) 287.
[109] F.C.S. da Silva, E.F. Ferrari, M. Knobel, I.L. Torriani, D.R. dos Santos, Appl. Phys. Lett. 77 (2000) 1375.
[110] P. Allia, M. Baricco, M. Knobel, P. Tiberto, F. Vinai, Mater. Sci. Eng. A 179&180 (1994) 361.
[111] P. Allia, P. Tiberto, M. Baricco, F. Vinai, Appl. Phys. Lett. 63 (1993) 2759.
[112] J.Y. Park, K.Y. Kim, T.H. Noh, M.B. Lee, S.J. Suh, Mater. Sci. Eng. A 226–228 (1996) 685.
[113] P. Gorria, I. Orue, F. Plazaola, J.M. Barandiarán, J. Appl. Phys. 73 (1993) 6600.
[114] M.V.P. Altoé, M.S. Lancarotte, H.R. Rechenberg, F.P. Missell, J.M. González, IEEE Trans. Magn. 31 (1995) 3614.
[115] A. Kojima, A. Makino, A. Inoue, J. Appl. Phys. 87 (2000) 6576.
[116] E. Illekova, P. Duhaj, Acta Phys. Slovaca 50 (2000) 525.
[117] A. Załuska, H. Matyja, Mater. Sci. Eng. 97 (1988) 347.
[118] W.B. Pearson, Lattice Spacings and Structures of Metals, vol. II, Pergamon, London, 1967, p. 935.
[119] N. Mattern, A. Danzig, M. Müller, Mater. Sci. Eng. A 194 (1995) 77.
[120] Y. Ueda, S. Ikeda, Y. Minami, Mater. Sci. Eng. A 181&182 (1994) 992.
[121] L. Battezzati, M. Baricco, Philos. Mag. 68 (1993) 813.
[122] J.M. Borrego, C.F. Conde, M. Millán, A. Conde, M.J. Capitán, J.L. Joulaud, Nanostr. Mater. 10 (1998) 575.
[123] P. Duhaj, F. Hanic, Phys. Status Solid 76 (1983) 467.
[124] T. Kulik, J. Latuch, Mater. Sci. Forum 360–362 (2001) 149.
[125] ASTM Card No. 4-787.
[126] L.F. Barquín, J.C. Gómez Sal, P. Gorria, J.S. Garitaonandia, J.M. Barandiaran, J. Phys.: Condens. Matter. 10 (1998) 5027.
[127] M.S. Leu, T.S. Chin, I.C. Tung, C.M. Lee, Jpn. J. Appl. Phys. 38 (1999) 707.

*Zbigniew Tucholski*

# Stop kolejowy bahnmetall prof. Jana Czochralskiego i jego zastosowanie w kolejnictwie

Pod koniec XIX wieku wraz z uformowaniem się procesów technologicznych produkcji masowej, zmieniła się w znacznym stopniu filozofia produkcji przemysłowej. Wymagało to przebudowania istniejących zakładów przemysłowych w celu optymalizacji produkcji. Nowa organizacja przemysłu zakładała powszechne wprowadzanie Tayloryzmu, jako nowego kierunku naukowej organizacji pracy. W projektowaniu zwrócono wówczas uwagę na znaczące ograniczenie kosztów, które stało się jednym z głównych cech klasycznej produkcji przedseryjnej. Technologia budowy maszyn, uzbrojenia i konstrukcji stalowych zakładała wówczas wprowadzanie całkowitej zamienność części z wykorzystywaniem tolerancji pasowań. Rozwój mechaniki szedł w kierunku doskonalenia konstrukcji z wykorzystaniem nowych metod matematycznych, równolegle z ulepszaniem stosowanych materiałów. W drugiej połowie XIX wieku czynniki te stały się przyczyną niezwykle szybkiego rozwoju nowoczesnego metaloznawstwa – wytrzymałości materiałów, krystalografii, metalografii i fizykochemii.

Europejscy i amerykańscy metaloznawcy rozpoczęli wówczas wyścig w zakresie opracowania materiałów zastępczych w oszczędności strategicznych metali. Bezpośrednią przyczyną tych badań były względy militarne. U progu wielkiej wojny poszukiwano w wielu dziedzinach techniki możliwości oszczędności materiałów, które można było zastosować bezpośrednio w produkcji zbrojeniowej. Na początku XX w., w prace nad opracowaniem nowoczesnych materiałów zastępczych zaangażował się jeden z wybitnych metaloznawców Jan Czochralski.

Panewki ślizgowe łożysk osi parowozów i wagonów kolejowych oraz układu napędowego lokomotyw, od zarania kolejnictwa wykonywano z brązu. Ze względu na konieczność ich kosztownej wymiany po zużyciu (pracochłonnego odlewania nowych panewek i ich obróbki mechanicznej) z czasem zaczęto stosować stopy do wylewania cienkiej warstwy w panewkach. Zastosowanie brązu do produkcji panewek było korzystne, w przypadku wytopienia stopu nie niszczyły czopów[1].

Do wylewania panewek wykorzystywano stop na osnowie cyny – tzw. babbit, wynaleziony w 1839 r. przez amerykańskiego złotnika Isaaca Babbitt'a[2], o składzie: 83-88% Sn, 8%-10% Sb, 3%-6% Cu oraz 0,5% Pb. Zbliżonym do babbitu stosowanym do wylewania łożysk ślizgowych w kolejnictwie okazał się stop Charpy'ego, o bardzo dobrych własnościach: Sn 83,4%, Sb 11,1%, Cu 5,5%. Od lat 80. XIX w. prowadzono intensywne prace badawcze w dziedzinie łożyskowych stopów cynowych.

[1] Dopiero u progu II wojny światowej na kolejach sowieckich (SŻD) rozpoczęto wymienianie panewek brązowych na żeliwne. Podczas wojny w taborze kolejowym wielu państw zastępowano panewki brązowe wykonanymi z miękkiego żeliwa, stosowano również brązowe wkładki mocowane w żeliwnych panewkach.

[2] Isaac Babbit (1799-1862), amerykański złotnik, wynalazca stopu łożyskowego babbit (1839).

Pod koniec XIX w. na Kolejach Pruskich (KPEV) używano stopu łożyskowego tzw. „białego metalu" (weissmetall) o składzie: Sn 83%, Sb 11%, Cu 6% lub Sn 85%, Sb 10%, Cu 5%[3]; na Kolejach Austro-Węgierskich (KKStB): Sn 82%, Sb 12%, Cu 6%; wcześniej wzorowany na stopie Kolei Bawarskich i Alzacko-Lotaryńskich zastosowano na Kolejach Rosyjskich[4]; na Kolejach Angielskich: Sn 91,17%, Sb 4,4%, Cu 3,9%, Ni 0,53%. Dodatek Ni w angielskich stopach nie poprawiał znacząco ich własności[5].

Na początku XX wieku w Niemczech rozpoczęto przyspieszoną militaryzacje, rozbudowywano infrastrukturę transportową oraz zaplecze techniczne, przygotowując się do przyszłej wojny. „Kręgosłupem" szybkiej mobilizacji armii pruskiej stała się wówczas rozbudowywana w tym celu sieć państwowych i prywatnych linii kolejowych.

Jednym z najistotniejszych zagadnień stała się kwestia zastosowania zamienników strategicznych metali kolorowych i stopów, które posiadały duże znaczenie przy produkcji uzbrojenia. Zwrócono wówczas uwagę na łożyska ślizgowe taboru kolejowego - do zalewania panwi osiowych stosowano na kolejach pruskich KPEV bardzo duże ilości cyny. Ze względu na znaczenie transportu kolejowego, rozbudowywanego od kilkudziesięciu lat dla celów militarnych według doktryny feldmarszałka Helmuta von Moltkego, stop ten musiał cechować się dużą niezawodnością. U progu wielkiej wojny zintensyfikowano prace w celu opracowania takiego materiału.

W 1912 r. prof. Jan Czochralski wspólnie ze swym mentorem, prof. Wichardem von Moellendorffem, opracował chronologicznie pierwszy stop zastępczy na osnowie ołowiu, z dodatkiem metali ziem alkalicznych (z przewagą Ca)[6]. Od tego wynalazku rozpoczął się intensywny wyścig największych niemieckich ośrodków naukowych w zakresie metaloznawstwa: „Praca nad tworzeniem nowych stopów ołowiu z metalami alkalicznymi i metalami ziem alkalicznych skoncentrowana była w Niemczech w ostatnim 20-leciu w towarzystwach: Lurgi-Gesellschaf, Metall bank und Metallurgische Gesellschaft a także Metallgesellschaft przy udziale prof. J. Czochralskiego w okresie jego pobytu w Niemczech."[7]Badania w celu opracowania nowych stopów podjął również koncern zbrojeniowy Friedrich Krupp AG Essen.

Po wybuchu wojny, w 1915 r. prof. Heinrich Hanemann[8]opracował stop ołowiu z dodatkami sodu metalicznego. Okazało się jednak, że ze względu na znaczną jego

[33] Des ingenieurstaschenbuchherausgegebenvomvereinhütte, abteilung II, Berlin 1899 j., s. 241; Otto LuegersLexikon der gesamteTechnik und ihrerHilfswissenschaften, VI Band, Studgart, Leipzig j. 1894-99, s. 53.

[4]W 1886 r. inż. Jan Petrozolin uzyskał w Niemczech recepturę na stop stosowany na Kolejach Bawarskich i Alzacko-Lotaryngskich. Stop został wprowadzony w taborze wagonowym Kolei Mikołajewskiej, a następnie innych rosyjskich kolei. Por. Tucholski Z., Wspomnienia Jana Petrozolina, inżyniera pociągu cara Aleksandra III, w: „Przegląd Historyczny", Z. 2, 2013, s. 367.

[5]Bolšaâtehničeskajâenciklopediâ 1927, T. 2, Hasło Antifrikcionnyesplawy, http://www.bte1927.ru/taxonomy/term/1, dostęp 12.04.2014 r.

[6]Czochralski J., Nowoczesne kolejowe metale łożyskowe jako klasyczny przykład rozwiązania namiastkowania stopów cynowych, w: Przegląd Mechaniczny, 1936, nr 12, s. 395. Najprawdopodobniej jest to informacja błędna, bowiem w 1909 r. w koncernie Kruppa opracowano stop na osnowie ołowiowej o składzie: 1,3% Na + 0,08% Sn + 0,11% Sb + reszta Pb; por. Feszczenko-Czopiwski J., O tanich stopach łożyskowych z osnową ołowianą, w: Przegląd Techniczny, nr 10, 1928 r., s. 196.

[7]Krupkowski A., Stop łożyskowy „B" w świetle oceny technicznej i gospodarczej, w: Przegląd Mechaniczny 1937, T. III, nr 1, s. 9.

[8]Heinrich Hanemann (1883-1960), inżynier, profesor, wybitny metaloznawca, wynalazca mikrotwardościomierzaHanemanna.

zawartość ulegała szybkiemu rozkładowi. Prawie równoległe prace prowadził radca ministerialny Halfmann[9], starając się udoskonalić stopy o osnowie cynowej – nie zdały jednak egzaminu i nie zostały wprowadzone do powszechnego użytku w taborze kolejowym[10].

W 1915 r. w wyniku wyniszczającej wojny, zapasy stosowanych materiałów stopniowo wyczerpywały się. Groziło to paraliżem transportu kolejowego, uniemożliwiającym przewozy wojskowe. Zważywszy na fakt, iż wielka wojna była „wojną kolejową", a do przerzucania pomiędzy frontami całych korpusów wykorzystywano transport kolejowy, groziło to klęską Niemiec. Metaloznawcy podjęli wówczas intensywne badania w celu opracowania odpowiedniego zamiennika wykorzystywanej w kolejnictwie cyny.

W 1917 r. prof. Walther Mathesius[11] opracował stop Calcium-Metall Ca, Mg, Cd, zawierający 2,5% Ca i prawie tyle samo cyny, miedzi, kadmu i sodu łącznie. W tym samym roku, William Kroll[12] wynalazł kolejny stop „Lurgi-Kroll" (nazwa handlowa lurgilager metall) zawierający od 2 do % Ba i jeszcze mniej Ca i Na – od 0,5 do 1%[13].

Stop ten odegrał decydującą rolę w końcowej fazie wojny, dzięki niemu możliwe było utrzymanie sprawności transportu kolejowego. Jego wadą była jednak niedostateczna trwałość, niemieccy metaloznawcy do końca wojny prowadzili intensywnie badania w celu jego ulepszenia. Prac w zakresie stopów zastępczych nie przerwano po zakończeniu wojny, ze względu na embargo na dostawy cyny dla Niemiec oraz prowadzoną już w latach 20. XX w. przez Reichswehre i sfery wojskowo-przemysłowe skrytą remilitaryzację.

W 1920 r. prof. Walther Mathesius opracował kolejny stop zawierający Ca, Sr. Dwa lata później starano się zastosować bez powodzenia stop na osnowie aluminiowej Silumin, opracowany przez Metallgeselschaft AG[14]. Należy podkreślić, iż konkurencja między laboratoriami badawczymi niemieckich koncernów, była czynnikiem inspirującym szybki rozwój niemieckiej nauki.

Jeszcze w 1916 r. Metallbank AG we Frankfurcie nad Menem, konsorcjum 10 wielkich firm metalurgicznych, ufundowało prof. Czochralskiemu doskonale wyposażony instytut metalurgiczny – Metall-Laboratorium der Metallgeselschaft. Jednym z jego głównych zadań było prowadzenie badań nad militarnym zastosowaniem materiałów zastępczych. W 1917 r. prof. Czochralski zorganizował instytut i objął funkcję jego dyrektora. Pierwszym osiągnięciem było opracowanie technologii produkcji pierścieni wiodących do pocisków artyleryjskich[15].

[9] Danych biograficznych nie ustalono.
[10] Czochralski J., Nowoczesne kolejowe metale…, op. cit., s. 395.
[11] Walther Mathesius (1859-1945), inżynier, wybitny metaloznawca, tajny radca i profesor metalurgii i hutnictwa, rektor Politechniki Berlińskiej.
[12] William Justin Kroll (1889-1973), inżynier, metaloznawca. Absolwent Politechniki w Berlinie-Charlotenburgu, wynalazca kilku stopów oraz procesu otrzymywania tytanu metalicznego z rud, wynalezionego w 1940, który otrzymał nazwę procesu Krolla.
[13] Czochralski J., Lagermetalle und IhreTechnologischeBewertung, Berlin 1924 j., s. 6.
[14] Czochralski J., Nowoczesne kolejowe metale…, op. cit., s. 395.
[15] Por. Archiwum Polskiej Akademii Nauk, Materiały Jana Czochralskiego 6, k. 48; Domański E., Czochralski Jan (1885-1953) profesor zwyczajny metalurgii i metaloznawstwa Politechniki Warszawskiej – w 1929 roku doktor honoris causa PW.

W 1924 r. prof. Jan Czochralski najprawdopodobniej[16] we współpracy z prof. Georgiem Welterem[17], opracował stop, który otrzymał nazwę bahnmetall (metal B). Stop na osnowie ołowiowej, o składzie 0,73% Ca, 0,58% Na, 0,04% Li i 0,02% – 0,2% Al, reszta Pb, utwardzono niewielkimi ilościami wapnia, sodu, litu i aluminium[18].

Stop bahnmetall okazał się znacznie lepszy od stopu prof. Mathesiusa z 1920 r.,26 sierpnia 1926 r. otrzymał niemiecki patent nr 433370 (zgłoszony 12 marca 1924 r.)[19], w klasie 40b, grupie 11. Został wydany przez Reichspatentamt, jego właścicielem był Metall bank und Metall gesellchaft A.G. we Frankfurcie nad Menem[20].

Biograf prof. Czochralskiego dr Paweł E. Tomaszewski przedstawił bliżej w swej pracy rozliczenia patentowe: „Dokumenty wskazują bowiem, że zyski z patentu na metal B dzielone były pomiędzy firmę (25%) i Czochralskiego (75%), który ze swej puli miał przekazać 25% Ernestowi Kochowi, Robertowi Hahnowi i dr Georesowi-Welterowi"[21].

Stop został wprowadzony do powszechnego użytku na kolejach niemieckich Deutsche Reichsbahn-Gesellschaft (DRG), stopniowo zastępując inne metale łożyskowe. Ze względu na mniejszą odporność na obciążenia dynamiczne, stosowano go do wylewania panewek wagonowych, natomiast do łożysk parowozowych na kolejach niemieckich nadal stosowano ujednolicony stop wysokocynowy WM80[22].Produkcję nowego stopu uruchomiono między innymi w zakładach Metall hüttenwerke Schaefer&SchaelBreslau[23].

W ten sposób o przyczynach gospodarczych i militarnych wynalezienia i wprowadzenia stopu bahnmetall pisał sam prof. Czochralski na łamach Przeglądu Mechanicznego: „Teza niemiecka »wszystko z własnych surowców, chociażby mniej ekonomicznie i bardziej żmudnymi sposobami fabrykacji«, jest konsekwencją polityki finansowo-dewizowej Niemiec. Finansowe przygotowanie już w czasie pokoju zostaje przez to osiągnięte, a oszczędności dewizowe mogą być zużyte na inne cele związane z przygotowaniem obrony. Zarządzenia te mogą mieć tylko jedno na celu: osiągnięcie za wszelką cenę najlepszych wyników w zakresie wyzyskania namiastek do wzmożenia pogotowia wojennego"[24]. Profesor Aleksander Krupkowski[25], w polemicznym artykule tak wyjaśniał genezę stopu: „[…] Blokada Niemiec w okresie ostatniej wojny światowej wywołała w tym państwie znaczne zainteresowanie się stopami łożysko-

[16] Świadczą o tym opisy patentowe w różnych językach oraz współautorstwo prac prof. Czochralskiego.

[17]Georges Francois Welter, Alzatczyk, Prof. metaloznawca, bliski współpracownik prof. Czochralskiego, został przez niego zaproszony do Polski. W 1932 r. rozpoczął wykłady zlecone i prowadził seminarium z metaloznawstwa specjalnego. Objął stanowisko zastępcy dyrektora Instytutu Metalurgii i Metaloznawstwa Politechniki Warszawskie. Por. Archiwum Polskiej Akademii Nauk, Materiały Jana Czochralskiego 6,k. 89; Bohdan Paszkowski, Kilka uwag związanych z artykułem opracowanym przez czł. PAN Henryka Szymczaka dla magazynu Gazeta nr 25 (276); 19/20 VI 1998.

[18]Według różnych źródeł występowały rozbieżności procentowej zawartości składników.

[19] Patent wygasł 12 marca 1942 r.

[20]Czochralski J., Lagermetalle…,op. cit., s. 6.; Tomaszewski P.E., Powrót. Rzecz o Janie Czochralskim, Wrocław 2012 r., s. 76.

[21]Tomaszewski P.E., Powrót…, op. cit., s. 79.

[22] Na kolejach niemieckich wprowadzono ujednolicony stop łożyskowy WM80, o składzie Sn 80%, Sb 12%, Cu 6%, Pb 2%. Por. Mozer W., Budowa i obliczanie części parowozowych, Lwów 1935 r., s. 71.

[23]Tomaszewski P.E., Powrót…, op. cit., s. 78. Była to powojenna Rafineria Metali „Wrocław", obecnie „Hutmen" S.A.

[24]Czochralski J., Nowoczesne kolejowe…, op. cit., s. 397.

[25] Aleksander Krupkowski (1894-1978), metalurg i metaloznawca, prof. AGH w Krakowie.

wymi o osnowie ołowiowej z dodatkami metali alkalicznych i metalami ziem alkalicznych. W tym czasie opatentowano w Niemczech szereg stopów tego typu. W chwili wkroczenia Niemców po wojnie w okres trudności gospodarczych, wywołanych ciężarami płatniczymi w stosunku do zagranicy, rygorystyczna konieczność oszczędzania walut obcych skierowała ich uwagę znów na bezcynowe stopy łożyskowe, oparte na ołowiu. Po szeregu prób państwowe koleje niemieckie wybrały spośród proponowanych stopów tego rodzaju tak zwany bahnmetall i wprowadzają go stopniowo do swego taboru w ciągu ostatnich lat 10. […]"[26]. Wprowadzenie stopu w Niemczech związane ze zmianami konstrukcyjnymi panewek ułatwiała normalizacja części wagonów kolei państwowych (KPEV), w tym łożysk, prowadzona już w latach 90. XIX w.

Dalsze upowszechnienie stopu związane było z dojściem Hitlera do władzy i rozpoczęciem powszechnej militaryzacji w połowie lat 30. XX w. Rozbudowa przemysłu zbrojeniowego była związana z wprowadzaną administracyjnie oszczędnością materiałów strategicznych. Powołano urzędy rejestrujące stany magazynowe i nadzorujące ich zużycie. Oszczędność materiałów i stosowanie ich zamienników osiągnęło wówczas wielkie rozmiary. Za nieuzasadnione używanie materiałów strategicznych bez zezwolenia, niezgodnie z militarnym przeznaczeniem, przewidziano surowe kary. Zarządzeniem Überwachungsstelle für unedle Metallen (Urzędu kontroli metali nieszlachetnych) z 23 października 1936 r. do stosowania w Niemczech dopuszczono jedynie panewki wylewane stopem bezcynowym lub o niskiej zawartości Sn (do 12%). W celu ułatwienia zastąpienia panewek nowymi wylewanymi oszczędnościowymi stopami Komisja Materiałoznawstwa VDI opracowała i wydała tabelę wraz z normą DIN 1703 U – stanowiące wytyczne zastosowania zastępczych materiałów łożyskowych[27]. Obejmowała ona stopy ołowiowe o zawartości 4, 6 i 10% Sn oraz bezcynowe stopy ołowiowe z domieszką antymonu i metali alkalicznych, stopy Sn-Zn i bezcynowe stopy cynkowe do wyrobu panewek. W tabeli podano również podstawowe własności tych stopów oraz przykłady zastosowań[28].

Po I wojnie światowej pod wpływem doświadczeń niemieckich większość państw europejskich rozpoczęła prace w celu zastąpienia drogiej cyny, trzema rodzajami stopów: bogato-cynowymi od 30-40% Sn, biedno-cynowymi o zawartości Sn do 10% oraz stopami bezcynowymi, w których głównym składnikiem był Pb (ok. 98%), a pozostałe 2% metale alkaliczne, jak Ca, Na, Li i inne[29].

W Polsce patent nr 4349 na „Metal panewkowy zawierający metale alkaliczne" zgłoszony został w Urzędzie Patentowym RP 2 marca 1925 r. z pierwszeństwem w Niemczech od 12 marca 1924 r., patent udzielono 2 marca 1926 r. Właścicielem patentu był Metall bank und Metal lgesellchaft A.G. we Frakfurcie nad Menem. Patent zastrzegał: m. in. „metal panewkowy z ołowiu z zawartością metalu alkalicznego, znamienny tym, że zawiera oprócz 0,1–0,8% sodu albo potasu albo obu tych metali jeszcze i 0,01–0,05% litu"[30]. W Polsce po opatentowaniu bahnmetall, zgodnie z prowadzoną wówczas polonizacją języka technicznego, otrzymał formalną nazwę „Metal-B".

[26]Krupkowski A., Stop łożyskowy „B"…, op. cit., s. 9.
[27]ZinnarmeundZinnfreieLagerausgussmetallefürGleitlagerundGleitflächen, Übersichtsblatt I. Beuht-Verlag.
[28] Przegląd Mechaniczny T. III, 1937, nr 20, s. 685.
[29]Dybowski J., Stopy łożyskowe taboru kolejowego i wyrób ich w stopowni PKP, w: XII [Dwunasty] Zjazd Techniczny Inżynierów Wydziałów Mechanicznych w Poznaniu 13, 14 i 15 listopada 1936, protokół obrad i referaty, Warszawa 1937 r., s. 81-82. Określenie bogato-cynowe i biedno-cynowe zgodne z ówczesna terminologią.
[30] Za Tomaszewski P.E., Powrót…, op. cit., s. 76-77 oraz Krupkowski A., Stop łożyskowy „B"…, op. cit., s. 9.

Po powrocie do Polski w 1928 r. prof. Czochralski podjął starania i zabiegi w sferach technicznych i urzędowych, w celu wprowadzenia swojego stopu. W tym czasie na PKP używano stopów wysokocynowych dwóch gatunków: „Według przepisów P.K.P. z 1920 r. dotyczących metali używanych do budowy taboru kolejowego na wylewy panewek stosowano stopy bogate w cynę: 1) do parowozów pośpiesznych i osobowych – stop marki $IX_1$ o składzie: cyny 83,3%, antymonu 11,1%, miedzi 5,6%; 2) do parowozów towarowych i przetokowych – stop marki $IX_2$ o składzie: cyny 42%, antymonu 16%, miedzi 2%, ołowiu 40%."[31]

Prof. Czochralskiemu udało się zainteresować swym stopem PKP, początkowo próby prowadzono w ciągu trzech lat, w znanej wytwórni metali kolorowych - Spółce Akcyjnej Fabryk Metalowych Norblin, Bracia Buch i T. Werner. Pomimo pozytywnych wyników podjęcie produkcji nie było opłacalne dla wytwórni[32].

Ostatecznie staraniem prof. Czochralskiego uruchomiono w odlewni Państwowych Zakładów Inżynieryjnych w Ursusie produkcję stopu dla kolejnictwa. Była prowadzona pod nadzorem dyrektora inż. Jerzego Kowtunowa[33], zaś kierownikiem odlewni był prof. Kazimierz Gierdziejewski. We własnościach nowego stopu pokładano wówczas bardzo duże nadzieje, w 1930 r. zakupiono 250.000 kg w dwóch partiach; pierwszą w ilości 167.000 kg w cenie 3 zł 10 gr za 1 kg, drugą w ilości 83.000 kg po cenie 2 zł 78 gr za 1 kg. Zakupiono go za sumaryczną kwotę 748 440 zł.[34]Stop bahnmetall przydzielono do stosowania w DOKP[35] Warszawa, Poznań i Katowice[36]: „[…] Dążność do uniezależnienia się od konieczności używania cyny spowodowała wprowadzenie także i do kolejnictwa polskiego stopów bezcynowych. Używanym dziś próbnie stopem jest metal łożyskowy „B" o składzie, podobnym do niemieckiego stopu >Bn<"[37].

Na PKP stosowano wówczas stopy o znacznej ilości cyny – przekraczającej często 60%. Początkowo były to stopy produkowane we własnym zakresie w warsztatach PKP, a następnie przez firmy prywatne. Na początku lat 30. XX w. zaprzestano zakupów stopów i rozpoczęto ich próby w trakcie eksploatacji. Prowadzono wówczas badania porównawcze różnych rodzajów stopów cynowych oraz bezcynowego stopu bahnmetall, patentu prof. Czochralskiego[38].

Badania stopów zakończono w 1932 r. Specjalna komisja zatwierdziła wówczas do stosowania na PKP gatunki stopów ołowiowo-cynowych[39], ubogich w cynę[40] – Fosforbabit marki $K_1$ (Sn 22,87%, Pb 59,03%, Sb 15,8%, Cu 2,3%) i marki $K_2$ (Sn 6,46%, Pb 80,16%, Sb 11,78%, Cu 1,6%); PolmetalBondrat$B_3$ (Sn 3,50%, Pb 76,4%,

[31] Mozer W., Budowa i obliczanie części parowozowych, op. cit., s. 71.
[32] Prof. Czochralski contra prof. Broniewski, w: „Gazeta Polska", nr 288, 15-X-1936 r., s. 6.
[33] Ibidem, s. 8.
[34] Krupkowski A., Stop łożyskowy „B"…, op. cit., s. 16.
[35] Dyrekcja Okręgowa Kolei Państwowych.
[36] Dybowski J., Stopy łożyskowe taboru kolejowego…, op. cit., s. 82.
[37] Mozer W., Budowa i obliczanie części parowozowych, op. cit., s. 72.
[38] Dybowski J., Stopy łożyskowe taboru kolejowego…, op. cit., s. 82.
[39] Stopy Fosforbabit oraz Bondrat wprowadzono na PKP w 1927 r.
[40] W 1932 r. używano na PKP pięciu podstawowych gatunków stopów łożyskowych: Fosforbabit I (cecha K 1), Fosforbabit II (cecha K 2), Fosforbabit III (cecha K 3); Bondrat I (cecha B 1), Bondrat II (cecha B 2), Bondrat III (cecha B 3), Turbosqirel (cecha TS), Ozet I (cecha O 1), Ozet II (cecha O 2), Ozet III (cecha O 3), Bezcynowy metal – B (cecha BM) oraz Metal nieznany (cecha N). Grupa stopów Ozet, był to stop wykonywany z wytopków sposobem gospodarczym w warsztatach PKP DOKP Gdańsk. Jako metal nieznany oznaczano stopy innych gatunków, dostarczane wraz z nowym taborem przez prywatne wytwórnie. Por. Dziennika Urzędowy MK, Nr 13, 1932 r., poz. 105, s. 131.

Sb 1,8%, Cd 1,5%, Cu 0,6%)[41] oraz „B-metal" patentu prof. Czochralskiego – oznaczany cechą BM wybijaną na panewkach.

29 grudnia 1932 r. Ministerstwo Komunikacji zatwierdziło *Przepisy o gospodarce stopami łożyskowymi na PKP*[42]. W przepisach tych czytamy: „Stop bezcynowy „B-metal", jako mający wielką przyszłość, lecz wymagający umiejętnego obchodzenia się z nim, będzie przydzielany wszystkim Dyrekcjom, na razie, w ograniczonej ilości, w celu obznajomienia się ze stopami bezcynowymi. Dyrekcje będą zalewać tym stopem, według własnego uznania, pewne jednostki taboru parowozowego i wagonowego, w granicach przydzielonego im rocznego zapasu."[43] Inaczej niż w Niemczech podjęto decyzję o wylewaniu tym stopem zarówno panwi wagonowych jak i parowozowych. Wszystkie panwie miały być w trakcie napraw dostosowywane do zalewania stopami cynowymi i bezcynowym[44].

Po zakończeniu badań stop bahnmetall został uznany przez komisję za nienadający się do powszechnego stosowania na PKP, ze względu na wysoką cenę nieproporcjonalną do stopów cynowych oraz konieczność wprowadzenia zmian konstrukcyjnych w panewkach i technologii zalewania. Przyjęto go do stosowania w niewielkiej ilości, jedynie w celu szkolenia pracowników kolejowych w zakresie stosowania stopów bezcynowych[45].

27 kwietnia 1932 r. Urząd Patentowy RP udzielił prof. Czochralskiemu patent nr 16254, w klasie 40b, 11/02, (zgłoszony 29 października 1929 r.) na „Stopy łożyskowe odporne na zżeranie stosowane zwłaszcza w kolejnictwie". Patent zastrzegał: „Stopy łożyskowe na osnowie ołowiu, odporne na zżeranie i z domieszką metali alkalicznych i metali ziem alkalicznych bez znanej domieszki metali ciężkich Sn, Sb, Cu, Ni i t.d. […] znamienne przez następujące domieszki: Mg, Ca i Ba oddzielnie lub razem w ilości do 2%, Ka i Na oddzielnie lub razem w ilości do 1%, Rb i Li oddzielnie lub razem w ilości do 10% oraz Be i Hg oddzielnie lub razem w ilości do 2%.[46]"

Interesujące jest, iż prof. Czochralski w tym opisie patentowym dokonał pewnej krytyki wcześniejszych stopów na osnowie ołowiowej: „Metale łożyskowe, utwardzone za pomocą metali ciężkich, odznaczają się niedomaganiami mechanicznymi, a na odwrót stopy, utwardzane za pomocą domieszek metali lekkich, brakiem odporności chemicznej. Brak odporności chemicznej ujawnia się w pierwszym rzędzie przez trudności ich przechowywania. Już po kilku dniach lub tygodniach wytwarzają się na ich powierzchni utlenione warstwy lub skorupy, które bardzo szybko przenikają w głąb, niszcząc nierzadko cały przekrój bloku."[47]

Ze względu na złą jakość stopów oraz niewłaściwe badania odbiorcze, w 1934 r. Ministerstwo Komunikacji opracowało nowe „Warunki techniczne dla odbioru stopów łożyskowych", które oparto na analizie chemicznej i próbie Brinella. W celu oceny opracowanych warunków oraz gospodarki stopami łożyskowymi Ministerstwo Komunikacji powołało komisję. W jej skład weszli między innymi wybitni specjaliści z za-

[41] Dziennik Urzędowy MK nr 1, 1932 r., poz. 8, s. 5.
[42] Ibidem, s. 5-16.
[43] Ibidem, s. 6.
[44] Ibidem, s. 6.
[45] Dybowski J., Stopy łożyskowe taboru kolejowego…, op. cit., s. 83.
[46] Urząd Patentowy RP, Opis patentowy nr 16254, Stopy łożyskowe odporne na zżeranie stosowane zwłaszcza w kolejnictwie, 20 lipca 1932 r., s. 3.
[47] Ibidem, s. 1.

kresu metalurgii i odlewnictwa: prof. Witold Broniewski[48] (Politechnika Warszawska), prof. Aleksander Krupkowski (Akademia Górnicza w Krakowie), prof. Kazimierz Gierdziejewski[49] (Politechnika Warszawska) i prof. Iwan Feszczenko-Czopiwski[50] (Akademia Górnicza w Krakowie)[51].

1 marca 1935 r. komisja przyjęła z niewielkimi zmianami opracowane warunki. W wyniku jej prac wprowadzono nowy stop Sn 86 (Sn 86%, Sb 10%, Cu 4%). Wysokocynowy, przeznaczony do zalewania panewek parowozów serii Pu29, Pt31, Okz32 i niektórych wagonów salonowych (As). Pod kierownictwem prof. Aleksandra Krupkowskiego, zorganizowano badania laboratoryjne stopów łożyskowych dla PKP. Na wniosek komisji również całkowicie wycofano z PKP stop bahnmetall. W wyniku prac komisji wstrzymano zakupy stopów łożyskowych i zorganizowano ich wytwórnię w PKP Warsztatach Głównych w Pruszkowie[52].

Według zatwierdzonych „Warunków technicznych dla odbioru stopów łożyskowych", oprócz stopu Sn 86, na PKP stosowano również stopy łożyskowe: Sn 23 (Sn 23%, Pb 59%, Sb 16%, Cu 2%) – przeznaczony do zalewania panewek parowozów i wagonów osobowych oraz Sn 6 (Sn 6,5%, Pb 80%, Sb 12%, Cu 1,5%) – przeznaczony do zalewania panewek wagonów towarowych[53].

W 1935 r. doszło do poważnego konfliktu pomiędzy prof. Czochralskim a prof. Broniewskim. Jego osią stały się w sposób pośredni zagadnienia dotyczące wartości wprowadzanego w Polsce stopu bahnmetall.

Początkowo stosunki między naukowcami były dobre, do konfliktu doszło podczas posiedzenia komisji senackiej Politechniki Warszawskiej[54].Istotą sporu było odmienne podejście do kwestii osiągania zysków podczas pracy naukowej oraz uwarunkowania ambicjonalne. Konflikt i późniejszy proces był tym tragiczniejszy, bowiem obaj profesorowie byli wybitnymi naukowcami o wielkich dokonaniach i zasługach.

Prof. Broniewski zarzucał prof. Czochralskimu interesowność, wyciąganie osobistych korzyści z zajmowanych funkcji oraz posiadanego podwójnego obywatelstwa polskiego i niemieckiego.

Spór zakończył się procesem o zniesławienie przed Sądem Okręgowym, który wytoczył prof. Czochralski za zniesławienie na łamach „Gońca Warszawskiego"[55]: „Wkrótce po rozprawie sądowej w »Gońcu Warszawskim« ukazał się cykl artykułów pióra prof. Broniewskiego i red. Zawadzkiego[56] atakujący prof. Czochralskiego jako

[48] Witold Firlej Broniewski (1880-1939), wybitny metaloznawca i metalurg, wykładowca Uniwersytetu Paryskiego, od 1919 r. prof. Politechniki Lwowskiej, od 1920 r. prof. Politechniki Warszawskiej, współzałożyciel i sekretarz generalny Akademii Nauk Technicznych, minister robót publicznych w II RP.

[49] Kazimierz Gierdziejewski (1888-1967), inż. technolog, budowniczy i kierownik odlewni Zakładów Mechanicznych „Ursus", profesor odlewnictwa na Wydziale Mechanicznym Politechniki Warszawskieji Akademii Górniczej w Krakowie.

[50] Iwan Feszczenko-Czopiwski (1884-1952), ukraiński działacz narodowy, minister przemysłu i handlu Ukraińskiej Republiki Ludowej, inż. metaloznawca i metalurg pracujący w Polsce. Podkreślając swoją ukraińską tożsamość odmówił przyjęcia polskiego obywatelstwa. Profesor Akademii Górniczej w Krakowie. W okresie międzywojennym zaangażowany w tajne badania wojskowe. Aresztowany w 1945 r. przez NKWD w Katowicach, wywieziony na Syberie zmarł w łagrze.

[51] Dybowski J., Stopy łożyskowe taboru kolejowego…, op. cit.,s. 84.

[52]Ibidem, s. 85.

[53]Ibidem, s. 86, 88.

[54]Prof. Czochralski contra prof. Broniewski, w: „Gazeta Polska", nr 289, 16-X-1936 r., s. 7.

[55] Ibidem, s. 8.

[56] Danych biograficznych nie ustalono.

doradcę technicznego Min. Spraw Wojskowych i posiadacza patentu na stop „B" do panewek wagonów i parowozów, który został od prof. Czochralskiego nabyty przez Min. Komunikacji. Stop ten jest namiastką używanego powszechnie stopu cynowego i zastosowano go na wypadek odcięcia dowozu cyny w czasie wojny. Artykuły zarzucały, że stop „B" jest jakościowo niższy od stopów cynowych, użycie jego może, w razie wojny, odbić się niekorzystnie na interesach obrony Państwa. Autorzy artykułów atakowali również prof. Czochralskiego z racji jego obywatelstwa niemieckiego. Prof. Czochralski wytoczył proces o zniesławienie."[57]

W trakcie procesu przesłuchano wielu świadków, miedzy innymi zeznawał dyrektor departamentu Ministerstwa Komunikacji inż. Suchodolski[58] który przedstawił następującą charakterystykę stopu: „Świadek stosował wynaleziony przez prof. Czochralskiego stop bezcynowy i stwierdza, że może on służyć jako namiastka stopu normalnego. Podczas wojny Niemcy stosowały go z powodzeniem[59]. Stop cynowy świadek uważa za lepszy, jednakże stop „B" może z powodzeniem zastępować."[60]

Proces relacjonowany przez prasę codzienną doprowadził do eskalacji konfliktu. Padały coraz bardziej ciężkie zarzuty korupcji i szpiegostwa. Przesłuchano wielu świadków, również z kręgów wojskowych, deklarujących całkowite zaufanie Ministerstwa Spraw Wojskowych do prof. Czochralskiego. W pewnym momencie rozprawa stała się sądem nad jego polskością i patriotyzmem.

Pomimo doskonałej obrony, prof. Czochralski wygrał proces we wszystkich trzech instancjach, uzyskując skazanie prof. Broniewskiego i red. Zawadzkiego na symboliczną karę więzienia w zawieszeniu[61].Skutki procesu miały jednak daleko idące konsekwencje i w perspektywie czasu zaciążyły negatywnie nad dalszymi losami i dobrym imieniem prof. Czochralskiego.

Konflikt wybitnych metaloznawców na tle wartości stopu metal B, przeniósł się również na łamy prasy technicznej i codziennej. W połowie lat 30. XX w. nasiliły się głosy krytyki własności stopu i oskarżeń o korupcję dotyczących zakupu przez PKP tego materiału.

W ten sposób komentował ten zakup prof. Krupkowski: „Wprowadzenie takiej ilości do taboru nie miało bez wątpienia na celu dokonania prób z tym stopem, lecz raczej chodziło o stopniowe usuwanie stopów cynowych i zastępowanie ich metalem B. Gdyby kolej nasza w ten sposób postępowała dalej, zakupując powyższy stop z importowanego sodu i litu, w takim razie na wypadek nieoczekiwanego wybuchu wojny znaleźlibyśmy się w bardzo ciężkiej sytuacji i zmuszeni bylibyśmy dopiero wtedy w niepomyślnych warunkach wojennych z pośpiechem uruchamiać własną produkcję sodu wobec grozy rozstrojenia transportu."[62]

Broniąc się przed tymi zarzutami prof. Czochralski w 1936 r. opublikował na łamach „Hutnika" artykuł pt. „Kolejowy metal-B klasyczny przykład namiastki stopów

[57]Prof. Czochralski contra prof. Broniewski, w: „Gazeta Polska", nr 288, 15-X-1936 r., s. 8.
[58] Danych biograficznych nie ustalono.
[59] Dyr. Suchodolski mylił się mając zapewne na myśli wcześniejsze stopy, bahnmetall wynaleziono dopiero w 1924 r.
[60]Prof. Czochralski contra prof. Broniewski, op. cit., s. 8.
[61]Por. Archiwum Polskiej Akademii Nauk, Materiały Jana Czochralskiego 6, k. 51; Domański E., Czochralski Jan (1885-1953) profesor zwyczajny metalurgii i metaloznawstwa Politechniki Warszawskiej – w 1929 roku doktor honoris causa PW.
[62]Krupkowski A., Stop łożyskowy „B"…, op. cit., s. 16.

cynowych”[63]. Zawarł w nim bardzo cenną dziś z punktu widzenia historii techniki chronologię wynalezienia zastępczych stopów łożyskowych w Niemczech. W tym samym roku, w celu upowszechnienia swych argumentów, opublikował ten artykuł w prawie niezmienionej formie na łamach „Przeglądu Mechanicznego”, pod zmienionym tytułem„Nowoczesne metale łożyskowe jako klasyczny przykład rozwiązania namiastkowych stopów cynowych”[64].

W 1938 r. na łamach „Przeglądu Mechanicznego” doszło do ostrej polemiki profesorów Czochralskiego i Krupkowskiego, w sprawie własności, składu chemicznego, uwarunkowań ekonomicznych, wartości i możliwości zastosowania stopu na PKP. W sukurs prof. Czochralskiemu przyszedł jego bliski współpracownik i zastępca na Politechnice Warszawskiej prof. Georg Welter, publikując artykuły na łamach tego samego czasopisma.

Ocena wartości stopu i opinii zawartych w polemicznych artykułach jest dziś bardzo trudna. Z analizy tekstów wynika, że obie strony polemiki zatraciły poczucie obiektywizmu. Prof. Czochralski starał się udowadniać za wszelką cenę, że stop nie ustępuję pod względem własności, a nawet pod wieloma względami przewyższa stopy wysokocynowe i nie posiada praktycznie żadnych wad. Widoczna jest sprzeczność i niespójność kolejnych polemicznych artykułów jego autorstwa dotyczących własności tego materiału.

Prof. Czochralski starał się intensywnie forsować swój stop, nie biorąc pod uwagę odmiennych od niemieckich warunków technicznych, ekonomicznych i gospodarczych polskiego kolejnictwa. Dążenie to z całą pewnością było konsekwencją jego twardego charakteru – nieustępliwości i wytrwałości, która umożliwiła polskiemu outsiderowi z krańców pruskiego imperium zrobić karierę naukową w Berlinie, dokonać wielkiego wynalazku i zdobyć znaczny majątek. Proces sądowy i ataki ze strony jego antagonisty prof. Broniewskiego miały niewątpliwie silny wpływ na jego stan emocjonalny. Dla Wielkopolanina pochodzącego z lokalnego Kcyńskiego środowiska poddawanego silnej germanizacji, niezwykle dojmujące musiały być zarzuty o brak patriotyzmu.

Uczestniczący w polemice prof. Krupkowski starał się udowodnić liczne wady stopu, w jego opinii całkowicie go eliminujące. Zapamiętał się w polemice i zatracił także poczucie obiektywizmu – dowodząc całkowitej wadliwości stopu również w warunkach niemieckich. Trudno przypuszczać, aby niezwykle pragmatyczny zarząd kolei niemieckich (DRG) wprowadził do eksploatacji całkowicie wadliwy stop, a następnie z pewnymi zmianami składu wprowadzono go w kolejnictwie Rosji Sowieckiej i USA. Konkluzja jego krytyki obejmowała następujące wnioski:

„1. Metal B jest technicznie gorszy od stopów bogato cynowych i własnościami zbliża się do stopów ołowiowych biedno cynowych.

2. Metal B jest stopem kosztowniejszym w porównaniu ze stopami cynowymi, głównie dlatego, że posiada tylko „jedno życie”. Pod tym względem jest on typową namiastką stopów łożyskowych.

3. Przy przejściu od stopów cynowych na metal B, w polskich warunkach nie należy przewidywać oszczędności dewizowych, gdyż mamy obecnie niedobór ołowiu,

[63]Czochralski J., Kolejowy metal-B…, op. cit., s. 219-223.
[64]Czochralski J., Nowoczesne kolejowe metale łożyskowe…, op. cit., s. 395-399.

poza tym uwzględnić należy deficytową pozycję, jaką stanowią opłaty licencyjne na rzecz niemieckiego towarzystwa.

4. Ewentualne wprowadzenie metalu B do naszego kolejnictwa nastręczyłoby w razie wojny duże kłopoty ze względu na konieczność natychmiastowego uruchomienia wytwórni sodu metalicznego i zabezpieczenia dostawy bezwodnego chlorku wapnia. Metoda całkowitego usunięcia stopów cynowych na korzyść metalu B, bez krajowej produkcji metalicznego sodu i bezwodnego chlorku wapnia, jest niebezpieczna z punktu widzenia obrony naszego Państwa."[65]

Na łamach „Przeglądu Mechanicznego" w kwestii sporu dotyczącego stopu głos w dyskusji zabrał również specjalista w zakresie budowy taboru kolejowego prof. Adolf Langrod[66]. W artykule na łamach Przeglądu Mechanicznego pt. „Zagadnienia taboru kolejowego w Polsce" w wyważony sposób skomentował zacięty spór profesorów:„Z innych metali półszlachetnych największe znaczenie w budowie taboru ma cyna, stosowana do brązów i stopów łożyskowych, a w kraju niewytwarzana. Możność zastąpienia cyny w stopach łożyskowych przez ołów była ostatnio u nas przedmiotem ożywionej dyskusji. Tylko doświadczenia na terenie kolejowym zdolne są tę sprawę wyjaśnić pod względem technicznym. W Niemczech tylko w parowozach stosowany jest wysokowartościowy łożyskowy stop cynowy, natomiast w pozostałych łożyskach stosuję się ołów z domieszką wapnia, sodu, litu i glinu, przy czym suma tych domieszek wynosi ok. 1 ½%. Ze stopem tym osiągnięto doskonałe wyniki (Dr.-Ing. e. h. G. Hammer, Die Deutsche Reichsbahnals Auftraggeberin der Deutschen Wirtschaft, 1932, s. 106). Jego wprowadzenie jednak wymagało gruntownej racjonalizacji odnośnych oddziałów w warsztatach naprawczych. U nas już pierwsze próby z tym metalem, zw. metalem kolejowym lub metalem B, wywołały przykre zatargi w kołach profesorskich, które nie przyczyniły się do wyjaśnienia sprawy, ani do wprowadzenia dalszych badań na właściwą drogę. Przykład ten poucza, że nie wolno iść ślepo śladem zagranicy, nie stwarzając dla nowych pomysłów odpowiednich warunków. Czy zaś stosowanie stopu ołowiowego zwiększy naszą autarchię w dziedzinie surowców lub przyniesie kolejom gospodarcze korzyści, powinno być przedmiotem osobnych badań"[67].

Interesującą opinię wobec stopu bahnmetall wyraził również jeden z najwybitniejszych polskich specjalistów w zakresie konstrukcji taboru kolejowego prof. Politechniki Lwowskiej Wilhelm Mozer[68]. W jego pracy „Budowa i obliczanie części parowozowych", czytamy: […] Niekorzystne położenie gospodarcze kazało w ostatnich latach sięgać do stopów białych, ubogich w drogą cynę lub pozbawionych jej zupełnie. W Niemczech uzyskano dodatnie wyniki ze stopem, zwanym „bahnmetall", (oznaczonym marką „Bn"), a zawierającym głównie ołów z domieszką metali alkalicznych i glinu. Skład tego stopu przedstawia się: ołowiu 98,4%, wapnia 0,69%, sodu 0,62%, litu 0,04%, reszta glinu. Domieszki metali alkalicznych podobnie jak i dodatek glinu – znajdujący się w stopie prawie w stanie rozproszenia atomowego, – wywojują znaczne stwardnienie osnowy ołowianej. Rozpowszechniający się stop ten wykazuje twardość

[65]Krupkowski A., Stop łożyskowy „B"…, op. cit., s. 16.

[66] Adolf Langrod (1876-1968), inż. kolejowy, prof. Politechniki Krakowskiej, konstruktor i specjalista w zakresie taboru kolejowego.

[67]Langrod A., Zagadnienia taboru kolejowego w Polsce, w: Przegląd Mechaniczny 1937, T. III, nr 17, s. 580.

[68] Wilhelm Mozer (1889-1958), inż., prof. Politechniki Lwowskiej, 1912-1923 komisarz maszynowy Dyrekcji Kolei we Lwowie, specjalista konstrukcji parowozów.

30°Brinella przy temperaturze 20°C, wytrzymałość na ciśnienie 17÷20 kg/mm$^2$, temperaturę topliwości 320°C i ciężar właściwy 10,56."[69] W opisie własności stopów tego typu, czytamy: „[…] Stopy te posiadają wielką zdolność do likwacji czyli dzielenia się na składniki i skurcz nieco większy od skurczu zwykłych cynowych metali łożyskowych. Wypełnienie panewek połączone jest z pewnymi trudnościami, wskutek niedostatecznego przylegania do podłoża brązowego. Przy każdym następnym przetapianiu składniki takie, jak bar, wapń, a częściowo sód i inne domieszki ulegają stopniowo utlenieniu, wskutek czego stopy te należy topić pod warstwą ochronną węgla drzewnego. Ponieważ stopy przetopione zawierają 0,6÷0,7% tlenu, nie należy używać wiórów, odpadków i starego materiału bez poprzedniej regeneracji. Wspomniane stopy są trwalsze od cynowych, topią się w wyższej temperaturze. Są jednak czułe na działanie wody i powietrza, dlatego natłuszcza się je lub chroni lakierem."[70]

Ocena możliwości zastosowania stopu na PKP, jest bardzo złożona. Prof. Czochralski wykorzystywał wszelkie możliwości, aby promować swój stop, nie zwracając uwagi na odmienne od niemieckich warunki techniczne, gospodarcze i polityczne. Niewątpliwie polemika a także proces sądowy ze strony jego antagonistów służyła całkowitej dyskredytacji tego stopu w Polsce.

Należy podkreślić, iż PKP były nieprzygotowane do wprowadzenia procesów technologicznych związanych z wylewaniem panewek nowym stopem. Pracochłonne było wykonywanie dodatkowych rowków klinowych, tzw. „jaskółczych ogonów" i otworów stożkowych w panewkach. Adaptację starych panewek utrudniała znaczna różnorodność parku wagonowego PKP i brak normalizacji łożysk osiowych. Stop wymagał utrzymania stałej temperatury topienia, zaś jej wahania powodowały wypalanie się domieszek. Nie było możliwości odzyskiwania stopu po zakończeniu eksploatacji w warunkach kolejowych zalewni stopów PKP.

Należy podkreślić, iż stop bahnmetall był zamiennikiem stopów wysokocynowych, jednak posiadał gorsze własności mechaniczne. Z tego względu nie stosowano go w panewkach parowozowych – w których działały bardzo duże siły.

Po uporządkowaniu i normalizacji gospodarki stopami w 1934 r. na PKP nie poszukiwano bezwzględnych oszczędności, bowiem koleje polskie stosowały materiały najlepszych gatunków, zaś oszczędności strategiczne w praktyce zaczęto wprowadzać powszechnie dopiero u progu wojny pod koniec lat 30. XX w.

Istotnym czynnikiem utrudniającym wprowadzenie stopu była pewna zachowawczość polskich inżynierów kolejowych i metaloznawców. Konserwatyzm kolejnictwa europejskiego sprawił również, iż nie wykorzystywano bardzo nowoczesnych amerykańskich wynalazków kolejowych. Prof. Adolf Langrod w ten sposób przedstawiał na przykładzie techniki amerykańskiej trudności w wprowadzeniu nowoczesnych wynalazków w kolejnictwie: „Technika amerykańska przoduje, a jej doświadczenia tylko zwolna przenikają do techniki europejskiej, przełamując konserwatyzm europejski. Tego rodzaju obawy można zobaczyć w wielu dziedzinach techniki kolejowej"[71]

[69]Mozer W., Budowa i obliczanie części parowozowych, op. cit., s. 72.
[70] Ibidem, s. 72.
[71]Langrod A., Zagadnienia taboru kolejowego…, op. cit., s. 573.

## Recepcja stopu bahnmetall w ZSRS

Prof. Jan Czochralski w swym artykule „Kolejowy Metal-B – Klasyczny przykład namiastki szlachetnych stopów cynkowych" opisał rozprzestrzenienie się stopów bezcynowych w kolejnictwie sowieckim i amerykańskim, na początku lat 30. XX w.: „[…] Podobne stopy (110) zostały w Sowietach oficjalnie zaprowadzone w r. 1930, w Ameryce w r. 1932 (111). Zainteresowanie w Sowietach nowymi stopami łożyskowymi było tak wielkie, że wydany wspólnie z G. Welterem podręcznik autora 1) została tam (zresztą, jak zwykle, bez wiedzy autora) żywcem przetłumaczony i wydany […]"[72].

Już po roku od wynalezienia stopu bahnmetall 4 kwietnia 1925 r. bliski współpracownik i przyjaciel prof. Czochralskiego dr inż. Georg Welter złożył w Rosji sowieckiej wniosek patentowy na stop. Dopiero po pięciu latach, 31 marca 1930 r. wydano na 15 lat patent, dla inż. Weltera i firmy Metall bank und Metallurgische Gesellschaft AG Frankfurt a. M, na stop łożyskowy na osnowie ołowiu, o składzie chemicznym: 99,97 – 97,95% Pb, z dodatkiem 0,01 – 1% Na lub Ca, 0,01 – 0,05% Li[73]. Patent wydano na rzecz dr inż. Georga Weltera - prawdopodobnie prof. Czochralski nie mógł wówczas osobiście udać się w tym celu do Rosji sowieckiej, ze względu na militarne znaczenie prowadzonych prac. Opatentowanie stopu w ZSRS świadczyło o wielkiej zapobiegliwości wynalazcy[74]. Należy podkreślić, iż był to pierwszy zagraniczny patent w ZSRS na stop łożyskowy.

Po tym patencie w Rosji opatentowali również swe stopy łożyskowe konkurenci prof. Czochralskiego. 21 sierpnia 1925 r. firma Jacob Neurath z Wiednia – inż. Paul Kemp i inż. Theodor Kittl złożyła patent na stop łożyskowy z osnową ołowiową. Został wydany 31 maja 1929 r. na stop o następującym składzie chemicznym: 65 – 77% Pb, 10 – 27% Sb, 3 – 14% Sn i 0,7 – 2,5% As[75]. 3 września 1926 r. patent złożyli Walter Mathesius i Martin W. Neufeld z Berlina-Charlotenburga, na stop ołowiowy z dodatkiem: 0,75 – 1% Ca, 0,6 – 0,65% Na, 0,2 – 0,25% Mg i do 0,1% Al[76]. Opatentowano zmianę jego składu przez dodanie do 0,1% Bi, Cu i Sn, razem lub osobno[77]. Patent wydano 31 maja 1929 r. na 15 lat. 17 stycznia 1928 r. firma Jacob Neurath z Wiednia, inż. P. Kemp złożyła wniosek patentowy na zmianę wcześniejszego patentu z 31 maja 1929 r. Obejmował on dodanie do wcześniejszego składu: 0,5 – 3,5% Cd, In – osobno albo razem[78].

Patentowanie stopów łożyskowych w ZSRS stało się możliwe, gdy w 1924 r. zorganizowano nieistniejącą od czasu rewolucji sowiecką służbę patentową[79]. Miało to na celu przyciągnięcie zagranicznego kapitału, w celu rozbudowy przemysłu realizowanej w ramach NEP.

[72]Czochralski Jan, Kolejowy metal-B…, op. cit., s. 220.
[73] Patent na izobretenie, № 14443, wydany 31 maja 1930 g.
[74] Ibidem.
[75] Patent na izobretenie, № 9344, wydany 31 maja 1929g.
[76] Patent na izobretenie, №9356, wydany 31 maja 1929 g.
[77] Ibidem.
[78] Patent na izobretenie, №10074, wydany 31 maja 1929 g.
[79]IstoriâRossijskihprivilegij i patentov, http://www.2fj.ru/istoriya/istoriya_rossijskix_privilegij_i.php, dostęp 13.04.2014 r.

Patenty objęły tylko część dziedzin techniki, zaś ochrona patentowa w Rosji sowieckiej w dużej mierze była całkowicie iluzoryczna. ZSRS nie podpisało międzynarodowych umów patentowych, lecz jedynie dwustronne umowy z krajami rozbudowującymi sowiecki przemysł i komunikację. W 1927 r. podpisano umowę sowiecko-niemiecką o wzajemnej ochronie patentowej własności przemysłowej[80].

W Rosji sowieckiej w 1928 r. zatwierdzono Pierwszy pięcioletni plan rozwoju gospodarki narodowej (1929–1933 zwany stalinowską pięciolatką). Jego wprowadzenie związane było z intensywną industrializacją i militaryzacją, realizowaną w myśl znamiennych słów Stalina:„Jesteśmy 50–100 lat za krajami rozwiniętymi, musimy nadrobić ten dystans w ciągu 10 lat, albo to zrobimy, albo nas zmiażdżą.”[81]

W tym czasie rozpoczęto pracę związane z modernizacją przemysłu ciężkiego i transportu kolejowego w oparciu, głównie o amerykańskie i niemieckie technologie. Rozpoczęto szeroko zakrojone prace w celu ich implementacji, wysyłano na zagraniczne staże sowieckich inżynierów i tłumaczono (oczywiście bez żadnych opłat autorskich) wielkie ilości światowego piśmiennictwa technicznego.

Na poziomie sowieckich kadr inżynieryjno-technicznych dostęp do nowoczesnych zagranicznych technologii zapewniać miała zorganizowana w tym czasie z dużym rozmachem służba informacji naukowo-technicznej i ekonomicznej.

Utworzone w większości zakładów przemysłowych i instytucji ośrodki informacji naukowo-technicznej i ekonomicznej ułatwiać miały dostęp do zagranicznego piśmiennictwa specjalistycznego.

Było to praktyczne wykorzystanie intensywnie rozwijanego wówczas „białego wywiadu” technologicznego. Tłumaczenie i wydawanie nowości technicznych służyć miało wprowadzeniu nowoczesnych technologii i metod organizacji przemysłu. Jednym z głównych założeń industrializacji i przestawienia gospodarki na tory wojenne było stosowanie oszczędności materiałów oraz wprowadzenie stalinowskiego współzawodnictwa pracy w formie morderczego wyścigu. Wprowadzenie stopów bezcynowych w kolejnictwie idealnie wpisywało się w prowadzoną wówczas politykę rozbudowy przemysłu zbrojeniowego, miało bardzo duże znaczenie dla jego rozwoju.

Swoistym paradoksem było bardzo szybkie wprowadzanie licznych nowoczesnych patentów i zachodnich rozwiązań konstrukcyjnych, w rodzaju upowszechnienia w sowieckim przemyśle i kolejnictwie spawania elektrycznego. Było to możliwe właśnie dzięki temu, że ZSRS nie należał do unii patentowej.

W ten sposób w 1928 r. bez wiedzy autorów, przetłumaczono na rosyjski i wydano w Państwowym Wydawnictwie Technicznym w Moskwie, w serii Biblioteki Inżynieryjno-Przemysłowej pracę Czochralski J., Welter G., Lagermetalle und ihretechnologische Bewertung, Berlin 1920 r.; rosyjski tytuł: Čohralskij I., Antifrikcionnyemetally i ihtehnologičeskaâocenka. Rukovodsstvodlâinž-rov, konstruktorov, proizvodstbennikov i tovarovedov, tłumaczenie inż. I.P. Šepeleva.

W 1930 r. najprawdopodobniej[82]wzorując się na stopie bahnmetall na kolejach sowieckich SŻD wprowadzono bezcynowy stop wapniowy na osnowie ołowiu Ca 0,75 – 1,10%, Na 0,65 – 0,95%, Pb – pozostałe; oznaczony marką БК (babbit wapniowy),

[80] Patent na izobretenie, № 25133, wydany 31 stycznia 1932 g.
[81] Stalin I.V., Sočinieniâ, T. 13, Moskva 1951, s. 29-42.
[82] Nie odnaleziono źródłowego potwierdzenia następstwa wynalazku, lecz podobieństwo obu stopów jest jednoznaczne.

według norm sowieckich 1935 r. – OST/WKC 6781, GOST 1209-41[83]. Nowy stop i metody zalewania nim panewek opracowany został przez prof. W. H. Wazingera i A.N. Celikowa. Stosowany był do wylewania panewek z maksymalny obciążeniem na nacisk 200 kg/cm$^2$. Jedyną zmianą w stosunku do stopu Czochralskiegobyła rezygnacja z domieszki litu[84]. Produkcję nowego stopu uruchomiono w odlewni zakładów budowy taboru kolejowego „Krasnoje Sormowo" w Niżnym Nowogrodzie[85].

Wprowadzenie stopu wiązało się początkowo z pewnym oporem sowieckich inżynierów kolejowych. W podręczniku projektowania parowozów D.D. Naumowa zawarto informację: „Babbit do zalewania panewek Sn 16%, Sb 16%, Pb 65%, Cu 3%. Zastąpienie cyny ołowiem nie jest korzystne, ponieważ cyna jest cztery razy twardsza od ołowiu, i może wytrzymać większe obciążenia"[86].W związku z przejściem na stop БК, opracowano nową konstrukcję panewek taboru kolejowego, z tzw. „jaskółczymi ogonami" oraz proces technologiczny topienia stopu i wylewania panwi.

27 listopada 1930 r. prof. Jan Czochralski złożył w Rosji sowieckiej wniosek patentowy na niekorodujący stop łożyskowy. Po trzech latach 31 sierpnia 1933 r. wydano mu na 15 lat patent, na stop na osnowie ołowiu, o składzie chemicznym: Pb z niewielkimi dodatkami metali alkalicznych, w tym do 2% Ba[87].

W latach 30. XX w. opracowano w ZSRS inne odmiany stopów łożyskowych dla kolejnictwa na osnowie ołowianej; gatunku БН (babbit niklowy), skład chemiczny: Sb 13 – 15%; Cu 1,5 – 2,0%; Sn 9 – 11%; Cd 1,25 – 1,75%; Ni 0,75 – 1,25%, As 0,5 – 0,9%, innych domieszek nie więcej 0,4%, reszta Pb; gatunku Б16[88](babbit ołowiowy), według GOST 1320-41, skład chemiczny: Sb 15 – 17%; Sn 15 – 17%; Cu 1,5 – 2,0%, pozostałych domieszek nie więcej 0,6, reszta Pb; gatunku Б6 (babbit ołowiowy), skład chemiczny: Sb 14 – 16%; Sn 5 – 6%; Cu 2,5 – 3,0%, Cd 1,75 – 2,25%; As 0,6 – 1,0%, innych domieszek nie więcej 0,4%, reszta Pb[89].

W ten sposób u progu wojny sowieckie kolejnictwo prawie całkowicie przeszło na stopy bezcynowe. Tylko w szczególnie odpowiedzialnych łożyskach taboru kolejowego SŻD, nadal stosowano babbit cynowy, gatunku Б83, skład chemiczny: Sb 10 – 12%; Cu 5,5 – 6,5%; Sn – pozostałe.

## Recepcja stopu bahnmetall w Stanach Zjednoczonych

Badania nad opracowaniem stopów ołowiowych podejmowano w USA już w latach 20. XX w. Opracowano wówczas stop Ulco-metal, autorstwa Frary i Temple, o składzie 1,6% Ba, 4% Ca, 97,6% Pb[90].

[83]Czochralski Jan, Kolejowy metal-B…, op. cit., s. 223.
[84]Jan Czochralski w swym artykule podawał informację jakoby sowieckie kolejnictwo przeszło w 1930 r. na stopy wzorowane na stopie bahnmetall, o składzie chemicznym Ca Na Mg. Informacja ta jest błędna, najprawdopodobniej wyniknęła z braku dostępu do informacji, które w warunkach sowieckich były utajnione. Por Czochralski Jan, Kolejowy metal-B op. cit., s. 219.
[85]Krupkowski A., Stop łożyskowy „B"…, op. cit., s. 8.
[86] Naumow D.D., Projektirowanieparowoza, Moskwa 1931 g., s. 59 (tłumaczenie ZT).
[87] Patent na izobretenie, № 31845, wydany 31 sierpnia 1933 g.
[88]Stopem tego gatunku wylewano brązowe panwie osiowe i panewki wiązarów i korbowodów parowozów wąskotorowych typu Kp4, budowanych wFabloku w Chrzanowie w dużych ilościach do końca lat 50. XX w. dla ZSRS. Por. CBK Nr 1 Poznań, Warunki Techniczne wykonania i odbioru parowozu Kp4, s. 39, 76.
[89] Parowozy obszyj kurs konstrukcji i elementy teorii, Moskwa 1949 g., s. 592.
[90]Feszczenko-Czopiwski J., O tanich stopach łożyskowych…, op. cit., s. 196.

W 1932 r.[91]inż. Robert JayShoemaker[92], w latach 1919–48, pracownik koncernu ołowiowego NationalLead Company w Nowym Jorku, zapewne wzorując się na stopie bahnmetall, opracował nowy łożyskowy stop ołowiowy[93]. Otrzymał on handlową nazwę Satco-metal.

W stosunku do pierwowzoru prof. Czochralskiego prawdopodobnie obniżono Pb z 98,6% na 98,0%, Ca z 0,7% na 0,5% oraz usunięto całkowicie Na i dodano niewielkie ilości Mg (0,075%), K (0,04%), Mn (0,25%), Sn (0,7%), Al (0,05%)[94]. Dzięki wprowadzonym zmianą w składzie stop miał znacznie lepsze własności i wytrzymałość od bahnmetall. Mógł być przetapiany bez wypalania składników i nie podlegał korozji[95].

Stop łożyskowy satco-metal zastosowany został do zalewania łożysk osiowych lokomotyw i wagonów oraz panewek kolejowych i okrętowych silników spalinowych. Wprowadzenie tego stopu zastępczego w prywatnych amerykańskich towarzystwach kolejowych i we flocie pozwoliło na zaoszczędzenie podczas drugiej wojny światowej dużych ilości strategicznych materiałów – cyny i miedzi[96]. W kolejnictwie amerykańskim stop znalazł zastosowanie w latach 30 XX w., w produkcji nowoczesnych panewek segmentowych firmy Hennessy Lubricator[97].

## Bezołowiowy stop łożyskowy ŁCaw Polsce

W okresie powojennym do wylewania panewek taboru kolejowego początkowo stosowano stopy o osnowie cynowej. Jeszcze wydane w 1951 r. „Warunki techniczne dostawy i odbioru stopów łożyskowych i brązów rafinowanych dla PKP M 97" dopuszczały do stosowania na PKP jedynie stopy cynowe o jej następujących procentowych zawartościach: (Ł83) Sn 83, (Ł20) Sn 20, (Ł10) Sn 10 i (Ł6) Sn 6[98]. W kolejnictwie stosowano również stopy cynowe: (Ł16) Sn 16.

Na początku lat pięćdziesiątych w okresie nasilającej się rozbudowy i militaryzacji przemysłu zbrojeniowego i komunikacji, według sowieckich wzorów zaczęto poszukiwać oszczędności we wszystkich dziedzinach gospodarki. Temu celowi służyło instytucjonalne wprowadzanie ruchu współzawodnictwa pracy oraz wdrażanie w polskich warunkach sowieckich technologii w zakresie stosowania oszczędnościowych materiałów i uproszczeniu procesów produkcyjnych. Współzawodnictwo oprócz oszczędności, służyć miało totalizacji i militaryzacji pracy – dokonano wówczas jej redefinicji - od tego czasu miała to być „Stachanowska praca uderzeniowa", a w zasadzie walkaprowadzona w każdej dziedzinie gospodarki.

[91]Czochralski Jan, Kolejowy metal-B…, op. cit., s. 220.
[92]Danychbiograficznychnieustalono.
[93]Ehlen, Ethel K., Consulting Engineer, On Visit Here, Developed Of Railroad Safety Devices w: Palm Beach Daily News, Palm Beach, Florida, Monday, april 5, 1954, s. 1.
[94] Jasik Z., Mickiewicz M., Stopy łożyskowe i technologia wylewania panwi, Warszawa 1961 r., s. 56.
[95] Symposium on Effect of Temperature on the Properties of Metals, American Society for Testing Materials 1932, s. 337.
[96]Ehlen, Ethel K., Consulting Engineer…, op. cit., s. 1.
[97] Hennessy mechanical journal lubricators for all journals of railway equipment, New York 1938.
[98]PKP, M 97 Warunki techniczne dostawy i odbioru stopów łożyskowych i brązów rafinowanych dla PKP, zatwierdzone przez Dyrektora Generalnego KP dn. 18/X-50 r., Warszawa 1951 r., Wojciechowski Z., Materiałoznawstwo kolejowe, tom II, Warszawa 1960 r., s. 414.

Powszechnie wprowadzano wówczas ze względów politycznych sowieckie technologie, które często nie przynosiły dużych korzyści, a w wielu wypadkach stawały się przyczyną znacznych strat. Przykładem tych tendencji może być nóż tokarski Kolesowa do szybkościowego skrawania metali. Przeznaczony był do forsownej i niebezpiecznej pracy na tokarkach przy bardzo dużych szybkościach. Zamiast iluzorycznych oszczędności stał się przyczyną wielu wypadków i uszkodzeń maszyn, a także licznych oskarżeń o sabotaż gospodarczy.

Instytucjonalne narzucanie sowieckich technologii powodowało zrozumiały opór ze strony przedwojennych środowisk inżynierskich i robotniczych. Dekonstruowało wykształcony od czasu industrializacji esprit de corps arystokracji robotniczej i rzemieślniczej.

W takiej atmosferze na PKP wprowadzono na początku lat 50. XX w. stopy na osnowie ołowiowej, bezcynowe i niskocynowe – wapniowe ŁCa i z małą zawartością cyny – arsenowe Ł10As. Stopów wapniowych ŁCa używano do zalewania panewek wagonów towarowych, zamiast stopu Ł6, arsenowych zaś Ł10As[99] – Ł6As[100] do zalewania panewek wagonów osobowych, zamiast stopów Ł10 i Ł20[101]. W ramach powszechnej wówczas działalności racjonalizatorskiej, stop ŁCa stosowano również w latach 50. XX w. do wylewania panewek osi tocznych parowozów manewrowych i osi tendrowych[102], podczas napraw w ZNTK Wrocław.

31 grudnia 1952 r. zatwierdzono normę PN-H-87112 na łożyskowy stop ołowiowo-wapniowo-sodowy ŁCa1NA PbCa1Na (skład chemiczny Ca 0,85 – 1,15%, Na 0,60 – 1,90%, Pb reszta). Stop ŁCa był polskim odpowiednikiem sowieckiego stopu БК (GOST 1209-41), o prawie identycznym składzie chemicznym: Ca 0,75 – 1,1%; Na 0,65 – 0,95%, innych domieszek nie więcej 0,3, reszta Pb. Jak widzimy odróżniały je jedynie niewielkie zawartości procentowe składu chemicznego. W przetłumaczonym na język polski sowieckim podręczniku A.P. Gulajewa Metaloznawstwo, tak opisano jego własności: „[…]Stop łożyskowy БК (ŁCa) stosowany w kolejnictwie jest, podobnie jak stop БС, stopem dość tanim. W strukturze tego stopu miękka osnowę stanowi ołów, a twardymi wtrąceniami są związki ołowiu z wapniem i sodem."[103]

Produkcję stopu ŁCa rozpoczęto w przedwojennych zakładach wytwarzających bahnmetall – Rafinerii Metali „Wrocław" (obecnie „Hutmen" SA) oraz w Zakładach Metalurgicznych „Pomet" w Poznaniu[104].

W ten paradoksalny sposób historia zatoczyła koło, stop opracowany w 1930 r. w ZSRS na podstawie receptury niemieckiego stopu prof. Jana Czochralskiego Bahn-Metall, po dwudziestu latach powrócił do Polski, jako sowiecki wynalazek „przodującego kolejnictwa sowieckiego".

W ten sposób opisano go w artykule w Przeglądzie Kolejowym Mechanicznym: „Trudność zaopatrzenia i konieczność wydawania dewiz za dostarczoną cynę zmusiła fachowców do poszukiwania stopów opartych na materiałach krajowych łatwo do-

[99]Znak PbSn10Sb14Cu2As, skład chemiczny: Sb 13 – 15%, Cu 1,5 – 2%, Cd 1,25 – 1,75%, Ni 0,75 – 1,25%, As 0,5 – 0,9%, Sn 9 – 11%, Pb reszta.
[100]Znak PbSn6Sb15Cu3As, skład chemiczny: Sb 14 – 16%, Cu 2,5 – 3,0%, Cd 1,75 – 2,25%, As 0,6 – 1,0, Sn 5 – 6%, Pb reszta.
[101]Langer J., Podręcznik rewidenta wagonów, Warszawa 1959 r., s. 44.
[102]Krajewski T., Technologia napraw taboru kolejowego, s. 321.
[103]Gulajew A.P., Metaloznawstwo, Katowice 1969 r., s. 575.
[104]Tomaszewski P.E., Powrót…, op. cit., s. 78.

stępnych. W dziedzinie stopów zastępczych uczeni radzieccy dokonali szeregu badań i opracowali składy chemiczne oraz sposoby wytwarzania oszczędnościowych stopów łożyskowych. Do takich stopów zalicza się między innymi stop łożyskowy oparty na osnowie ołowiu z dodatkiem wapnia metalicznego."[105]

W okresie stalinowskiej industrializacji częste było zjawiskotóre określiłem jako -wtórny transfer technologii. Była to dość powszechna praktyka, gdy wiele amerykańskich przestarzałych technologii, które zakupił w latach 30. ZSRS trafiło do Polskich w latach 50. XX w. W identyczny sposób trafiały do polski niemieckie technologie zdobyte przez Armię Czerwoną i wywiezione na wschód, często z nowymi tabliczkami rysunkowymi pisanymi cyrylicą. Ze względu na ścisłą izolację od zachodniej nauki, w zakresie nauk ścisłych również wtórny transfer nowoczesnych zachodnich technologii i wiedzy odbywał się via ZSRS, za pośrednictwem tanich sowieckich tłumaczeń literatury zachodniej.

Z wprowadzeniem stopu wapniowego związane było szereg trudności technologicznych, zwiększających koszta robocizny – które niwelowały samą oszczędność cyny. Trudności te zasadniczo były zbliżone do powodowanych wadami stopu bahnmetall. Panewki musiano wylewać cienka warstwą stopu, ponieważ gruba warstwa, w miarę docierania się stopu do czopa, powodowała łuszczenie i zawalcowanie powierzchni trącej. Stop ŁCa miał znacznie gorsze własności przylegania do panewki niż stop cynowy.

Konieczne było frezowanie kanałów o kształcie klinowym tzw. „jaskółczych ogonów" i wiercenie stożkowych otworów w panewkach – w celu dodatkowego mechanicznego połączenia stopu[106]. Najlepsze połączenie stopu uzyskiwano, gdy panewki wykonywano z żeliwa modyfikowanego. Ponieważ głównymi składnikami nadającymi twardość był wapń i sód, nie można było dopuścić do niewielkiego nawet przegrzania stopu. Powodowało to intensywne utlenianie składników utwardzających i zmniejszenie twardości stopu (wylana warstwa miała gruboziarnistą strukturę)[107]. Nie można było przetapiać w warunkach warsztatowych wytopek i wiórów stopu, należało je przekazywać do rafinerii do regeneracji[108]. Jak widzimy były to identyczne wady ze stopem bahnmetall prof. Czochralskiego.

Ze względu na złe własności chemiczne i wytrzymałościowe oraz trudności technologiczne związane z zalewaniem panwi, bezpośrednio po 1956 r. rozpoczęto wycofywane z PKP stopu ŁCa. Stopy te zastąpiono ponownie wprowadzonymi stopami cynowymi, pozostawiono również w użyciu stopy Ł10As i Ł6As. W pracy inż. Zdzisława Wojciechowskiego pt. „Materiałoznawstwo kolejowe, wydanej w 1960 r.", znajduje się informacja o wycofaniu stopów bezcynowych[109]. Norma PN-H-87112 na stop ŁCa została wycofana 1 kwietnia 1963 r., zastąpiono ją normą PN-H-87111 na stopy cynowe i cynowo-ołowiowe[110]. W ten sposób zakończył się kilkuletni eksperyment z wprowadzeniem na PKP sowieckiego stopu БК.

---

[105] Bielecki S., Technologia zalewania panewek stopem ŁCa, w: Przegląd Kolejowy Mechaniczny, nr 12, 1954 r., s. 369.
[106] Na kolejach sowieckich przy tego typu stopie, w panewkach stosowano specjalne wkładki brązowe.
[107] Krajewski T., Technologia napraw taboru kolejowego, op. cit., s. 323.
[108] Ucieszyński J., Maźnice wagonów osobowych, op. cit., s. 69-70.
[109] Wojciechowski Z., Materiałoznawstwo kolejowe, T. 2, Warszawa 1960 r., s. 413.
[110] Wojciechowski Z., Materiałoznawstwo…, op. cit., s. 413.

## Podsumowanie

W publikacjach dotyczących prof. Jana Czochralskiego brak było dotychczas szczegółowego wyjaśnienia przyczyn powstania i wprowadzenia do eksploatacji w kolejnictwie stopu bahnmetall. Artykuł ten jest jedynie szkicową próbą przybliżenia powstania wynalazku, jego wprowadzenia w niemieckim kolejnictwie i późniejszej recepcji w transporcie kolejowym innych państw. W celu szczegółowego zbadania zagadnień związanych ze stopem bahnmetall konieczne jest przeprowadzenie obszernych kwerend archiwalnych w Niemczech i Rosji, Czechach oraz w USA i Kanadzie. Niezwykle ważnym zagadnieniem w zakresie stopów patentowanych przez prof. Czochralskiego, jest przeprowadzenie szczegółowych zagranicznych kwerend w urzędach patentowych oraz zbiorach archiwalnych norm.

W historiografii dotychczas powszechny był błędny pogląd, iż stop ten posiadał znacznie lepsze własności eksploatacyjne od stopów cynowych. Pogląd ten jest odzwierciedleniem tez artykułów dotyczących stopu, publikowanych przez prof. Czochralskiego i prof. Weltera, na łamach polskiej prasy technicznej w połowie lat 30. XX w.

Zapomina się o tym, iż był to zamiennik stopów cynowych, powstały w warunkach związanych z zapewnieniem funkcjonowaniem zmilitaryzowanego transportu kolejowego. Sukces stopu wyrażał się znacznymi oszczędnościami cyny przy zapewnieniu bezawaryjnej pracy transportu kolejowego w warunkach wojny. Należał do tych wynalazków, które posiadały stosunkowo krótki okres życia, jego ostateczny kres nastąpił wraz z powszechnym zastępowaniem łożysk ślizgowych w kolejnictwie tocznymi w latach 60/70 XX w.

Ocena własności stopu jest bardzo trudna, niewątpliwie w Polsce zaciążyło nad nim fatum w postaci sporu profesorów Czochralskiego i Broniewskiego. Pretekstem do krytyki prof. Czochralskiego stał się wówczas zarzut niskiej jakości stopu. Zacięta polemika jego zwolenników i przeciwników była bezpośrednią przyczyną wykorzystywania przez obie strony pozamerytorycznych argumentów oraz manipulowania wynikami badań, w celu udowodnienia swych racji za wszelką cenę.

Analiza zagranicznej recepcji stopu jest również niezwykle trudna, bowiem poza informacjami i opiniami zawartymi w artykułach prof. Czochralskiego i jego adwersarzy oraz patentach, normach i opisach technicznych, brak dotychczas dostępnych źródeł bezpośrednich.

Należy podkreślić, iż historycy techniki nie dotarli dotychczas do dokumentacji archiwalnej obrazującej pracę naukową profesora w Niemczech. W trakcie analizy następstw wprowadzenia stopu oraz chronologii tych zdarzeń trzeba było się oprzeć na pracach prof. Czochralskiego, szeroko stosując metodę – per analogiam.

Niewątpliwie stop miał wielkie znaczenie dla oszczędności materiału strategicznego jakim była cyna. Jego wynalezienie w Niemczech związane było z powszechnym programem oszczędności materiałów, wprowadzonym w tym kraju w końcowej fazie pierwszej wojny światowej. Warto zaznaczyć, iż instytut kierowany przez prof. Czochralskiego założono w celu opracowywania strategicznych materiałów zastępczych.

W okresie międzywojennej militaryzacji i oszczędności wywołanych drugą wojną światową, stosowanie namiastek – tzw. ersatzów osiągnęło wielkie rozmiary. Wprowadzenie programu produkcji zastępczych surowców i materiałów było jedną

z zasadniczych przyczyn zachowania sprawności i żywotność gospodarki niemieckiej do końca wojny.

Wynalezienie stopu wpisywało się w koncepcję oszczędności materiałów prowadzoną przez totalitarne państwa prowadzące intensywne zbrojenia, jakimi były Niemcy i Sowiecka Rosja. Podobny stop wprowadzono w USA, gdzie odmienna filozofia nowoczesności w powiązaniu z rygorystycznym poddawaniem każdego ulepszenia analizie finansowej, ułatwiała wprowadzenie ekonomicznie uwarunkowanych innowacji.

Gorsze od stopów cynowych własności stopu, pozwalały ponadto na jego bezawaryjną eksploatację na kolejach sowieckich i amerykańskich, dzięki znacznie większym odległościom międzystacyjnym (niezbyt częsty rozruch i hamowanie pociągów).

**Porównanie składów stopu bahnmetall i innych wzorowanych na nim stopów bezcynowych[111]**

| Cecha Stopu | Kraj | Pb | Ca | Na | Li | Mg | K | Mn |
|---|---|---|---|---|---|---|---|---|
| Bn | Niemcy | 98,6 | 0,7 | 0,6 | 0,04 | --- | --- | --- |
| BK | ZSRS | reszta | 0,75 – 1,10 | 0,65 – 0,95 | --- | --- | --- | --- |
| Satco | USA | 98,0 | 0,5 | --- | 0,04 | 0,075 | 0,04 | 0,25 |
| ŁCa | Polska | reszta | 0,85 – 1,15 | 0,60 – 1,90 | --- | --- | --- | --- |

W warunkach polskich wprowadzenie metalu B było nieracjonalne ze względu na odmienne warunki rozwoju przemysłu i transportu. Od czasu normalizacji metali łożyskowych stosowanych na PKP w 1934 r., władze kolejowe dążyły do stosowania najwyższej jakości materiałów do budowy taboru kolejowego. Podjęto słuszną decyzję o organizacji własnych odlewni stopów PKP, w celu ograniczenia kosztów i uniezależnienia się od innych dostawców.

Niewątpliwie na decyzję o zakończeniu zakupów stopu Metall-B miała wpływ skomplikowana technologia wylewania stopu oraz konieczność wprowadzenia zmian konstrukcyjnych w panewkach wagonowych. Jak już wspomniano, nie bez znaczenia był również konflikt prof. Czochralskiego z prof. Broniewskim i liczne artykuły dyskredytujące metal B.

Tabor wagonowy PKP składał się z wówczas z dużej ilości typów wagonów trzech państw zaborczych i wielu innych europejskich zarządów kolejowych. Brak normalizacji łożysk osiowych powodował, że duża ilość typów stosowanych w tym taborze panewek praktycznie uniemożliwiała wprowadzanie osłabiających konstrukcję – rowków i otworów polepszających związanie warstwy stopu z panewkami. Wykonanie obliczeń panewek w celu sprawdzenia możliwości zmian, byłoby bardzo pracochłonne i zwiększyłoby koszt wprowadzenia stopu.

Stop bahmetal przeznaczony był do zalewania łożysk ślizgowych pracujących pod średnim obciążeniem, głównie w wagonach towarowych. Z powodzeniem mógł zastąpić stopy niskocynowe w urządzeniach pracujących pod obciążeniem jednostkowym nie przekraczającym 200 kg/cm$^2$. Miał mniejszą od stopów cynowych wytrzymałość na obciążenia dynamiczne. Do wad stopu należał znaczny spadek twardości wraz

[111] Jasik Z., Mickiewicz M., Stopy łożyskowe…, op. cit., s. 56.

ze wzrostem temperatury. Miał skłonności do starzenia się, na skutek wzrostu w określonym czasie twardości, spowodowanym zwiększeniem się w osnowie ilości twardych kryształów związku chemicznego $Pb_3Ca$. Najbardziej widoczny wzrost twardości występował w pierwszych piętnastu dniach od czasu wyprodukowania stopu. Bahnmetall w porównaniu ze stopami niskocynowymi był bardziej wrażliwy na korozję. Posiadał jednak dostateczną odporność w przypadku składowania w suchych pomieszczeniach. Stop ze zużytych panewek po wytopieniu nie mógł być ponownie użyty do zalewania, ze względu na nadmierne wypalanie się składników. Z tego względu istniała konieczność jego regeneracji w specjalistycznych wytwórniach.

Stop nie miał dostatecznej przyczepności, dlatego stosowano dodatkowe wiązanie mechaniczne z panewką, za pomocą rowków klinowych (jaskółczych ogonów) i otworów, które po zalaniu ich stopem nie pozwalały na oderwanie się warstwy stopowej od podłoża panewki. Rowki nie mogły mieć ostrych krawędzi, gdyż były zaczątkiem pęknięć warstwy stopu łożyskowego w czasie pracy.

Nie mniej istotnym czynnikiem utrudniającym wprowadzanie nowoczesnych rozwiązań konstrukcyjnych w kolejnictwie był konserwatyzm techniczny wyższych urzędników kolejowych PKP, którzy preferowali sprawdzone i wypróbowane od wielu lat konstrukcje. Przykładem tych tendencji mogą być trudności PKP Biura Elektryfikacji Węzła Kolejowego Warszawskiego związane z elektryfikacją w połowie lat 30. XX w. Węzła Kolejowego Warszawskiego.

Wprowadzenie stopu ŁCaw latach 50. XX w. w ramach wtórnego transferu technologii wykazało w warunkach polskich identyczne z bahnmetall wady stopu i trudności technologiczne związane z jego wylewaniem. Jedną z istotną przyczyn jego szybkiego wycofania po 1956 r., oprócz oczywistych wad technicznych, było administracyjne narzucenie tego materiału w formie „przodującej technologii sowieckiej" – powodowało to naturalny opór ze strony inżynierów i pracowników kolejowych.

Pomimo wszystkich wymienionych wad przy dostosowaniu technologii produkcji, zalewania panwi, składowania stopu i eksploatacji taboru, stop mógł stać się na kolejach polskich źródłem znacznych oszczędności cyny. Oczywiście przy spełnieniu ekonomicznego warunku wprowadzenia odpowiedniej technologii w warsztatach oraz powszechnego zastosowania stopu w całym taborze wagonowym PKP.

Niewątpliwie wprowadzenie stopu bahnmetall było wielkim sukcesem wynalazcy. Przyczyniło się do znacznych oszczędności cyny i zapewnienia sprawności transportu kolejowego. Równocześnie stało się źródłem dużych dochodów wynalazcy z opłat za patenty. Należy podkreślić, iż był to jedyny wynalazek Polaka związany z kolejnictwem, który uzyskał powszechne zastosowanie w Niemieckim kolejnictwie i tak szeroką recepcję w transporcie kolejowym innych państw.

*A. Królikowski, J. R. Przygodzki, Metody badawcze prof. Jana Czochralskiego. Pomiary, Automatyka, Kontrola 2014 vol. 60, nr 8, s. 525–528*

**Andrzej KRÓLIKOWSKI*,** Jacek Ryszard PRZYGODZKI**
* WYDZIAŁ CHEMICZNY, POLITECHNIKA WARSZAWSKA, ul. Noakowskiego 3, 00-664 Warszawa
**WYDZIAŁ MECHANICZNY, ENERGETYKI I LOTNICTWA, POLITECHNIKA WARSZAWSKA, ul. Nowowiejska 21/25, 00-665 Warszawa

# Metody badawcze profesora Jana Czochralskiego

**dr inż. Andrzej KRÓLIKOWSKI**

Dr inż. Andrzej Królikowski ukończył studia na kierunku Technologia Chemiczna w Politechnice Warszawskiej. Doktoryzował się w 1980 r. Pracuje w Katedrze Chemii Nieorganicznej i Technologii Ciała Stałego na Wydziale Chemicznym Politechniki Warszawskiej, obecnie na stanowisku prodziekana ds. studenckich. Zajmuje się strukturalnymi aspektami korozji stopów, korozją stali w betonie oraz elektrochemicznymi badaniami korozyjnymi.

*e-mail*: rabbit@ch.pw.edu.pl

**dr hab. inż. Jacek Ryszard PRZYGODZKI**

Dr hab. inż. Jacek Ryszard Przygodzki, prof. nzw. uzyskał stopień mgr inż. na Wydziale Elektrycznym Politechniki Warszawskiej w 1957 r., tytuł doktora n.t. na tym samym wydziale w 1968 r., a tytuł dr hab. na Wydziale Elektrycznym Politechniki Śląskiej w 1992 r. Pracował w Politechnice Warszawskiej i Świętokrzyskiej. Jest metrologiem, zajmującym się pomiarami wielkości magnetycznych i nieelektrycznych, członkiem IEEE i PTETiS.

*e-mail*: jacekprzygodzki@wp.pl

**Streszczenie**

Wielki polski uczony, Jan Czochralski, patron roku 2013 w Polsce, jest powszechnie znany jako wynalazca metody wzrostu monokryształów, zwanej po prostu metodą Czochralskiego. Jednak Czochralski opracował także wiele innowacyjnych, ilościowych metod badawczych w obszarze metaloznawstwa i metalurgii. W tej pracy przedstawiono jego metodologiczne dokonania w zakresie badania szybkości krystalizacji, zmian strukturalnych stopów metalicznych w następstwie ich rekrystalizacji, zniszczeń korozyjnych i wtrąceń niemetalicznych w stopach. Wskazano także możliwe związki pomiędzy oryginalnymi rozwiązaniami opracowanymi przez Czochralskiego i współczesnymi metodami badawczymi.

**Słowa kluczowe:** Czochralski, pomiary, krystalizacja, rekrystalizacja, korozja, wtrącenia niemetaliczne

## Research methods of professor Jan Czochralski

**Abstract**

The great Polish scientist, professor Jan Czochralski, the patron of 2013 year in Poland, is widely known from the worldwide famous methods for growing single crystals, called just Czochralski method. This is now the irreplaceable technique for generation of semiconductor single crystals, which are key elements in modern electronic devices. Other achievements of Czochralski are less recognized. However, Czochralski was also involved in development of innovative, quantitative research techniques in the field in metal chemistry and metallurgy. In this paper his methodological achievements in the research of crystallization rate, structural modifications in metals induced by recrystallization, corrosion damages and nonmetallic inclusions in alloys are outlined. Special attention is paid for research methods developed by Czochralski during his work at Warsaw University of Technology in years 1928-1939, which are less known to larger audience. The innovative testing methods, invented by Czochralski, combined scientific excellence with practical usability. Conceivable relations between approaches proposed by Czochralski and recent research methods are indicated.

**Keywords:** Czochralski, measurements, crystallization, recrystallization, corrosion, nonmetallic inclusions

## 1. Wstęp

Rok 2013, ogłoszony w Polsce rokiem Czochralskiego, zaowocował wieloma publikacjami, referatami, wystawami i kilkoma książkami na temat tego wielkiego polskiego uczonego, dotąd słabo rozpoznawalnego w naszym kraju. Można mieć nadzieję, że wiedza o dokonaniach profesora dotarła do szerszych kręgów społeczeństwa.

Czochralski urodził się w 1885 r. w wielodzietnej rodzinie w Kcyni (Wielkopolska) w zaborze pruskim. Nie posiadał formalnego wykształcenia. Przerwał naukę w szkole średniej, ale konsekwentnie rozwijał swoje zainteresowania chemią i zdobywał umiejętności poprzez praktykę w drogeriach, aptekach i laboratoriach. Brak matury uniemożliwiał mu podjęcie studiów wyższych, ale uczęszczał jako wolny słuchacz na wykłady na uczelniach berlińskich. Usilne samokształcenie, wielka determinacja i ciężka praca pozwoliły mu zdobywać uznanie środowiska i coraz wyższe stanowiska w laboratoriach metaloznawczych Berlina i Frankfurtu nad Menem. Działalność naukowo-badawczą kontynuował na Wydziale Chemicznym Politechniki Warszawskiej. Uzyskał tytuł doktora honoris causa tej uczelni, potem - tytuł profesora zwyczajnego. Został kierownikiem Zakładu, a potem Instytutu Metalurgii i Metaloznawstwa, które sam tworzył. Po II wojnie światowej pozbawiony został możliwości pracy na uczelni. Zmarł w zapomnieniu w 1953 r. Dopiero w 2012 r., po wielu latach dyskusji pełnej kontrowersji Senat Politechniki Warszawskiej przyjął ustawę rehabilitującą Czochralskiego. Stało się to po uzyskaniu wyników wszechstronnej kwerendy archiwalnej.

Czochralski był wybitnym naukowcem, ale jednocześnie inżynierem praktykiem i genialnym wynalazcą. Jego niestandardowe, nowatorskie podejście do rozwiązywanych trudnych zagadnień wynikało z interdyscyplinarnego podejścia. Określa się go jako chemika, krystalografa, metalurga i metaloznawcę. Z drugiej strony, jego dewizą było równoczesne prowadzenie badań podstawowych i stosowanych, co pozwało na efektywne rozwiązywanie problemów praktycznych, czego się chętnie podejmował.

Światową sławę przyniosła Czochralskiemu metoda wzrostu monokryształów, zwana powszechnie metodą Czochralskiego. Ta technika, zmodyfikowana w Krzemowej Dolinie w połowie ubiegłego wieku, przyczyniła się do gwałtownego rozwoju elektroniki, opartej na elementach półprzewodnikowych. Czochralski jest często nazywany ojcem nowoczesnej elektroniki. Uzyskał też wiele patentów dotyczących stopów łożyskowych (w tym słynnego metalu B – metalu kolejowego), które przyniosły mu duże profity finansowe. Prowadził pionierskie badania nad otrzymywaniem oraz kształtowaniem struktury i właściwości funkcjonalnych stopów na bazie aluminium i magnezu.

Czochralski jest znany dotąd głównie w środowiskach krystalografów, metaloznawców i oczywiście elektroników, którzy są użytkownikami elementów półprzewodnikowych, wytwarzanych metodą jego imienia. Pora, żeby poznało go środowisko metrologów, ponieważ Czochralski opracował wiele nowatorskich metod badawczych.

Celem artykułu jest przedstawienie wybranych metod badawczych stworzonych przez profesora Czochralskiego oraz wskazanie ich związków ze współczesnymi technikami pomiarowymi.

## 2. Pomiar szybkości krystalizacji

W 1916 r. Czochralski opracował metodę pomiaru szybkości krystalizacji metali. Wcześniej znano sposoby wyznaczania szybkości krystalizacji, ale nie można było ich zastosować dla procesu krystalizacji metali z roztopu (stopionego metalu), z uwagi na jego nieprzezroczystość. Wynaleziona przez Czochralskiego metoda pomiaru była prosta [1]. W tyglu utrzymywano roztop metalu w temperaturze nieznacznie przekraczającej temperaturę krzepnięcia. Do powierzchni roztopu zbliżano szklaną kapilarę. Stykający się z kapilarą roztop ulegał zestaleniu. Następnie kapilara była podnoszona i wskutek postępującej krystalizacji roztopu na jej końcu powstało długie, cylindryczne włókno metaliczne, nazywane „igłę krystaliczną". Stałą prędkość podnoszenia kapilary, zawieszonej na jedwabnej nici, zapewniał mechanizmu zegarowy, a obliczano ją obserwując przemieszczanie się sprzężonego z kapilarą wskaźnika wzdłuż wyskalowanej prowadnicy [1]. Stąd początkowo Czochralski nazywał swój sposób pomiaru metodą kapilarną.

Pomiar szybkości krystalizacji polegał na wyznaczeniu największej prędkości, przy której otrzymywana igła metaliczna nie traciła kontaktu z roztopem [1]. Przy zbyt wolnym wyciąganiu otrzymywano igłę krystaliczną o rosnącej średnicy. Wyniki pierwszych pomiarów, wykonanych przez Czochralskiego, pokazano w tablicy 1. Wykonał je dla łatwotopliwych metali i wyznaczone szybkości krystalizacji wynosiły kilka – kilkanaście cm/min, a średnica otrzymanych igieł krystalicznych nie przekracza 2 mm.

Tab. 1. Wyniki pierwszych pomiarów szybkości krystalizacji metali przeprowadzonych przez Czochralskiego [1]
Tab. 1. Results of first measurements of metals crystallization rate done by Czochralski [1]

| metal | temperatura topnienia, ºC | szybkość krystalizacji, mm/min | średnica uzyskanego kryształu, mm | długość uzyskanego kryształu, cm |
|---|---|---|---|---|
| cyna | 232 | ~90 | < 2 | do 15 |
| ołów | 320 | ~140 | < 2 | do 12 |
| cynk | 416 | ~100 | < 2 | do 19 |

Czochralski badał strukturę otrzymanych igieł krystalicznych i stwierdził, że w zależności od warunków krystalizacji, mają one strukturę monokrystaliczną (pojedynczy kryształ) lub polikrystaliczną (wiele krystalitów). Dodatkowo mierzył szybkość tworzenia zarodków krystalizacji. Na podstawie tych dwóch wielkości (szybkości krystalizacji i szybkości tworzenia zarodków) określał średni wymiar powstających krystalitów. Stwierdził, że osadzenie na końcówce kapilary cząstek metalicznych, na przykład przez pocieranie nią o miękkie metale [1] lub stosowanie zamiast kapilary drutów metalowych [2], ułatwia zapoczątkowanie krystalizacji i wpływa na orientację powstających kryształów.

Czochralski rozwijał metodę badania szybkości krystalizacji w okresie pracy na Politechnice Warszawskiej. Wykonał pomiary dla reaktywnych metali: bizmutu i sodu [2]. Przydatna była tu jego wiedza chemiczna. Zaprojektował układy pomiarowe tak, aby możliwe było zastosowanie atmosfer ochronnych, eliminujących utlenianie tych metali w kontakcie z powietrzem. Czochralski analizował warunki odprowadzania ciepła krystalizacji, występujące w jego metodzie i stwierdził, że szybkość krystalizacji jest odwrotnie proporcjonalna do ciepła krystalizacji metalu [2]. Określił wpływ temperatury roztopu (stopnia przechłodzenia) i czystości metalu na przebieg krystalizacji.

Metoda Czochralskiego została zaprojektowana do pomiaru szybkości krystalizacji, a otrzymywane w ten sposób cienkie, cylindryczne monokryształy nie nadawały się do badań ich właściwości. Przełom nastąpił w połowie poprzedniego wieku, gdy pomysł Czochralskiego wykorzystano do wyciągania monokryształów półprzewodników. Po modyfikacjach (inicjacja krystalizacji na zorientowanej zarodzi - fragmencie monokryształu, mała szybkość wyciągania, ruch obrotowy powstającego kryształu, ogrzewanie indukcyjne) okazała się ona prostą, stosunkowo tanią i bardzo efektywna metodą otrzymywania monokrystalicznych półprzewodników dla potrzeb współczesnej elektroniki. Najpierw przeprowadzono monokrystalizację germanu i krzemu, potem zastosowano tę metodę do wyciągania monokryształów związków półprzewodnikowych. Metodą Czochralskiego otrzymuje się obecnie ok. 95% monokrystalicznych materiałów półprzewodnikowych. Możliwe jest wytworzenie cylindrycznych monokryształów o imponujących wymiarach: średnica do 30 cm, długość do 2 m, masa ponad 250 kg.

To wszystko zaczęło się od prostego pomysłu, ale - jak się później okazało - o olbrzymim potencjale aplikacyjnym. Ze zwykłej metody pomiarowej powstała nowatorska technologia materiałowa, a Czochralski został zasłużenie nazwany ojcem nowoczesnej elektroniki. Ale informacje o wielkim triumfie jego metody nie dotarły prawdopodobnie do niego. Czochralski zmarł w zapomnieniu w 1953 r.

## 3. Badania rekrystalizacji metali

Rekrystalizacja to proces polegający na przywróceniu zdeformowanemu metalowi równowagowej struktury krystalicznej. Dla większości metali ten proces w temperaturze pokojowej zachodzi bardzo wolno. Zastosowanie podwyższonej temperatury (wyżarzanie) powoduje przyspieszenie rekrystalizacji. Proces ten jest m.in. związany ze zmniejszeniem gęstości defektów strukturalnych (zdrowieniem) i rozrostem krystalitów. Takie modyfikacje struktury prowadzą do zmian właściwości chemicznych i fizycznych metalu i mają duże zastosowanie praktyczne.

W swoich badaniach rekrystalizacji metali Czochralski określał rozmiary ziaren po tym procesie. Próbki metali poddawał najpierw obróbce plastycznej na zimno (różny stopień zgniotu), a potem wyżarzał w różnych temperaturach w określonym czasie. Następnie określał metalograficznie (pod mikroskopem) wielkość ziaren na wytrawionym przekroju próbek. Wielkość powstających ziaren zależała od stopnia zgniotu oraz temperatury i czasu wyżarzania. Do opisu takiej zależności Czochralski stosował przestrzenne (trójwymiarowe) wykresy przedstawiono zależność średniego wymiaru ziaren od stopnia zgniotu i temperatury wyżarzania przy ustalonym czasie. Na rys. 1 pokazano taki wykres uzyskany przez Czochralskiego dla procesu rekrystalizacji brązu aluminiowego [3].

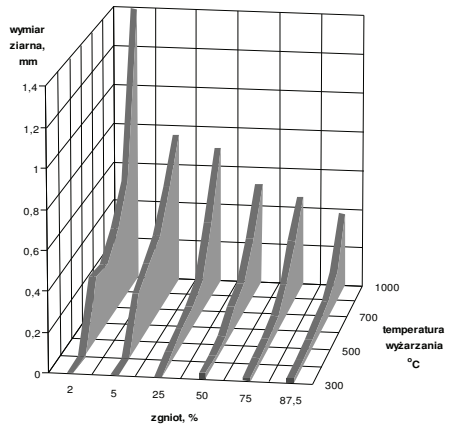


Rys. 1. Wykres rekrystalizacji dla brązu aluminiowego (5% Al) - czas wyżarzania 0,5 godziny [3]
Fig. 1. Recrystallization diagram for aluminum bronze (5% Al) - annealing time: 0,5 h [3]

Czochralski opracował wykresy rekrystalizacji także dla innych metali, m.in. złota, srebra, cynku i cyny. Pokazywały one technologom, jak można nadawać metalom pożądane właściwości funkcjonalne, dobierając odpowiednio warunki ich obróbki plastycznej i wyżarzania. Wielkość ziaren wpływa nie tylko na właściwości mechaniczne (wytrzymałość, plastyczność, twardość), ale także na właściwości elektryczne, magnetyczne i odporność na korozję. Analogiczne wykresy rekrystalizacji do dzisiaj są przytaczane w podręcznikach metaloznawstwa, ale bardzo rzadko można tam znaleźć nawiązanie do nazwiska Czochralskiego.

## 4. Pomiary zniszczeń korozyjnych

Stopień zniszczeń korozyjnych stopów metalicznych jest powszechnie określany na podstawie zmian ich stanu powierzchni lub ubytku masy. Jednak na przełomie XIX i XX wieku poznano nowe zjawiska korozyjne, charakteryzujące się daleko posuniętą degradacją metalu przy niewielkim ubytku masy. Należą do nich m.in.: korozja selektywna (korozji ulega jedna faza wielofazowego stopu, co może prowadzić do jego dezintegracji) i naprężeniowe pękanie korozyjne (stop pęka lokalnie - w strefie koncentracji naprężeń rozciągających, a związany z tym ubytek masy jest nieznaczny).

Czochralski stwierdził, że obserwacje stanu powierzchni czy pomiary ubytku masy korodujących próbek są mało przydatne do oceny odporności korozyjnej materiałów. Był jednym z pionierów nowego podejścia do pomiarów korozyjnych. Uważał, że lepszym kryterium rozwoju zniszczeń korozyjnych są zmiany takich właściwości korodującego materiału, które odpowiadają przemianom jego wewnętrznej struktury. Promował więc pomiary właściwości mechanicznych (wytrzymałości na rozciąganie i wydłużenia przed zerwaniem) i elektrycznych (przewodności) po ekspozycji stopów w środowiskach korozyjnych [4,5].

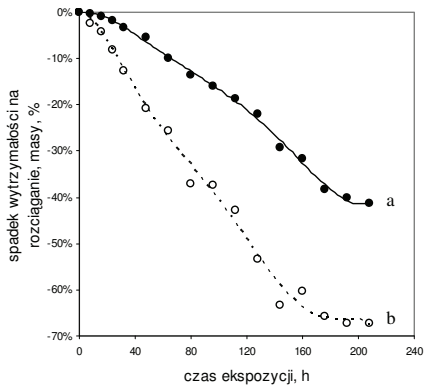


Rys. 2 Zmiany masy (a) i wytrzymałości na rozciąganie (b) podczas korozji mosiądzu 60/40 w 17% HCl [4]
Fig. 2. Changes of mass (a) and tensile strength (b) during corrosion of 60/40 brass in 17% HCl [4]

Na rys. 2 pokazano wyniki przeprowadzonych przez Czochralskiego badań korozji mosiądzu 60/40. Próba została przeprowadzona w roztworze kwasu chlorowodorowego i trwała 210 godzin. W tych warunkach ten dwufazowy stop ulegał korozji selektywnej, tzw. odcynkowaniu (preferencyjnie roztwarzała się w faza międzymetaliczna CuZn). Czochralski wykonywał pomiary wytrzymałości i ubytku masy próbek mosiądzu po różnych okresach ekspozycji. Stwierdził spadek wytrzymałości stopu prawie o 70%, podczas gdy ubytek masy wynosił tylko 40%. Towarzyszył temu spadek wydłużenia przed zerwaniem stopu od początkowej wartości 10% praktycznie do zera [4]. Te zmiany parametrów mechanicznych lepiej odpowiadały obserwowanemu rozwojowi zniszczeń korozyjnych mosiądzu niż ubytek masy.

Takie podejście do pomiarów korozyjnych stało się normą w przypadku korozji naprężeniowej i zmęczeniowej. M.in. stosował je później doktorant Czochralskiego – Śmiałowski w pionierskich badaniach korozji wodorowej stopów metalicznych (zniszczeń w wyniku wnikania wodoru).

Często porównuje się zachowanie korozyjne nowych materiałów z zachowaniem znanych tworzyw, traktowanych jako materiał referencyjny. Czochralski zwracał uwagę na potrzebę charakteryzowania stosowanych materiałów referencyjnych [5]. Są to często metale po obróbce plastycznej (walcowanie, wyciąganie), która wywołuje ich anizotropię i powoduje zróżnicowanie zachowania korozyjnego w zależności od kierunku badania. Ten aspekt jest wciąż aktualny w pomiarach korozyjnych.

## 5. Oznaczanie wtrąceń niemetalicznych

Wtrącenia niemetaliczne (głównie zanieczyszczenia) stanowią nieciągłości w osnowie metalu i niekorzystnie wpływają na jego właściwości funkcjonalne (wytrzymałość, odporność korozyjną czy przewodność elektryczną). Oznaczanie obecności wtrąceń ma duże znaczenie praktyczne, np. przy kontroli jakości stopów.

Wpływ wtrąceń zależy od ich ilości, rozmieszczenia i rozmiarów. Wtrącenia były charakteryzowane na podstawie obserwacji mikroskopowych przekroju próbki metalowej, jednak takie podejście było subiektywne, niejednoznaczne i dawało słabo powtarzalne wyniki.

Czochralski poszukiwał obiektywnej, ilościowej metody określania częstości występowania i wymiarów wtrąceń niemetalicznych w metalach. W okresie pracy w Niemczech opracował tzw. radiomikroskop [6]. Było to połączenie mikroskopu metalograficznego i układu odbiorczego radia kryształkowego. Badana próbka stopu była umieszczana na stoliku mikroskopu i połączona z anteną. Stalową igłę, połączoną ze słuchawką, przesuwano po powierzchni stopu. Gdy natrafiano na wtrącenie o charakterze półprzewodnikowym, w słuchawce rozlegał się sygnał rozgłośni, na którą dostrojony był odbiornik radiowy. Obserwując miejsce styku, w którym otrzymano efekt prostujący, Czochralski tworzył konturowe mapy wtrąceń niemetalicznych, pokazujące ich rozmieszczenie i kształt. Takie badania przeprowadził dla siluminów (stopy aluminium i krzemu) [6] i stali krzemowych [7].

Radiomikroskop jest uważany za jedno z najważniejszych osiągnięć Czochralskiego, a stosowana w nim zasada skanowania powierzchni metalu w poszukiwaniu wtrąceń jest czasem wiązana z ideą skaningowego mikroskopu analizującego (SPM). Jednak Czochralski stwierdził ograniczoną przydatność radiomikroskopu do identyfikacji wtrąceń, ponieważ tylko nieliczne z nich wykazują właściwości półprzewodnikowe, nawet w przypadku wtrąceń bogatych w krzem [6,7].

Czochralski poszukiwał lepszego, bardziej niezawodnego sposobu oznaczania wtrąceń niemetalicznych i kolejne metody opracował podczas pracy na Wydziale Chemicznym Politechniki Warszawskiej (tab. 1). Pierwszą z nich była metoda ilościowej analizy obrazów mikroskopowych [8]. Aby ograniczyć subiektywność obserwacji mikroskopowych i błąd oznaczeń wynikający z niejednorodności stopu, Czochralski znormalizował warunki analizy obrazów mikroskopowych:

- określił zasadę doboru badanych przekrojów próbki metalu (prostopadle i równolegle do kierunku obróbki plastycznej, na trzech głębokościach),
- ustalił powiększenie (x100), przy który wykonuje się oznaczenie i pole powierzchni, podlegające ocenie,
- zdefiniował sposób określania pola powierzchni i średniej długości wtrąceń,
- wynik był uśredniany z trzech pomiarów dla każdego kierunku badania.

Wyniki obserwacji określał ilościowo podając ilość wtrąceń na jednostkę pola powierzchni, średni wymiar wtrąceń i sumaryczne pole powierzchni wtrąceń [8].

Tab. 2. Metody oznaczania wtrąceń niemetalicznych w stopach - opracowane przez J. Czochralskiego
Tab. 2. Techniques for determination of nonmetalic inclusions in alloys - developed by J. Czochralski

| | data | zasada | uwagi |
|---|---|---|---|
| radiomikroskop [6] | 1925 | efekt prostujący na styku wtrącenie – ostrze metalowe | tylko wtrącenia pół-przewodnikowe |
| mikroskopowa / mikrograficzna [8] | 1935 | analiza obrazu mikroskopowego | analiza ilościowa |
| pomiar lokalnej przewodności [9] | 1936 | różnica przewodności metalu i wytrącenia | małe wtrącenia mogą pozostać niewykryte |
| mikrofotometr rejestrujący [10] | 1936 | różnice współczynnika odbicia światła faz | pomiar automatyczny |

Kolejna metoda, zaproponowana przez Czochralskiego, wykorzystywała różnicę rezystancji wtrąceń niemetalicznych i matrycy metalowej [9]. Umieszczona na stoliku krzyżowym pod mikroskopem próbka metalu była połączona z jednym biegunem źródła napięcia (bateria + potencjometr), a do wypolerowanej powierzchni metalu lekko dociskano igłę stalową, przyłączoną do drugiego bieguna. Prąd płynący przez próbkę mierzono miliamperomierzem. Następnie przesuwano próbkę ruchem jednostajnym za pomocą manipulatorów stolika mikroskopowego. Gdy natrafiono na wtrącenie niemetaliczne, następował spadek mierzonego prądu. W ten sposób otrzymywano obraz ilości, wielkości i rozmieszczenia wtrąceń. Tak określano stopień zanieczyszczenia stopów żelaza [9]. Uzyskane wyniki korelowano z mikroskopowymi obrazami badanych powierzchni. Czochralski przedstawił skrupulatną analizę możliwych błędów przy stosowaniu tej metody, wynikających m.in. z rezystancji styku zależnej od stopnia docisku igły i możliwości pomijania wtrąceń mniejszych od średnicy ostrza igły (początkowo wynosiła 0,1 mm, ale zwiększała się miarę stępienia się igły).

Najbardziej zaawansowanym technicznie sposobem ilościowego oznaczania wtrąceń niemetalicznych, opracowanym w Instytucie Metalurgii i Metaloznawstwa, kierowanym przez Czochralskiego, był pomiar przy pomocy mikrofotometru rejestrującego, zwanego inkluzometrem [10]. To urządzenie jest pomijane przy omawianiu osiągnięć Czochralskiego. Zostało ono opracowane przez jego współpracownika - Śmiałowskiego, jednak powstało z inicjatywy i przy wsparciu Czochralskiego.

Inkluzometr działał na zasadzie pomiaru różnic natężenia zogniskowanego światła odbitego od wypolerowanej powierzchni metalu [10]. Próbkę metalu umieszczano na stoliku mikroskopu i wprawiano automatycznie w ruch zygzakowaty względem osi optycznej mikroskopu. Towarzyszące temu zmiany natężenie odbitego światła mierzono przy pomocy komórki fotoelektrycznej sprzężonej z galwanometrem zwierciadłowym. Promień świetlny odbity od zwierciadła galwanometru pozostawiał ślad na papierze fotograficznym nawiniętym na bęben, którego ruch był zsynchronizowany z ruchem próbki. Jeden pomiar trwał 2 godziny. W ten sposób otrzymywano powiększony wykres zawierający zbiór linii, których odchylenia odpowiadały zmianom natężenia światła odbitego od różnych miejsc powierzchni metalu. Ten wykres odwzorowywał strukturę metalu: obecność faz stopowych o różnej zdolności odbijania światła, w tym wtrąceń. Określono zasady interpretacji otrzymanych wykresów, m.in. związek pomiędzy wielkością wtrącenia a odchyleniem od linii prostej na wykresie.

Działanie inkluzometru weryfikowano wykonując pomiary dla płytki mikrometrycznej z rysami, stopów o znanej zawartości wtrąceń: żeliwa szarego (wtrącenia grafitu), stali węglowej i stopu łożyskowego Sn-Sb [10]. Określono źródła błędów pomiarowych, związanych z niedostatecznym przygotowania powierzchni metalu (rysy), uchybieniami działania systemu mechanicznego inkluzometru i niedokładnością przy interpretacji wykresów (planimetrowanie odchyleń od linii prostych). Na tej podstawie oszacowano średni błąd oznaczeń ilości, średnich wymiarów i łącznej powierzchni wtrąceń na 5%.

Inkluzometr pozwalał określić nie tylko zawartość wtrąceń niemetalicznych, ale równie innych składników strukturalnych stopu. Ważnym rozwiązaniem był automatyczny system przesuwu próbki, co istotnie zwiększyło obiektywność i powtarzalność oznaczeń. Ten przyrząd może być uważany za pierwowzór tak powszechnie dzisiaj stosowanych systemów analizy obrazów mikroskopowych.

## 6. Wnioski

Czochralski jest znany jako wynalazca metody wzrostu monokryształów, ale mało kto wie, że wywodzi się ona z opracowanego przez niego sposobu pomiaru szybkości krystalizacji. Jeszcze mniej znane są inne metody badawcze wprowadzone i stosowane przez Czochralskiego. Próbował on ilościowo opisać zjawiska, trudne do skwantyfikowania i był autorem wielu nowatorskich metod pomiarowych. Czynił mierzalnym to, co wydawało się trudne do zmierzenia. Opracowane przez niego metody pomiarowe są pomysłowe i zarazem proste, ale bardzo innowacyjne i nakierowane na rozwiązywanie praktycznych problemów. Niektóre, zaproponowane przez Czochralskiego rozwiązania, dotyczące prowadzenia pomiarów i interpretacji ich wyników, są nadal stosowane. We współczesnych metodach pomiarowych można znaleźć nawiązania do pomysłów Czochralskiego: mikroskopia ze skanującą sondą jest wiązana z zasadą działania radiomikroskopu, analiza obrazów mikroskopowych z inkluzometrem, a rozwój korozji naprężeniowej ocenia się na podstawie pomiarów wytrzymałościowych. Te dokonania Czochralskiego zasługują na szerszą popularyzację.

## Podziękowania

Publikacja została częściowo sfinansowana ze środków MNiSzW - zadanie 988/P-DUN/2013 z zakresu działalności upowszechniającej naukę „Jan Czochralski na Wydziale Chemicznym Politechniki Warszawskiej"

## 7. Literatura

[1] Czochralski J., Ein neues Verfahren zur Messung der Kristallisationsgeschwindigkeit der Metale, Z. Phys. Chem., vol. 92, s. 219-221, 1918.
[2] Czochralski J., Garlicka W., O szybkości krystalizacji sodu oraz o związku między atomowym ciepłem krzepnienia i szybkością krystalizacji pierwiastków, Wiad. Inst. Met. Met., vol. 3(1), s. 39-44, 1936.
[3] Czochralski J., Lewicka N., Wykres rekrystalizacji brązów aluminiowych 2% i 5% Al, Wiad.. Metal. Metal, vol. 4, s. 61-64, 1937.
[4] Czochralski J., Schmid E., Neue Wege der Korrosionsforschung, Z. Metallk., vol. 20(1), s. 1-7, 1928.
[5] Królikowski A., Wkład Jana Czochralskiego w rozwój inżynierii korozyjnej, Ochr. Przed Koroz., vol. 57(11), s. 474-477, 2013.
[6] Czochralski J., Radjotechnika na usługach metaloznawstwa, Przegl. Techn., vol. 51(27), s. 404-405, 1925.
[7] Czochralski J., Sznuk W., Spostrzeżenia na detektorowymi własnościami związków występujących jako wtrącenia w stali, Wiad. Inst. Met. Met., vol. 3(1), s. 3-4, 1936.
[8] Czochralski J., Metoda ilościowego oznaczania wtrąceń niemetalicznych, Wiad. Inst. Met. Met., vol. 2(1), s. 34-36, 1935.
[9] Czochralski J., Sznuk W., Próby obiektywnego określenia zawartości wtrąceń niemetalicznych na szlifie, Wiad. Inst. Met. Met., vol. 3(1), s. 5-6, 1936.
[10] Śmiałowski M., O nowym mikrofotometrze rejestrującym i jego zastosowaniu do ilościowego oznaczania wtrąceń niemetalicznych, Wiad. Inst. Met. Met., vol. 3(1), s, 46-55, 1936.

# Laureaci Nagrody im. Jana Czochralskiego

*Andrzej Królikowski, Tadeusz Kulik*

# Konkurs o Nagrodę im. Prof. Jana Czochralskiego

W marcu 2013 r. Krajowy Koordynator Obchodów Roku Jana Czochralskiego – prof. Mirosław Nader (Wydział Transportu Politechniki Warszawskiej) wystąpił z inicjatywą zorganizowania przez Politechnikę Warszawską Ogólnopolskiego Konkursu o Nagrodę im. Prof. Jana Czochralskiego. Na jego prośbę, dr inż. Andrzej Królikowski (Wydział Chemiczny PW) przygotował wniosek do MNiSzW o ustanowienie takiego konkursu pod egidą Rektora Politechniki Warszawskiej i dofinansowanie w ramach działalności upowszechniającej naukę. Do wniosku dołączono projekt regulaminu Konkursu, opracowany po konsultacjach z prof. Mirosławem Naderem i doc. Janem Grabskim (Wydział Fizyki PW).

W czerwcu 2013 r. MNiSzW podjęło decyzję o merytorycznej zasadności wniosku i jego finansowaniu, jednak umowa określająca warunki i finansowanie zadania została podpisana dopiero we wrześniu 2013 r. W tej sytuacji nie było możliwe dotrzymanie terminów, określonych w harmonogramie zadania i pierwsza edycja Konkursu została przesunięta na I kwartał 2014 r. (aneks podpisano w grudniu 2013 r.).

W grudniu 2013 r. JM Rektor Politechniki Warszawskiej prof. dr hab. inż. Jan Szmidt powołał prof. dr hab. inż. Tadeusza Kulika (Wydział Inżynierii Materiałowej PW) na stanowisko Pełnomocnika Rektora PW ds. Nagrody im. Prof. Jana Czochralskiego, a dr inż. Andrzej Królikowskiego – na Sekretarza Konkursu. Powołał też Kapitułę Konkursu w składzie:

1) Rektor Politechniki Warszawskiej,
2) Przedstawiciel Ministerstwa Nauki i Szkolnictwa Wyższego,
3) Przedstawiciel Polskiej Akademii Nauk,
4) Krajowy Koordynator Obchodów Roku Jana Czochralskiego,
5) Pełnomocnik Rektora PW ds. nagrody im. Jana Czochralskiego,
6) Dziekan Wydziału Chemicznego Politechniki Warszawskiej,
7) Dziekan Wydziału Inżynierii Materiałowej Politechniki Warszawskiej,
8) Dziekan Wydziału Fizyki Politechniki Warszawskiej,
9) Dziekan Wydziału Inżynierii Chemicznej i Procesowej Politechniki Warszawskiej,
10) Dziekan Wydziału Elektroniki i Technik Informacyjnych Politechniki Warszawskiej,
11) Prezes Polskiego Towarzystwa Wzrostu Kryształów,
12) Prezes Polskiego Towarzystwa Chemicznego,
13) Prezes Polskiego Towarzystwa Fizycznego,
14) Prezes Stowarzyszenia Inżynierów i Techników Przemysłu Chemicznego,
15) Prezes Stowarzyszenia Inżynierów i Techników Mechaników Polskich.

Równocześnie Rektor zatwierdził regulamin Konkursu i wzory wniosków konkursowych. Zgodnie z regulaminem na Konkurs mogą być zgłaszane prace z obszaru działalności naukowo-technicznej prof. Jana Czochralskiego, dotyczące następujących zagadnień:

a) procesy krystalizacji i rekrystalizacji,
b) otrzymywanie, badania struktury i właściwości oraz zastosowania monokryształów,
c) otrzymywanie i właściwości stopów łożyskowych,
d) metody badania struktury stopów metalicznych,
e) sprężyste i plastyczne odkształcenia metali, wpływ składu i struktury
f) badania korozyjne sprzężone z badaniami wytrzymałościowymi,
g) stopy metali lekkich, ich struktura, właściwości i zastosowania,
h) innych obszarów działalności naukowo-technicznej prof. Czochralskiego, które znajdują potwierdzenie w jego dorobku publikacyjnym lub innych przekazach.

Na przełomie stycznia i lutego 2014 r. JM Rektor PW ogłosił pierwszą edycję konkursu za rok 2013. Nagrody były przyznawane w dwóch kategoriach:
a) Nagroda Naukowa z wybitne osiągnięcia naukowe i/lub aplikacyjne w zakresie w/w zagadnień,
b) Nagroda Promocyjna dla autora najlepszej pracy dyplomowej (inżynierskiej, licencjackiej lub magisterskiej) lub doktorskiej, dotyczącej w/w zagadnień.

Na tę edycję konkursu wpłynęło 5 wniosków o nagrodę naukową i 9 wniosków o nagrodę promocyjną. Na posiedzeniu w marcu 2014 r. Kapituła po dokonaniu wnikliwej oceny zgłoszonych prac konkursowych, biorąc pod uwagę ich poziom naukowy, zbieżność tematyki z obszarem działalności prof. Jana Czochralskiego oraz aspekty praktyczne i możliwości wdrożenia wyników, postanowiła wnioskować do Rektora Politechniki Warszawskiej, *ex officio* Przewodniczącego Kapituły, o przyznanie:
– nagrody specjalnej (25.000 zł): prof. dr hab. Annie Pajączkowskiej (Instytut Technologii Materiałów Elektronicznych) za wybitne osiągnięcia naukowe i całokształt działań na rzecz przywrócenia dobrego imienia prof. Jana Czochralskiego,
– nagrody naukowej (25.000 zł): prof. dr hab. inż. Małgorzacie Lewandowskiej (Politechnika Warszawska) za zbiór publikacji dotyczących kształtowania struktury i właściwości materiałów metalicznych o strukturze manometrycznej,
– nagrody promocyjnej (7.500 zł): dr Agnieszce Czapik (Uniwersytet im. Adama Mickiewicza w Poznaniu) za pracę doktorską pt. Badanie wpływu systematycznych modyfikacji chemicznych cząsteczek na ich upakowanie w krysztale.

W trakcie obrad Kapituły zostały złożone deklaracje wyasygnowania środków na ufundowanie jednorazowej nagrody specjalnej ze strony: Politechniki Warszawskiej, Polskiego Towarzystwa Chemicznego, Polskiego Towarzystwa Fizycznego i Polskiego Towarzystwa Wzrostu Kryształów. Kapituła podjęła też decyzję o dokonaniu zmiany w regulaminie Konkursu i wprowadzeniu oddzielnych nagród za najlepszą pracę doktorską oraz dyplomową (inżynierską, licencjacką lub magisterską).

Kapituła jednomyślnie poparła pomysł prof. Bogusława Buszewskiego, Prezesa Polskiego Towarzystwa Chemicznego aby laureatom Nagrody wręczać, oprócz dyplomu i nagrody pieniężnej, również okolicznościowe statuetki. Za zgodą dr Pawła Tomaszewskiego z Instytutu Niskich Temperatur i Badań Strukturalnych PAN we Wrocławiu wykorzystano w tym celu jego projekt „*Pióro Czochralskiego*". Sporządzenie projektu statuetki i jej wykonanie powierzono prof. Alicji Majewskiej z Wydziału Sztuk Pięknych Uniwersytetu Mikołaja Kopernika w Toruniu.

Dokonano też zastrzeżenia w Urzędzie Patentowym Rzeczypospolitej Polskiej znaku słownego „Konkurs im. Prof. Jana Czochralskiego".

Uroczystość wręczenia Nagród im. Prof. Jana Czochralskiego za rok 2013 odbyła się w dniu 30 maja 2013 r. w Sali Senatu Politechniki Warszawskiej. Program obejmował:

– wystąpienie Podsekretarza Stanu w MNiSzW prof. dr hab. Jacka Gulińskiego,
– wystąpienie Rektora Politechniki Warszawskiej prof. dr hab. inż. Jana Szmidta,
– wystąpienie Krajowego Koordynatora Obchodów Roku Jana Czochralskiego prof. dr hab. inż. Mirosława Nadera,
– wręczenie nagród laureatom,
– wystąpienia laureatów (prezentacja nagrodzonych osiągnięć).

W dniu 8 października 2014 r. JM Rektor Politechniki Warszawskiej ogłosił drugą edycję Konkursu. Zgodnie ze zmianami wprowadzonymi do regulaminu, Nagroda im. Prof. Jana Czochralskiego będzie przyznana w trzech kategoriach:

– za wybitne osiągnięcia naukowe i/lub aplikacyjne (20 000 zł) – nagroda indywidualna lub zespołowa,
– za najlepszą pracę doktorską w roku akademickim 2013/14 (7 500 zł), oraz
– za najlepszą pracę dyplomową (inżynierską, licencjacką lub magisterską) w roku akademickim 2013/14 (5 000 zł).

Wnioski do Konkursu o Nagrodę im. Prof. Jana Czochralskiego przyjmuje Biuro Rektora Politechniki Warszawskiej, a obsługę administracyjną Konkursu prowadzi mgr Joanna Kuźmicz. Ogłoszenie werdyktu kapituły i wręczenie nagród drugiej edycji Konkursu planowane jest w listopadzie 2014 r.

*Październik 2014 r.*

Agnieszka Czapik

# BADANIE WPŁYWU SYSTEMATYCZNYCH MODYFIKACJI CHEMICZNYCH CZĄSTECZEK NA ICH UPAKOWANIE W KRYSZTALE

Streszczenie rozprawy doktorskiej wykonanej w Zakładzie Krystalografii Wydziału Chemii Uniwersytetu im. Adama Mickiewicza w Poznaniu
pod kierunkiem prof. dr hab. Marii Gdaniec

Powielanie jakiegoś schematu supramolekularnego w pewnej grupie struktur krystalicznych pozwala na dostrajanie ich budowy poprzez modyfikacje czynione w strukturze tworzących je cząsteczek. Stwarza to również możliwość śledzenia tolerancji tych struktur na wprowadzane zmiany w budowie cząsteczkowej. Celem mojej rozprawy doktorskiej było prześledzenie zmian w strukturze supramolekularnej kryształów dwuskładnikowych, w których główną rolę odgrywały wiązania wodorowe i oddziaływania układów aromatycznych. Badaniom poddałam dwie grupy kryształów dwuskładnikowych złożonych z cząsteczek o stosunkowo prostej budowie chemicznej. Powtarzającym się elementem budowy badanych kryształów była aromatyczna zasada heterocykliczna, której cząsteczka zawierała pierścień pirazynowy.

Pierwszą grupę badanych kryształów tworzyły kompleksy chinoksaliny z kwasami dikarboksylowymi. W tej serii otrzymałam szesnaście nowych kompleksów molekularnych i wyznaczyłam ich struktury metodami rentgenowskiej analizy strukturalnej. Badania te pokazały, że chinoksalina tworzy z kwasami dikarboksylowymi kompleksy, w których stosunek kwas:zasada wynosi 1:1 lub 1:2, podczas gdy w podobnych kompleksach pirazyny i fenazyny stosunek ten wynosi 1:1 lub 2:1. Kryształy o stechiometrii 1:1 zbudowane były z łańcuchów cząsteczek połączonych wiązaniami wodorowymi $COOH\cdots N_{arom}$ natomiast elementem budowy kompleksów 1:2 były symetryczne heterotrimery utworzone przez te wiązania. Uzyskane wyniki wskazują na istotną rolę jaką w tworzeniu kryształów wieloskładnikowych, obok czynników chemicznych, może odgrywać aspekt symetrii komponentów cząsteczkowych. Badane kompleksy chinoksaliny z kwasami karboksylowymi dały możliwość prześledzenia współzawodnictwa dwóch typów syntonów

supramolekularnych zaliczanych do stosunkowo niezawodnych, $R_2^2(7)$ lub $R_2^2(8)$, na które składają się silne i słabe wiązanie wodorowe (Rys. 1). Uzyskane przeze mnie wyniki wskazują na większe prawdopodobieństwo utworzenia płaskiego syntonu $R_2^2(7)$, jednakże ze wzrostem odległości O···N w wiązaniu wodorowym O-H···N prawdopodobieństwo utworzenia płaskiego syntonu $R_2^2(8)$ znacznie wzrasta.

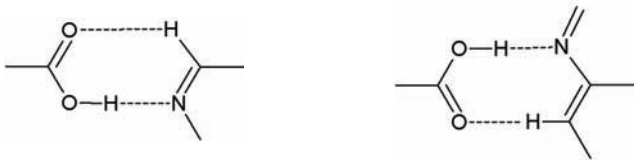

a b

Rys. 1. Cykliczny synton suparmolekularny: a) $R_2^2(7)$, b) $R_2^2(8)$

Drugą grupą badanych kryształów dwuskładnikowych były kompleksy tworzone przez aromatyczne zasady heterocykliczne z difenolami, aminofenolami oraz pierwszorzędowymi aminami aromatycznymi. W tej serii wyznaczyłam struktury kryształów dla 35 nowych kompleksów molekularnych. Otrzymane przeze mnie wyniki pokazują, że zarówno zmiany w budowie zasady heterocyklicznej jak i w funkcjonowanej cząsteczce aromatycznej (zamiana pierścienia benzenowego na układ naftalenowy, zmiana położenia i liczby grup OH, zamiana grup OH na $NH_2$ ) nie wpływa w większości przypadków na ogólny schemat budowy supramolekularnej kompleksu, która oparta jest na dwóch ortogonalnych podjednostkach strukturalnych. Podobieństwo dotyczy pewnego ogólnego schematu budowy oraz podobnego udziału w stabilizacji kryształu silnych wiązań wodorowych, oddziaływań warstwowych i oddziaływań C-H···π (Rys. 2). Próba naruszenia udziału tych ostatnich oddziaływań w stabilizacji kryształu poprzez obniżenie gęstości elektronowej układu aromatycznego, który jest akceptorem tych oddziaływań, zakończyła się przebudową całej struktury kompleksu. Badany w rozprawie układ powinien być doskonałym modelem do dalszej ilościowej charakterystyki zależności między słabymi oddziaływaniami aromatycznymi i silnymi wiązaniami wodorowymi w krysztale.

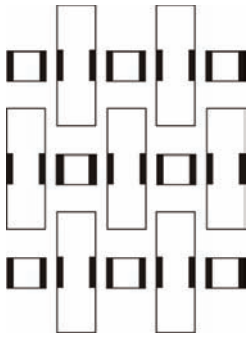

Rys. 2. Schemat budowy kompleksów molekularnych oparty na ortogonalnch podjednostkach strukturalnych.

Odrębnym elementem rozprawy było zastosowanie metod mechanochemicznych do syntezy kokryształów oraz do badania przemian zachodzących między różnymi formami krystalicznymi. W ostatnich latach reakcje inicjowane energią mechaniczną cieszą się coraz większą popularnością. Polegają one na ucieraniu mieszaniny substratów bez dodatku rozpuszczalnika lub ze śladowym jego dodatkiem. Mechanochemia z sukcesem stosowana jest w syntezie układów bazujących zarówno na wiązaniach kowalencyjnych, koordynacyjnych jak i oddziaływaniach supramolekularnych. Ciągle rosnąca liczba zastosowań kokryształów, a także rozwój strategii ich projektowania, stanowią inspirację do badań nad wydajnymi metodami otrzymywania kryształów wieloskładnikowych. Reakcje mechanochemiczne pozwalają na otrzymywanie tych samych produktów co krystalizacja z roztworu, jak również produktów trudnych do uzyskania poprzez współkrystalizację. Dużą zaletą stosowania tej metody jest także ograniczenie ilości stosowanych rozpuszczalników, co jest bardzo istotne z punktu widzenia ochrony środowiska.

Rozprawa może być traktowana jako ilustracja aktualnych możliwości inżynierii krystalicznej w zakresie projektowania, przewidywania struktur oraz otrzymywania kryształów wieloskładnikowych.

Wykaz publikacji związanych z tematem rozprawy doktorskiej:

1. A. Czapik, M. Gdaniec – „Quinoxaline – 3-aminophenol – water (2/1/2)" (2008) *Acta Cryst*. **E64**, o895;
2. A. Czapik, M. Gdaniec – „Phenazine – naphthalene-1,5-diamine – water (1/1/2)" (2009) *Acta Cryst*. **E65**, o3177;
3. A. Czapik, H. Konowalska, M. Gdaniec - „p-Phenylenediamine and its dihydrate: two-dimensional isomorphism and mechanism of the dehydration process, and N-H···N and N-H···$\pi$ interactions" (2010) *Acta Cryst.* **C66**, o128;
4. A. Czapik, M. Gdaniec – „A new polymorph of benzene-1,2-diamine: isomorphism with 2-aminophenol and two-dimensional isostructurality of polymorphs" (2010) *Acta Cryst.* **C66**, o198;
5. A. Czapik, M. Gdaniec – „Cocrystals of 2,3,5,6-tetrafluoro-1,4-dihydroxybenzene with diazaaromatic compounds" (2010) *Acta Cryst.* **C66**, o356;
6. A. Czapik, M. Gdaniec – „5:1 and 2:1 cocrystals of 2,3,4,5,6-pentafluorophenol with phenazine" (2011) *Acta Cryst.* **C67**, o341.

Materials Science & Engineering A 609 (2014) 80–87

Contents lists available at ScienceDirect

Materials Science & Engineering A

journal homepage: www.elsevier.com/locate/msea

# Precipitation strengthening of ultrafine-grained Al–Mg–Si alloy processed by hydrostatic extrusion

W. Chrominski [a,*], M. Kulczyk [b], M. Lewandowska [a], K.J. Kurzydlowski [a]

[a] Warsaw University of Technology, Faculty of Materials Science and Engineering, Woloska 141, 02-507 Warsaw, Poland
[b] Institute of High Pressure Physics, Polish Academy of Sciences, Sokolowska 29/37, 01-142 Warsaw, Poland

ARTICLE INFO

*Article history:*
Received 18 January 2014
Received in revised form
24 April 2014
Accepted 25 April 2014
Available online 2 May 2014

*Keywords:*
Aluminium alloys
Age hardening
Ultrafine-grained
Transmission electron microscopy

ABSTRACT

Precipitation strengthening of an ultrafine-grained Al-Mg-Si alloy has been studied using samples obtained by hydrostatic extrusion. It has been demonstrated that the microstructure after hydrostatic extrusion consists of two types of grains: (1) nano-sized free of dislocations and surrounded with high angle grain boundaries and (2) micron-sized with dislocation substructure. After ageing at 160 °C, small needle-like precipitates appear in grain interiors of both nano- and micron-sized grains, bringing about a significant strength improvement. However, the precipitates are smaller than those in their coarse grained counterparts. As a consequence, they constitute weaker barriers for dislocations and induce a lower strengthening effect. In addition, one may observe intensive precipitation at nano-grains boundaries, which further reduces the strengthening effect. It was also shown that peak ageing and overageing take place for much shorter time than in the case of coarse grained samples and are caused by the grain growth rather than a change in the precipitation state.



## 1. Introduction

Aluminium and its alloys are widely used in industry because of the combination of good mechanical properties and low density. They also exhibit good corrosion resistance in many service environments and possess relatively good formability. The good formability refers especially to the 6xxx series aluminium alloys which are typically hot extruded followed by immediate water quenching and ageing [1,2]. However, the maximum yield strength of extruded products does not exceed a level of 350 MPa and wider use of these alloys shall be possible only if it is significantly increased. An enhancement of mechanical characteristics of these alloys can be achieved if their grain size is reduced below 1 μm to obtain ultrafine-grained (UFG) structures bringing about effective grain boundary strengthening quantitatively described by the Hall–Petch relationship [3,4].

UFG structures in aluminium alloys can be obtained by severe plastic deformation (SPD) in which an unconventionally high strain is applied, e.g. equal channel angular pressing (ECAP) [5], high pressure torsion (HPT) [6,7], accumulative roll bonding (ARB) [8]. The grain size reduction in this case is related to rearrangement of defects (primarily dislocations) generated during deformation, which leads to grain subdivision into smaller parts. The mechanisms of grain size refinement and UFG structure formation were studied extensively for pure aluminium processed by ECAP using EBSD [9] and TEM [10]. The results revealed that the grain refinement proceeds through the formation of new low angle grain boundaries, whose misorientation angles increase with imposed strain reaching the values typical for high angle grain boundaries (HAGB). The fraction of HAGB tends to saturate at a level of 70%. Despite intense grain size refinement, some fractions of dynamically recrystallized coarse grains are frequently observed in severely deformed aluminium alloys [11,12].

6xxx series aluminium alloys are precipitation hardened. Therefore a question automatically arises whether it is possible to combine grain refinement with precipitation hardening, which seems to be a promising method to improve their mechanical properties. To achieve such a combination, the process of dynamic precipitation during ECAP deformation has been studied [13]. It was revealed that spherical $\beta''$ particles form dynamically during ECAP at room and elevated temperature, instead of the needle-like ones observed in coarse grained material [14]. It was also shown that the strengthening effect depends on the processing temperature [13]. In the case of 6061 aluminium alloy, the hardness of ECAP processed samples increases with processing temperature up to 150 °C. A higher processing temperature brings about a decrease in the final properties of the alloy.

* Corresponding author. Tel.: +48 22 234 8441; fax: +48 22 234 8415.
*E-mail addresses:* wichr@inmat.pw.edu.pl (W. Chrominski), mariusz@unipress.waw.pl (M. Kulczyk), malew@inmat.pw.edu.pl (M. Lewandowska), kjk@inmat.pw.edu.pl (K.J. Kurzydlowski).

http://dx.doi.org/10.1016/j.msea.2014.04.092
0921-5093/

Another approach to combine precipitation and grain boundary strengthening is post SPD ageing. The results of the process revealed a significant strength increase during ageing of ECAP processed samples [15–20] with the highest reported yield strength of 484 MPa for 6xxx series aluminium alloys [21]. It was also shown that the heat treatment enhances the ductility, which is relatively low after ECAP processing [17–19]. In addition, the peak ageing condition for deformed material was reached in a shorter time in comparison to coarse grained material [17,19].

Microstructure investigations of UFG 6xxx aluminium alloys after ageing are relatively scarce [15,17] and their results are contradictory. For peak aged samples, the strengthening precipitates were recognized as $\beta''$ needles localized at grain boundaries and grain interiors [17] or accidentally situated spherical particles with larger size than for coarse grained samples [15]. A more detailed analysis of precipitation phenomena in age hardenable aluminium alloys was carried out for UFG 7075 alloy obtained by ball milling and consolidation by hot isostatic pressing and warm extrusion followed by solution annealing, water quenching and ageing in conditions typical for coarse grained material [22]. The extrusion of consolidated powders resulted in homogeneously distributed GP zones in fine grains without dislocations. Pronounced precipitation at grain boundaries has been noticed for UFG samples. However, such a detailed analysis of precipitation morphology and their location in UFG structure has not been conducted for 6xxx series aluminium alloys.

Therefore, the major purpose of the study was to investigate the possibility of two-mechanism strengthening of UFG alloys. The emphasis was put on the precipitates as the precipitation behaviour in 6xxx series UFG aluminium alloys has not, to date, been adequately reported in the literature and the published results have been incoherent. In the traditional heat treatment of 6xxx aluminium alloys, the peak strength of the aged material is achieved due to the presence of coherent needles commonly considered to be $\beta''$ phase with a diameter of a few nanometres and length of 50–100 nm [23,24]. In this context, a question arises whether or not such particles could precipitate in the grains having sizes below 500 nm.

In the present study, room temperature hydrostatic extrusion (HE) was used to obtain UFG structure in the 6082 aluminium alloy. Reports on HE induced grain refinement are given in [25,26]. In the process, a billet is placed in a chamber filled with a special liquid as shown in Fig. 1(a). A piston compresses the liquid generating high hydrostatic pressure (about 1 GPa) which causes extrusion through the die located at the bottom of the chamber. The main advantages of HE are the prevention of cracking and the possibility of producing relatively large (long) products compared to the other methods of SPD [27]. It should also be noted that the extruded material undergoes deformation with a high strain rate approaching 100 1/s. As a result, there is a considerable effect of adiabatic heating.

## 2. Experimental

The material used in this study was the commercially available 6082 aluminium alloy of the following mass% composition: Mg 0.6–1.2%, Si 0.7–1.3%, Mn 0.4–1.1%. The billets were solution annealed at 520 °C for 2 h and water quenched to obtain supersaturated solid solution. Subsequently, they were subjected to four stage HE with a total true strain of 4.6 to obtain UFG structure. (The initial diameter was 50 and the final 5 mm with intermediate diameters of 20, 10 and 7 mm). The HE processed samples were next aged at 160 °C, which is a standard for 6xxx series. The entire processing route is shown schematically in Fig. 1(b)

The mechanical properties were measured by microhardness and tensile tests which made it possible to determine such parameters as yield strength (YS), ultimate tensile strength (UTS), uniform elongation ($A_g$) and elongation to break ($A$). Three samples were tested for each ageing condition. The microstructure was studied using a JEOL JEM 1200EX transmission electron microscope with an accelerating voltage of 120 kV. Thin foils were cut perpendicularly to the extrusion direction using a wire saw, ground down to 150 μm and electropolished using Struers Tenupol-5 system operating at a voltage of 35 V. The grain size was characterized in terms of an equivalent diameter ($d_2$) (diameter of a circle with an area identical as that of the measured grain) and grain size diversity using the variation coefficient (CV) defined as the ratio of standard deviation to the mean value. The results obtained for HE processed samples were compared with the properties of coarse grained (CG) material subjected to conventional precipitation hardening.

## 3. Results

### 3.1. Mechanical properties

The microhardness as a function of ageing time for both CG and UFG samples is plotted in Fig. 2. For CG samples, the microhardness increases from 108HV0.2 for the solution annealed and water quenched sample to 140HV0.2 after ageing for 14 h. Longer ageing time causes microhardness decrease, the effect often referred to as overageing. In the case of UFG samples, the microhardness also increases from 134HV0.2 for HE processed to a maximum of 150HV0.2 for samples aged for 4 h. This means 70% reduction in

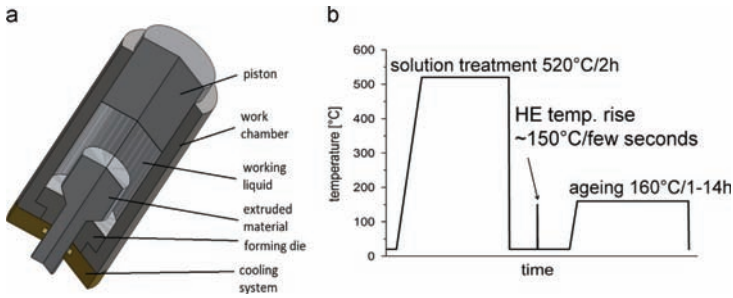


**Fig. 1.** The scheme of hydrostatic extrusion (HE) (a) and processing route of 6082 aluminium alloy used in this study (b).

the ageing time needed to achieve the highest hardness. On the other hand, the ageing effect as measured by microhardness increase is lower for UFG samples (16 versus 36HV0.2, which correspond to 10% and 27% increase, respectively).

The changes of YS and UTS as a function of ageing time for UFG samples, plotted in Fig. 3, follow the same tendency as microhardness. The strength reaches the maximum for ageing time of 4 h. It should be noted that the YS and UTS of aged UFG samples are much higher than those of the peak aged CG sample. In fact, YS as high as 486 MPa has been achieved, which is the highest value to have been reported so far for 6082 aluminium alloy. This is nearly 40% higher value than YS of CG alloy.

The results of mechanical testing thus revealed that the combination of grain boundary and precipitation strengthening is possible for HE processed samples and it is an effective way to improve mechanical properties of 6xxx aluminium alloys. However, the results obtained indicate that an improvement in mechanical strength comes at the expense of ductility. The uniform elongation and the elongation to break of UFG samples are significantly lower than those for the CG ones. Moreover, they decrease with ageing time and become particularly low for peak and overageing conditions. For short annealing time, the values of both $A$ and $A_g$ increase but ageing longer than 1 h brings about a sharp drop in uniform elongation to a level below as-HE condition. Also, a large difference between $A$ and $A_g$ measured in tensile tests means that there is a relatively high plastic deformation localized in neck after reaching UTS point. On the other hand, the tensile sample in peak aged condition shows almost negligible deformation strengthening region (difference between YS and UTS is 4 MPa) and uniform elongation is 0.3%. It means that necking occurs almost immediately after the beginning of plastic deformation.

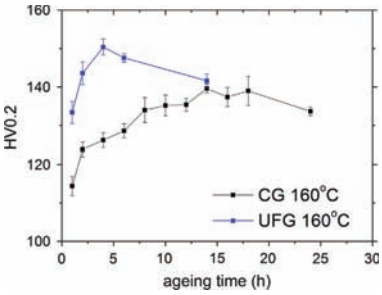


**Fig. 2.** Microhardness versus ageing time for CG and UFG samples.

### 3.2. Microstructure after HE process

The microstructure of 6082 aluminium alloy after HE process consists of two types of grains: (1) relatively large (about 1 μm in diameter) with the dislocation cells (Fig. 4(a)) and (2) small (about 120 nm in diameter) and free of dislocations (Fig. 4(b)). The diffraction pattern (DP) analysis revealed that large grains have orientation with [001] parallel to extrusion direction (further referred to as "⟨001⟩ grains"). The diffraction pattern consists of spots, which suggests that the misorientation angles between the dislocation cells are relatively low. These grains also feature the presence of second phase particles with spherical shape (Fig. 4(c)) homogeneously distributed inside them.

The DP taken from the area containing small grains (see insert in Fig. 4(b)) indicates that they have [111] direction parallel to extrusion direction (further referred to as "⟨111⟩ grains"). In the diffraction pattern, a ring formed by scattering on {220} planes is visible. Such a DP also suggests high misorientation angles of the grain boundaries. The ⟨111⟩ grains reveal a relatively large number

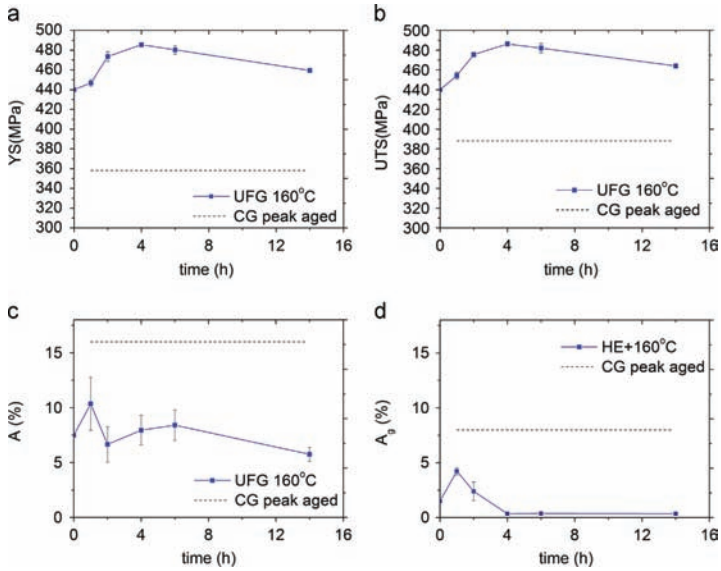


**Fig. 3.** Mechanical properties of UFG 6082 aluminium alloy for various ageing time at 160 °C: (a) yield strength (YS), (b) ultimate tensile strength (UTS), (c) elongation to break (A) and (d) uniform elongation ($A_g$). Dashed line indicates the values for CG peak aged sample.

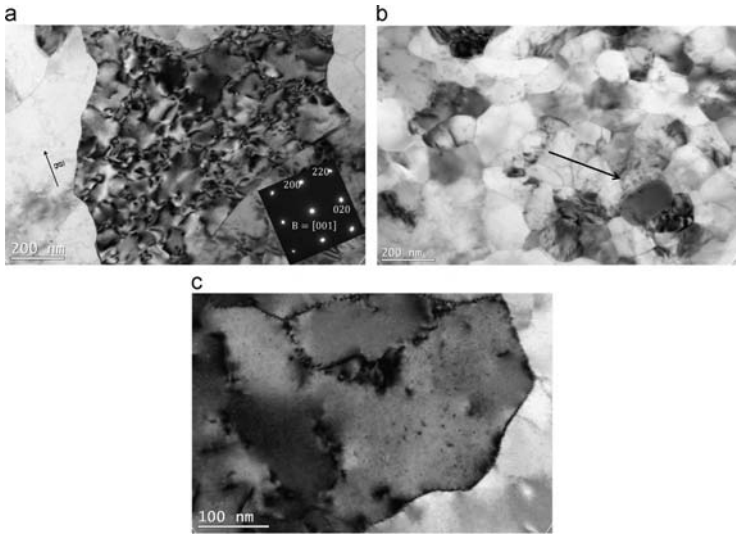


**Fig. 4.** TEM images of UFG 6082 aluminium alloy processed by HE, (a) as-HE, foil normal close to [001], (b) as-HE, foil normal close to [111] and (c) high magnification of [001] oriented grain.

of particles located at the boundaries. In Fig. 4(b), one can also see a large particle (indicated by an arrow at the bottom of the image in Fig. 4(b)) which is an intermetallic inclusion that has not been dissolved during solution annealing. Particles of such a type have been reported before in UFG 6xxx series aluminium alloys [17,28].

### 3.3. Microstructure after ageing

Fig. 5 represents a set of images taken from UFG samples aged in different conditions. The left column is representative for ⟨001⟩ grains and the right for ⟨111⟩ ones. Fig. 5(a) shows spherical particles inside a [001] grain after 1 h ageing. In Fig. 5(b), one can observe particles with a diameter of about 5–10 nm located at grain boundaries of the ⟨111⟩ grains. The number of these particles is much higher than in the sample before ageing. This suggests that they precipitate during 1 h ageing.

Ageing for 4 h brings about changes in the morphology of precipitates. In ⟨001⟩ grains, needles are visible aligned along ⟨100⟩ directions and homogeneously distributed in the grain interior (Fig. 5(c)). It should be noted that the particles feature strong strain contrast which suggests their coherence with the matrix. For ⟨111⟩ grains, a number of relatively large particles (20 nm in diameter) at grain boundaries are present as well as some small needle-like particles in the grain interiors presented in Fig. 5(g).

Annealing for 1 and 4 h does not change grain size and dislocation arrangements. In the ⟨001⟩ grains, one can see dislocation cells with small misorientation angles. The ⟨111⟩ grains retain their size and remain free of dislocations. The observations carried out for the sample subjected to 14 h ageing (Fig. 5(e) and (f)) show that at 160 °C precipitates become stable (their size and morphology do not change when compared to shorter ageing times). However, a significant growth in ⟨111⟩ grains has been noticed, which explains some decrease in the flow stress for the sample aged for 14 h. The microstructural parameters and mechanical properties of samples investigated in the present work are summarized in Table 1.

## 4. Discussion

### 4.1. Precipitates in as-HE sample

The results obtained in the present study have shown that precipitates are observed already in the as-HE sample. The HE process proceeds at a very high strain rate and may cause adiabatic heating phenomena. The temperature rise for aluminium alloys can be estimated from the following formula:

$$Q_V = c\rho\Delta T$$

where $Q_V$ is the heat per volume unit (equal to extrusion pressure), $c$ the specific heat (900 J/kg K for aluminium), $\rho$ the density (2700 kg/m$^3$ for aluminium) and $\Delta T$ the temperature rise.

With the extrusion pressure of 0.3–0.4 GPa in the current study, the temperature rise can be estimated at 150 °C and may last for a few seconds since the extruded billets were water cooled at the die exit. In the static ageing conditions, such temperature impulse is too short for precipitation to occur on a measurable scale. However, in as-HE samples one may expect strain induced phenomena, commonly observed in micro-alloyed steels [29,30] taking place in static conditions between deformation operations at elevated temperature. It should be noted that for 6xxx aluminium alloys, the room temperature is already elevated as it is $0.4T_m$.

In the as-extruded samples, three types of particles have been found:

1. Micron-sized (size of about 1 μm) randomly distributed in the entire volume, which as shown in [17,31] are $Mg_2Si$ phase. Those particles remain stable up to 570 °C and as solution

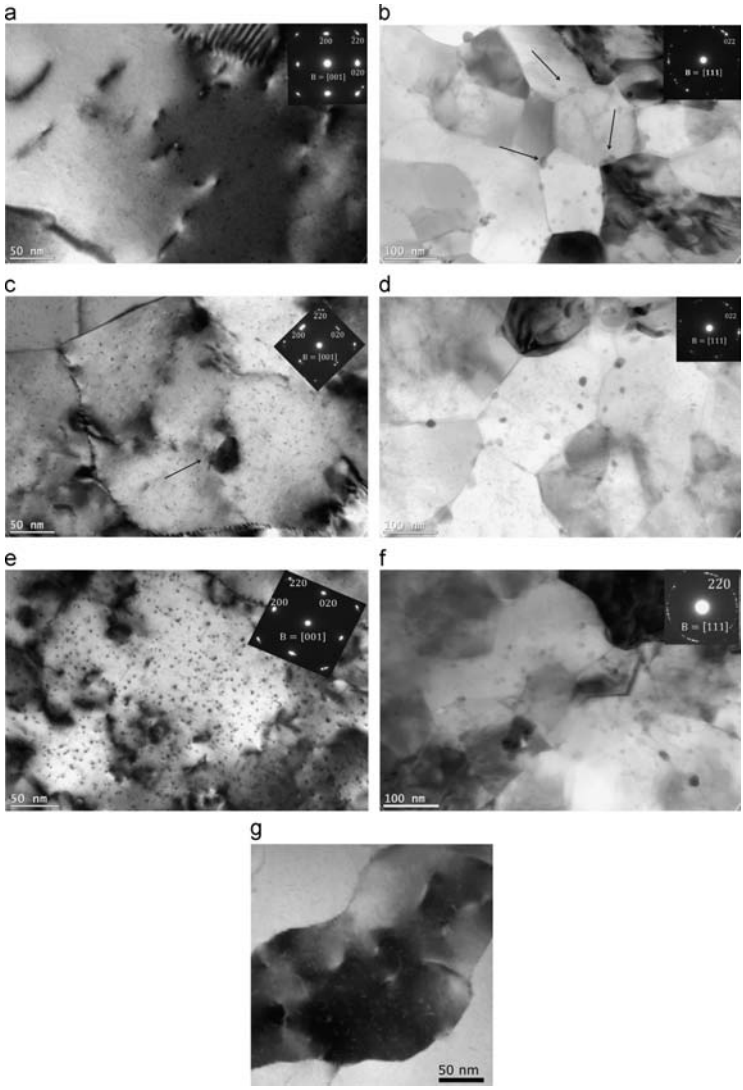


**Fig. 5.** TEM images of UFG 6082 aluminium alloy processed by HE followed by ageing, (a) underaged – 160 °C for 1 h, foil normal close to [001], (b) underaged – 160 °C for 1 h, foil normal close to [111], (c) peak aged – 160 °C for 4 h, foil normal close to [001], (d) peak aged – 160 °C for 4 h, foil normal close to [111], (e) overaged – 160 °C for 14 h, foil normal close to [001], (f) overaged – 160 °C for 14 h, foil normal close to [111] and (g) precipitates in [111] grain – peak aged – 160 °C for 4 h.

annealing was at 520 °C, their presence can be easily explained. They are hard and they cannot be shared by dislocations so they act as stress concentrators.

2. Nano-sized (size of about 5–10 nm) particles located at high angle grain boundaries among ⟨111⟩ grains. Their presence at grain boundaries can be explained by the fast diffusion along high angle grain boundaries and adiabatic heat released during HE. It should be noted that there are no such particles in ⟨001⟩ grains.
3. Spherical (in the interiors of ⟨001⟩ grains) whose spatial distribution suggests that their nucleation is homogeneous. Energy for their nucleation and growth is supplied by adiabatic heating during extrusion and strain induced phenomena as discussed previously.

**Table 1**
Mechanical properties and microstructural parameters of UFG 6082 aluminium alloy, SS – supersaturated solution, YS – yield strength, UTS – ultimate tensile strength, $A_g$ – uniform elongation, $A$ – elongation to break, GB – grain boundaries.

| Condition | Ageing time [h] | YS [MPa] | UTS [MPa] | $A_g$ [%] | $A$ [%] | $d_2$ [nm] | CV ($d_2$) | Particles characteristics |
|---|---|---|---|---|---|---|---|---|
| SS + 160 °C ageing | 14 | 358 | 388 | 6 | 16 | ~70,000 | | • Needles (50–100 nm in length) along ⟨100⟩ |
| SS + HE | – | 436 | 440 | 1.5 | 7.5 | 129 | 0.32 | • Spherical (2–5 nm in diameter) in ⟨001⟩ grains<br>• Spherical (5–10 nm in diameter) located on GB of ⟨111⟩ grains |
| SS + HE + 160 °C ageing | 1 | 450 | 457 | 4.5 | 12.5 | 124 | 0.41 | • Spherical (2–5 nm in diameter) in ⟨001⟩ grains<br>• Spherical (5–10 nm in diameter) located on GB of ⟨111⟩ grains |
| | 4 | 486 | 488 | 0.3 | 8 | 183 | 0.27 | • Needles (10–15 nm in length) along ⟨100⟩ in ⟨001⟩ grains<br>• Spherical (up to 20 nm in diameter) located on GB and fine needles inside of ⟨111⟩ grains |
| | 14 | 459 | 464 | 0.3 | 9.2 | 262 | 0.36 | • Needles (10–15 nm in length) along ⟨100⟩ in ⟨001⟩ grains<br>• Spherical (up to 20 nm in diameter) located on GB and fine needles inside of ⟨111⟩ grains |

### 4.2. Precipitation processes in UFG and CG samples during ageing

In CG 6xxx aluminium alloys, the precipitation proceeds along the following steps: Al supersaturated solid solution → clusters of alloying elements → GP zones→$\beta''$→$\beta'$→$\beta$ ($Mg_2Si$) [23]. In all steps, the next phase nucleates at the one undergoing transformation. Discussing the precipitation processes, it should be noted that the microstructure before ageing differs significantly from that of the CG one because of the small grain size, high dislocation density and the fact that precipitates are already present before ageing. Some of these defects provide privileged sites for nucleation of new precipitates as well as fast diffusion path.

First, it should be emphasized that although precipitates are present in the as-HE sample, there are still enough elements dissolved in the solid solution to cause further precipitation during ageing and the strengthening effect. The results have shown that short-time ageing (1–4 h) at 160 °C brings about an increase in microhardness, YS and UTS, as illustrated in Figs. 2 and 3.

Second, the precipitation process is strongly influenced by the grain size and dislocation substructure. When the grains are small (about 120 nm in diameter), free of dislocations and surrounded with high angle grain boundaries, as it is in the case of ⟨111⟩ grains, the precipitates form preferentially at the boundaries, as presented in Fig. 5(b), (d) and (f). These are equilibrium $\beta$ phase, spherical in shape and relatively large (up to 20 nm in diameter). Their shape results from their incoherency and high value of interface energy. The spherical shape ensures the smallest surface to volume ratio, thus minimizing the internal energy of the system. Apart from these grain boundary precipitates, in ⟨111⟩ grains there are some needle-like precipitates in the grain interiors (Fig. 5(g)) but they are much smaller than in the case of ⟨001⟩ grains and their density is relatively low. They nucleate homogeneously in the matrix due to the presence of supersaturated atoms but the driving force for their growth is much smaller because most of the alloying elements are already captured in the precipitates at grain boundaries.

When grains are relatively large (~1 μm) with dislocation substructure, as it is for ⟨001⟩ grains, the precipitates nucleate homogeneously in the matrix. No precipitates at dislocation boundaries were detected. The precipitates in ⟨001⟩ grains change their morphology with ageing time. In the early stage of ageing (1 h), they are spherical but after longer time, they transform into needle-like precipitates lying along ⟨100⟩ directions. Their morphology is similar to $\beta''$ phase and they produce the strain contrast, which indicates that they are coherent with the matrix (see Fig. 5(c)). The length of the needles varies from 10 to 15 nm and does not change with increasing ageing time. It should be noted that no preferred precipitation at dislocations is observed although dislocations are known to attract solute atoms in aluminium alloys [22] due to the stress field around their core. However, in the ⟨001⟩ grains, dislocation cells are to be found rather than free dislocations. The dislocation cells belong to low energy dislocation structures, which limits the stress field of every single dislocation core to the dislocation wall [32]. Due to this, there is no stress field near dislocation walls which could drive the segregation of alloying elements.

In order to provide a better insight into precipitation processes in UFG material, an attempt has been made to compare the precipitate state in HE processed and CG sample subjected to ageing in the same conditions. The results of microstructure observations are illustrated in Fig. 6. Comparing needle-like precipitates inside the grains, one could notice that in the CG sample, they are larger for the same ageing time. In addition, longer ageing time leads to a significant growth of the needles (see Fig. 6(b) and (d)), which is not the case for the HE processed samples (see Fig. 6(a) and (c)). The major microstructure change in the latter samples for longer ageing time is the grain growth, as described quantitatively in Table 1. The precipitates at grain boundaries, which are a typical feature of small ⟨111⟩ grains, do not form in CG material, as visible in Fig. 6(e) and (f). Instead, relatively wide precipitation free zones are observed, which depicts the size effect of precipitation at grain boundaries.

As for the precipitation sequence in UFG material, first, GP zones are observed which, after longer ageing time, transform into needle-like $\beta''$ precipitates. It indicates that the precipitation sequence is the same as in the CG counterparts. However, as already mentioned, the precipitates inside the grains are much smaller in HE processed samples as presented in Fig. 6. After 14 h ageing the needle precipitates are only 15 nm in length whereas in the CG sample their length can reach 100 nm.

The difference in the size of needle-like precipitates in UFG and CG samples can be explained in terms of the kinetics of their nucleation and growth. It is commonly accepted that in CG alloys homogeneous nucleation and growth of precipitates at relatively low temperatures of ageing are possible, thanks to a high concentration of vacancies frozen during water quenching. It was also revealed that SPD processing may lead to a significant increase in the vacancies concentration [22,33]. However, the measurements

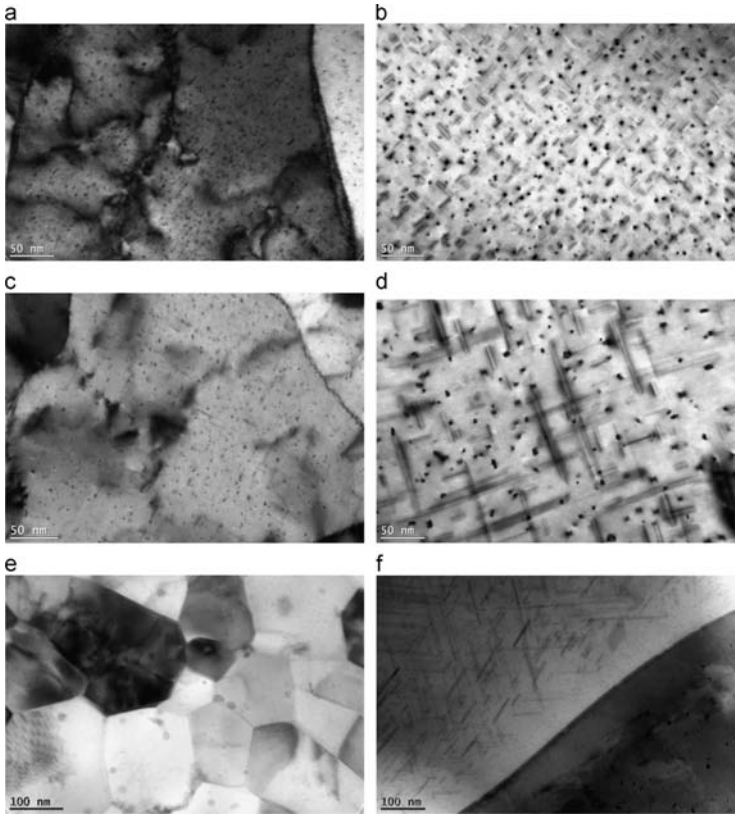


**Fig. 6.** The comparison of precipitates in UFG and CG material (a) UFG material aged at 160 °C for 4 h(peak ageing condition), (b) CG material aged at 160 °C for 4 h, (c) UFG material aged at 160 °C for 14 h, (d) CG material aged at 160 °C for 14 h (peak ageing condition), (e) UFG material aged at 160 °C for 4 h(peak ageing condition) and (f) precipitation free zone in peak aged CG material (a)–(d) images foil normal is close to [001].

were performed for an annealed material, in which initial concentration of vacancies was low. In our case, HE processing of solution annealed and water quenched samples leads to a considerable decrease in the vacancies concentration due to adiabatic heating during deformation. As a result, volume diffusion is slower and the size of precipitates is smaller too.

### 4.3. Effect on mechanical properties

The data summarized in Table 1 clearly indicate that ageing of UFG samples brings about significant improvement in strength, which is an effect of precipitation processes taking place in grain interiors. For ageing times up to peak strength, the grain structure does not change while precipitation process occurs inside the grains and at grain boundaries depending on grain size, orientation and grain boundary character. When compared to other processing methods, see Table 2, the combination of HE and ageing leads to a significantly higher strength. However, the high strength comes at the expense of ductility, which becomes negligible and does not increase even for longer ageing time.

**Table 2**
Comparison of mechanical properties of 6082 Al alloy obtained via various SPD techniques and heat treatment combinations, pa – peak aged.

| condition | YS [MPa] | UTS [MPa] | *A* [%] | reference |
|---|---|---|---|---|
| ECAP + pa | 345 | 363 | 11 | [19] |
| pa + ECAP | – | 397 | – | |
| ECAP + pa | 437 | 447 | 17 | [34] |
| T6 | 326 | 349 | 14 | This paper |
| SS + HE | 436 | 440 | 7.5 | |
| SS + HE + pa | 486 | 488 | 8 | |

The microstructural analysis for this annealing condition revealed an intensive precipitation process at grain boundaries which may have a detrimental effect on ductility.

Comparing microhardness and yield strength changes versus ageing time, one can notice that the maximum is reached after shorter time in the UFG samples (4 h when compared to 14 h for the CG one). In the literature, this phenomenon is explained by the excessive energy stored in the UFG material which accelerates

precipitation processes [16–18,35]. However, the results obtained in the present study indicate that the size of precipitates formed in the UFG structure is significantly smaller than in the CG sample and does not change for ageing times from 4 to 14 h. On the other hand, in the UFG sample precipitation processes are accompanied by the grain growth (see Table 1). It indicates that the observed decrease in YS results primarily from the changes in the grain size as the precipitation state is almost the same.

The other characteristic feature of the UFG sample is that ageing strengthening effect is significantly smaller compared to the CG ones. There are at least two reasons for that. First, as mentioned before, the needle-like $\beta''$ precipitates which are responsible for a maximum strengthening effect are much smaller in the UFG sample (see Fig. 6). As a consequence, their contribution to strengthening is smaller since it depends on the size of precipitates which was also reported in the CG material [36]. Second, a significant fraction of the precipitates is located at grain boundaries and as such they do not contribute to strengthening effect since they do not act as barriers for moving dislocations. On the other hand, they may also significantly inhibit precipitation inside the grains because of the reduction of solute content in the solid solution. Thus, the overall precipitation strengthening effect in the UFG sample is smaller. A similar observation on the complexity of precipitation phenomena in ultrafine-grained aluminium on mechanical properties was presented in Ref. [37].

## 5. Conclusions

1. A significant strength improvement of 6082 aluminium alloy was achieved by means of grain size refinement using HE processing followed by ageing with the highest reported strength for this alloy (486 MPa). However, the effect of precipitation strengthening is smaller than that for CG samples. This was attributed to the enhanced grain boundary precipitation (such precipitates do not act as obstacles for moving dislocations) and the smaller size of precipitates in the grain interiors (which are weaker barriers for moving dislocations).
2. The precipitation process in HE processed 6082 aluminium alloy is strongly influenced by the grain size, grain boundary character and dislocation substructure. For micron-size grains, the needle-like precipitates are homogeneously distributed in the grain interior. No privileged nucleation of precipitates at dislocations and dislocation boundaries was observed. Enhanced precipitation at grain boundaries occurs for nano-sized grains, which are separated by grain boundaries predominately of high angle type.
3. A decrease in hardness on ageing curve of HE processed samples occurs for shorter time than in the case of CG material. However, it is caused by grain growth rather than a change in the precipitation state.

## Acknowledgements

This work was carried out within a NANOMET Project financed under the European Funds for Regional Development (Contract no. POIG.01.03.01-00-015/08).

## References

[1] I.J. Polmear, Light Alloys. From Traditional Alloys to Nanocrystals, Elsevier, 2006.
[2] J. Dwight, Aluminium Design and Construction, Taylor & Francis e-Library, 2002.
[3] E.O. Hall, Proc. Phys. Soc. B 64 (1951) 747–753.
[4] N.J. Petch, J. Iron Steel Inst. 174 (1953) 25–28.
[5] R.Z. Valiev, T.G. Langdon, Prog. Mater. Sci. 51 (2006) 881–981.
[6] P.W. Bridgman, Phys. Rev. 48 (1935) 825.
[7] R.Z. Valiev, N.A. Krasilnikov, N.K. Tsenev, Mater. Sci. Eng. A 137 (1991) 35–40.
[8] Y. Saito, N. Tsuji, H. Utsunomiya, T. Sakai, R.G. Hong, Scr. Mater. 39 (1998) 1221–1227.
[9] P.B. Prangnell, J.R. Bowen, P.J. Apps, Mater. Sci. Eng. A 375–377 (2004) 178–185.
[10] M. Cabibbo, E. Evangelista, C. Scalabroni, Micron 36 (2004) 401–414.
[11] R.Z. Valiev, R.K. Islamagliev, I.V. Alexandrov, Prog. Mater. Sci. 45 (2000) 103–189.
[12] M.V. Markushev, C.C. Bampton, M.Y. Murashkin, D.A. Hardwick, Mater. Sci. Eng. A 234–236 (1997) 927.
[13] M. Vaseghi, A.K. Taheri, S.I. Hong, H.S. Kim, Mater. Des. 31 (2010) 4076–4082.
[14] C.D. Marioara, S.J. Andersen, H.W. Zandbergen, R. Holmestad, Metal. Mater. Trans. 36A (2005) 691–702.
[15] J.K. Kim, H.G. Jeong, S.I. Hong, Y.S. Kim, W.J. Kim, Scr. Mater. 45 (2001) 901–907.
[16] M. Vaseghi, H.S. Kim, Mater. Des. 36 (2012) 735–740.
[17] K. Hockauf, L.W. Meyer, M. Hockauf, T. Halle, J. Mater. Sci. 45 (2010) 4754–4760.
[18] M. Hockauf, L.W. Meyer, B. Zillman, M. Hietschold, S. Schulze, L. Krueger, Mater. Sci. Eng. A 503 (2009) 167–171.
[19] S. Dadbakhsh, A.K. Taheri, C.W. Smith, Mater. Sci. Eng. A 527 (2010) 4758–4766.
[20] J.K. Kim, H.K. Kim, J.W. Park., W.J. Kim, Scr. Mater. 53 (2005) 1207–1211.
[21] M. Cai, D.P. Field, G.W. Lorimer, Mater. Sci. Eng. A 373 (2004) 65–71.
[22] T. Hu, K. Ma, T.D. Topping, J.M. Schoenung, E.J. Lavernia, Acta Mater. 61 (2013) 2163–2178.
[23] G.A. Edwards, K. Stiller, G.L. Dunlop, M.J. Couper, Acta Mater. 46 (1998) 3893–3904.
[24] F. Delmas, M.J. Casanove, P. Lours, A. Couret, A. Couju, Mater. Sci. Eng. A 373 (2004) 80–89.
[25] M. Lewandowska, K.J. Kurzydlowski, J. Mater. Sci. 43 (2008) 7299–7306.
[26] M. Lewandowska, Solid State Phenom. 114 (2006) 109–116.
[27] L. Olejnik, M. Kulczyk, W. Pachla, A. Rosochowski, Int. J. Mater. Form. 2 (Suppl. 1) (2009) S621–S624.
[28] H.J. Roven, M. Liu, C.J. Werenskiold, Mater. Sci. Eng. A 483–484 (2008) 54–58.
[29] W.J. Liu, J.J. Jonas, Metall. Trans. 19A (1988) 1415–1424.
[30] Z. Wang, X. Sun, Z. Yang, Q. Yong, C. Zhang, Z. Li, Y. Weng, Mater. Sci. Eng. A 573 (2013) 84–91.
[31] M. Cabibbo, H.J. McQueen, E. Evangelista, S. Spigarelli, M. DiPaola, A. Falchero, Mater. Sci. Eng. A 460–461 (2007) 86–94.
[32] D. Kuhlmann-Wilsdorf, Mater. Sci. Eng. A 113 (1989) 1–41.
[33] W. Lechner, W. Puff, B. Mingler, M.J. Zehetbauer, R. Wurschum, Scr. Mater. 61 (2009) 383–386.
[34] H.J. Roven, H. Nesboe, J.C. Werenskiold, T. Seibert, Mater. Sci. Eng. A 410–411 (2005) 426–429.
[35] Z.H. Ismail, Scr. Mater. 32 (1995) 457–462.
[36] C.D. Marioara, S.J. Andersen, J. Jansen, H.W. Zandbergen, Acta Mater. 51 (2003) 789–796.
[37] K. Ma, H. Wen, T. Hu, T.D. Topping, D. Isheim, D.N. Seidman, E.J. Lavernia, J. M. Schoenung, Acta Mater. 62 (2014) 141–155.

ELSEVIER

Journal of Crystal Growth 171 (1997) 387–391

JOURNAL OF CRYSTAL GROWTH

# Czochralski growth of $SrLaAlO_4$ and $SrLaGaO_4$ single crystals and its implications for the crystal morphology

A. Pajaczkowska [a,*], A. Gloubokov [a], A. Klos [a], C.F. Woensdregt [b]

[a] *Institute of Electronic Materials Technology, P-01 919 Warsaw, Poland*

[b] *Faculty of Earth Sciences, Geodynamical Research Institute, P.O. Box 80021, 3508 TA Utrecht, The Netherlands*

Received 28 July 1996

**Abstract**

Single crystals of $SrLaAlO_4$ (SLA) and $SrLaGaO_4$ (SLG) have been grown from nonstoichiometric melts by the Czochralski method making use of different seed orientations, [100] (SLA, SLG), [110] (SLA) and [001] (SLG). The anisotropic properties of the crystal structure are reflected in the growth morphology of the crystals. In the case of (SLA) {101} facets appear at the crystal/melt interface and in that of [100] SLG {101} and {103} facets occur, while for [001] SLG {001} and {103} facets are present. SLA crystals are very similar to the theoretical growth forms computed according to the Hartman–Perdok theory for models with an effective charge on oxygen, $q_O = -2|e|$. However the habit of SLG crystals corresponds better to the theoretical growth forms based on an effective charge $q_O = -1.5|e|$ due to the presence of oxygen vacancies.

## 1. Introduction

$SrLaAlO_4$ (SLA) and $SrLaGaO_4$ (SLG) belong to the group of $ABCO_4$ type compounds, where A = Sr,Ca; B = La,Y and C = Ga,Al or a mixture thereof. They are interesting substrates for high $T_c$ superconductors [1,2]. SLA and SLG crystallize with a tetragonal structure of the $K_2NiF_4$ type (space group I4/mmm). Their lattice constants are $a = b = 0.3756$ nm and $c = 1.2636$ nm [3,4] and $a = b = 0.3843$ nm and $c = 1.268$ nm [5,6], respectively. The crystal is built up along the $c$ axis, as a sequence of alternating layers consisting of $AlO_6$ octahedra and of layers with $Sr^{2+}$ and $La^{3+}$ ions on nine-coordinated sites of $C_{4v}$ symmetry. There are two independent positions of oxygen atoms, one (O1) in the $a$–$b$ plane with fractional coordinates $(x,0,0)$ and the other one (O2) with $(0,0,z)$. Cleavage planes are parallel to {001}.

The first crystals of SLA and SLG were obtained by Brown et al. [7] and Nakamura et al. [5], respectively. The latter authors reported that SLG crystals melt incongruently as has been recently confirmed by Uecker et al. [8]. Crystals of SLA and SLG were grown by means of the Czochralski method from a nonstoichiometric melt [5,6,9]. Uecker et al. [8] grew SLG crystals from two melt compositions ($Sr_{1.01}La_{0.95}Ga_{1.04}O_4$ [6] and $Sr_{0.964}La_{0.972}Ga_{1.10}O_4$) at low and high temperature gradients. Finally, Berkowski and Gloubokov [10] reported that the appropriate melt compositions for Czochralski grown SLA and SLG single crystals are $SrLa_{1.03}Al_{0.97}O_4$

* Corresponding author.


*PII* S0022-0248(96)00699-9

and $Sr_{0.959}La_{1.010}Ga_{1.072}O_4$. The crystals are twin free. Second order transitions take place at about 500 K in both SLA and SLG [11,12].

Crystals are colored depending on the temperature gradient at the crystal–melt interface, the melt composition and the oxygen pressure [4,6,12,13]. The color of the crystals varies from colorless to yellow and green. There is a controversial discussion about the origin of the color. It is certainly related to the appearance of facets and may be caused by ordering of Sr/La and oxygen ions in the structure [3,9,14].

Good quality SLA crystals can be grown by the Czochralski method using convex {101} interfaces [4,9,15]. Nakamura et al. [5] have grown SLG crystals by pulling along the direction of ⟨100⟩ and with a flat crystal melt interface of {100}. The rotation rate was 40–43 rpm and the pulling rate 0.8–2.5 mm/h. Dabkowski et al. [6] described for the same pulling direction that {101} is favorable and {100} facets were never observed. The pulling rate was about 1.25 mm/h and the rotation rate 1.5–10 rpm. Uecker et al. [8] reported that [100] SLG crystals grew with {101} central facets which covered 20–90% of the whole interface as a function of the growth conditions. The central part was lighter than the outer side of the crystal. They suggested that the lighter part of the crystal is associated with incongruent melting and poor growth conditions.

Since the effect of constitutional supercooling might influence the growth of good quality crystals, the proper conditions of growth should be found by lowering the pulling rate in order to avoid distortions, by increasing the temperature gradient in the melt for a better mixing and by searching the most appropriate composition near the transformation point (eutectic or peritectic reaction). The aim of the present paper is to explain the Czochralski growth of SLA and SLG crystals by comparing the observed growth morphology with the theoretical morphology.

## 2. Crystal growth

Single crystals of SLA and SLG were grown by the Czochralski method. Chemicals of $SrCO_3$, $La_2O_3$ and $Al_2O_3$ were prepared according to the method described in Ref. [4]. $Ga_2O_3$ of 4N purity was annealed at 800°C, for 6 h. Melts were prepared according to the above reported compositions [10].

In our experiments the temperature gradient was about 100°C/cm above the surface of the melt by using a passive afterheater. The seed orientations used for SLA were ⟨100⟩ and ⟨110⟩ and for SLG ⟨100⟩ and ⟨001⟩. The rotation rate was changed from 5 to 45 rpm and the pulling rate from 0.7 to 3 mm/h. The growth atmosphere was nitrogen with an oxygen content of $4 \times 10^{-3}$ vol% and for some experiments with an oxygen content of 0.15 vol%.

Light yellow SLA and SLG crystals (diameter between 17 and 20 mm and length of 80 mm) were grown in iridium crucibles (diameter and height 50 mm) at conditions of low oxygen concentration. At higher oxygen concentration the SLG crystals are green.

## 3. Theoretical morphology of crystals

The Hartman–Perdok theory (HPT) describes the relationship between the internal crystal structure and the external crystal morphology [16,17]. This approach has been used in order to explain the appearance of various facets on the grown crystals.

Theoretical growth morphology uses the crystallographic data of $CaYAlO_4$ [3] as a model for all tetragonal $ABCO_4$ compounds. The computed attachment energies are a function of the effective charge on oxygen, $q_O$, when taking into account the covalency of the Al–O and Ca–O bonds. The effect of ordering of Ca/Y and oxygen ions on the boundaries of elementary growth layers is also discussed.

The geometry of crystals grown by the Czochralski method is given in Fig. 1. The crystal growth starts on the seed with the top conical part followed by the cylindrical part and the end conical part. The

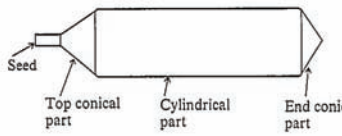


Fig. 1. Scheme of SLA and SLG crystals grown by the Czochralski method.

Table 1
Theoretical morphology of $ABCO_4$ crystals

| Growth direction | Oxygen charge, $e$ | Appearance of theoretical facets on different parts of crystals | |
|---|---|---|---|
| | | Conical top/end | Cylindrical |
| [100] | −2.0 | $\{101\}_o$, $\{110\}_o$, $\{101\}_d$ | $\{001\}$, $\{101\}_{o,d}$, $\{100\}$ |
| | −1.5 | $\{110\}_o$, $\{103\}$, $\{101\}_{o,d}$, $\{121\}$ | $\{001\}$, $\{103\}$, $\{101\}_{o,d}$ |
| [110] | −2.0 | $\{101\}_{o,d}$, $\{100\}$, $\{110\}$ | $\{001\}$, $\{110\}_{o,d}$ |
| | −1.5 | $\{103\}$, $\{101\}_{o,d}$, $\{110\}$, $\{121\}$ | $\{001\}$, $\{110\}_{o,d}$, $\{112\}$ |
| [001] | −2.0 | $\{101\}_{o,d}$, $\{110\}_o$, $\{002\}$ | $\{110\}_{o,d}$, $\{100\}$ |
| | −1.5 | $\{002\}$, $\{110\}$, $\{103\}$, $\{121\}$ | $\{110\}_{o,d}$ |

Note that the subscripts o and d indicate ordered and disordered slice boundary configurations [18], respectively.

morphologically most important crystal forms $\{hkl\}$ determined by means of the HPT are F faces since they are the slowest growing faces according to a layer mechanism. The F faces of $ABCO_4$ crystals grown parallel to different crystallographic orientation are given in Table 1 for top/end conical and cylindrical parts of crystals. The facets are arranged in order of their theoretical morphological importance.

It is assumed that for an ionic crystal the charge of the oxygen ion equals $-2.0e$ and for a covalent crystal it is higher than $-2.0|e|$. In our case we discuss oxygen charges $-2.0|e| \le q_O \le -1.5|e|$. It should be noted that at $q_O \ge -1.5|e|$ $\{101\}_d$ is replaced by $\{103\}$ (Table 1).

## 4. Observation on the growth morphology

### 4.1. SLA

SLA crystals grown with seed orientations $\langle 100\rangle$ and $\langle 110\rangle$ have a uniform color (light yellow) and do not show any cracking at all. The crystals were grown with a convex interface that has $\{101\}$ facets forming an angle of about 146° (Fig. 2b, 3a) [9,15]. During the initial stage of dipping the seed into the melt $(100)$ and $\{110\}$ appear at the end of the seed of the SLA crystals pulled along [100] and [110]. After that the shape of the interface changes and $\{101\}$ facets appear. It is known for the Czochralski method that the crystal–melt interface can change by a variation of the rotation rate and the temperature gradient. In the case of SLA crystals changing the rotation rate does not induce other type of facets. Only the crystal/melt interface is stepped with $\{101\}$ facets (Figs. 2a and 2b). The observed facets on SLA and SLG crystals are given in Table 2 in order of their surface area and their relation to the seed orientation.

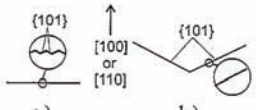


Fig. 2. SLA crystal–melt interface: (a) pseudo-flat; (b) conical smooth.

Table 2
Observed facets on SLA and SLG as-grown crystals

| Crystal | Growth direction | Appearance of facets on different parts of the crystal | | |
|---|---|---|---|---|
| | | Conical top | Cylindrical | Conical end |
| SLA | [100] | $\{101\}$, $\{110\}$ | $\{001\}$, $\{101\}$, $\{100\}$ | $\{101\}$ |
| SLA | [110] | $\{101\}$, $\{100\}$, $\{010\}$ | $\{001\}$, $\{110\}$ | $\{101\}$ |
| SLG | [100] | $\{101\}$, $\{103\}$, $\{110\}$ | $\{001\}$, $\{101\}$, $\{103\}$ | $\{103\}$, $\{101\}$ |
| SLG | [001] | $\{101\}$ | $\{110\}$, $\{010\}$ | $\{103\}$,$(001)$, $\{101\}$ weak |

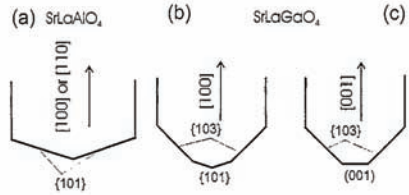


Fig. 3. Conical crystal/melt interface: (a) SLA crystal, (b) and (c) SLG crystal seed orientations [100] and [001], respectively.

### 4.2. SLG

SLG crystals were grown with seed orientations ⟨100⟩ and ⟨001⟩. The [100] SLG crystals grow with {101} facets in the central part and with the {103} facets in the outer part of the crystal (Fig. 3b). The {103} facets appear at the beginning of seeding. It should be noted that {110} facets were not observed. The [001] SLG crystals grown with a rotation rate of about 18 rpm, show at the end conical part {103} and {001} facets (Fig. 3c). When the rotation rate is increased to 45 rpm, (001) facets were occupying more than 50% of the whole interface while {103} facets are only present in the outer part of the interface (Fig. 3c). The (001) and {101} facets in the central part and {103} in the outer part of crystals form the core of the SLG crystals. The core observed in the [001] SLG crystals shows weak striations (change of colors from yellow to colorless). Although {001} is the cleavage plane and generally should be avoided for that reason, it can be used in the case of SLG. However weak striations are observed on (001).

## 5. Discussion

Comparing the experimental results with the theoretical morphology calculation (Table 1 and Table 2), one may conclude that the experimental forms of SLA crystals are very similar to the theoretical growth form of $ABCO_4$ crystals at $q_0 = -2.0|e|$. The (101) facets dominate at the conical parts of the SLA crystal. This is associated with the fact that differences in attachment energy, and, consequently, in growth rates, between (101) and the other faces are relatively large in the case of an effective oxygen charge of about $-2.0|e|$.

The morphology of SLG crystals differs from the morphology of SLA crystals. In the case of the ⟨100⟩ growth direction {101} and {103} facets appear at the interface and for the ⟨001⟩ growth direction (001) and {103} facets. Differences in the morphology of SLG and that of SLA can be explained from the point of view that the SLG structure has many more point defects than the SLA structure. These defects which are induced by the presence of oxygen vacancies compensated by a change of the gallium valence $(3+ \rightarrow 1+)$ may lower the total effective charge on oxygen in the SLG structure. It is shown that the order of morphological importance of the faces is changed with the degree of ionic bonding [18]. In the case of SLG, the experimentally observed morphology agrees with the calculations for an oxygen charge of $q_O = -1.5|e|$.

The influence of the pulling rate on the morphology was investigated for crystals grown in the [100] direction. A change of the pulling rates in the range 1–2.5 mm/h does not influence the morphology of the facets on the conical parts but does change that on the cylindrical parts of the crystals. The influence of the pulling rate on the appearance of different faces on the cylindrical parts of the crystals is presented in Table 3.

During the crystal growth process with high pulling rates, the facets of a low growth rate do not have enough time to grow and are smooth and they appear on the crystal surface. It can be concluded that all facets with growth rates less than the pulling rate will appear on the surface of a crystal. To avoid faceting the pulling rates of the SLA and SLG crystals were about 1 mm/h.

Table 3
Relation between pulling rate and appearance of facets on the cylindrical part of [100] grown SLA and SLG crystals

| Pulling rate (mm/h) | Facets on SLG crystal | Facets on SLA crystal |
|---|---|---|
| 1.0 | small (001) | small (001), {101} |
| 1.5 | (001), {101}, small {103} | (001), {101} |
| 2.5 | (001),{101}, {103} | large (001), {101} |

Model calculations demonstrate that in the case of {110} the oxygen boundary ions might be ordered [18]. In the case of ordering $\{110\}_0$ facets should appear on the crystal–melt interface of SLG and SLA crystals (Table 1). However, {110} facets were never observed on the crystal–melt interface (Table 2). Sometimes {110} facets appear on the top conical part in [100] orientation grown crystals (Table 2). For that reason it might be concluded that ordered $\{110\}_0$ facets are energetically unfavorable. Therefore the conclusion is that the oxygen ions are disordered following the {110} planes. Another indication is that the optimal ESR effect which is related to the presence of point defects [4,12] is obtained along the [110] direction.

Color changes in crystals are mainly due to point defects. The oxygen defect structure may be influenced by the local Sr/La ordering as point defects could be associated with the presence or absence of bivalent or trivalent ions. Some of these defects are related to color centers [4,14]. The boundary of {103} is flat with oxygen (O1), Sr/La and Ga as boundary ions. Additionally in the case of SLG, the reduction of $Ga^{3+}$ to $Ga^{1+}$ was found at conditions of superheating [19]. Sometimes orange-brown colored {103} facets appear on the top conical part of the SLG crystal.

## 6. Conclusions

The Hartman–Perdok theory explains the form of the crystal–melt interface of SLA and SLG crystals grown from the melt by the Czochralski method. The experiments confirm that (001) is the most stable face of the tetragonal $ABCO_4$ structure. The appearance of {103} on SLG crystals can be explained by assuming that the Ga–O bonding is much weaker than the Al–O bonding especially at the conditions of superheating. This aspect has also be taken into account in the models with reduced effective oxygen charges. The conclusion is that {110} and {103} facets should be avoided at the beginning of the growth as they are not appropriate for crystal growth due to their association with coloring and point defects. The best quality crystals are grown on {101} faces.

## Acknowledgements

This work was supported by the Projekt KBN (Poland) No. 8T11B03810.

## References

[1] M. Berkowski, J. Fink-Finowicki, A. Pajaczkowska, K. Mazur and J. Sass, Proc. Eur. Conf. on HTSc Thin Films and Single Crystals, Sept. 30–Oct. 4, 1989, Ustron, Poland; in: Progress of High Temperature Superconductivity, Vol. 24, Eds. W. Gorzkowski, M. Gutowski, A. Reich and H. Szymczak (World Scientific, Singapure, 1990) pp. 710–714.
[2] R. Sobolewski, P. Gierlowski, W. Kula, S. Zarembinski, S.J. Lewandowski, M. Berkowski, A. Pajaczkowska, B.P. Gorshunov, D.B. Lyudmirski and O.I. Sirotinski, IEEE Trans. Magn. 27 (1991) 876.
[3] R.D. Shannon, R.A. Oswald, J.B. Parise, B.H.T. Chai, P. Byszewski and A. Pajaczkowska, J. Solid State Chem. 98 (1992) 90.
[4] A. Gloubokov, R. Jablonski, W. Ryba-Romanowski, J. Sass, A. Pajaczkowska, R. Uecker and P. Reiche, J. Crystal Growth 147 (1995) 123.
[5] K. Nakamura, R. Katuno and I. Aoyama, Phase Trans. 42 (1993) 99.
[6] A. Dabkowski, H.A. Dabkowska and J.E. Greedan, J. Crystal Growth 132 (1993) 205.
[7] R. Brown, V. Pendrick, D. Kalokitis and B.H.T. Chai, Appl. Phys. Lett. 57 (1990) 1351.
[8] R. Uecker, P. Reiche, U. Geissler, D.-C. Uecker and D. Schultze, J. Crystal Growth, to be published.
[9] A. Pajaczkowska and P. Byszewski, J. Crystal Growth 128 (1993) 694.
[10] M. Berkowski and A. Gloubokov, XXXVIth Polish Crystallographic Meeting, 27–28.06.1994, Wroclaw, Poland, Abstr. p. 77.
[11] P. Byszewski, J. Domagala, J. Fink-Finowicki and A. Pajaczkowska, Mater. Res. Bull. 27 (1992) 483.
[12] A. Pajaczkowska, J. Domagala, A. Gloubokov, R. Jablonski and A. Klos, Cryst. Res. Technol. 31 (1996) 873.
[13] R. Jablonski, A. Pajaczkowska and A. Gloubokov, Mol. Phys. Rep. 12 (1995) 103.
[14] W. Ryba-Romanowski, S. Golab, A. Gloubokov and A. Pajaczkowska, Opt. Mater. 4 (1995) 515.
[15] K. Mazur, J. Sass and A. Pajaczkowska, in: Proc. SPIE 1845 (1992) 103.
[16] P. Hartman, in: Crystal Growth: An Introduction, Part A. Structure and Morphology, Ed. P. Hartman (North-Holland, Amsterdam, 1973) pp. 367–402.
[17] C.F. Woensdregt, Faraday Discuss. 95 (1993) 97.
[18] C.F. Woensdregt, H.W.M. Janssen, A. Gloubokov and A. Pajaczkowska, to be published.
[19] A. Gloubokov, PhD Thesis, IEMT, Warsaw (1996).

# Acta Physica Polonica A

Special Anniversary Issue: Professor Jan Czochralski Year 2013 — Invited Paper

# Will Czochralski Growth of Sapphire Once Again Prevail?

F.J. BRUNI[a,*], C.-M. LIU[b] AND J. STONE-SUNDBERG[c]
[a]Consultant, P.O. Box 2413, Santa Rosa, California, 95405, USA
[b]Sino-American Silicon Products Inc., Innovation Technology Research Center, No. 8, Industry E. Rd. II
Hsinchu Science Park, Hsinchu 30075, Taiwan, R.O.C.
[c]Current address: Adjunct Research Faculty, Department of Physics, Portland State University
P.O. Box 751, Portland, OR 97207-0751, USA

In the past decade there has been an explosive growth in the consumption of sapphire driven by the demands of the next generation of energy efficient general lighting based on GaN LEDs. This application requires orienting these rhombohedral corundum crystals such that the substrate surface is the $c$-plane; a basal plane defined using hexagonal axes. Sapphire crystals form a strong facet on the $c$-plane, and growth in that direction generally results in crystals with high defect densities, particularly dislocations, and low angle grain boundaries. To overcome this drawback, the usual methodology is to grow the crystal in the $a$-direction and then core drill rods perpendicularly which are then sliced into $c$-plane substrates. For all crystal growth techniques commonly employed for sapphire, this approach suffers from poor material utilization. Although this has generally been viewed as an acceptable trade-off in the manufacturing process as long as $2''$ substrates were the dominant market, as substrate diameters have increased towards 150 mm and larger, this compromise is no longer seen as a viable alternative because of the low material utilization and the high energy consumption of the growth process. This has led to a renewed look at the Czochralski process for more efficient $c$-axis substrate production.

DOI: 10.12693/APhysPolA.124.213
PACS: 81.10.Fq, 81.10.Aj, 61.72.−y

## 1. Introduction

Sapphire ($\alpha$-$Al_2O_3$) has been in continuous production for nearly 125 years either in its pure form or doped with chromium (ruby). Every major crystal growth technique has been used at one time or another for sapphire crystal growth Verneuil, Czochralski, Kyropoulos, Bridgman, edge-defined film-fed growth (EFG), heat exchanger method (HEM) and even solution growth [1]. The applicability of sapphire to so many different crystal growth approaches stems from its unique combination of properties including having a congruent melting point, being relatively chemically inert, hard, tough and having a high thermal conductivity (for an oxide ceramic). This makes it compatible with a variety of crucibles (tungsten, molybdenum and iridium), insulation types (zirconia, graphite and refractory metal radiation shields), heating methods (induction, resistance heating with either refractory metals or graphite, and even gas torches as in the Verneuil method) and furnace ambients (vacuum, inert gas and oxidizing atmospheres).

Sapphire's unique combination of chemical, mechanical, electrical and optical properties make it suitable for a wide range of product applications, so many of these crystal growth methodologies remain commercially viable for niche markets as in the case of EFG for its ability to produce near net shape sapphire parts. The dominant sapphire market today is for substrates used in the manufacture of blue LEDs via the growth of a GaN layer on a sapphire substrate by vapor phase epitaxy. In addition to filling out the color spectrum for LEDs and thus making full-color, solid-state displays practical, GaN blue LEDs can be combined with a phosphor to produce white light. This makes them ideal for backlighting of flat screen displays but it also makes them exactly suited for the general lighting market. The substitution of high-brightness LEDs for incandescent and fluorescent light bulbs is expected to make a significant impact on worldwide energy consumption and its effect on the environment. It is a measure of the complexity of achieving the size, orientation and crystalline quality of sapphire LED substrates that there are no fewer than five different crystal growth processes currently in commercial use [2] and one additional in possible development [3].

Corundum, the crystalline form of alpha-aluminum oxide, has trigonal symmetry and belongs to the $R\text{-}3C$ space group. It is usually described with hexagonal axes when identifying specific axes and planes. The sapphire basal plane (0001) is a low energy surface and forms a facet during crystal growth. To grow a crystal in the $c$-direction, one must deal with facets on the growth interface and the crystalline defects that result. The standard way to overcome this issue for the production of $c$-plane sapphire substrates has been to grow the crystal in the $a$-direction $[11\bar{2}0]$ and "core" out rods perpendicular to the growth direction. This has been the method of choice for Czochralski, Kyropoulos and HEM-grown crystals.

As long as wafer diameters were small ($2''$ is still the dominant market in Taiwan, for example), the

*corresponding author; e-mail: fjbruni@aol.com

Czochralski process could compete with others, mainly Kyropoulos. However, as in the silicon industry, processes demanding larger wafer sizes are always being developed. The limitations of iridium crucibles make Czochralski-grown sapphire crystals with diameters much above 150 mm problematic. Thus, using the standard $a$-axis growth and perpendicular coring technology, they are limited to a maximum product wafer diameter of 100 mm, and, even then, the material utilization is rather poor. More recently, Sumitomo Metal Mining announced the development of the Czochralski growth of 300 mm diameter $a$-axis sapphire crystals for the production of 150 mm diameter wafers [4].


Fig. 1. A 90 kg Kyropoulos-grown sapphire crystal mapped for core drilling two 6″ rods and several 2″ rods.

The ability of the Kyropoulos process to grow significantly larger crystals has enabled this procedure to largely displace the Czochralski method at the present time. Figure 1 shows a 90 kg sapphire crystal grown in a Thermal Technology Kyropoulos furnace and "mapped" for two 6″† cores and several 2″ cores. Figure 2 shows a typical Kyropoulos crystal after coring, ready to be cleaned up and recycled into the growth process. This figure also graphically demonstrates the large volume of crystallized sapphire in the Kyropoulos process that goes unused representing a significant energy investment due

Fig. 2. A Kyropoulos-grown sapphire crystal after core drilling 2″ rods and ready to be recycled into the growth process along with several broken or rejected rods.

to the high melting point of sapphire as well as the slow growth rate.

Another issue related to the Kyropoulos and HEM growth processes is that the growth rate is difficult to measure. This in turn leads to relatively slow crystallization rates in order to stay below the critical rate that would nucleate defects, a factor which adds to the production cost both in terms of energy consumption and capital hardware.

The crystal grown on the Thermal Technology Kyropoulos system shown in Fig. 1 was controlled using load cells to calculate the growth rate and a feedback control algorithm. However, this can only be used during the first half of the growth process before the crystal interface touches the bottom of the crucible, after which the remainder of the crystal was grown using downward ramping of the power. In general though, Kyropoulos systems do not employ any growth rate measurement or feedback procedures. The Czochralski process on the other hand readily lends itself to precise growth rate control. These factors have led to renewed interest in its use for $c$-axis growth of sapphire.

## 2. Bridgman and variants

The first attempt to commercialize a melt growth process for sapphire along the $c$-axis was the recent combined heat extraction system (CHES) process by ARC Energy. This is a variation on the HEM process with a somewhat more sophisticated method of controlling the growth rate by vertical crucible translation as in the Bridgman method. Crystals as large as 250 mm diameter have been grown [5]. $c$-axis growth has been demon-

†In the electronics industry substrates smaller than 100 mm are in English units (inches) and those larger than 3″ are measured in metric units (millimeters). However, it is typical to refer to the metric sizes by their nearest English equivalent.

strated in a more traditional Bridgman furnace by Miyagawa et al. for crystals up to 76 mm in diameter [3]. Crystals grown by both of these methods show high dislocation densities and a tendency toward low-angle grain boundaries (LAGB) also known as "lineage".

### 3. Czochralski growth

One of the earliest attempts to grow *c*-axis (or what is sometimes called 0°) sapphire was by Belt and Puttbach [6]. They grew $\approx 25$ mm diameter crystals which had very high dislocation densities ($10^4$–$10^5/\mathrm{cm}^2$) and LAGB. Yip and Brandle [7] also observed that sapphire "grown in the 0° (i.e. [0001]) orientation frequently has an irregular, cascade-like subboundary network on the boule surface". They went on to say that, when examined using a low power microscope, the (0001) plane contained a massive network of subgrain boundaries. It is for this reason that growth of *c*-axis sapphire has been confined to applications such as missile domes where the requirement of the optical axis is more important than defects.

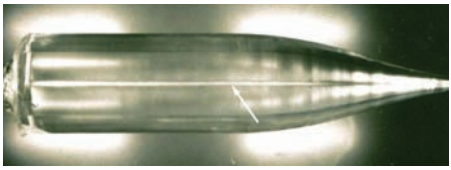

Fig. 3. A neodymium doped yttrium aluminum garnet crystal viewed with polarized light. The bright line down the center (arrow) is the stressed "core" region caused by {112} type facets on the growth interface. The angle of the arrow approximates the shape of the growth interface.

Sapphire differs from the garnets such as yttrium aluminum garnet (YAG) and gadolinium gallium garnet (GGG), to cite two examples. The garnets also form facets on the growth interface, and these facets result in a highly strained region in the crystal as shown in Fig. 3. The bright line down the central axis of the crystal is called the "core" and represents unusable material. However, the material grown away from the core region, which crystallizes on an atomically rough surface, has a low defect density and high optical quality. Sapphire, which also grows with a convex growth interface, does not have its defects concentrated in a core region. Rather, the entire crystal cross-section is impacted by defects when grown in the 0° orientation.

### 4. Low angle grain boundaries

The elimination of low angle grain boundaries in *c*-axis sapphire is the primary challenge. It has been found that, with the proper control of the temperature gradient and the hot zone design as well as with strict limits on the seed lift rate, sizable *c*-axis sapphire crystals

Fig. 4. One of the authors holding a 2″ diameter, 18″ long *c*-axis sapphire crystal grown free of LAGBs.

Fig. 5. A 4″ diameter *c*-axis sapphire crystal grown at Sino-American Silicon. The surface texture is an indication of lineage.

can be grown without low angle boundaries (LAGB). Yip and Brandle [7] also pointed out that careful attention to the seeding and necking steps in the Czochralski growth was critical to eliminating low angle grain boundaries. Figure 4 shows one of the authors with a 2″ diameter, *c*-axis sapphire crystal, 18″ long grown with no observable lineage. Figure 5 shows a 4″ diameter *c*-axis sapphire crystal, and Fig. 6 is a detailed view of the same crystal through crossed polarizers showing the clearly evident

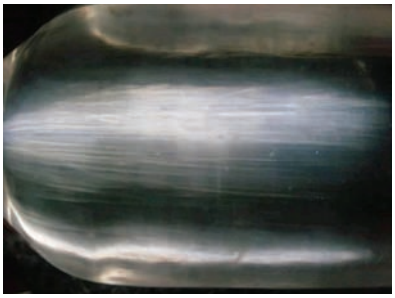

Fig. 6. View of a 4″ *c*-axis sapphire crystal with polarized light showing the lineage of LAGBs.

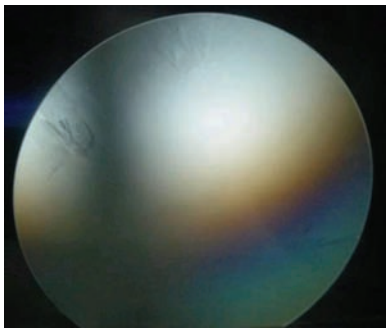

Fig. 7. View of a 4″ $c$-axis sapphire wafer with polarized light showing the lineage of LAGBs.

Fig. 8. A 4″ $c$-axis sapphire crystal grown successfully without LAGBs. Note the smoother exterior surface.

LAGBs. Figure 7 shows a wafer sliced from this crystal, again with the LAGBs evident. Figures 8 and 9 show another 4″ $c$-axis boule and wafer without LAGBs. These crystals were grown at Sino-American Silicon. Thus it has been demonstrated that the problem of low angle grain boundaries can be overcome in the Czochralski process with careful attention to the growth conditions.

## 5. Dislocations

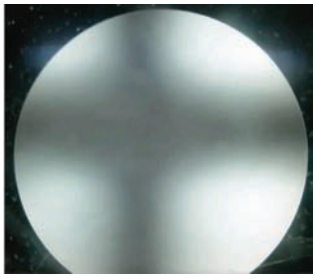

Fig. 9. A polished wafer cut from the crystal shown in Fig. 8 viewed in polarized light and exhibiting no LAGBs.

While there is no doubt that sapphire crystals grown along the $c$-axis have a much higher dislocation density than $a$-axis material regardless of the growth process employed, perhaps by at least an order of magnitude, there is reason to believe that this is not a severe impediment to their use as a substrate for GaN epilayers. Due to the significant ($\approx$ 16%) lattice parameter mismatch between sapphire and GaN [8, 9], even epilayers grown on a dislocation-free substrate will have as many as $10^9$ threading dislocations per square centimeter [10]. Several techniques have been developed to mitigate this issue. One is to grow a buffer layer of either AlN or GaN on the substrate that serves to block dislocation propagation into the active device layer [11, 12]. Another is to cut patterns into the sapphire surface so that islands of GaN are nucleated on sapphire "mesas" and then grow laterally to form a continuous layer of GaN [8]. The pattern can be comprised of various forms including grooves or dots.

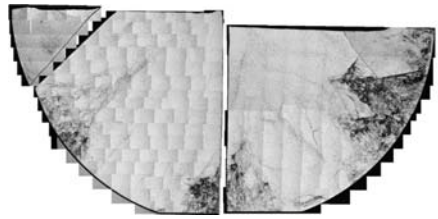

Fig. 10. A mosaic of photos of an etched $c$-axis grown wafer showing how dislocations (indicated by etch pits) are focused into regions along the $a$-axes.

During the Czochralski crystal growth, when a dislocation propagates from one layer of crystal to the next, it assumes the shape of lowest energy which would be the shortest length, assuming no variation of energy with crystallographic orientation. The shortest length would be a straight line perpendicular to the growth interface. However, if the dislocation energy varies with crystallographic orientation, dislocations propagate at an angle to the growth interface and will be "focused" into particular zones in the crystal. This can be seen in Fig. 10 which shows dislocations in a wafer from a $c$-axis grown crystal which are preferentially propagating towards the $a$-planes $\{11\bar{2}0\}$. Yet, even with the high dislocation densities seen here it is likely that they can be overcome with the processing techniques described above. However, buffer layers and patterned substrates are not a solution for LAGB.

## 6. Process economics

While the previous discussion has centered on the physical capabilities of the Czochralski process to produce crystals of adequate quality, the question of process economics must be addressed. This aspect of the problem focuses on several issues: crucible material, heating

methodology, growth speed and furnace design. Traditionally, Czochralski-grown sapphire has required iridium crucibles and induction heating. Iridium is a costly precious metal, and, while some iridium is lost to oxidation which can usually be recovered, the major concern for a large scale production process is the large amount of capital tied up in crucibles. There is another issue, however, that would limit the feasibility of the use of iridium crucibles for large sapphire crystals. Melt growth processes required a temperature gradient to define the position of the solid–liquid interface. As the geometry scales to larger dimensions, if the gradient is maintained at the same value, one ultimately encounters a situation where the temperature at the crucible wall exceeds the melting point of iridium (2446 °C) which is only 400 °C degrees higher than the melting point of sapphire. At that point, no further scaling of the process is possible. The issues of metal costs and melting point can be resolved through the use of molybdenum ($T_\mathrm{m} = 2623\,^\circ\mathrm{C}$) or tungsten ($T_\mathrm{m} = 3422\,^\circ\mathrm{C}$) crucibles. Although, unlike iridium, molybdenum and tungsten lose much of their value as scrap, a sufficient number of runs can be obtained from each crucible that the cost can easily be amortized to an acceptable value. Tungsten crucibles are routinely used in the Kyropoulos method, and molybdenum is the crucible material generally employed for HEM. Typically, a molybdenum crucible survives for only one crystal growth cycle in the HEM process.

Heating methodology must also be considered. Traditionally, iridium crucibles used to grow sapphire are heated inductively. However, resistance heating is generally more efficient, and graphite heating elements are a cheap and reliable way of providing heat to a high temperature furnace. The Kyropoulos process is generally heated using refractory metal (tungsten) heating elements in a vacuum chamber while the HEM process uses graphite heaters in an argon atmosphere. The crystals shown in Figs. 5 and 8 were grown in a Czochralski system using graphite heaters and molybdenum crucibles.

Perhaps the biggest advantage that the Czochralski process has relative to competing methodologies is the precision of growth rate control. The growth rate of the crystal can be exactly determined by the seed lift rate and the induced melt drop rate and can be controlled with great precision using several feedback measurements such as crystal weight. Neither the Kyropoulos nor HEM processes lend themselves readily to growth rate control which contributes to their long cycle times (typically $\approx 18$ days to produce a crystal of 90–100 kg). However, as mentioned above, the crystals shown in Figs. 1 and 2 were grown on a Kyropoulos system that uses load cells to control the growth rate for at least the first half of the crystallization process [2].

The use of graphite insulation versus oxide insulation contributes to a substantial reduction in the cost of energy in a Czochralski system. The authors estimate a cycle time of about 13 days for a 6″ diameter Czochralski sapphire crystal with a net "length at diameter" of 16 inches (equivalent to the 6″ core yield of the Kyropoulos crystal shown in Fig. 1). We also estimate that, at diameters of 6″ and larger, Czochralski growth overtakes the Kyropoulos growth in terms of energy required for crystallization, even when taking into consideration the energy cost of post growth annealing. Support for this argument was found with industry expert and analyst Eric Virey who commented that 0°, on-axis growth (Czochralski or otherwise) starts making economic sense at 6″ wafer diameters and above, depending upon growth speed and material yields (E. Virey, private communication, June 18, 2013).

## 7. Thermodynamics

Although the use of molybdenum crucibles, graphite resistance heaters and graphite insulation combine to make a Czochralski system that is more economical than a Kyropoulos system for the growth of large sapphire crystals, the thermodynamic issues cannot be ignored. Figure 11 is an Ellingham [13] diagram of the key components in such a system. This diagram uses data from Reed [14] and shows oxygen partial pressure scales, $H_2/H_2O$ and $CO/CO_2$ ratios after Richardson and Jeffes [15].

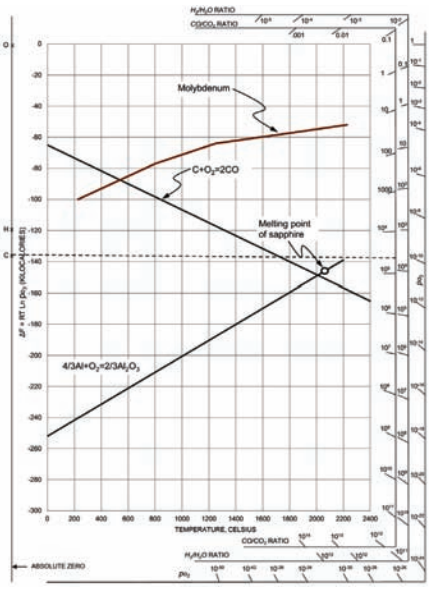


Fig. 11. An Ellingham diagram showing the equilibria with oxygen for the various components of a molybdenum–graphite–sapphire system.

The line labeled C–CO represents the free energy as a function of temperature for the lowest oxidation state

of carbon. Similarly, the line labeled 4/3 $Al_2O_3$ + $O_2$ = 2/3 $Al_2O_3$ shows the free energy change for the reaction that forms alumina (sapphire). In order to stabilize the sapphire phase while not simultaneously oxidizing the graphite components, one must be in an ambient that sets the oxygen partial pressure that is above the line for Al–$Al_2O_3$ and below the line for C–CO. Clearly, at the melting point of sapphire, it is impossible to be above the line for the alumina equilibrium while simultaneously being below the line for the carbon–CO equilibrium. So a compromise condition must be established. The dotted line represents the oxygen partial pressure resulting from a $CO/CO_2$ ratio of $\approx 5 \times 10^4$. Setting the $CO/CO_2$ ratio at this level will provide an ambient atmosphere that is oxidizing with respect to alumina and reducing with respect to carbon for all graphite components below $\approx 1700\,^{\circ}C$. Graphite components above that temperature would find themselves in a slightly oxidizing atmosphere and would be consumed over time. This compromise may be required in order to grow sapphire crystals of sufficient quality for LED substrates in a graphite-heated system. Growth in a tungsten-heated, vacuum system would not have this limitation.

## 8. Conclusions

The market for sapphire wafers is projected to be dominated by 6″ wafers (rising from 27% in 2014 to 70% in 2019) while 2″ wafers will disappear by 2020, and 8″ wafers will represent 20% of the market by then [16]. By that time, Kyropoulos- and HEM-grown crystals will face the same issues that have plagued Czochralski in the recent past. The utility of coring rods perpendicularly to the growth axis will be a limiting factor for volume production. An ever increasing level of scrap will add to the cost of the substrates. While, if the results shown here for 4″ boules can be scaled to 6″ and 8″ crystals, there is a strong logical argument that the Czochralski process can ultimately retake the role of the dominant production method for sapphire LED substrates. The Czochralski process is not without its own issues, not the least of which are overcoming the thermodynamic problems associated with melting large volumes of sapphire in graphite-heated systems or temperature limitations associated with iridium crucibles of large diameters.

## References


[1] D.C. Harris, in: *Proc. 10th DoD Electromagnetic Windows Symp., Norfolk, Virginia (USA)*, 2004.

[2] M.S. Akselrod, F.J. Bruni, *J. Cryst. Growth* **360**, 134 (2012).

[3] C. Miyagawa, T. Kobayashi, T. Taishi, K. Hoshikawa, *J. Cryst. Growth* **372**, 95 (2013).

[4] Commencement of Mass Production of Large Sapphire Substrates, `www.ledinside.com/news/2012/11/sumitomo_metal_mining_large_sapphire_substrates_20121116` (Accessed May 27, 2013).

[5] H.L. Tang, H.J. Li, J. Xu, in: *Advanced Topics for Crystal Growth*, Ed. S.O. Ferreira, 2013, p. 321.

[6] R.F. Belt, R.C. Puttbach, *Mater. Res. Bull.* **4**, 403 (1969).

[7] V.S.F. Yip, C.D. Brandle, *J. Am. Ceram. Soc.* **61**, 8 (1978).

[8] F. Degave, P. Ruterana, G. Nouet, J.H. Je, C.C. Kim, *J. Phys. Condens. Matter* **14**, 13019 (2002).

[9] L. Liu, J.H. Edgar, *Mater. Sci. Eng. R* **37**, 61 (2002).

[10] C.I.H. Asby, C.C. Mitchell, J. Han, N.A. Missert, P.P. Provencio, D.M. Follstaedt, G.M. Peake, L. Griego, *Appl. Phys. Lett.* **77**, 3233 (2000).

[11] M. Gonsalves, W. Kim, V. Narayanan, S. Mahajan, *J. Cryst. Growth* **240**, 347 (2002).

[12] M.J. Kappers, M.A. Moram, D.V. Sridhara Rao, C. McAleese, C.J. Humphreys, *J. Cryst. Growth* **312**, 363 (2010).

[13] H.J.T. Ellingham, *J. Soc. Chem. Ind.* **63**, 125 (1944).

[14] T.B. Reed, *The Free Energy of Formation of Binary Compounds*, MIT Press (1971). [Also available through the Biomass Energy Press, 2000.].

[15] F.D. Richardson, J.H.E. Jeffes, *J. Iron Steel Inst.* **160**, 261 (1948).

[16] Yole Sapphire Market Forcast, `www.i-micronews.com/upload/Rapports/Yole_Sapphire_Market_November_2011_Flyer.pdf` (Accessed May 28, 2013).

Special Anniversary Issue: Professor Jan Czochralski Year 2013 — Invited Paper

# Constitutional Supercooling in Czochralski Growth of Heavily Doped Silicon Crystals

J. FRIEDRICH[a,b,*], L. STOCKMEIER[a] AND G. MÜLLER[b]
[a]Fraunhofer THM, Am St.-Niclas-Schacht 13, 09599 Freiberg, Germany
[b]Fraunhofer Institut IISB, Schottkystr. 10, 91058 Erlangen, Germany

This study analyses the phenomenon of constitutional supercooling, which is one of the major problems in industrial growth of heavily doped ($> 10^{20}$ atoms/cm$^3$) silicon crystals by the Czochralski technique. The systematic study is based on theoretical models and experimental data considering the effect of three important dopants (B, P, and As) in dependence of the relevant growth parameters for the Czochralski process. Based on these results, conclusions will be drawn for the stability limits of the Czochralski growth of dislocation-free heavily doped silicon crystals in dependence of the doping species and their concentration.

DOI: 10.12693/APhysPolA.124.219
PACS: 81.10.Aj, 61.72.S–, 61.72.uf, 81.10.Fq

## 1. Introduction

An important application of silicon crystals is their use for power electronic devices. Certain vertically structured power electronic devices need silicon wafers with an electrical resistivity in the lower limit of 1 5 mΩ cm. This relatively low resistivity is required in order to minimize the switching losses and thus to increase the efficiency of the electronic devices [1]. According to Fig. 1 an electrical resistivity of less than 5 mΩ cm corresponds to a carrier concentration exceeding $1 \times 10^{19}$ cm$^{-3}$, i.e. a doping concentration higher than $1 \times 10^{19}$ atoms/cm$^3$. Such heavily doped silicon crystals can only be grown by the Czochralski (CZ) technique because these high doping levels cannot be achieved by the floating zone method. Heavy doping of silicon in CZ is commonly realized by adding boron, phosphorus, or arsenic to the silicon melt by special sophisticated techniques, e.g. [3 5] which are differing considerably from the doping techniques used for standard or shallow doping levels in CZ growth of silicon. The typical resistivity ranges which are feasible today are 0.5 20 mΩ cm for boron, 1 2 mΩ cm for phosphorus, and 2 10 mΩ cm for arsenic [6].

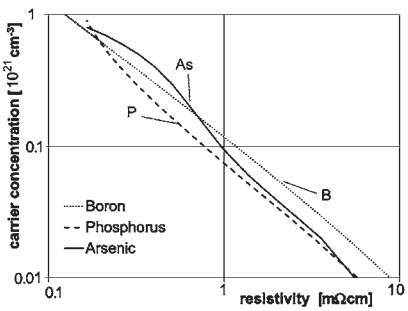


Fig. 1. Carrier concentration versus electrical resistivity in silicon doped with boron, phosphorus and arsenic. The curves were calculated according to the semi standard SEMI MF723-0307 [2].

It is well known in the literature that the probability of the occurrence of dislocations and grain boundaries (called "structure loss" by CZ growers) is strongly increased in CZ growth by high doping concentrations [6 15]. One major origin for the increased occurrence of structure loss is considered to be a morphological instability of the solid liquid interface [16]. This phenomenon which is illustrated by the example in Fig. 2 can be caused by the so-called constitutional supercooling. It originates from the strong enrichment of the dopant concentration in front of the solid liquid interface (due to segregation) and the resulting reduction of the liquidus temperature by several degrees (shown quantitatively below).

The goal of this paper is to present a systematic study of the phenomenon of constitutional supercooling, i.e. morphological instability of the interface in CZ growth of heavily doped silicon. The study will be based on theoretical models and experimental data considering various material properties of the different doping elements and pulling parameters. Based on the results, conclusions will be drawn for stability limits for the CZ growth of dislocation-free heavily doped silicon crystals in dependence of the doping species and their concentration.

## 2. Constitutional supercooling

### 2.1. Phenomenological description

The segregation coefficient $k$ is defined by the ratio of the concentration of the solute in the crystal $C_S$ to its concentration in the melt $C_L$ (see Fig. 3):

*corresponding author; e-mail: jochen.friedrich@iisb.fraunhofer.de

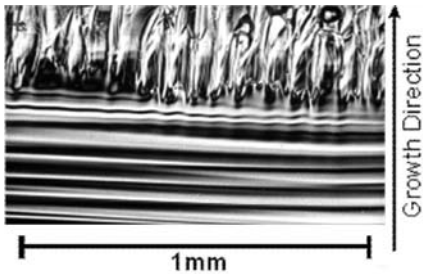


Fig. 2. Etched longitudinal section of a silicon crystal heavily doped with As ($1 \times 10^{19}$ at./cm$^{-3}$) grown in a laboratory setup by the floating zone method [17].

$$k = \frac{C_S}{C_L}. \tag{1}$$

For all relevant dopants of Si (e.g. B, P, and As) $k$ is smaller than unity ($k < 1$). This means that the dopant concentration $C_S$ which is incorporated into the crystal is smaller compared to the concentration $C_L$ in the melt. In this case the solute is rejected from the growing interface and an enrichment of the solute in the melt will take place during crystal growth as shown by the pile up of the solute concentration $C_L(x)$ in Fig. 4a. A so-called solute boundary layer is formed with a thickness $\delta$ according to the phase diagram (Fig. 3). This locally depending solute concentration $C_L(x)$ results in a locally depending liquidus temperature $T'_e(x)$ which is plotted in Fig. 4b versus the distance $x$ from the interface in the same scaling of $x$ as the plot $C_L(x)$ above (Fig. 4a). Additionally two possible temperature profiles $T'(x)$ and $T''(x)$ are shown in Fig. 4b which may be given by two different designs of the hot zone or the heating conditions in a certain CZ growth setup.

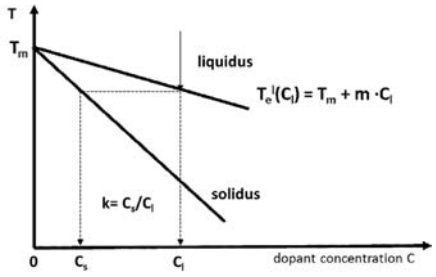


Fig. 3. Liquidus and solidus temperatures versus concentration of a dopant in the solid ($C_S$) and in the liquid ($C_L$). $T_m$ = melting point of pure silicon ($C_S = C_L = 0$). $m$ = slope of liquidus line $T'_e(C_L)$. $k = C_S/C_L$ is the definition of the segregation coefficient.

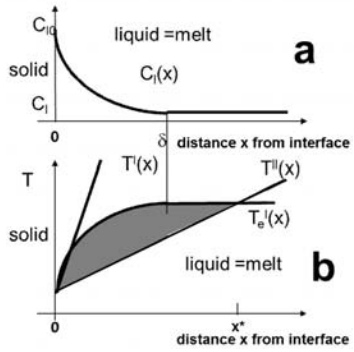


Fig. 4. (a) Concentration $C_L(x)$ of a dopant in the melt versus distance $x$ from the growth interface. $C_{L0}$ = concentration in the melt at the interface ($x = 0$). $\delta$ is the width of the boundary layer. (b) Liquidus temperature $T'_e(x)$ corresponding to the concentration profile $C_L(x)$ plotted in (a) versus distance $x$ from the growth interface, plotted in the same scaling as in (a). The temperature profiles $T'(x)$ and $T''(x)$ are two cases which are discussed in the text. The shaded area marks the region where the melt is "constitutionally supercooled" in front of the growth interface reaching up to position $x^*$ in the case of temperature profile $T''(x)$.

Constitutional supercooling occurs in the case of temperature profile $T''(x)$ because the actual melt temperature $T''(x)$ is smaller than the liquidus temperature $T'_e(x)$. The region where the melt is constitutionally supercooled is marked by the shaded area in Fig. 4b. It reaches from the interface until position $x^*$. This range extends a bit more than the extension of the boundary layer ($x^* > \delta$). In this situation the interface is *morphologically unstable* because any fluctuation forms a protuberance of the interface which grows into the supercooled melt region. This growth again increases the solute concentration in the melt by segregation and hence lowers the liquidus temperature $T'_e$. This effect amplifies again the growth of the protuberance. It can be theoretically shown that a number of such projections will be formed in a close packed array separated by distances which are determined by the local transport conditions [18]. The regions between the projections become progressively richer in solute and will finally be included in the crystal. This can be observed in the experiments by a breakdown of the regular interface (compare Fig. 2). It is typically accompanied by the formation of various crystal defects which cause for example the "structure loss" in CZ growth of silicon.

Constitutional supercooling can be avoided if hot zone and heating conditions are selected to result in a temperature profile like $T'(x)$ in Fig. 4b or any profile with $T(x) > T'(x)$, i.e. with a larger temperature gradient $G_L$.

These conditions will be discussed in the following sections in detail for the CZ growth of silicon heavily doped with B, P, and As.

### *2.2. Mathematical models for a constitutional stability limit*

The theoretical description of constitutional supercooling goes back to the pioneering works of Tiller et al. [19] for purely diffusive species transport in the melt and of Hurle [20] for convective mixing in the melt. According to their theory the ratio of the actual temperature gradient in the melt $G_L$ to the growth velocity $V$ must exceed a critical value which is a function of the segregation coefficient $k$, the slope $m$ of the liquidus temperature $T_e'(x)$, the solute concentration $C_L$ in the melt and the diffusion coefficient $D$ of the solute in the melt.

#### *2.2.1. Purely diffusive species transport in the melt—Tiller's formula*

For the case of purely diffusive species transport in the melt the stability criterion is defined in Eq. (2) according to Tiller et al. [19]:

$$\frac{G_L}{V} \geq \frac{(1-k)(-m)C_L}{kD}. \tag{2}$$

The temperature gradient $G_L$ in the melt in front of the interface can be related to the temperature gradient $G_S$ in the crystal at the interface by the conservation law of the heat fluxes at the interface

$$\lambda_S G_S = \lambda_L G_L + VL\rho. \tag{3}$$

$\lambda_S$, $\lambda_L$ are the thermal conductivities of solid (crystal) and liquid (melt), $L$ — the latent heat (heat of crystallization), $\rho$ — the density of the melt.

The slope $m = \Delta T_L/\Delta C_L$ in Fig. 2 can be estimated according to Thurmond and Kowalchik [21] for diluted alloys (like doping concentrations) by

$$m = \frac{T_\mathrm{m}^2 R}{L} = 8.26 \times 10^{-27} \left[\frac{\mathrm{Km}^3}{\mathrm{atoms}}\right]. \tag{4}$$

$T_\mathrm{m}$ is the melting point temperature of the pure material (here Si), $R$ — the gas constant and $L$ — the heat of crystallization. According to Hurle [20] this estimation of the slope $m$ by Eq. (2) has proven to be accurate enough for all dopants in the case of a rough, non-facetted interface, i.e. all crystal orientations except the $\langle 111\rangle$.

By introducing Eqs. (1) and (3) into Eq. (2) a stability criterion can be defined which relates the ratio of the axial temperature gradient in the solid $G_S$ and the growth rate $V$ to the doping level in the melt $C_L$. For simplicity it is assumed that V is equal to the pulling speed in Cz crystal growth, although the actual growth rate can be slightly higher than the pulling speed.

$$\frac{G_S}{V} = \frac{\lambda_L}{\lambda_S}\frac{(1-k)(-m)}{kD}C_L + \frac{L\rho}{\lambda_S}. \tag{5}$$

Results for the stability limit for CZ growth of silicon are shown in Fig. 5. In this figure the critical temperature gradient $G_S$ calculated from Eq. (5) for boron, phosphorus, and arsenic in the purely diffusive case is shown as dashed lines in dependence of the doping concentration $C_L$ in the melt for a pulling speed $V = 1$ mm/min.

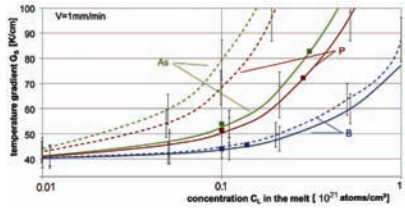


Fig. 5. Critical axial temperature gradient $G_S$ in the crystal versus solute concentration $C_L$ in the melt for a pulling speed $V = 1$ mm/min for B, P, and As. The dashed lines were calculated after Eq. (5) for the purely diffusive case. The solid lines were calculated after Eq. (9) for the case with melt convection assuming a rotation rate of the crystal of $\omega = 10$ rpm. The symbols highlight the critical temperature gradients for the case with melt convection and a solute concentration $C_L = 1\times10^{20}$ atoms/cm$^{-3}$ at the beginning of the body growth and the corresponding values at a solidified fraction $g$ of 80%. The error bars are due to the uncertainty of the material properties, especially for the diffusion coefficient $D$ used for the calculation of the temperature gradient $G_S$.

TABLE I

Material properties of silicon used to calculate the critical temperature gradient $G_S$ after Eq. (5) and Eq. (9).

| | |
|---|---|
| Kinematic viscosity $\nu$ | $3 \times 10^{-7}$ m$^2$/s |
| Thermal expansion $\beta$ | $1.4 \times 10^{-4}$ K$^{-1}$ |
| Melting point $T_\mathrm{m}$ | 1683 K |
| Thermal conductivity (solid) $\lambda_S$ | 18.9 W/(m K) |
| Thermal conductivity (liquid) $\lambda_L$ | 60.0 W/(m K) |
| Latent heat $L$ | $1.8 \times 10^6$ J/kg |
| Density $\rho$ | 2520 kg/m$^3$ |

The material properties of silicon and the physical properties of the dopants are compiled in Table I and Table II. For the calculations the D values given in the third raw were used which are within the published range. It is obvious that the smaller the segregation coefficient $k$ the higher must the temperature gradient $G_S$ in the crystal be to avoid constitutional supercooling. For a concentration $C_L = 1\times10^{20}$ atoms/cm$^{-3}$ in the melt and a pulling speed $V = 1$ mm/min the temperature gradient $G_S$ in the crystal must exceed 45 K/cm for boron ($k_\mathrm{B} = 0.8$; $D_\mathrm{B} = 2.4 \times 10^{-4}$ cm$^{-2}$/s), 69 K/cm for phosphorus

TABLE II

Segregation coefficient $k$ and diffusion coefficient $D$ of $B$, $P$, and As in silicon after [6, 22]. In the third raw the $D$ values used in the present calculations are given.

| Dopant | Boron | Phosphorus | Arsenic |
|---|---|---|---|
| $k$ | 0.8 | 0.35 | 0.3 |
| $D$ [m$^2$/s] | $1.2$–$2.4 \times 10^{-8}$ | $2.0$–$5.1 \times 10^{-8}$ | $1.9$–$3.3 \times 10^{-8}$ |
| $D_\mathrm{cal}$ [m$^2$/s] | $2.4 \times 10^{-8}$ | $3.0 \times 10^{-8}$ | $2.7 \times 10^{-8}$ |

($k_P = 0.35$; $D_P = 3.0 \times 10^{-4}$ cm$^{-2}/s$) and 79 K/cm for arsenic ($k_{As} = 0.3$; $D_{As} = 2.7 \times 10^{-4}$ cm$^{-2}/s$). Thereby, it must be taken into account that the values of the diffusion coefficients $D$ reported for the various doping elements in literature can vary strongly depending of the doping element [6, 22], for example in case of phosphorus between 2.0–5.1 $\times 10^{-4}$ cm$^{-2}$/sec (see Table II). This results in an error of the calculation of the critical temperature gradient $G_S$. For simplicity, an average error of +/-10% independent on the doping element was assumed to plot the error bars in Fig. 5.

*2.2.2. With convective species transport in the melt—Hurle's formula*

In Czochralski crystal growth the transport conditions in the melt are typically dominated by convective melt flow [23]. In order to take into account convective solute transport in the melt Hurle modified Eq. (3) by implementing an effective segregation coefficient $k_{eff}$, see Eq. (6):

$$\frac{G_L}{V} = \frac{(1-k)(-m)C_L}{kD} k_{eff}. \tag{6}$$

In a simple approximation the effective segregation coefficient $k_{eff}$ can be estimated according to Burton et al. [24]:

$$k_{eff} = \frac{k}{k + (1-k)\exp(-V\delta/D)}. \tag{7}$$

$\delta$ is a free parameter which can be estimated by a boundary layer thickness (compare Fig. 4a). The melt–crystal interface of a rotating Czochralski crystal can be approximated by a rotating disk in contact with a liquid. The boundary layer thickness $\delta$ of such a rotating disk is given according to Cochran [25] by

$$\delta = 1.6 D^{1/3} \nu^{1/6} \omega^{-1/2} \tag{8}$$

with kinematic viscosity of the melt $\nu$ and rotation rate of the disk (= crystal) $\omega$. Using Eqs. (1), (3), and (6)–(8) one can derive an expression similar to Eq. (5) for the ratio of the temperature gradient $G_S$ in the crystal versus the pulling speed $V$ in dependence on the doping level in the melt $C_L$ for the case including convective melt flow

$$\frac{G_S}{V} = \frac{\lambda_L}{\lambda_S} \frac{(1-k)(-m)}{kD} C_L k_{eff} + \frac{L\rho}{\lambda_S}. \tag{9}$$

Assuming a typical value of the crystal rotation $\omega$ = 10 rpm and a pulling speed $V = 1$ mm/min the critical temperature gradient in the crystal $G_S$ calculated according to Eq. (9) in dependence of the doping concentration in the melt $C_L$ is shown in Fig. 5 by the solid lines for B, P, and As. It is obvious that under consideration of a melt flow $G_S$ is reduced compared to the case without melt flow and must exceed for an initial doping concentration $C_L = 1 \times 10^{20}$ cm$^{-3}$ only 44 K/cm for boron (98% of pure diffusive case), 51 K/cm for phosphorus (75%) and 54 K/cm for arsenic (68%) as shown by the symbols in Fig. 5. This phenomenon is well known that the smaller the segregation coefficient $k$, the more sensitive the solute transport depends on convection.

## 3. Phenomena and parameters affecting constitutional supercooling during CZ growth of heavily doped silicon crystals

### *3.1. Enrichment of dopants in the melt due to segregation*

During pulling of the crystal the solute (dopant) will be rejected into the melt as all relevant dopants have $k < 1$. Therefore, an increase of the solute concentration in the melt will take place with increasing process time. Assuming that the system is conservative, i.e. no solute is lost or added during growth and assuming total mixing by convection, the solute concentration in the crystal respectively in the melt can typically be described by Scheil's equation [26] in dependence of the solidified fraction $g$:

$$C_L = C_0 (1-g)^{k-1}. \tag{10}$$

We assume that at the beginning of the growth of the cylindrical crystal body the solute concentration in the melt is $C_0 = 1 \times 10^{20}$ cm$^{-3}$. The growth of the whole cylindrical crystal body shall correspond to a solidified fraction $g$ of 80%. This means that the concentration of the solute $C_L$ in the melt would increase from $C_0 = 1 \times 10^{20}$ cm$^{-3}$ to $1.4 \times 10^{20}$ cm$^{-3}$ for boron, to $2.9 \times 10^{20}$ cm$^{-3}$ for phosphorus and to $3.1 \times 10^{20}$ cm$^{-3}$ for arsenic at a solidified fraction $g = 0.8$. As it is shown by the symbols in Fig. 5, this would theoretically require an increase of the critical temperature gradient $G_S$ in the crystal from 44 K/cm at the start of the cylindrical body to 45 K/cm at the end of the body for boron, from 51 K/cm to 72 K/cm for phosphorus and from 54 K/cm to 83 K/cm for arsenic. Alternatively, the pulling velocity $V$ has to be lowered from $V = 1$ mm/min down to 0.97 mm/min, 0.72 mm/min, and 0.67 mm/min for B, P, and As respectively, while keeping the critical temperature gradient $G_S$ in the crystal constant from the beginning ($g = 0$) to the end ($g = 0.8$) of the cylindrical body.

Thereby, it must be stated that for boron these theoretical changes of either the temperature gradient or the pulling speed due to the segregation effect are negligible within the limits of error. Furthermore, the theoretically determined changes for P and As do not correspond to the real situation of CZ growth, because both solutes (P and As) are evaporating quantitatively from the silicon melt during growth. The evaporation rate depends on the argon pressure inside the puller [27]. Therefore, the evaporation of the volatile P and As can compensate the above segregation effect. This phenomenon can be used to control the homogeneity of the doping distribution by properly adjusting the argon pressure, respectively, the argon flow along the free melt surface during CZ pulling [28]. This effect of evaporation can be taken into account in the Scheil equation (Eq. (10)) by an additional parameter $k_{ev}$ [27]:

$$C_L = C_0 (1-g)^{k+k_{ev}-1}. \tag{11}$$

Several models to estimate $k_{ev}$ can be found in literature

e.g. [11, 27, 29–31] and thus to calculate the criterion for constitutional supercooling taking into account segregation and evaporation.

### *3.2. Crystal orientation*

Usually the [100] and [111] orientation are used in CZ growth of heavily doped silicon crystals. In case of the [111]-orientation a central facet can form which exhibits a higher doping concentration than the non-facetted periphery which grows with an atomically rough interface [32]. The higher doping of the central region for the growth with the facetted {111} interface is explained by the higher effective segregation coefficient $k_{\mathrm{fac}}$ [33]. For P, $k_{\mathrm{fac}}$ is up to 0.43 ($k = 0.3$) and for As is 0.41 ($k = 0.35$) [33]. Unfortunately no value of $k_{\mathrm{fac}}$ for B was found in literature. By replacing $k$ by $k_{\mathrm{fac}}$ in Eq. (9) the critical temperature gradient $G_S$ can be estimated for a facetted interface. In case of phosphorus the critical temperature gradient $G_S$ becomes theoretically 49 K/cm for the facetted interface instead of 51 K/cm for the rough interface and in case of arsenic $G_S$ is 51 K/cm for the facetted interface instead of 54 K/cm for the non-facetted one. These changes are within the error limits of the model assumptions. Therefore, it can be concluded that the presence of a facetted interface in case of pulling a [111]-oriented crystal has a negligible influence on the stability limit for constitutional supercooling.

### *3.3. Pulling rate and variations thereof*

During a typical Czochralski growth run of silicon the pull rate $V$ differs significantly during the different process steps. This is illustrated by Fig. 6 where the pulling rate $V$ and the crystal diameter are displayed during a typical CZ growth run of a silicon crystal with a diameter of 100 mm of the cylindrical body [34]. At the beginning the pull rate $V$ is increased up to several mm/min during the necking procedure called after Dash [35]. Then, $V$ is reduced to enlarge the crystal diameter during growth of the starting cone. During shoulder growth, i.e. the transition from the starting cone to the cylindrical crystal body, $V$ is increased again to counteract an uncontrolled increase of the crystal diameter. In the present case the pull rate jumps from 0.5 mm/min during growth of the middle part of the shoulder to around 1.7 mm/min at the end of the shoulder. During growth of the cylindrical crystal body $V$ is on average around 1.2 mm/min and its variations are relatively small, nevertheless with $V$ as parameter for controlling and achieving a CZ crystal with a constant diameter. The crystal diameter is decreased at the end ("end cone") by a slight increase of the pull rate compared to the value during body growth, before the crystal is finally detached from the melt.

As the critical temperature gradient $G_S$ in the crystal is nearly proportional to the pull rate $V$ (according to Eq. (9)), $G_S$ must be expected to vary also significantly during the different process phases of a typical CZ growth run as shown in Fig. 6. This is illustrated by Fig. 7 where

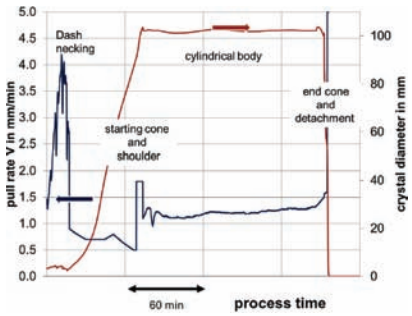


Fig. 6. Pull rate $V$ (left ordinate) and crystal diameter (right ordinate) as detected by the control system versus process time for CZ pulling of a silicon crystal with a diameter of 100 mm in the cylindrical part (body) [35].

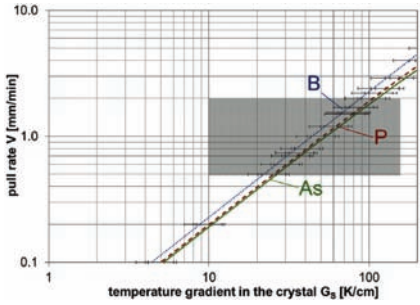


Fig. 7. Pull rate $V$ versus critical temperature gradient $G_S$ in the crystal computed after Eq. (9) for a rotation rate of the crystal $\omega = 10$ rpm and a solute concentration in the melt $C_L = 1 \times 10^{20}$ at./cm$^{-3}$ for B (dotted line), P (dashed line), and As (solid line). The grey area marks typical pulling rates which are used to grow silicon crystals with diameters of 100–200 mm (compare Fig. 6). The error bars are due to the uncertainty of the material properties, especially for the diffusion coefficient $D$ used for the calculation of the temperature gradient $G_S$.

the relationship between the pulling rate $V$ and the critical temperature gradient $G_S$ in the crystal is plotted for B, P, and As. The curves were computed by Eq. (9) for an initial doping concentration of $1 \times 10^{20}$ cm$^{-3}$ in the melt. If one assumes a pull speed $V$ of the cylindrical body of around 1 mm/min, then the required critical temperature gradient $G_S$ in the crystal is at least 100% higher during the Dash necking ($V_{\mathrm{neck}} > 2$ mm/min) than during growth of the crystal body. The growth of the starting cone and the transition from the starting cone to the cylindrical body seem to be also very critical with re-

spect to constitutional supercooling. The high values of the pull rate $V$ which are used during this process phase are corresponding to large values of the critical temperature gradient $G_S$, which should be at least 70% higher than for the growth of the body in the given case. Finally, it can be assumed that the pulling of the end cone is critical, too. The solute has enriched in the remaining shallow (poorly mixed) melt and the pulling speed is increased to decrease the crystal diameter. However, no quantitative data neither for the pulling speed nor for the actual temperature gradient in the crystal are available for the region of the end cone. Therefore, the growth of the end cone cannot be considered in the further discussion.

TABLE III

Available data in literature about pulling rates $V$ (column 2) and temperature gradients $G$ (column 3) used for certain CZ process phases: necking, starting cone and shoulder, and body growth of silicon crystals with diameters of 100–200 mm. The last three columns denoted by B, P, and As contain the critical temperature gradients $G_S$ calculated after Eq. (9) using the values of $V$ from column 2 for a solute concentration $C_L = 1 \times 10^{20}$ at./cm$^3$.

| 1 | 2 | 3 | B | P | As |
|---|---|---|---|---|---|
| Process phase | $V$ [mm/min] | $G$ [K/cm] | $G_S$ [K/cm] | | |
| necking | $> 2$ | 50–100 | 88 | 106 | 112 |
| shoulder | 0.5–1.5 | 25–80 | 22–60 | 25–78 | 26–82 |
| body | 0.8–1.2 | 20–60 | 35–53 | 40–62 | 43–65 |

## 4. Discussion

In this chapter an attempt is undertaken to discuss the limitations of CZ growth of heavily doped silicon crystals with respect to constitutional supercooling under "industry-like" conditions. The problem of such a consideration is the fact that temperature distribution in a CZ puller and therefore in the crystal is depending strongly on the actual hot-zone design and process parameters which are usually confidential in industrial production. However, there are some reports [36–42] and also references therein where the temperature distribution in the crystal for different puller geometries and process conditions have been analyzed. Furthermore, studies exist about modeling of the heat transfer in CZ pulling of silicon crystals. These published experimental and numerical results are used in the following in order to estimate the range of the typical temperature gradient in the crystal $G$ during the different process phases and for different crystal diameters. These ranges of temperature gradients will be compared to the critical temperature gradients $G_S$ which are needed to avoid constitutional supercooling.

Table III shows the results of such a quantitative comparison. Column 1 denotes the different CZ process phases according to Fig. 6. Column 2 contains the realistic pulling rates $V$ in the three different process phases which were used to calculate by Eq. (9) the corresponding critical temperature gradients $G_S$ which are needed to avoid constitutional supercooling for a B, P and As concentration in the melt $C_L = 1 \times 10^{20}$ cm$^{-3}$ (columns 4, 5 and 6 in Table III). The actual temperature gradients $G$ which are given in column 3 were estimated from published experimental and simulation data as follows.

The temperature gradient $G$ in the crystal during the seeding and necking phase is in the order of 50–100 K/cm according to direct measurements performed in a CZ puller for growing silicon crystals with 300 mm diameter [42] and according to experiments [36, 40] with smaller crystal diameters. For the growth of the cylindrical body $G$ is typically decreased with increasing crystal diameter regardless of the doping level and the actual hot-zone design. The reported values of $G$ are in the range of 20–60 K/cm for crystals with 100 mm and 200 mm diameter at pulling rates $V$ of around 1 mm/min [39, 40, 43]. The temperature gradient can also vary along the length of the cylindrical body as reported e.g. in [40]. For the transition from the starting cone to the cylindrical body it is concluded from very few experimental data [39, 40] that $G$ is about 10–50% higher than in the subsequent cylindrical body phase. More precise data could only be obtained by fully time-dependent simulations which are still very challenging [23].

In the criterion of constitutional supercooling (according to Fig. 4b and Eq. (3)) the actual temperature gradient $G$ has to be taken in a crystal position very close to the growth interface. Measured temperature gradients represent usually values which are either averaged over the whole crystal length or which are determined at a certain distance away from the solid–liquid interface. However, it is known from numerical simulations that the temperature gradient can be e.g. 20% to 30% higher directly at the interface than at a distance of a few centimeters away from the phase boundary [38, 43]. This means that the actual $G$ values are most likely higher than the $G$ values given in Table III.

In any case it follows clearly from a comparison of columns 3 and 4–6 in Table III that the avoidance of constitutional supercooling during growth of heavily doped silicon crystals is very challenging. The critical temperature gradients $G_S$ which are needed for a stable growth are very close to the upper limit of the values of the temperature gradients $G$ which are reported in the literature for various CZ growth conditions. If one considers the different doping elements it is also obvious that the avoidance of constitutional supercooling is more difficult for growth of As-doped Si crystals than for P-and B-doped ones (compare columns 4, 5 and 6 in Table III).

An increase of the crystal diameter (e.g. from 100 mm to 200 mm) would intensify the problem because it has to be considered that for a given hot-zone typically the temperature gradient $G$ decreases with increasing crystal diameter [44]. Furthermore, it has to be considered that the axial temperature gradient $G$ varies along the radial position. It is typically higher at the periphery of the crystal compared to the center [43]. This means

that a breakdown of the interface caused by constitutional supercooling will preferentially begin in the core of the crystal rather than at its periphery. This prediction is confirmed by several experimental results [3, 7 15].

From the arguments above, it can be easily understood that the growth of silicon crystals heavily doped with P or As with 300 mm diameter would be extremely difficult. Although the pulling speed $V$ is typically only 0.5 0.6 mm/min for shallow doped crystals with 300 mm diameter during the growth of the cylindrical body [45, 46], the temperature gradients $G$ reported in literature are also only in the order of 30 40 K/cm during body growth [45]. This means that the growth of silicon crystals with 300 mm diameter would take place again very close to the criterion of constitutional supercooling for P and As (see Fig. 7). In addition, it has to be considered that the larger mass of the melt ($> 250$ kg typically used for 300 mm diameter instead of 30 kg for 100 mm [46]) would require the handling of ten times more mass of the hazardous phosphorus and arsenic. This is extremely challenging from a safety and security point of view. For silicon heavily doped with B the growth of crystals with 300 mm diameter might become more feasible from both, the occurrence of constitutional supercooling and the doping issues independently of economic considerations.

## 5. Conclusions and recommendations

It has been shown in the previous sections that it is very challenging to grow silicon crystals by the CZ technique with high doping levels ($> 10^{20}$ atoms/cm$^3$) of B, P, and As without running into the problem of constitutional supercooling followed by the "loss of structure".

From the theoretical background one can conclude that the following measures should be considered to avoid constitutional supercooling:

- optimization of the hot-zone of the puller e.g. by introducing additional heat shields in order to establish a higher temperature gradient $G$;
- decrease of the pulling speed $V$ in order to decrease the pile up of doping atoms in the melt in front of the growth interface;
- increased convective melt transport in order to decrease the pile up of doping atoms in the melt in front of the growth interface.

On the other hand, for economic reasons it is not desirable to decrease the pulling rate $V$. Moreover, an increase of the temperature gradient $G$ would result in an increase of the thermal stress in the crystal [44]. This could lead to the formation of crystal defects, like dislocations and finally structure loss even without violating the criterion for constitutional supercooling.

It is also discussed in literature that the structure loss during CZ growth of heavily doped silicon crystals may depend on the concentrations of oxygen and intrinsic point defects, e.g. [6, 12, 15]. So far there are only a few publications et al. [47 50] in which the influence of doping on the concentration of intrinsic point defects is studied. It is discussed that high doping concentrations of B, P, and As can have a considerable influence on the formation of three-dimensional crystal defects like voids, crystal originated particles (COPs), oxygen precipitates and the position of the oxygen induced stacking fault (OFS) ring [47 50]. However, no clear picture exists so far in literature especially regarding the correlation of the occurrence of structure loss with the point defect content of heavily doped silicon crystals.

Therefore, it will remain difficult to prove in a certain case whether constitutional supercooling is responsible for a "structure loss" or whether other phenomena were limiting the dislocation-free growth of heavily doped silicon crystals by the Czochralski technique.

## Acknowledgments

The authors would like to thank Dr. Lothar Lehmann from Siltronic AG for fruitful discussions. The research and development activities were carried out within the Power-on-Si Project (project number: 100128500) with Siltronic AG. The project is funded partly by the European Regional Development Fund (ERDF) and by the Saxony State Ministry for Science and Art (SMWK).

## References

[1] B. Jayant Baliga, Advanced Power MOSFET Concepts, Springer, New York 2010, Ch. XVI.

[2] `www.semi.org`; SEMI Document 5307, 2011.

[3] H.D. Chiou, *J. Electrochem. Soc.* **147**, 345 (2000).

[4] M. Kulkarni, M. Banan, C. Luers, US-Patent 7 131 091 B2, 2006.

[5] R. Falster, V. Voronkov, G. Borionetti, US-Patent 8 026 145 B2, 2011.

[6] R. Scala, M. Porrini, G. Borionetti, *Cryst. Res. Technol.* **46**, 749 (2011).

[7] W. Bardsley, J.M. Callan, H.A. Chedzey, D.T.J. Hurle, *Solid State Electron.* **3**, 142 (1961).

[8] K.M. Kim, *J. Electrochem. Soc., Solid State Sci. Technol.* **126**, 875 (1979).

[9] W. Bardsley, D.T.J. Hurle, M. Hart, A.R. Lang, *J. Cryst. Growth* **49**, 612 (1980).

[10] T.G. Digges, R. Shima, *J. Cryst. Growth* **50**, 865 (1980).

[11] H.M. Hobgood, T.T. Braggins, M.M. Sopira, J.C. Swartz, R.N. Thomas, *IEEE Trans. Electron Dev.* **27**, 14 (1980).

[12] H.D. Chiou, *Electrochem. Soc. Proc.* **99**, 511 (1999).

[13] T. Taishi, X. Huang, M. Kubota, T. Kajigaya, T. Fukami, K. Hoshikawa, *Jpn. J. Appl. Phys.* **38**, 223 (1999).

[14] T. Taishi, X. Huang, M. Kubota, T. Kajigaya, T. Fukami, K. Hoshikawa, *Mater. Sci. Eng. B* **72**, 169 (2000).

[15] H.D. Chiou, *J. Electrochem. Soc.* **152**, G295 (2005).
[16] J.W. Rutter, B. Chalmers, *Can. J. Phys.* **31**, 15 (1953).
[17] A. Cröll, University Freiburg, private communication.
[18] W.W. Mullins, R.F. Sekerka, *J. Appl. Phys.* **35**, 444 (1964).
[19] W.A. Tiller, K.A. Jackson, J.W. Rutter, B. Chalmers, *Acta Metall.* **1**, 428 (1953).
[20] D.T.J. Hurle, *Solid State Electron.* **3**, 37 (1961).
[21] C.D. Thurmond, M. Kowalchik, *Bell Syst. Tech. J.* **39**, 169 (1960).
[22] A.G. Ostrogorsky, *J. Cryst. Growth*, accepted for publication.
[23] G. Müller, J. Friedrich, *J. Cryst. Growth* **266**, 1 (2004).
[24] J.A. Burton, R.C. Prim, W.P. Slichter, *J. Chem. Phys.* **21**, 1987 (1953).
[25] W.G. Cochran, *Math. Proc. Cambr. Philos. Soc.* **30**, 365 (1934).
[26] E. Scheil, *Z. Metallkunde* **34**, 70 (1942).
[27] S.E. Bkadshaw, A.I. Mlavsky, *J. Electron. Control* **2**, 134 (1956).
[28] W. Zulehner, *J. Cryst. Growth* **65**, 189 (1983).
[29] T.F. Ciszek, *J. Cryst. Growth* **75**, 61 (1986).
[30] Z. Liu, T. Carlberg, *J. Electrochem. Soc.* **140**, 2052 (1993).
[31] A.Ya. Nashelsky, E.O. Pulner, *J. Cryst. Growth* **171**, 94 (1997).
[32] J.C. Brice, *J. Cryst. Growth* **6**, 205 (1970).
[33] K.T. Wilke, J. Bohm, *Crystal Growth (Kristallzüchtung)*, Harry Deutsch Verlag, Frankfurt 1988 (in German).
[34] A. Molchanov, PVA Tepla AG, private communication.
[35] W. Dash, *J. Appl. Phys.* **30**, 459 (1959).
[36] E. Kuroda, H. Kozuka, *J. Cryst. Growth* **63**, 276 (1983).
[37] T. Fujiwara, S. Inami, S. Miyahara, S. Kobayashi, T. Kubo, H. Fujiwara, *J. Cryst. Growth* **128**, 275 (1993).
[38] E. Dornberger, E. Tomzig, A. Seidl, S. Schmitt, H.-J. Leister, Ch. Schmitt, G. Müller, *J. Cryst. Growth* **180**, 461 (1997).
[39] H.D. Chiou, T.-Y.T. Lee, S. Teng, *J. Electrochem. Soc.* **144**, 2881 (1997).
[40] T. Abe, in: *Defects in Silicon III*, Eds. T. Abe, W.M. Bullis, S. Kobayashi, W. Lin, P. Wagner, Electrochemical Society Proceeding, Vol. 99-1, Seattle 1999, p. 414.
[41] X. Huang, T. Taishi, T. Wang, K. Hoshikawa, *J. Cryst. Growth* **229**, 6 (2001).
[42] N. Banos, M.Sc. Thesis, University Erlangen — Nuremberg 2002 (in German).
[43] E. Dornberger, W. von Ammon, J. Virbulis, B. Hanna, T. Sinno, *J. Cryst. Growth* **230**, 291 (2001).
[44] W. von Ammon, E. Dornberger, P.O. Hansson, *J. Cryst. Growth* **198/199**, 390 (1999).
[45] M. Krause, J. Friedrich, G. Müller, *Mater. Sci. Semicond. Proc.* **5**, 361 (2003).
[46] W. von Ammon, in: *Crystal Growth — from Fundamental to Technology*, Eds. G. Müller, J.J. Metois, P. Rudolph, Elsevier, Amsterdam 2004, p. 239.
[47] V.V. Voronkov, B. Falster, *Microelectron. Eng.* **56**, 165 (2001).
[48] V.V. Voronkov, R. Falster, M. Porrini, J. Duchini, *Phys. Status Solidi A* **209**, 1898 (2012).
[49] M. Suhren, D. Graef, U. Lambert, P. Wagner, *J. Electrochem. Soc.* **144**, 4041 (1997).
[50] W. Sugimura, T. Ono, S. Umeno, M. Hourai, K. Sueoka, K. Koji, *Electrochem. Soc. Trans.* **2**, 95 (2006).

Special Anniversary Issue: Professor Jan Czochralski Year 2013 — Invited Paper

# Czochralski Growth of Decagonal AlCoNi Quasicrystals from Al-rich Solution

G. Meisterernst, B. Bauer and P. Gille*
Ludwig-Maximilians-Universität München, Department of Earth and Environmental Sciences
Crystallography section, Theresienstr. 41, D-80333 Munich, Germany

Czochralski growth of cm size decagonal AlCoNi single crystals from Al-rich high-temperature solutions is described using native seeds oriented parallel to all symmetrically different crystal directions. Morphological observations allow first hints with respect to anisotropic growth rates. But only classical detachment experiments according to the original idea of Jan Czochralski reveal quantitative results of kinetically limited growth rates. Geometric conditions of wetted plane interfaces as well as aspects of constitutional supercooling affect the detachment experiments. Thus, in only one specific orientation of the decagonal quasicrystal quantitative data for the maximum growth rate could be obtained.

DOI: 10.12693/APhysPolA.124.344

PACS: 61.44.Br, 81.10.Aj

## 1. Introduction

With the discovery of quasicrystals in the binary Al–Mn system by Shechtman et al. [1] a new principle of arrangement of condensed matter was found. The studied phase showed icosahedral symmetry which is not compatible with three-dimensional translation periodicity in a conventional crystallographic understanding. Here the new ordering principle is quasiperiodicity which is characterised by long-range order but simultaneously missing periodicity. With the discovery of decagonal quasicrystals by Bendersky [2] it could be shown that the two contradictory principles of periodic and quasiperiodic ordering can be realised in just one solid at the same time.

Up to now, quite a few intermetallic systems exist in which thermodynamically stable decagonal quasicrystals occur. The decagonal phase in the Al–Co–Ni system has been studied most intensively and the crystals in this system are characterised best. These so called axial quasicrystals are geometrically built up of quasiperiodic layers which are stacked along a periodic axis. The description of these planes in a conventional crystallographic way leads to higher-dimensional space. The quasiperiodic planes can be regarded periodic in the (4+1)-dimensional space. Four reciprocal basis vectors $\boldsymbol{a}_i^* = a^*(\cos 2\pi i/5, \sin 2\pi i/5, 0)$ $(i = 1, 2, 3, 4)$ are needed in the quasiperiodic plane, while the fifth vector $\boldsymbol{a}_5^*$ is parallel to the stacking direction [3]. Therefore, five independent indices $\{h_1h_2h_3h_4h_5\}$ describe crystallographic forms of decagonal quasicrystals. The point group symmetry is $10/mmm$. The stereographic projection of the morphological forms, which we observed in several growth experiments of AlCoNi quasicrystals [4] is shown in Fig. 1.

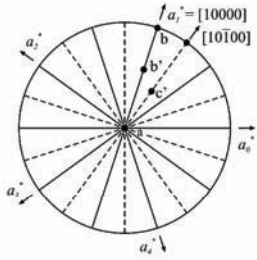


Fig. 1. Stereographic projection of the observed forms occurring in the crystal class $10/mmm$: a {00001}: pinacoid; b {10000}: decagonal prism; b' {0$\bar{1}\bar{1}$01}: decagonal dipyramid; c {10$\bar{1}$00}: decagonal prism; c' {10$\bar{1}$02}: decagonal dipyramid.

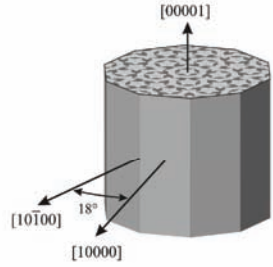


Fig. 2. The two symmetrically non-equivalent twofold axes [10000] and [10$\bar{1}$00] span the quasiperiodic layers, represented here by the famous Penrose tiling [5], which are stacked along the tenfold rotation axis [00001].

*corresponding author; e-mail: gille@lmu.de

Figure 2 shows the two symmetrically non-equivalent directions [10000] and [10$\bar{1}$00] which span the quasiperiodic layer. The angle between these directions is 18°. They correlate with the two different twofold axes in this crystal class, while the tenfold rotation axis runs parallel to [00001], the stacking direction of the quasiperiodic planes. It is the aim of this paper to contribute to the understanding of anisotropic growth kinetics observed in crystal growth of decagonal AlCoNi quasicrystals using the Czochralski method from Al-rich solutions. For this aim, we describe detachment experiments to determine the maximum crystallization rates of crystallographic forms that could be identified during the Czochralski growth experiments [4].

## 2. Czochralski growth of decagonal quasicrystals

In the ternary Al–Co–Ni system, the decagonal phase melts peritectically, but can be grown directly from an Al-rich solution. In Fig. 3 the isothermal section of the Al-rich part of the Al–Co–Ni phase diagram at 1050 °C [6] shows the two-phase coexistence region between the liquid (L) and the solid decagonal phase (D).

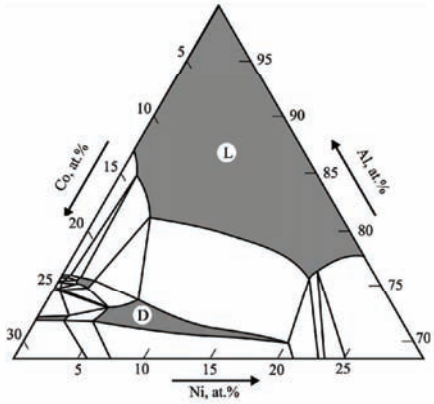


Fig. 3. Isothermal section of the Al-rich part of the Al–Co–Ni phase diagram at 1050 °C, after [6].

According to this phase diagram the decagonal phase can only be grown from off-stoichiometric melts. The Czochralski method is the most favourable method to grow this kind of single crystals, because it allows perfect observation of the growth process. Large decagonal AlCoNi single crystals have been grown using different initial melt compositions. Exemplarily, crystals grown from the initial melt composition of $Al_{77}Co_6Ni_{17}$ will be discussed further. The composition of crystals obtained from this melt was measured to be $Al_{72}Co_9Ni_{19}$ using electron probe microanalysis.

Growing crystals from off-stoichiometric melts or rather Al-rich solutions involves some specifics that have to be considered. During growth the composition of the melt continuously changes depending on the amount of material already crystallized. Therefore, the liquidus temperature of the melt decreases permanently which has to be accommodated by using an appropriate temperature programme. More precisely, in the case of Al-rich solutions, rejected aluminium will be enriched in the melt, so the liquidus temperature will drop during growth. Accordingly, a progressively decreasing temperature programme in the range of 0.1–1 K/h has to be applied to ensure a stable height of the meniscus and a constant diameter simultaneously. To ensure an adequate transport of the excess component away from the phase boundary good mixing of the melt and a low pulling velocity have to be guaranteed. For realisation, counter rotation of crystal and crucible cares for the good mixing of the melt and a pulling velocity of 0.15 mm/h has found to be sufficient for the growth of decagonal AlCoNi quasicrystals. In addition to the good observation of the growth process which allows to check the crystal quality already at a very early stage, the possibility to grow crystals in different crystallographic orientations by using appropriate seeds is one of the main advantages of the Czochralski method.

## 3. Anisotropy of growth rates and morphology

From the Czochralski growth experiments of decagonal quasicrystals anisotropic growth rates of different crystallographic orientations could be observed. In case of choosing one of the symmetrically non-equivalent twofold rotational axes as pulling direction, the cross-section will be oval shaped with the longer extension parallel to the periodic direction [00001] (see Fig. 4a). Although the anisotropy is not directly measurable in a growth experiment, this is a strong hint that despite the forced rotationally symmetrical conditions within the melt the oval shape of the crystals is due to different growth velocities parallel and perpendicular to the periodic direction with the growth parallel to the periodic direction being faster. Quasicrystals pulled parallel to the tenfold rotational axis [00001] show a circular cross-section (see Fig. 4b). From this can be deduced that the two symmetrically non-equivalent twofold rotational axes [10000] and [10$\bar{1}$00], which are perpendicular to the tenfold axis, have similar crystallization rates. Using a pulling direction somewhat inclined to the tenfold rotational axis causes a change in shape of the cross-section of the quasicrystal as well. The contribution of the tenfold direction with its large growth rate causes the quasicrystal to extend into this direction, leading to a crystal that grows inclined to the pulling axis.

Growing crystals parallel to one of the symmetrically non-equivalent twofold axes results in different morphologies of the solid–liquid interface. Crystals grown parallel to the [10000] direction show a flat (10000) interface, while for crystals grown parallel to the other twofold

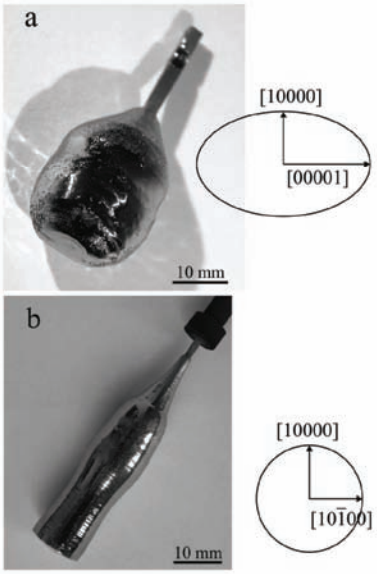


Fig. 4. (a) Crystal grown parallel to the aperiodic direction [10$\bar{1}$00] and (b) along the periodic direction [00001] and the corresponding cross-sections, respectively.

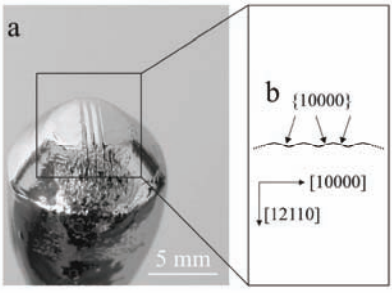


Fig. 5. (a) Interface of a crystal grown parallel [12110]; (b) sketch of the axial cut through the interface with facets of the form {10000}.

direction [10$\bar{1}$00] the corresponding perpendicular plane does not develop. Here, the interface is made up of a sequence of {10000} facets as shown in Fig. 5. For crystals grown along the periodic direction [00001] no interface faceting was observed and the interface follows a curved isotherm.

## 4. Detachment experiments

As mentioned before, it is the Czochralski method, which is most suitable concerning observability and control of the crystal growth process. Here it will be used in its original intent to determine the growth rate of different crystallographic orientations of decagonal quasicrystals. In his original paper [7], Czochralski suggested a method to determine the growth velocity of low-melting metals. This was done by pulling a thin single-crystalline metal fibre from the melt. When a pulling rate higher than the specific maximum crystallization velocity of the metal is applied, the crystal separates from the melt.

### *4.1. Background of Czochralski's detachment experiment*

In Czochralski's original paper [7], it was already mentioned that the crystal–liquid interface is at a level well above the average melt surface and the crystal diameter is determined by the meniscus shape. The latter can be influenced by differences between the experimentally chosen pulling rate $v_p$ and the axial growth rate $v_g$ which is driven by thermal and kinetic conditions. Under equilibrium conditions (Fig. 6a) growth at constant crystal diameter occurs at $v_g = v_p$ while at a higher pulling rate $v_p^+$ the difference $(v_p^+ - v_g)$ leads to a narrowing of the crystal diameter that is e.g. used in Dash's necking procedure [8] as to eliminate dislocations in Si crystal growth.

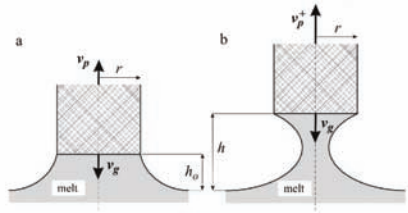


Fig. 6. Schematic sketch of the meniscus shape in Czochralski growth from the melt under steady-state conditions where the axial growth rate $v_g$ equals the pulling rate $v_p$ (a), and with an increased pulling rate $v_p^+$ that exceeds the maximum growth rate and ends with the detachment of the crystal from the melt (b).

Under equilibrium conditions, the height $h_0$ of the increased meniscus can be theoretically described, e.g. by Hurle's formula [9]. The question at which maximum meniscus height $h_{max}$ the melt can no longer be held in contact with the crystal is simply a mechanical problem resulting from the balance of surface tension and gravitational forces.

Following Czochralski's original idea [7], we assume that a maximum growth rate $v_{g,max}$ exists for some reason, e.g. caused by kinetic constraints. With a constant pulling rate $v_p^+$ that exceeds this limit, the meniscus height increases with time $t$ to a position $h > h_0$

(Fig. 6b) and can be expressed by

$$h = h_0 + t(v_p^+ - v_{g,max}). \quad (1)$$

It reaches its maximum height $h_{max}$ after applying the too high pulling rate during a time $t_{max}$ and ends with the detachment of the melt from the growing crystal

$$t_{max} = (h_{max} - h_0)/(v_p^+ - v_{g,max}). \quad (2)$$

Experimentally, the pulling rate in the Czochralski growth experiment described above has to be suddenly increased at $t = 0$ to $v_p^+$ and held constant up to the moment $t_{max}$ where the crystal loses contact to the melt. Using a series of different pulling rates all of them exceeding the maximum possible crystallization rate, Eq. (2) permits to calculate the maximum possible growth rate $v_{g,max}$ just from measuring the time $t_{max}$ needed to detach the growing crystal from the melt. A linear plot of the reciprocal detachment time $(t_{max})^{-1}$ versus the various applied pulling rates $v_p^+$ gives the maximum growth rate by the extrapolation towards $(t_{max})^{-1} = 0$.

### *4.2. Quasicrystal detachment experiments*

To determine the maximum growth rates $v_{g,max}$ of the decagonal quasicrystals along the $[h_1h_2h_3h_4h_5]$ growth direction, a series of experiments was performed. After seeding and stable growth of the crystal at constant diameter in the specific orientation, the pulling speed $v_p$ was increased abruptly to a value $v_p^+ > v_p$ and the time $t_{max}$ between increase of the pulling speed and separation of the crystal from the melt was measured. By repeating this procedure with applying different pulling velocities $v_p^+$ a series of $t_{max}(v_p^+)$ values could be obtained. The result of the analysis of these values is the maximum crystallization velocity $v_{p,max}$ of the specific orientation $[h_1h_2h_3h_4h_5]$.

In the course of the experiment the crystal was detached several times from the melt after having grown the crystal at stable conditions for some time. Just when the pulling rate was increased to a higher value $v_p^+$, the recording of the time until the detachment of the crystal from the melt was started. The time measurement was done by video monitoring the situation at the elevated meniscus with a resolution of one frame per minute. This resolution is precise enough compared to the typical duration $t_{max}$ of one single detachment experiment which is in the range of several hours.

With the first separation of the crystal from the melt, the first $t_{max}(v_p^+)$ pair of values was gained. By detaching the crystal at full diameter from the melt as well as by wetting the crystal again, the resulting thermal shock induces structural imperfections that could influence further growth and affect the determination of the maximum crystallization rate $v_{g,max}$. Therefore, in order to achieve a state of stable crystal growth at a constant diameter, the disordered part of the crystal was remelted completely prior to each new detachment experiment. Dissolving a length of about 5 mm has shown to be adequate to reach undisturbed single-crystalline regions. Beginning at this position, a new crystal growth run to achieve a state of constant diameter could be started.

To compensate the decreasing liquidus temperature during growth due to the enrichment of aluminium in the melt, an appropriate temperature programme was applied simultaneously to each growth or dissolution step. This ensures the continued growth at a constant diameter. After a period of stable growth at constant diameter at a pulling velocity of $v_p = 0.15$ mm/h, the pulling rate was again increased to a value $v_p^+ > v_p$ to gain the next $t_{max}(v_p^+)$ pair of values. This procedure of dissolving, growing and detaching followed by another growth run was repeated for every single $t_{max}(v_p^+)$ pair of values. Because of the low growth rates during normal growth at $v_p$ and the additional time used for dissolving, the procedure of the detachment experiments took about eight weeks for each crystallographic direction $[h_1h_2h_3h_4h_5]$. An absolute requirement for the feasibility of these detachment experiments were the stable conditions in the Czochralski setup. To prevent the growth atmosphere against oxygen the growth chamber is fully metal-sealed.

In decagonal quasicrystals three types of crystallographic directions differ qualitatively:

i) orientation parallel to the tenfold axis [00001]; perpendicular to the pinacoid,

ii) orientation parallel to one of the two symmetrically non-equivalent twofold axes $\langle 10000 \rangle$ and $\langle 10\bar{1}00 \rangle$; perpendicular to the faces of the two different decagonal prisms, and

iii) orientation parallel to a so-called inclined direction $\langle h_1h_2h_3h_4h_5 \rangle$, where at least one of the indices $h_1$, $h_2$, $h_3$, or $h_4 \neq 0$ and $h_5 \neq 0$; with faces of a decagonal dipyramid perpendicular; in other words: any crystallographic direction showing a periodic *and* an aperiodic component.

The qualitative difference of these types of orientations expresses itself in the growth morphology of crystals grown parallel to these directions. Because of the known anisotropy of growth rates, as described before (see Sect. 3), the crystal cross-section at the liquid–solid interface is strongly influenced by the maximum growth velocities $v_{g,max}$ of the different crystallographic orientations $\langle h_1h_2h_3h_4h_5 \rangle$.

## 5. Results of detachment experiments

### *5.1. Parallel to the tenfold [00001] and the inclined directions*

After successful seeding parallel [00001], conditions for a constant diameter growth at $v_p = 0.15$ mm/h was set. On applying a higher pulling rate $v_p^+$ the crystal did not detach from the melt even after some hours of continued growth. Also by repeated increase of the pulling rate to values $v_p^+ \gg v_p$ it was not possible to separate the crystal from the melt. Instead, the loss of the cylindrical shape of the growing crystal was observed. Detaching this crystal was only possible by a dramatic increase of the pulling rate to $v_p^+ = 36$ mm/h. The investigation of this crystal

has shown that the liquid–solid interface decomposes into separated decagonal needles with residual Al-rich melt in between [10]. This structural decomposition of the growth interface can be explained by the effect of constitutional supercooling [10]. Single-crystalline growth parallel to [00001] at pulling rates close to detachment conditions is not possible and therefore the maximum growth rate $v_{g,max}$ parallel to the tenfold axis cannot be determined. From this result it is obvious that it will not be possible to determine the maximum growth rate $v_{g,max}$ of any crystallographic orientation of a decagonal quasicrystal that includes a component of the periodic direction [00001]. This leads to an exclusion of any inclined direction from the detachment experiments.

### 5.2. *Parallel to the twofold directions [10000] and [10100]*

While pulling a crystal parallel to one of the two crystallographically non-equivalent twofold directions [10000] and [10$\bar{1}$00] no component of the tenfold direction [00001] is parallel to the pulling direction. As known from previous growth experiments, the liquid–solid interface for crystals grown parallel to the twofold directions [10000] and [10$\bar{1}$00] is formed by crystallographic faces of the decagonal prism {10000} whereas the decagonal prism {10$\bar{1}$00} has no morphological relevance as a growth face. The pulling speed used for constant diameter growth was 0.15 mm/h for both directions. During the detachment experiment by choosing the twofold direction [10$\bar{1}$00] as pulling direction, the crystal was eight times grown and separated from the melt. The $t_{max}(v_p^+)$ data so obtained show a linear dependence as shown in Fig. 7.

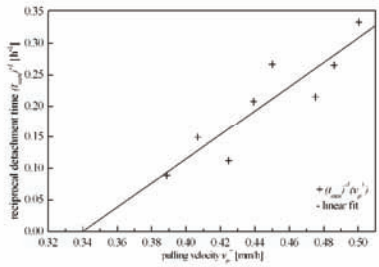


Fig. 7. Linear plot of $(t_{max})^{-1}$ vs. $v_p^+$ for pulling parallel to [10$\bar{1}$00].

Using a simple linear regression (see Eq. (3)) the maximum growth rate $v_{g,max}$ for the growth parallel to the [10$\bar{1}$00] direction was found at the intersection for the reciprocal detachment time $(t_{max})^{-1} = 0$:

$$(t_{max})^{-1} = (-0.65 \pm 0.17) + (1.9 \pm 0.4) \times v_p^+. \quad (3)$$

Accordingly, the maximum growth rate $v_{g,max}$ for the [10$\bar{1}$00] direction amounts to $(0.34 \pm 0.04)$ mm/h.

The situation changes by performing the experiment parallel to the second twofold axis [10000] as the pulling direction. In this case, the process of growing, detaching, and dissolving the crystal has been repeated nine times in the same range of pulling rates $v_p^+$. But in contrast to the experiment parallel to the other twofold direction a much higher scattering of data was obtained making a linear regression not meaningful. Since in both cases the liquid–solid interface is formed by large facets of the crystallographic form {10000}, the only reason for this different behaviour could be the different orientation of the interface with respect to the pulling direction and the melt surface. In the case of pulling parallel to the [10000] direction the growth front is formed by a single (10000) facet that is perpendicular to the growth direction and parallel to the melt surface. In contrast, the growth front in case of pulling parallel to the [10$\bar{1}$00] direction is formed by a set of {10000} facets that are inclined by 18° with respect to the melt surface (see Fig. 5). We regard this to be a simple geometrical problem instead of something that is driven by the growth kinetics, since the growth interface is the same one in both cases.

To investigate the influence of these different geometries at the two-phase boundary a model experiment was built up. Two simple test species of the same diameter made of stainless steel have been shaped in order to represent the two interfaces under investigation. For these two interface models detachment experiments were performed using water as a model melt and the maximum possible elevation of the water meniscus after wetting was determined. With wetting and detaching each model interface many times, the repeatability for each type of interface could be determined. As a result, the water meniscus at that model representing the complex interface perpendicular to the [10$\bar{1}$00] direction with inclined faces could be elevated to its maximum height much more precisely than with the model representing the singular flat interface (10000) perpendicular to the vector of gravity showing the same data scattering as in the detachment experiments with the quasicrystal described above.

With this, the difference in the accuracy of the results for the maximum growth rates $v_{g,max}$ of the two different twofold directions [10000] and [10$\bar{1}$00] could be better understood. But, we end up with the somehow disappointing result that only one of all tested growth directions allowed a quantitative analysis of the maximum possible growth rate.

## 6. Summary

The Czochralski method has proved to be a suitable technique to grow decagonal AlCoNi crystals from an Al-rich solution at temperatures of about 1050 °C. Highly perfect single crystals were grown from native seeds by pulling either parallel to the tenfold axis [00001] which is the periodic direction of decagonal quasicrystals or along one of the crystallographically non-equilvalent twofold rotational axes [10000] and [10$\bar{1}$00] having quasiperiodic order. Hints of anisotropic growth can already be obtained from the cross-section of decagonal quasicrystals that has

an elliptical shape with the larger extension along the periodic [00001] direction.

In order to investigate the growth anisotropy quantitatively we adopted the original idea of Jan Czochralski and used his method to measure the maximum possible growth rate along all qualitatively different directions of the decagonal AlCoNi quasicrystal. Since crystal growth parallel to the periodic axis is very fast, kinetic limits of growth could not be found prior to the onset of constitutional supercooling. This is also true for pulling along any direction that includes a component of the periodic axis, i.e. parallel to so-called inclined directions.

The Czochralski growth parallel to one of the twofold axes is kinetically limited allowing the classical detachment experiments when pulling at a higher rate than the maximum possible growth rate. But, geometric reasons depending on the orientation of the plane interfaces with respect to the vector of gravity determine whether or not the detachment experiments give clear results. Pulling decagonal AlCoNi quasicrystals parallel to the $[10\bar{1}00]$ axis has resulted in a kinetically limited maximum growth rate of $(0.34 \pm 0.04)$ mm/h.

**Acknowledgments**

The work has been supported by the Deutsche Forschungsgemeinschaft under contract Gi 211/5.

**References**

[1] D. Shechtman, I. Blech, D. Gratias, J.W. Cahn, *Phys. Rev. Lett.* **53**, 1951 (1984).

[2] L. Bendersky, *Phys. Rev. Lett.* **55**, 1461 (1985).

[3] W. Steurer, T. Haibach, in: *Physical Properties of Quasicrystals*, Ed. Z.M. Stadnik, *Springer Series in Solid-State Sciences*, Vol. 126, Springer-Verlag, Berlin 1999.

[4] P. Gille, G. Meisterernst, N. Faber, *J. Cryst. Growth* **275**, 224 (2005).

[5] R. Penrose, *Bull. Inst. Math. Appl.* **10**, 266 (1974).

[6] T. Gödecke, M. Scheffer, R. Lück, S. Ritsch, C. Beeli, *Z. Metall.* **89**, 687 (1998).

[7] J. Czochralski, *Z. Phys. Chem.* **92**, 219 (1918).

[8] W.C. Dash, *J. Appl. Phys.* **30**, 459 (1959).

[9] D.T.J. Hurle, B. Cockayne, in: *Handbook of Crystal Growth. Bulk Crystal Growth*, Vol. 2a, Ed. D.T.J. Hurle, North-Holland, Amsterdam 1994, p. 99.

[10] G. Meisterernst, Ph.D. Thesis, Ludwig-Maximilians-Universität München, Munich 2006.

Special Anniversary Issue: Professor Jan Czochralski Year 2013 — Invited Paper

# Czochralski-Based Growth and Characteristics of Selected Novel Single Crystals for Optical Applications

K. SHIMAMURA[a,b,*] AND E.G. VÍLLORA[a]

[a]National Institute for Materials Science, 1-1 Namiki, Tsukuba, 305-0044, Japan

[b]Faculty of Science and Engineering, Waseda University, 3-4-1 Okubo, Shinjuku, 169-8555, Japan

In the Year of Professor Jan Czochralski, we with pleasure review the representative recent works of our group, Optical Single Crystals Group, NIMS, Japan. Our group has been working on the development of novel single crystals for optical applications based on the Czochralski technique. Here, 4 kinds of topics are reviewed. 1st one is ferroelectric fluoride $BaMgF_4$ single crystals for UV nonlinear optical applications including quasi-phase matching device fabrications. 2nd one is transparent conductive $\beta$-$Ga_2O_3$ single crystals as semiconductor, which has large band-gap, 4.8 eV, for LED applications. 3rd one is F-doped core-free $Y_3Al_5O_{12}$ single crystals as a potential new lens material for UV/VUV wavelength region. Last one is superior magneto-optical $\{Tb_3\}[Sc_{2-x}Lu_x](Al_3)O_{12}$ single crystals for near infrared to visible region, and $CeF_3/PrF_3$ single crystals for UV region.

DOI: 10.12693/APhysPolA.124.265

PACS: 81.10.St, 77.84.−s, 85.60.Jb, 42.79.Bh, 78.20.Ls, 85.70.Sq

## 1. Introduction

Recently, optical technology progress in a wide range of applications, and at the same time, still demands the further development. One of the key issue is to present new optical sources in UV/VUV wavelength region. Another one is to increase laser power. Since conventional crystal materials face some of the limitations, these issues require new optical single crystals.

From these view points, we have been working on the development of novel single crystals for the diverse optical applications. In this review, ferroelectric fluoride, $\beta$-$Ga_2O_3$, F-doped core-free $Y_3Al_5O_{12}$ and magneto--optical garnet single crystals including some of the additional topical crystals, which have advantageous characteristics toward the above demands, will be introduced as representative recent research subjects of our group (homepage of our group: `www.nims.go.jp/group/oscg/index_e.html`).

The Czochralski technique is actually one of the most important and widely used technique among all the crystal growth techniques. Especially for industrial applications, Czochralski technique is remarkably precious one, which enables the large size and low cost crystal growth. Several famous crystal growth techniques are also derived from the Czochralski technique. For instance, Kyropoulos technique is used for sapphire growth. Liquid encapsulated Czochralski (LEC) technique enables the growth of volatile semiconductors such as GaAs and InP. Edge--defined, film-fed growth (EFG) technique is also developed to realize a shaped crystal growth. One of the most favorable characteristic of the Czochralski technique is that we can feel we are "growing" beautiful bulk single crystals. We can see all the growth process by our eyes, and when we change parameters, crystals show/reply to us during growth at very high temperature. This is really a delicious flavor of the crystal growth. At the same time, nothing can be worse than to see grown crystals sank into the melt and disappear.

Since the Czochralski technique is successfull to satisfy both industrial severe requirements and happiness of crystal growers, we mainly work with this technique. At the same time, we use the derived technique from the Czochralski one, mostly EFG technique. In this article, some of our novel crystals grown by these techniques are reviewed with biggest pleasure inYear of Professor Jan Czochralski. If we could show the great importance of the Czochralski technique for the science and industry, that would be the ultimate happiness.

## 2. Ferroelectric fluoride $BaMgF_4$

Excimer lasers are the currently used coherent light sources for UV/VUV wavelength region, namely, ArF (193 nm) and KrF (248 nm). These present several disadvantages such as fast degradation, toxicity and low beam quality, and therefore alternative sources are strongly requested. All solid-state lasers (ASSL) emitting at short wavelengths are realized by second-, third- and fourth--harmonic generation using oxide nonlinear crystals such as $\beta$-$BaB_2O_4$, $CsLiB_6O_{10}$, $LiB_3O_5$, and $Li_2B_4O_7$, which can be birefringent phase matched [1], whereas the lack of optical grade nonlinear crystals transparent in the UV, as well as large Poynting-vector walk-off inherent to the birefringent phase matching at short wavelengths, have fundamentally made impossible the SHG in the UV/VUV. A new approach, the quasi-phase matching (QPM), which was theoretically predicted already in the 60's [2], is being developed since the beginning of the 90's [3]. By this method, the frequency conversion is obtained by the use of a ferroelectric crystal, which has been periodically poled (PP) in $\mu$m order domains. SHG by QPM has been shown in well-known nonlinear crystals, such as $LiNbO_3$ or $LiTaO_3$ [4]. These crystals, however, cannot be used in the UV/VUV wavelength region, since

*corresponding author; e-mail: SHIMAMURA.Kiyoshi@nims.go.jp

their cutoff wavelengths lie in the near UV at 330 and 280 nm, respectively.

Ferroelectricity has been shown by a pulsed-field technique on the pyroelectric fluoride $BaMF_4$ family (M = Mg, Mn, Fe, Co, Ni, Zn), except in the case of M = Mn and Fe [5]. Among these, $BaMgF_4$ is attracting much attention since it is transparent in the UV/VUV [6, 7], with a decreasing transparency towards the cutoff wavelength at approximately 130 nm. The origin of the optical losses in the UV/VUV has not been cleared yet, but a correlation with the concentration of scattering centers in the VIS has been observed [7]. $BaMgF_4$ has been studied as a host crystal doped with transition metal and rare earth for ASSL applications [8, 9]. Further, thin films of $BaMgF_4$ have been investigated for memory applications, namely metal-ferroelectric-semiconductor field-effect transistors [10, 11]. The ferroelectric properties, however, are not established yet; Eibschuetz et al. [5] obtained the reversal of the spontaneous polarization (7.7 $\mu C/cm^2$) at electric fields in the order of 50 kV/cm, while the hysteresis loop measured on a thinned sample (10 $\mu$m) by Sinharoy et al. [11] indicated 8.5 $\mu C/cm^2$ and 95.4 kV/cm for the spontaneous polarization and the coercive field, respectively.

We have selected $BaMgF_4$ as the most promising material for UV/VUV SHG-QPM after several material search [7, 12–14]. Then, we have grown large size single crystals of $BaMgF_4$, and determined the ferroelectric properties of bulk single-crystals by the measurement of the polarization hysteresis. The coercive field was analyzed as a function of the applied frequency and used for the periodical poling of $\mu$m order ferroelectric domains. The selective etching of ferroelectric domains on a PP $c$-plane plate was examined. Further, SHG emission in different wavelength was demonstrated.

Crystal growth was carried out by the Czochralski (Cz) technique with a 30 kW RF-generator. High purity powders (> 99.99%) of commercially available $BaF_2$ and $MgF_2$ powders were weighted and mixed in stoichiometric composition. $CF_4$ gas (> 99.999%) was flowed into the furnace and the powders were melted at approximately 920 °C [15]. An oriented $BaMgF_4$ single crystal was used as a seed. The crystal rotation and pulling rate were fixed at 10 rpm and 1 mm/h, respectively. A detailed description of the growth characteristics is reported elsewhere [7]. Figures 1 and 2 are examples we have grown by the same technique [16].

Ferroelectric hysteresis loops were measured with an FCE-1 equipment from Toyo Corporation. The voltage was applied in triangle wave form at frequencies varying between 0.05 and 100 Hz. The $c$-oriented plate had a thickness of 0.5 mm and a gold electrode area of 10.4 $mm^2$. Selectively etched domains were observed with an Olympus BX51 microscope.

As fundamental laser sources for the testing of the PP-$BaMgF_4$ frequency converters, we used (a) a pulsed Nd:$Y_3Al_5O_{12}$ (YAG) laser YAG 5000 series from B.M. Industries Co., Ltd (10 ns pulse width at a repetition rate of 10 Hz), (b) a pulsed Ti:sapphire Mira Optima 900-P from Coherent (3 ps pulse width at a repetition rate of 76 MHz), and (c) a master oscillator power amplifier (MOPA) from Spectra physics (7 ns pulse width at a repetition rate of 10 Hz).

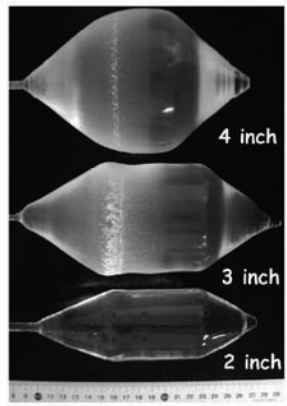


Fig. 1. Ce-doped $LiCaAlF_6$ single crystals grown by the Czochralski technique for VUV laser applications.

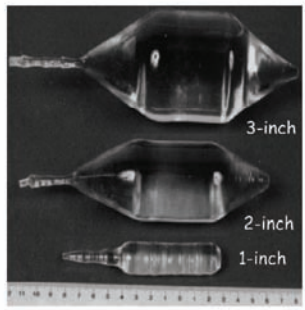


Fig. 2. Tm and Ho co-doped $LiLuF_4$ single crystals grown by the Czochralski technique for IR laser applications.

Figure 3 shows $BaMgF_4$ single crystal with 2 inch in diameter without cracks [17]. Precise control of a diameter, especially to extend a diameter slowly at the shoulder part was fundamentally important. Otherwise, large crack formations frequently occurred. The growth of 2 inch size crystals are required to fabricate QPM devices.

Three representative polarization hysteresis loops are shown in Fig. 4. The loops are very symmetric, exhibiting a close to ideal shape with a loop squareness

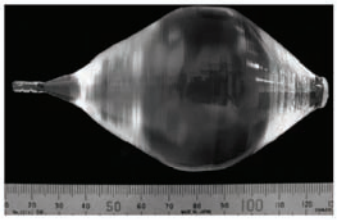

Fig. 3. 2 inch size $BaMgF_4$ single crystal grown by the Czochralski technique.

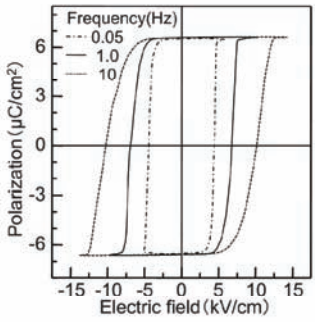


Fig. 4. Polarization hysteresis loop of $BaMgF_4$.

over 99% (calculated as the ratio between the remanence and the spontaneous polarization, $P_r/P_s$). Ferroelectric properties obtained from these loops are summarized in Table. The spontaneous polarization, with a value of 6.6 $\mu C/cm^2$, is lower than the reported ones [5, 11] and about a third of $KTiOPO_4$. On the other hand, the coercive field varies between 4 and 24 kV/cm [13].

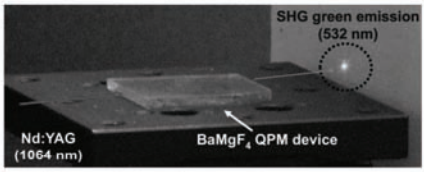


Fig. 5. Green SHG from IR using a BMF-QPM device.

As-grown crystals are found to be single domain for the most part. The polarization reversal is induced by an electric field through the displacement of the Ba atoms along the $c$ axis and the rotation of the Mg-F6 octahedra around the Mg atoms. The theoretically predicted matching conditions for SHG QPM have been

TABLE

Ferroelectric properties obtained from the hysteresis loops of $BaMgF_4$ as a function of the frequency.

| Frequency | $\nu$ [Hz] | 0.05 | 1.0 | 10 |
|---|---|---|---|---|
| maximum applied field | $E_{max}$ [V] | 275 | 500 | 700 |
| coercive field | $E_c$ [kV/cm] | 4.4 | 6.8 | 10.2 |
| spontaneous polarization | $P_s$ [$\mu C/cm^2$] | 6.53 | 6.63 | 6.63 |
| remanence polarization | $P_r$ [$\mu C/cm^2$] | 6.52 | 6.60 | 6.58 |
| loop squareness | $P_r/P_s$ [%] | 99.8 | 99.5 | 99.2 |
| resistance | $R$ [M$\Omega$ cm] | 842 | 93 | 15 |

tested. Devices with different periods have been processed and checked. With an initial period of 70 $\mu$m we succeeded in frequency-doubling the emission from a 1064 nm Nd:YAG laser using the $d_{33}$ nonlinear coefficient. A photograph of the emitting device is shown in Fig. 5.

Fig. 6. 396 nm SHG using a BMF-QPM device.

Fig. 7. 277 nm SHG using a BMF-QPM device.

As a next step we reduced the period to match the tunable range of a Ti:sapphire laser. Periods between 24 and 40 $\mu$m were used to obtain SHG in the VIS and near-UV wavelength regions. The photograph of Fig. 6 shows as an example the 396 nm SHG visualized on a phosphorescent paper. Subsequently, 368 nm SHG, which is close to the limit of the pulsed Ti:sapphire laser, was also obtained.

The shortest emission obtained so far is 277 nm from 554 nm laser of MOPA as fundamental source, shown in Fig. 7 [18]. In order to achieve emission at shorter wavelengths similar to those of the gas excimer lasers, the grating period needs to be considerably shortened. The realization of these periods gets towards the limit of


Fig. 8. Periodically poled $BaMgF_4$ $c$-plate.

standard photolithographical processes, which use contact masks and a minimum pitch of approximately 1 $\mu$m.

The shortest period achieved so far is shown in Fig. 8. This photograph shows a $c$-cut $BaMgF_4$ sample after the poling process. The ferroelectric domain structure is visualized by a selective etching process of $+$c and $-c$ surfaces. The obtained period is 6.6 $\mu$m, just about double of the one necessary for 193 nm emission.

### 3. Substrate single crystal $\beta$-$Ga_2O_3$

Although heteroepitaxial growth of gallium nitride compounds on sapphire is well established, sapphire does not represent an adequate candidate because of its insulating character. SiC is at present the most used conductive substrate for the growth of gallium nitrides [19]. However, due to the lack of transparency in the blue wavelength region, optical losses have to be taken into account for the design of LEDs. The search for alternative substrates has been pursued intensively [20], and it is still a remaining issue.

$\beta$-$Ga_2O_3$ belongs to the group of the transparent conductive oxides (TCOs). It exhibits the largest band gap among them, $E_g = 4.8$ eV (260 nm) [21], and thus a unique transparency from the VIS into the UV region. This is an important property for the future generations of optoelectronic devices operating at shorter wavelengths. Due to the high transparency in the VIS wavelength region and the $n$-type conductivity, $\beta$-$Ga_2O_3$ is a new substrate candidate for the growth of gallium nitrides. The crystal structure of $\beta$-$Ga_2O_3$ has the monoclinic symmetry, with space group $C2/m$ [22], lattice parameters $a = 12.23$ Å, $b = 3.04$ Å, $c = 5.80$ Å and $\beta = 103.7°$.

$\beta$-$Ga_2O_3$ is the only stable modification at high temperature, which remains stable upon cooling. Here, the stable crystal growth of $\beta$-$Ga_2O_3$, which is indispensable to achieve large size single crystals, was analyzed. By this approach, wafers of 2 inches in diameter $\beta$-$Ga_2O_3$ single crystals were obtained. Subsequently, the possibility to use $\beta$-$Ga_2O_3$ as a substrate for the epitaxial growth of GaN was examined. The blue emission from an InGaN multi-quantum-well (MQW) deposited on a $\beta$-$Ga_2O_3$ substrate and with vertical current injection was demonstrated.

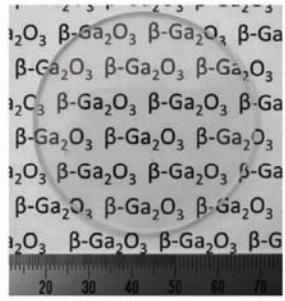


Fig. 9. Polished 2 inch size $\beta$-$Ga_2O_3$ single crystal wafer, presented by Koha Co., Ltd.

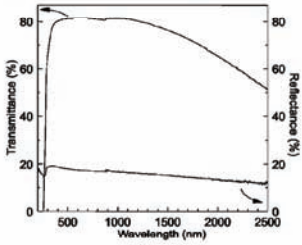


Fig. 10. Transmittance and reflectance of a 0.5 mm $\beta$-$Ga_2O_3$ wafer.

The EFG technique, which is one of the most important derivative of the Cz technique, was a successful one for the growth of large size $\beta$-$Ga_2O_3$ single crystals. Figure 9 shows a $\beta$-$Ga_2O_3$ single crystal with 2 inch size grown by the EFG technique. The crystal shown in Fig. 9 was obtained by the both side polishing [17]. Presented achievements are noteworthy since they show for the first time the way how to grow large size single crystals, as well as the capability to cut them in wafers, in spite of the remarkable cleavage nature of $\beta$-$Ga_2O_3$.

The wafers were highly transparent in the VIS wavelength region. The transmittance and reflectance spectra of a both sides polished wafer without antireflection coating are shown in Fig. 10 [23]. Scattering and absorption losses in the VIS wavelength region are negligibly small and the increasing absorption in the near infrared (IR) wavelength region is well known for TCOs, and indicates the presence of free carriers.

The electrical conductivity is shown as a function of the Si concentration in the double logarithmic plot of Fig. 11. The conductivity continuously increases by over three orders of magnitude, from a value as low as 0.03 $\Omega^{-1}$ cm$^{-1}$ for 6N-purity crystals to 50 $\Omega^{-1}$ cm$^{-1}$ for crystals with a high Si concentration. The Si incorporation saturates at about 0.2 mol.% when second-phase segregation appears [24–26].

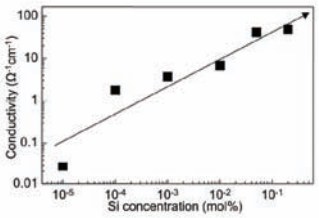


Fig. 11. Electrical conductivity of $\beta$-$Ga_2O_3$ as a function of the nominal Si concentration. The arrow indicates a systematical increase.

In addition to the high transparency and electrical conductivity, $\beta$-$Ga_2O_3$ exhibits an extraordinary high resistance to chemical agents, as well as mechanical hardness and stability at high temperature. All these properties make $\beta$-$Ga_2O_3$ an attractive substrate candidate for semiconductor materials.

(100) $\beta$-$Ga_2O_3$ substrates were used for the GaN deposition. GaN growth took place at 100 Torr by the metalorganic vapor phase epitaxy (MOVPE) technique. Low pressure processes, so-called LP-MOVPE, are widely used for the growth of conventional III–V compounds. Trimethyl-gallium (TMG) and $NH_3$ were used as the source gases. The flow rate of $NH_3$ was 1200 sccm. The deposition was done in two steps: firstly a low temperature (LT) GaN buffer layer was deposited at 600 °C, subsequently a GaN layer of 1000 nm was grown at 1070 °C.

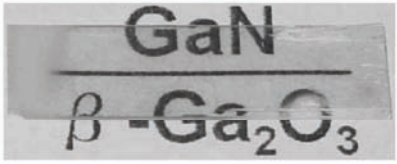


Fig. 12. Outlook of InGaN-MQW grown on $\beta$-$Ga_2O_3$.

A single GaN layer was deposited on an un-doped buffer layer. The GaN layer grown on the $\beta$-$Ga_2O_3$ substrate exhibits a very flat surface. After the successful deposition of a single GaN epi-layer, we proceeded with the fabrication of LED with vertical current injection. In order to enable the current flow between the substrate and the GaN layers, the $n$-type buffer layer doped with Si was employed by flowing $SiH_4$ as source gas. The surface morphology of a GaN epilayer grown on a conductive buffer layer was unchanged. Next, a $In_{0.12}GaN$/$In_{0.03}GaN$ MQW was deposited on the GaN layer, followed by a $p$-GaN layer. Figure 12 shows a top view of the deposited substrate [27]. It is seen that transparent InGaN-MQW epilayers have been deposited on the transparent $\beta$-$Ga_2O_3$ substrate. $p$- and $n$-electrodes were deposited on the epilayers and the rear side of the substrate, respectively. Blue emission was obtained after the vertical current injection with a current of 30 mA. Higher light yield with higher electric current was also obtained. Based on these investigations, several types of packaged InGaN-MQW/$\beta$-$Ga_2O_3$ LEDs have been successfully obtained.

Fig. 13. Blue emission from InGaN-MQW/$\beta$-$Ga_2O_3$ SMD-type LEDs.

Figure 13 shows SMD type LEDs. Although the electrical properties of the buffer layer, as well as the energy band alignment to the substrate are a matter of future investigations, present results demonstrate the successful LED fabrication on the $\beta$-$Ga_2O_3$ substrate.

### 4. Lens material F-doped core-free $Y_3Al_5O_{12}$

Industrial semiconductor related facilities such as next generation optical lithography and optical related facilities such as microscope and digital camera, require new types of UV/VUV optical lens materials. Typical required characteristics are high transparency, different wavelength dispersion of refractive indices, uniformity of refractive index, and low cost. However, materials which can satisfy these requirements are limited.

Recently, $Lu_3Al_5O_{12}$ has been reported as a potential candidate for this. Although $Lu_3Al_5O_{12}$ may have potential high transmittance at UV/VUV and large refractive, 2.1435, several serious problems have been pointed out, such as practical low transmittance, difficulty to grow high quality and uniform crystals leading to the high inhomogeneity of refractive index.

In this work, we have developed F-doped core-free $Y_3Al_5O_{12}$ single crystals, by re-examining the standard $Y_3Al_5O_{12}$ single crystals [17].

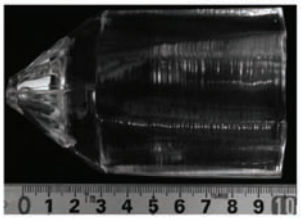


Fig. 14. 2 inch size F-doped core-free $Y_3Al_5O_{12}$ single crystal, presented by Dai-Ichi Dentsu Ltd.

Figure 14 shows 2 inch size F-doped core-free $Y_3Al_5O_{12}$ single crystal, grown by the Cz technique. Core-free nature was confirmed by the polarizing microscope observation of the vertically sliced wafers toward

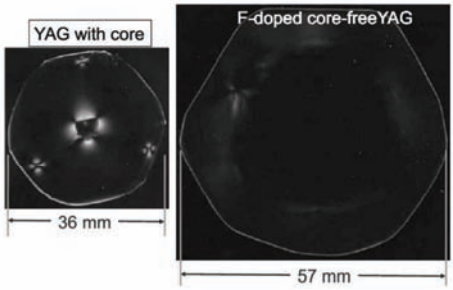


Fig. 15. Polarizing microscope photos of core-free $Y_3Al_5O_{12}$ (Fig. 14) and standard $Y_3Al_5O_{12}$.

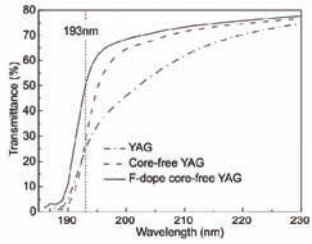


Fig. 16. Transmission spectra of different type of $Y_3Al_5O_{12}$ single crystals.

the growth axis (Fig. 15). This realizes the high uniformity of refractive index distribution. The improvement of transmittance, especially at UV/VUV, was revealed by F-doing into $Y_3Al_5O_{12}$ single crystal (Fig. 16). Additionally, this F-doped core-free $Y_3Al_5O_{12}$ crystal has shown quite large refractive index, 2.145, which is even slightly larger than that of $Lu_3Al_5O_{12}$ (Fig. 17).

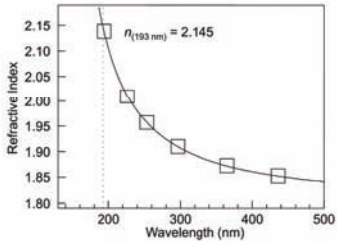


Fig. 17. Precisely measured refractive indices of $Y_3Al_5O_{12}$ single crystal.

## 5. Faraday rotator $\{Tb_3\}[Sc_{2-x}Lu_x](Al_3)O_{12}$

Optical isolators (OIs) are fundamental components for optical communications, high-power fiber-laser machinery and others. OIs prevent from optical feedback, which causes parasitic oscillations in amplifier systems or frequency instabilities in laser diodes. The central part of an OI is a Faraday crystal, which rotates the polarization plane of the laser beam. $Y_3Fe_5O_{12}$ (YIG) is so far the most commonly used crystal in OIs. It is characterized by a high transparency in the IR region, a large Faraday rotation angle, and a low saturation magnetization. However, $Y_3Fe_5O_{12}$ cannot be used at shorter wavelengths (< 1100 nm) due to its poor transparency. Taking advantage of the magneto-optical (MO) properties of $Tb^{3+}$ ions, optically isotropic terbium-garnets are the material systems considered for wavelengths below 1100 nm. $Tb_3Al_5O_{12}$ (TAG) has been reported to show resonable properties as the Faraday rotator (FR) [28, 29], however, its incongruent melting nature makes impossible the growth of large crystals [30]. Instead, $Tb_3Ga_5O_{12}$ (TGG) [31] is industrially grown by the Cz technique to fabricate OIs. Although it melts congruently at approximately 1825 °C, its growth is not exempt of difficulties [32].

We have designed a new garnet single crystal, $\{Tb_3\}[Sc_{2-x}Lu_x](Al_3)O_{12}$ (TSLAG), by the substitution of $Al^{3+}$ of $Tb_3Al_5O_{12}$ in the octahedral site with a proper mixture of $Sc_{2-x}Lu_x$ which can stabilize the garnet structure adjusting the average cationic size [33]. A detailed analysis of the optical and MO properties of $\{Tb_3\}[Sc_{2-x}Lu_x](Al_3)O_{12}$ crystals is carried out [34].

Fig. 18. 2 inch size $\{Tb_3\}[Sc_{2-x}Lu_x](Al_3)O_{12}$ single crystal grown by the Czochralski technique, presented by Fujikura Ltd.

Nominal TSLAG single crystals with $x = 0.05$ were grown by the Cz technique. As starting materials commercial oxides of $Tb_4O_7$, $Sc_2O_3$, $Lu_2O_3$, and $Al_2O_3$ of 4N purity were used. These were weighted in the corresponding nominal cationic ratios. Mixed powders were charged in an Ir crucible and molten with a 30 kW RF generator. Figure 18 shows the representative 2 inch size $\{Tb_3\}[Sc_{2-x}Lu_x](Al_3)O_{12}$ single crystal. The pulling and rotation rates were fixed to 0.5 mm/h and 10 rpm, respectively. The $Tb_3Ga_5O_{12}$ single crystal reference was purchased from Furuuchi Chemical Corporation.

Figure 19 shows the absorption coefficient, $\alpha$, as a function of the wavelength obtained from the transmittance

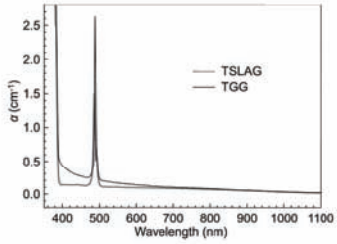


Fig. 19. Absorption coefficient of $\{Tb_3\}[Sc_{2-x}Lu_x](Al_3)O_{12}$ and $Tb_3Ga_5O_{12}$ crystals.

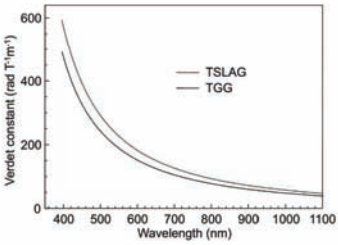


Fig. 20. Verdet constant of $\{Tb_3\}[Sc_{2-x}Lu_x](Al_3)O_{12}$ in comparison with $Tb_3Ga_5O_{12}$.

and reflectance spectra for $\{Tb_3\}[Sc_{2-x}Lu_x](Al_3)O_{12}$ and $Tb_3Ga_5O_{12}$. In both compounds, the $Tb^{3+}$ $^7F_6 \rightarrow {}^5D_3$, $^5D_2$ absorption bands start below 390 nm and the transition $^7F_6 \rightarrow {}^5D_4$ lies at about 488 nm. Both crystals are practically transparent in the near IR region, however, it is noteworthy the continuous increase in absorbance observed in $Tb_3Ga_5O_{12}$ from the IR to shorter wavelengths. This feature contrasts with the low absorption of $\{Tb_3\}[Sc_{2-x}Lu_x](Al_3)O_{12}$ in the whole VIS-IR.

The results of the Faraday rotation angle measurements are displayed in Fig. 20. The Verdet constant ($V$) dispersion of $\{Tb_3\}[Sc_{2-x}Lu_x](Al_3)O_{12}$ is shown in comparison with that of $Tb_3Ga_5O_{12}$. It is seen that $\{Tb_3\}[Sc_{2-x}Lu_x](Al_3)O_{12}$ possesses a higher $V$ value, with an increment of 20% independently of the considered wavelength.

After the precise determination of $\alpha$ and $V$, the MO figure of merit (FM), defined as $V/\alpha$, has been estimated and is plotted in Fig. 21. It is seen that the FM of $\{Tb_3\}[Sc_{2-x}Lu_x](Al_3)O_{12}$ is larger than that of $Tb_3Ga_5O_{12}$ at all wavelengths. In the near IR region this is mainly attributed to the higher $V$ value, while in the VIS also the higher transparency of $\{Tb_3\}[Sc_{2-x}Lu_x](Al_3)O_{12}$ contributes to the remarkably higher FM of $\{Tb_3\}[Sc_{2-x}Lu_x](Al_3)O_{12}$ with respect to $Tb_3Ga_5O_{12}$.

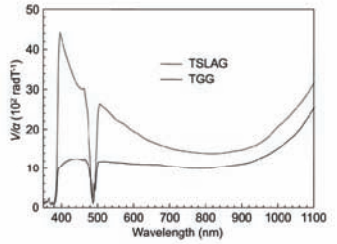


Fig. 21. Figure of merit of $\{Tb_3\}[Sc_{2-x}Lu_x](Al_3)O_{12}$ and $Tb_3Ga_5O_{12}$.

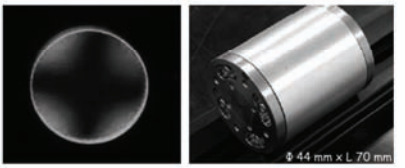


Fig. 22. (Left) $\{Tb_3\}[Sc_{2-x}Lu_x](Al_3)O_{12}$ under crossed polarizers. (Right) A prototype of $\{Tb_3\}[Sc_{2-x}Lu_x](Al_3)O_{12}$-based optical isolator.

In order to check the potential substitution of $Tb_3Ga_5O_{12}$ by $\{Tb_3\}[Sc_{2-x}Lu_x](Al_3)O_{12}$, the optical quality of the crystals was further analyzed. The photograph of a 10 mm long sample with 3 mm in diameter under crossed polarizers is shown in Fig. 22 (left). It is seen that the crystal is very homogeneous, free from scattering, defects, and twinning. Antireflection coatings were deposited on three crystals, and their extinction ratios were measured. The values obtained for all crystals were over the highest value of $Tb_3Ga_5O_{12}$ (40 dB), ranging between 41 and 47 dB. Using one of these crystals, a first $\{Tb_3\}[Sc_{2-x}Lu_x](Al_3)O_{12}$-based prototype was assembled with the standard optics for a polarization independent $Tb_3Ga_5O_{12}$-based OI (Fig. 22 (right)). This device was tested with an Yb high-power fiber-laser operating at 1080 nm. The Gaussian profile of the fundamental transverse mode, $TEM_{00}$, was photographed before and after passing through the OI.

As can be observed in Fig. 23, the circularity of the beam remained almost unchanged, showing a value very close to the ideal 1, and the insertion loss was found to be below 0.1 dB. Additionally, the crystal damage threshold of $\{Tb_3\}[Sc_{2-x}Lu_x](Al_3)O_{12}$ was above that of $Tb_3Ga_5O_{12}$, which broke at a continuous power of 300 W focused in a 100 $\mu$m spot. These results further confirm the high optical quality of the $\{Tb_3\}[Sc_{2-x}Lu_x](Al_3)O_{12}$ crystal.

Although $\{Tb_3\}[Sc_{2-x}Lu_x](Al_3)O_{12}$ presents the superior properties in VIS–NIR region, it shows the strong

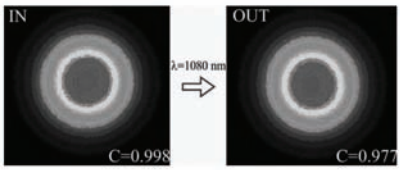


Fig. 23. Circularity, ratio between maximum and minimum diameter, of original and transmitted 1080 nm laser beams.

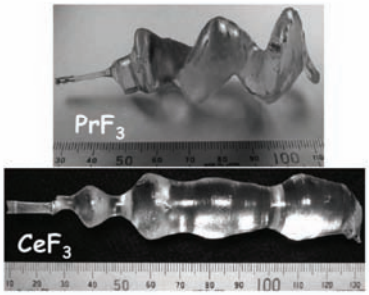


Fig. 24. $CeF_3$ and $PrF_3$ single crystals grown by the Czochralski technique.

absorption bands in the near UV and blue wavelength region. These are originated in the partially spin-allowed $4f-4f$ transitions of the MO active ion $Tb^{3+}$, and therefore this crystal cannot be used at wavelengths neither below 400 nm nor at around 490 nm. Consequently, there is a need to find FRs which can be used in non-covered UV and VIS wavelength regions. We have found that $CeF_3$ and $PrF_3$ single crystals are highly promising materials. Single crystals of these crystals were grown by the Cz technique (Fig. 24). $CeF_3$ could grow rather straightly though $PrF_3$ has shown the strong tendency of the spiral growth [35, 36]. FM of these crystals were measured and summarized in Fig. 25. These results indicate the high potential of $CeF_3$ and $PrF_3$ as optical isolators in the UV-visible, where at present there are no alternative candidates [37, 38].

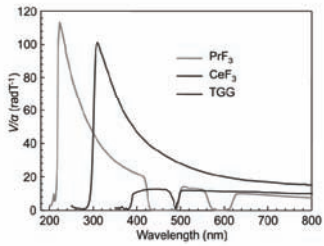


Fig. 25. Figure of merit of $CeF_3$ and $PrF_3$ in comparison to $Tb_3Ga_5O_{12}$.

## 6. Conclusion

In this article, we introduced the representative recent works of our group. The Cz and its derived techniques have been showing and will continue to show the marvelous importance for the science and industry. That is the reason why we have been and will keep working on these techniques. In this article, 4 kinds of our topics were reviewed.

2 inch size $BaMgF_4$ single crystals without cracks have been grown by the Cz technique. The ferroelectric properties of bulk $BaMgF_4$ have been measured by polarization hysteresis at different frequencies. The spontaneous polarization is 6.6 $\mu C/cm^2$, while the coercive field varies between 4 and 10 kV/cm according to the Ishibashi–Orihara model. Periodical domain poling is achieved and evidenced by selective etching. SHG QPM has been obtained for Nd:YAG, Ti:sapphire and MOPA lasers. This is the first report on QPM using a PP ferroelectric fluoride, emitting in the ultraviolet wavelength region. The shortest period and shortest SHG wavelength realized so far is 6.6 $\mu$m and 277 nm, respectively. Present results show the high potential of $BaMgF_4$ for the fabrication of UV/VUV frequency converters, in particular, for the ASSL generation at 193 nm.

2 inch $\beta$-$Ga_2O_3$ single crystals were grown by the EFG technique. GaN was grown on the $\beta$-$Ga_2O_3$ substrate for the first time by the MOVPE technique. Very flat epitaxial growth of the wurtzite $c$-plane GaN was obtained on the $\beta$-$Ga_2O_3$ substrate after the deposition of a LT buffer layer. LED structure was fabricated on the substrate using a conductive buffer layer. Blue emission was successfully realized by the different packaging types of InGaN/$\beta$-$Ga_2O_3$ LEDs with the vertical current injection. These results demonstrate the high potential of $\beta$-$Ga_2O_3$ as a new substrate for GaN based LED.

2 inch size F-doped core-free $Y_3Al_5O_{12}$ single crystals have been grown. These crystals confirmed several advantageous characteristics, such as improved transmittance at UV/VUV, large refractive index, and high uniformity of refractive indices. These advanced properties of F-doped core-free $Y_3Al_5O_{12}$ toward the high potential as a new lens materials for industrial and optical facilities.

$\{Tb_3\}[Sc_{2-x}Lu_x](Al_3)O_{12}$ single crystal has shown superior properties in comparison with $Tb_3Ga_5O_{12}$ from any point of view related with OIs. $\{Tb_3\}[Sc_{2-x}Lu_x](Al_3)O_{12}$ has more favorable growth characteristics than $Tb_3Ga_5O_{12}$, and a higher damage threshold. The increase of 20% in the Verdet constant is very significant, giving the possibility to reduce the intensity of the necessary magnetic fields specially in the IR. In the visible the FM of $\{Tb_3\}[Sc_{2-x}Lu_x](Al_3)O_{12}$ is much larger mainly due to the absence of absorpion losses

that are present in $Tb_3Ga_5O_{12}$. The measured features and device performance of $\{Tb_3\}[Sc_{2-x}Lu_x](Al_3)O_{12}$ clearly indicate that this crystal is industriallization mature. $\{Tb_3\}[Sc_{2-x}Lu_x](Al_3)O_{12}$ has a high potential to substitute commercial $Tb_3Ga_5O_{12}$ crystals used in OIs in the IR region (below 1100 nm), and more specially in the VIS. $CeF_3$ is noteworthy for its higher transparency and FM in the whole VIS, as well as a superior FM in the regions 300 to 400 nm and around 490 nm, where $Tb_3Ga_5O_{12}$ is already opaque. Below the cutoff of $CeF_3$ only $PrF_3$ can be used. $PrF_3$ possesses a superior FM in the UV region from 220 to 300 nm. These results indicate that $CeF_3$ has a high potential to be implemented in OIs operating in the near UV-VIS wavelength region, while $PrF_3$ is the unique candidate for devices that should work in the UV, below 300 nm.

**Acknowledgments**

We appreciate to introduce our work in the Year celebrating Professor Jan Czochralski. The work on $BaMgF_4$ has been partially supported by the Industrial Technology Research Grant Program in 2007 from New Energy and Industrial Technology Development Organization (NEDO) of Japan. Authors would like to thank to Mr. K. Sumiya and Dr. H. Ishibashi of Hitachi Chemical Co., Ltd., Mr. T. Masui and Mr. K. Aoki of Koha Co., Ltd., Dr. Y. Kuwano of Dai-Ichi Dentsu Ltd., and Mr. A. Funaki, Mr. T. Hatanaka, and K. Naoe of Fujikura Ltd., for the great contributions on these works.

**References**

[1] T. Sasaki, Y. Mori, M. Yoshimura, Y.K. Yap, T. Kamimura, *Mater. Sci. Eng. R* **30**, 1 (2000).

[2] J.A. Armstrong, N. Bloembergen, J. Duncan, P.S. Pershan, *Phys. Rev.* **127**, 1918 (1962).

[3] M.M. Fejer, G.A. Magel, D.H. Jundt, R.L. Byer, *IEEE J. Quant. Electron.* **28**, 2631 (1992).

[4] J.-P. Meyn, M.M. Fejer, *Opt. Lett.* **22**, 1214 (1997).

[5] M. Eibschuetz, H.J. Guggenheim, S.H. Wemple, I. Camlibel, M. DiDomenico Jr., *Phys. Lett. A* **29**, 409 (1969).

[6] S.C. Buchter, T.Y. Fan, V. Liberman, J.J. Zayhowski, M. Rothschild, *Opt. Lett.* **26**, 1693 (2001).

[7] K. Shimamura, E.G. Víllora, K. Muramatsu, N. Ichinose, *J. Cryst. Growth* **275**, 128 (2005).

[8] J.M. Rey, H. Bill, D. Lovy, H. Hagemann, *J. Alloys Comp.* **268**, 60 (1998).

[9] N. Kodama, T. Hoshino, M. Yamaga, N. Ishizawa, K. Shimamura, T. Fukuda, *J. Cryst. Growth* **229**, 492 (2001).

[10] T. Hayashi, M. Yoshihara, S. Ohmi, E. Tokumitsu, *Appl. Surf. Sci.* **117**, 418 (1997).

[11] S. Sinharoy, H. Buhay, M.H. Francombe, W.J. Takei, N.J. Doyle, J.H. Fieger, D.R. Lampe, E. Stepke, *J. Vac. Sci. Technol. A* **9**, 409 (1991).

[12] E.G. Víllora, K. Shimamura, K. Muramatsu, H. Kimura, K. Kitamura, N. Ichinose, *J. Cryst. Growth* **280**, 145 (2005).

[13] K. Shimamura, E.G. Víllora, H. Zeng, M. Nakamura, S. Takekawa, K. Kitamura, *Appl. Phys. Lett.* **89**, 232911 (2006).

[14] E.G. Víllora, K. Shimamura, F. Jing, A. Medvedev, S. Takekawa, K. Kitamura, *Appl. Phys. Lett.* **90**, 192909 (2007).

[15] M. Rolin, M. Clausier, *Rev. Int. Hautes Temp. Refract.* **4**, 39 (1967).

[16] F. Jing, K. Shimamura, E.G. Víllora, A. Medvedev, K. Kitamura, K. Asai, A. Sato, *J. Am. Ceram. Soc.* **91**, 296 (2008).

[17] K. Shimamura, E.G. Víllora, N. Ichinose, *Adv. Electroceram. Mater. II*, **221**, 137 (2010).

[18] E.G. Víllora, K. Shimamura, K. Sumiya, H. Ishibashi, *Opt. Expr.* **17**, 12362 (2009).

[19] K. Domen, A. Kuramata, R. Soegima, K. Horino, S. Kubota, T. Tanahashi, *IEEE J. Sel. Topics Quantum Electron.* **4**, 490 (1998).

[20] L. Liu, J.H. Edgar, *Mater. Sci. Eng. R* **37**, 61 (2002).

[21] H.H. Tippins, *Phys. Rev.* **140**, A316 (1965).

[22] S. Geller, *J. Chem. Phys.* **33**, 676 (1960).

[23] E.G. Víllora, K. Shimamura, Y. Yoshikawa, K. Aoki, N. Ichinose, *J. Cryst. Growth* **270**, 420 (2004).

[24] K. Shimamura, E.G. Víllora, T. Ujiie, K. Aoki, *Appl. Phys. Lett.* **92**, 201914 (2008).

[25] E.G. Víllora, K. Shimamura, T. Ujiie, K. Aoki, *Appl. Phys. Lett.* **92**, 202118 (2008).

[26] E.G. Víllora, K. Shimamura, Y. Yoshikawa, K. Aoki, *Appl. Phys. Lett.* **92**, 202120 (2008).

[27] K. Shimamura, E.G. Víllora, K. Domen, K. Yui, K. Aoki, N. Ichinose, *Jpn. J. Appl. Phys., Exp. Lett.* **44**, L7 (2005).

[28] M. Geho, T. Sekijima, T. Fujii, *J. Cryst. Growth* **275**, E663 (2005).

[29] C.B. Rubinstein, L.G. Van Uitert, W.H. Grodkiewicz, *J. Appl. Phys.* **35**, 3069 (1964).

[30] S. Ganschow, D. Klimm, P. Reiche, R. Uecker, *Cryst. Res. Technol.* **34**, 615 (1999).

[31] R.Z. Levitin, A.K. Zvezdin, M. von Ortenberg, V.V. Platonov, V.I. Plis, A.I. Popov, N. Puhlmann, O.M. Tatsenko, *Phys. Solid State* **44**, 2107 (2002).

[32] R.C. Linares, *Solid State Commun.* **2**, 229 (1964).

[33] K. Shimamura, T. Kito, E. Castel, A. Latynina, P. Molina, E.G. Víllora, M. Prakasam, P. Veber, J.P. Chaminade, A. Funaki, T. Hatanaka, K. Naoe, *Cryst. Growth Des.* **10**, 3466 (2010).

[34] E.G. Víllora, P. Molina, M. Nakamura, K. Shimamura, T. Hatanaka, A. Funaki, K. Naoe, *Appl. Phys. Lett.* **99**, 011111 (2011).

[35] K. Shimamura, E.G. Víllora, S. Nakakita, M. Nikl, N. Ichinose, *J. Cryst. Growth* **264**, 208 (2004).

[36] E.G. Víllora, K. Shimamura, S. Nakakita, M. Nikl, N. Ichinose, *Nucl. Instrum. Methods Phys. Res. A* **537**, 139 (2005).

[37] P. Molina, V. Vasyliev, E.G. Víllora, K. Shimamura, *Opt. Expr.* **19**, 11786 (2011).

[38] V. Vasyliev, E.G. Víllora, M. Nakamura, Y. Sugahara, K. Shimamura, *Opt. Expr.* **20**, 14460 (2012).

Special Anniversary Issue: Professor Jan Czochralski Year 2013 — Invited Paper

# A Review of the Automation of the Czochralski Crystal Growth Process

J. Winkler[a,*], M. Neubert[b] and J. Rudolph[c]

[a]Institut für Regelungs- und Steuerungstheorie, Technische Universität Dresden, Germany

[b]Leibniz-Institut für Kristallzüchtung, Berlin, Germany

[c]Lehrstuhl für Systemtheorie und Regelungstechnik, Universität des Saarlandes, Saarbrücken, Germany

On the occasion of the centennial of the invention of the Czochralski crystal growth process by the Polish scientist Jan Czochralski, a review of selected strategies for the automatic control of this process is given. This review provides a sketch of the fundamental challenges of controlling the Czochralski process and the basic concepts of feedback control. Both early and modern approaches to the control of the Czochralski process are described. The discussion focuses on questions related to feed-forward control, feedback control, and state estimation. The presented methods rely on simple mathematical process models in contrast to the finite element model-based approaches typically used in crystal growth process design and analysis. Such mathematical models motivate both the structure and parameters of the chosen controller. A comprehensive list of references to background literature on this topic completes this survey.

DOI: 10.12693/APhysPolA.124.181

PACS: 81.10.Fq, 81.10.Aj, 02.30.Yy

## 1. Introduction

This contribution presents an overview about the challenges as well as about past and present strategies for automatic control of the Czochralski (Cz) crystal growth process, one of the most important growth technologies used in industrial crystal growth. The demand for crystals of well defined structural, chemical and electrical properties produced with a maximum rate of yield and reproducibility was — and still is — the driving force to develop highly sophisticated automatic control systems. In this growth method, as it is mostly practiced nowadays, the crystals are grown freely from the melt, i.e., there are no shaping devices ensuring a constant or well defined diameter which is mainly important in matters of technological requirements. (Some variants of the Cz process used a so-called coracle — a floating diameter--defining aperture made from sintered silicon nitride — to ensure a stable thermal regime around the growing crystal and hence to stabilize a constant diameter, cf. [1].) The better it meets the desired diameter and the better its constancy, the less material has to be cut off after growth. On the other hand, strong diameter changes influence the structural properties of the crystal [2–6].

Not only the diameter, also other quantities like the crystal growth rate are of special importance. The growth rate directly influences the properties of the growing crystal. It correlates with the amount of imperfections, like polycrystalline growth, twins, dislocations as well as the amount of native point defects, residual impurities and that of intentionally introduced dopants. Consequently, for process technology there is a huge interest in growth rate control also, especially in silicon crystal growth where the relation between growth rate and thermal gradients at the interface is of great importance in order to ensure an extremely low content of point defects [7–12].

No matter which control strategy is chosen to address these issues, the Cz system is an extremely challenging control object giving control engineers a headache for decades now. These issues are subject of Sect. 2.

When designing a control system the first task is to characterize the dynamic relations between the manipulated and the controlled variables. Based on these results a control structure is chosen. A large variety of approaches are provided by modern control theory. Such a control system does not only consist of a feedback controller, but also on equipment realizing the feed-forward control, the reference trajectory planning and the reconstruction of not directly measured variables. Different levels of mathematical complexity, questions about linear or nonlinear control design, robustness and real-time capability make things more difficult. Section 3 gives an introduction to the basic terms and approaches used in control technology as required for the Cz process.

When the Cz process was introduced into industrial germanium growth [13, 14] the weight measurement of the crucible or of the growing crystal to control the heater power [15] was used. In contrast to that Patzner et al. used an optical sensor manipulating the pull rate for silicon [16]. Nowadays, diameter control has been developed for a variety of different materials and system configurations, where many complex problems have been identified such as materials with hard to control conditions that resulted either in high dislocation densities or large growth and shape variations, as well as the challenges in scale up of the process for larger crystal sizes [8, 11, 17–22]. Other

*corresponding author; e-mail: Jan.Winkler@tu-dresden.de

examples are the use of a liquid encapsulant [23, 24] introducing time delays into the process [25, 26] or more sophisticated variants of the Cz process, like the vapor pressure controlled Czochralski (VCz) method [27] which intentionally leads to reduced axial and radial temperature gradients making diameter control even more difficult [28, 29]. More recently, the focus of control design has been extended to maintain additional degrees of freedom which affect crystal quality as well as crystal shape during the neck, shoulder and tail sections in addition to the main body [30, 31]. In Sect. 4 selected strategies will be discussed.

## 2. Specific characteristics of the Cz process

The aim of process analysis is to gain insight into its dynamical behavior using powerful methods provided by systems theory. For this purpose a wide range of analysis methods exist. First analysis of the principal system behavior in order to improve diameter feedback control were presented by Bardsley et al. in the 70's [32–36]. Some of the main results are summarized in the following.

### 2.1. Meniscus region

The most important region in the Czochralski crystal growth is the meniscus, the interconnection between melt and crystal, cf. Fig. 1. The meniscus and its shape result from gravitational forces and surface tension. At its upper end the so called phase boundary, or interface, is located where crystallization takes place. Thereby heat of fusion (latent heat) is released. Because the crystal is pulled upward into colder regions of the furnace a temperature gradient is established, which leads to a heat flow by conduction from the hot interface into the colder crystal [18]. By this mechanism crystallization is maintained throughout the growing process.

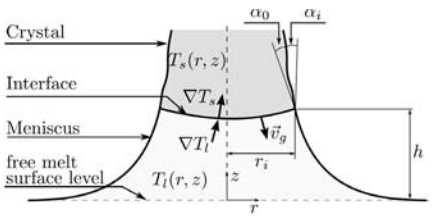


Fig. 1. Sketch of the interface region with important physical quantities.

The amount of heat transported into the crystal consists of two components: the amount of heat transported from the meniscus region into the interface with radius $r_\mathrm{i}$ and the amount of heat released by crystallization. In general, the following relation holds for the vector $\boldsymbol{v}_\mathrm{g}$ of the growth rate along the phase boundary described by $z = \mathcal{Z}(r)$, $r \in [0, r_\mathrm{i}]$:

$$\boldsymbol{v}_\mathrm{g}(r,\ \mathcal{Z}(r)) = \frac{1}{\rho_\mathrm{s}\Delta H_\mathrm{f}}\big(\lambda_\mathrm{m}\nabla T_\mathrm{m}(r,\mathcal{Z}(r)) - \lambda_\mathrm{s}\nabla T_\mathrm{s}(r,\mathcal{Z}(r))\big), \quad r \in [0, r_\mathrm{i}]. \tag{1}$$

In this equation the specific latent heat is denoted by $\Delta H_\mathrm{f}$, the heat conductivities of the solid and the melt are given by $\lambda_\mathrm{s}$ and $\lambda_\mathrm{m}$, respectively, and $T_\mathrm{s}(r,z)$ and $T_\mathrm{m}(r,z)$ represent the temperature of the solid and the melt. The density of the crystal at the interface (at melting temperature $T_\mathrm{i}$) is given by $\rho_\mathrm{s}$. A necessary condition for growth is that the growth rate is positive, i.e. the heat flux is directed from the melt into the crystal.

Changes in the temperature gradients on the melt or solid side of the phase boundary lead to an immediate change of the growth rate, as can be easily seen from Eq. (1). On the one hand, a local change of the growth rate results in a deformation of the phase boundary and in a change of the crystal diameter if this deformation is located at the rim of the interface. On the other hand, a change in interface geometry again initiates a change in heat transport. Furthermore, the shape of the meniscus strongly depends on the radius $r_\mathrm{i}$ of the crystal at the interface as well as on the growth angle $\alpha = \alpha_0 + \alpha_\mathrm{i}$ with the equilibrium growth angle $\alpha_0$ and the crystal slope angle $\alpha_\mathrm{i}$ [37–39], cf. Fig. 1. This means that changes in the meniscus shape initiated by changes in the geometry result in an immediate change of the heat balance in this region, with the consequences described above. This consideration leads to the conclusion that the demand of growing crystals of well defined shape requires exact control of the thermal conditions in the interface region. Without any precise measurements characterizing the state of this region this is an overwhelming task. An approach trying to realize such a direct control by blowing inert gas around this region is presented by Brice [40]. However, usually any measurements available at the process are more or less distant to this region complicating the control of the process.

### 2.2. Measurement issues

The quantities which one would like to control are the crystal diameter and the crystal growth rate. Unfortunately, these quantities cannot be directly measured. As an alternative the force acting on the pulling rod (or the crucible) [15] or the diameter of a bright ring on the meniscus resulting from reflections of the hot glowing heaters [41] are available. For example, in the liquid encapsulated Czochralski (LEC) process the crystal diameter is not directly measured because of a boron oxide layer covering the melt. Hence, in this process the weighing method is used.

The idea behind the weighing technique is that — at a first glance — the rate of change of the force acting on the load cell might be proportional to the crystal cross-section area at the growing interface. This can be evaluated by a controller. However, the measured force is also influenced by forces resulting from the meniscus [34, 42] making the correct interpretation of the signal more complicated. Furthermore, if the density of the solid is smaller than the density of the liquid, a well known anomaly comes into play which consists of the

fact that, e.g., an increase in the differential weight gain signal does not necessarily reflect an increase of the crystal diameter. The reason for this effect is that an increasing crystal diameter first results in a decrease of the meniscus-height and of its volume (cf., Fig. 2, middle). Since the density of the melt is larger than the density of the solid, a decreasing meniscus-volume makes the differential weight gain signal decreasing at first although the crystal diameter is increasing (cf., Fig. 2, bottom). For materials which do not completely wet their solids, i.e., $\Theta_0 \neq 0$, a similar effect can be observed since an increase in crystal diameter ($\alpha_i > 0$) leads to a reduction of the vertical component of the surface tension acting on the crystal (its vertical component is proportional to $\cos(\Theta_0 + \alpha_i)$). Unfortunately, all commonly grown semiconducting materials show this effect.

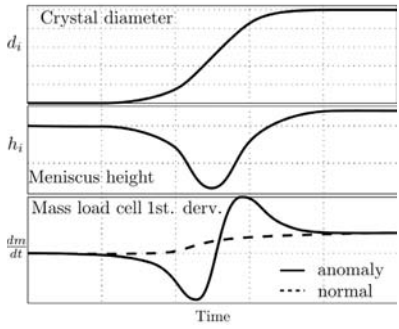


Fig. 2. A slight change of the crystal diameter (top) results in a temporarily break-in of the differential weight gain signal (bottom). The reason for that is the reduction of the meniscus height during the diameter transfer (middle). After [34].

The anomaly also leads to crucial problems during the transfer from the shoulder into cylindrical growth, cf., Fig. 3 (top): a sudden increase of the derivative of the force acting on the load cell with respect to time is observed just before the crystal diameter reaches the cylinder. This behavior can be explained by the fact that the shape of the meniscus changes significantly at this phase of the process [30].

More detailed discussions with respect to this subject can be found in [42–44]. The strength of the effect depends on several factors discussed in detail in [35]. Especially the growth rate is of great importance. Roughly speaking it can be summarized that the lower the pulling speed the stronger the effect. Measurement of the diameter of the bright meniscus ring, as it is widely used in silicon growth, is affected by a similar anomaly [17].

Yet another factor limiting the weighing technique is the diameter of the crystal body. The larger it is the stronger the load cell measuring the force has to be. However, the stronger the load cell the more inaccurate it becomes for small loads. This is problematic especially during the initial phase of the process.

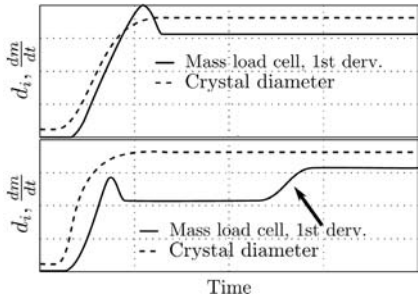


Fig. 3. Top: increase of the derivative of the differential weight gain signal before the crystal reaches the phase of cylindrical growth. Bottom: in case of the LEC-process an "aftershock" occurs in the differential weight gain signal when the crystals emerge from the boron oxide layer. The dashed curves represent the corresponding diameter trends.

### *2.3. Batch character and time delays*

The Cz process is a so-called batch process. This means that it does not have a steady state operating point. This mainly results from the fact that the whole system configuration changes during the growth: while in the beginning one has a crucible filled with melt, one has a nearly empty crucible and a crystal at the end of the process. The falling melt level leads to an ever-changing heat entry from the heaters into the system. Thus, the process dynamics changes heavily throughout the process. Understanding the influence of these variations on the process dynamics provides a foundation for developing a robust process control system. Detailed discussions on these subjects can be found in [2, 17, 45, 46].

In case of LEC growth, the influence of the boron oxide layer comes into play. One has to take into account the buoyancy as well as the time delay introduced by the emerging crystal, resulting in additional dynamical effects. For example, Fig. 3 (bottom) shows an "aftershock" occurring in the differential weight gain signal when the crystal begins to emerge from the boron oxide layer. These effects are discussed in [25, 47, 48] and must be carefully considered during control system design.

### *2.4. Modeling issues*

Today, modeling and computer simulation play an important role in crystal growth process design as well as in control applications. For example, whenever no direct access to certain quantities in a process is possible dynamic mathematical models are used to establish some kind of connection between the measured and the not measured quantities in order to reconstruct the values of the latter ones. However, since the dynamics of the

process is mainly driven by complex nonlinear radiative, conductive, and convective heat transport phenomena, it cannot be fully captured through a linear model [2, 8]. Especially the fact that the warm regions of this process are found at the bottom while the colder ones are located at the top of the plant leads to strong convection phenomena which cannot be neglected. Hence, one has to switch to nonlinear multi-dimensional time dependent models which are more complicated to handle. Above all, the Cz process is a system with free boundaries (the solid–liquid interface and the crystal shape) making it even more complicated to solve the underlying dynamic equations. Many unknown physical parameters and the complex structure of the inner assemblies worsen the situation. Here, from a control technological point of view, one has to find a balance between accuracy and real time capability of the model [21, 30].

### 2.5. Stability

An important matter in control theory is the question if the system under consideration is stable or not, since unstable systems have a limitation to achievable control performance. When discussing this subject it is very important which type of model is used for stability analysis and which physical effects are included in the model: Surek's initial stability analysis was only of the capillary problem, i.e., for the meniscus region [49]. He came to the conclusion that the capillary system is unstable. However, if the heat fluxes are taken into account, one comes to a different conclusion, depending on the assumptions made during modeling. Thus, Refs. [39, 50–52] as well as [53] show stable behavior of the growth system under certain operating conditions. Nevertheless, Refs. [54] and [55] show that the system is unstable for the cases they evaluated, even if the thermal effects are included in the analysis.

## 3. Components of a control system

The intention of this section is to introduce some of the basic concepts used in control technology as far as they are required for an understanding of the numerous strategies for control of the Cz process. For this purpose the essential components of a control system are shortly summarized (cf. Fig. 4) followed by a discussion of the way mathematical models are used for control purposes, which differs from the way they are used for thermal analysis or plant and process design.

### 3.1. Reference trajectory generator

Depending on time or crystal length a *reference trajectory generator* calculates reference values for crystal radius and growth rate or other useful quantities. In the simplest case the trajectory generator holds a fixed value, often called the setpoint or "hand value". Planning of trajectories has to consider the physical properties of the system in order to avoid, e.g., impossible values for the control inputs. Furthermore, one cannot request physically impossible behavior from the system, such as steps in any of the system quantities or their derivatives.

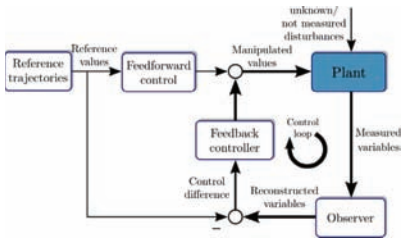


Fig. 4. Sketch of a modern feedback control loop.

It may be useful to reschedule the reference trajectories during growth to guarantee smooth behavior of the controller.

### 3.2. Feed-forward controller

The *feed-forward control* calculates the manipulated values (like heater power or crystal pulling rate) from the reference values generated by the trajectory generator. This can be done empirically or by means of a mathematical model describing the system behavior. The latter strategy is also known as the solution of the *inverse problem*, in contrast to the *forward problem* which consists of the solution of a dynamic model depending on given initial values and given trajectories for the inputs. For example, one has a system with the manipulated variable $u \in \mathbb{R}$, the output variable (to be controlled) $y \in \mathbb{R}$ and two internal states $x_1, x_2 \in \mathbb{R}$. Its dynamics is captured by the following model:

$$\dot{x}_1 = x_2, \tag{2a}$$

$$\dot{x}_2 = x_1^2 + (x_2 + 2)u, \tag{2b}$$

$$y = x_1. \tag{2c}$$

From this model a model based feed-forward control can be easily calculated. Solving Eq. (2b) for $u$ one obtains

$$u = \frac{\dot{x}_2 - x_1^2}{x_2 + 2}. \tag{3}$$

Now, one would like to steer the system, namely the output $y$, along a reference trajectory $t \mapsto y_{\mathrm{ref}}(t)$. This reference trajectory is assumed to be twice continuously differentiable, i.e., $\dot{y}_{\mathrm{ref}}(t)$, $\ddot{y}_{\mathrm{ref}}(t)$ exist. Since according to system (2) one has $x_1 = y$, $x_2 = \dot{x}_1 = \dot{y}$, and $\dot{x}_2 = \ddot{y}$ the resulting reference trajectory for the manipulated variable $u$ reads (cf. Eq. (3)):

$$u_{\mathrm{ref}} = \frac{\ddot{y}_{\mathrm{ref}} - y_{\mathrm{ref}}^2}{\dot{y}_{\mathrm{ref}} + 2}. \tag{4}$$

Using the values from the feed-forward control one might be able to *steer* the system along its reference trajectory if the system is stable, only small perturbations are acting on the system, and the model is accurate enough.

### 3.3. Feedback controller

The *feedback controller* compensates for disturbances acting on the process. Furthermore, it is responsible for

correction of modeling errors resulting in inaccuracies of the feed-forward control. This is achieved by feedback of the measured variable (or its estimate) and a correction of the input calculated by the feed-forward control.

It is common practice to realize feedback control by means of a PID controller. The PID controller processes a deviation $e(t)$ between the desired and the real value of the variable to be controlled in order to calculate a change $\Delta u(t)$ of the manipulated variable

$$\Delta u(t) = K_{\mathrm{P}} e(t) + K_{\mathrm{I}} \int_{t_0}^{t} e(\tau)\mathrm{d}\tau + K_{\mathrm{D}} \frac{\mathrm{d}e}{\mathrm{d}t}(t). \qquad (5)$$

The dynamic behavior of the PID controller is determined using the three real constants $K_{\mathrm{P}}$, $K_{\mathrm{I}}$, and $K_{\mathrm{D}}$. It is an implementation of the following natural assumptions: (i) The larger the control deviation, the larger one has to counter steer, an implication which is covered by the proportional part $K_{\mathrm{P}} e(t)$. (ii) The longer the control deviation is pending, the larger the manipulated variable has to be changed in order to reduce it. This behavior is realized by the integral part parameterized using the factor $K_{\mathrm{I}}$, the second term in Eq. (5). (iii) The faster the control deviation changes, the stronger one has to counteract — this is covered by the third term in Eq. (5) — the differential part with parameter $K_{\mathrm{D}}$.

The PID controller has several advantages: its operating principle is simple, it can be easily implemented, if certain conditions are hold it can be adjusted using some simple rules, it is suitable for a wide range of technological systems found in practice. However, there are some drawbacks: it is a linear controller. This means that its parameterization is adjusted for a certain operating point of the process. If one does not have an operating point (as it is the case in the Czochralski growth, cf. Sect. 2.3), parameters have to be continuously changed during the growth. The same holds for an intentionally initiated change of the operating point during the process. The performance of PID controllers is limited if the system shows nonlinear behavior. The reason for this is the fact that a change of the manipulated variable is processed nonlinearly in the process resulting in "unexpected" reactions (in comparison to a linear one) of the system. Situation worsens if the system contains time delays. In this case a reaction of the system to a change of the manipulated variable appears delayed by the delay time $\tau$. This may result in an undamped increasing integral of the PID algorithm (cf. Eq. (5)). In the Czochralski crystal growth the LEC process with its boron-oxide layer covering the melt belongs to the class of delay systems. In summary, a PID controller does not necessarily fit the dynamics of the system, especially if the order of the system is larger than two. Therefore, it may be very time consuming to find appropriate parameters. Consequently, the performance of diameter control based on the use of linear PID controllers, the parameters of which are chosen heuristically, is limited [8, 43, 56, 57].

Fortunately, theory and application of control systems have been developed very rapidly in the last decades. Increasing capacity of micro-controllers and programmable logic controllers (PLC) combined with powerful mathematical control design methods prepared the ground for the use of sophisticated model based controllers in practice. A model based controller uses a mathematical model of the system, i.e., its structure and parameters fit to the system. This means that the controller can be used in a wide range of operating points and reflects the nonlinear system characteristics as well as time delays. In addition, parameterization effort is dramatically reduced. Anyhow, although model based control sounds promising, such controllers do show good performance only if the underlying model matches the structure and the parameters of the system appropriately. It will be shown in the following sections that this fact is the crucial point when trying to enhance the capability of conventional control systems.

In order to make the strategy of model based control more clear, the design of a simple nonlinear feedback controller based on a lumped parameter model is sketched. Again, the system (2) of the previous section is used. One wants to make the output $y$ follow a reference trajectory $y_{\mathrm{ref}}(t)$. For this one defines the tracking error $y - y_{\mathrm{ref}}$. Now the controller is designed in such a way that the tracking error satisfies the linear second order differential equation

$$(\ddot{y} - \ddot{y}_{\mathrm{ref}}) + k_1(\dot{y} - \dot{y}_{\mathrm{ref}}) + k_0(y - y_{\mathrm{ref}}) = 0 \qquad (6)$$

with $k_0, k_1 > 0$.

The values of $y_{\mathrm{ref}}$, $\dot{y}_{\mathrm{ref}}$, and $\ddot{y}_{\mathrm{ref}}$ are defined by the reference trajectory. If one desires the dynamics of the tracking error to satisfy Eq. (6) the second time derivative of the output $y$ *must* behave as

$$\ddot{y} = \ddot{y}_{\mathrm{ref}} - k_1(\dot{y} - \dot{y}_{\mathrm{ref}}) - k_0(y - y_{\mathrm{ref}}). \qquad (7)$$

This can be achieved by a proper choice of the input $u$ because by inserting the right hand side of (7) in the equation used for calculation of $u$ (cf. Eq. (3)) one obtains

$$u = \frac{\dot{x}_2 - x_1^2}{x_2 + 2} = \frac{\ddot{y} - y^2}{\dot{y} + 2}$$

$$= \frac{\ddot{y}_{\mathrm{ref}} - k_1(\dot{y} - \dot{y}_{\mathrm{ref}}) - k_0(y - y_{\mathrm{ref}}) - y^2}{\dot{y} + 2}. \qquad (8)$$

This equation determines the manipulated variable $u$ in such a way that the tracking error satisfies the given error dynamics (6). The coefficients $k_0, k_1$ in Eq. (6) are the controller parameters, the real value inputs are $y, \dot{y}$, and the desired value inputs are $y_{\mathrm{ref}}, \dot{y}_{\mathrm{ref}}, \ddot{y}_{\mathrm{ref}}$. The coefficients $k_0, k_1$ define the dynamical behavior of the tracking error, i.e., the way the error converges to zero (e.g. fast with an overshooting or slowly creeping).

### *3.4. State estimator*

Finally, it is not always possible to measure the controlled variable (in case of the Czochralski method the radius) directly. In that case one can reconstruct this variable from the measured variable by means of a (possibly nonlinear) *observer* if a suitable model of the sys-

tem is available and the system is observable (a system property discussed later).

In order to overcome this difficulty one has to reconstruct the crystal radius from the measured force. This can be done by a so-called "observer". It is based on the following idea. Assume a mathematical model

$$\dot{x}(t) = f_1(x(t), u(t)),\ y(t) = f_2(x(t), u(t)),\ x(0) = x_0$$

of a process with $(x(t), u(t)) \in \mathbb{R}^n \times \mathbb{R}^r$ and $y(t) \in \mathbb{R}^m$. If some components of $x$ are not directly measured, one might implement a "copy"

$$\dot{\hat{x}}(t) = f_1(\hat{x}(t), u(t)),\ \hat{y}(t) = f_2(\hat{x}(t), u(t)),\ \hat{x}(0) = \hat{x}_0$$

of the system model in a computer program. The trajectories of the manipulated variables $u$ acting on the real system are fed into this computer program, too. Then one has access to all components of $\hat{x}$. Since the initial values of $\hat{x}$ are not known, i.e., $\hat{x}_0 \neq x_0$, and because of model inaccuracies as well as disturbances acting on the system, generally the values calculated for $\hat{x}(t)$ will not be equal to the real values $x(t)$. However, under certain circumstances it is possible to inject the error $\hat{y} - y$ between the estimated value $\hat{y}$ and the measured value $y$ in such a way that the difference between the calculated value $\hat{x}$ and the real value $x$ will converge to zero as time advances [58]. In this case the system

$$\dot{\hat{x}}(t) = h\big(\hat{x}(t),\, u(t),\, \hat{y}(t) - y(t)\big), \quad \hat{x}(0) = \hat{x}_0,$$
$$\hat{y}(t) = f_2(\hat{x}(t), u(t))$$

is called an *observer*.

Design and dimensioning of the injection of the error related to the measured variable is the key task when developing an observer. However, it is important to know if it is possible to reconstruct a quantity from the measured variable at all. This property is commonly referred to as "observability".

*3.5. Modeling in crystal growth analysis and control*

A short comparison on how models are used in automatic control in contrast to numerical approaches in crystal growth will be given here, since between both fields the approaches and requirements differ quite a bit.

A mathematical model which takes the spatial distribution as well as the time dependence of material parameters into account leads to a system of coupled *partial* differential equations with the corresponding initial, boundary, and compatibility conditions. They belong to the so-called infinite dimensional or distributed parameter systems. Such systems are usually solved numerically using finite element methods (FEM). Using this approach one can obtain results reflecting the reality rather accurately. FEM is an absolutely essential resource in solving problems in plant design, thermal and stress analysis, etc. However, computational effort increases dramatically depending on the accuracy required, especially for solving *time dependent* problems.

The approach used in model based control is to keep the models as simple as possible. This is done in order to be able to run the models on the limited computer hardware usually available at the growth furnaces. This is achieved by partitioning the system under consideration into domains which may reasonably well be considered as homogeneous, i.e., the material parameters which are assumed to be constant. Heat and mass transfer between these domains are calculated from appropriate mass and energy balance equations. Since spatial dependence of the parameters is neglected, one ends up with a set of *ordinary* differential equations. Such models are called finite dimensional or lumped parameter models. Using such models one can calculate the basic system behavior leading to a qualitatively and quantitatively sufficient insight into the process. Powerful methods for controller and observer design, trajectory planning, and dynamic analysis exist for this class of models. The lack of accuracy can be admitted by the introduction of feedback.

A *global* lumped parameter model of the overall Czochralski crystal growth system was first presented by Steel and Hill [59]. In order to simplify and improve parameterization of PID controllers they analyzed a linearized model in terms of a transfer function in several growth stages. The central idea of their approach consists in partitioning the Czochralski system into the four areas: melt — meniscus — crystal — ambient. This is still the basis of all lumped parameter models of the Czochralski process used to date. Using their method an a priori controller design could be dramatically improved, thus, avoiding time consuming empirical parameterization of PID controllers. However, this requires sufficient accuracy of the model.

Analysis of steady state conditions, the dynamics of the process, and optimal control design using lumped parameter models (in terms of a state space model) is subject of investigations presented by Satunkin and Rossolenko for the standard Cz process [20] as well as for the LEC process [60]. Considerations of optimal reference trajectory planning based on such models has been given by the same author in [61]. A compilation and extension of these results is presented in [31].

A very comprehensive and detailed model based analysis of the global Czochralski system is presented by Gevelber et al. [17, 43, 56, 57]. The first two publications of this series are based on a 7th order lumped parameter model of the process while the latter ones make use of a more refined model.

Thorough analysis approaches based on distributed parameter models (treated for the quasi-stationary case) have been presented by Derby et al. [18, 19, 62, 63]. The great advantage of these approaches is the fact that the heat flow in the plant can be modeled quite accurately. However, much effort is necessary to adapt the models to the actual plant design and to determine the physical parameters needed in the model with sufficient accuracy.

## 4. Approaches for control of the Cz process

*4.1. State estimation*

In case of the Czochralski crystal growth the measurement of the crystal diameter, the primary variable to be controlled, is quite a complex task. Three different approaches exist:

1. Optical capturing of meniscus shape, typically by detecting the bright meniscus ring [16, 41, 64, 65].
2. Evaluation of the force acting on a load cell mounted at the top of the pulling rod [15, 32, 34–36]. Also weighing of the crucible is possible [66, 67].
3. Image processing of the whole crystal [68, 69].

Optical imaging of the bright meniscus ring, which results from reflections of light emitted by the heaters, is the most important measuring technique used in silicon crystal growth. Here, one has to take into account that what is measured is the diameter of the meniscus at a certain height, not the crystal diameter at the three phase boundary. This means that the anomaly (cf. Sect. 2.2) comes into play: if the crystal radius begins to decrease, first the meniscus height will increase. This means that the diameter of the bright meniscus ring will increase which might result in incorrect reactions of the controller if it is not adapted to this behavior [17]. A detailed discussion on how to obtain an estimate of the real crystal diameter from the camera system is given in [70, 71].

In case of the liquid encapsulated Czochralski process where melt and meniscus are covered by a layer of boron oxide only the second technique can be applied. It is also often used when no camera system for the detection of the bright meniscus ring is available or applicable. It is based on the following idea: the gravitational force $F_c$ of a rotationally symmetric crystal of length $l$ and density $\rho_s$ can be calculated by integration of

$$F_c = \pi g \rho_s \int_0^l r_i^2(\lambda)\,\mathrm{d}\lambda \tag{9}$$

with crystal radius $r_i$ and gravitational acceleration $g$. Actually the force measured by the load cell is not equal to $F_c$ in Eq. (9). In fact it is also influenced by forces resulting from the surface tension of the meniscus, the hydrostatic pressure of the melt raised over the melt level, and in case of LEC by the buoyancy forces resulting from the liquid boron oxide. For this reason things become considerably more complicated as it might seem from a first glance on Eq. (9). Details are discussed in [22].

The reconstruction of the crystal diameter and other quantities by means of an observer (cf. Sect. 3.4) is the subject of several publications. Satunkin and Leonov discuss the question of observability in case of Cz and LEC growth in [44]. The discussion is based on a linearized model of the overall process which is bound to the knowledge of some thermodynamical parameters. An elegant approach is presented in [72, 73] where, roughly speaking, an iterating algorithm is used which fits the theoretically calculated mass of the load cell to its real value by heuristically changing the crystal diameter in every step. However, this algorithm contains a parameter which must be empirically determined to guarantee convergence. A reduced order nonlinear tracking observer for the Cz and the LEC system including full meniscus dynamics is presented in [22]. As far as the system is tracked along its reference trajectory this approach produces very accurate results.

If the influence of the changing meniscus can be more or less neglected, a simple approach is presented in [74, 75]. Here the basic idea is to exclude the meniscus dynamics from the model making it easy to solve the remaining equations for the radius. This method is useful for reconstruction of the radius during cylindrical growth and for crystals with slowly increasing diameter in the cone. If one is obliged to grow crystals with large slope angles in the shoulder this method fails, especially when fading into the cylinder.

The third method has no technological relevance because, on the one hand, it is very complicated to be realized and, on the other hand, because changes in growth are detected when they have already influenced the crystal (which is actually not the case when using the first and second technique where changes in the meniscus preceding a change in the crystal are detected) [76].

### *4.2. Feed-forward control*

As described in Sect. 3.2, feed-forward control is an essential part of the overall control system. In crystal growth, a common method in practice is to determine the feed-forward control by careful analysis of repeated growth runs, resulting in a trajectory for the control inputs which can then be used as part of the recipe.

While this method is widely accepted it suffers from the fact that it is extremely time consuming and, thus, expensive, but functions if the same conditions are repeated and there are no significant variations from run to run. However, any change in plant setup or change in desired crystal cylinder diameter means repeating this procedure. Finally, not all details of the system dynamics can be determined by this empirical approach. If a sufficiently exact model of the process is available, this model can be used as a basis for determining proper feed-forward control trajectories which then can be fine-tuned in an empirical manner afterwards.

Such lumped parameter approaches are presented in [45] (4″ silicon), [75] (InP), and [77]. Since the underlying models neglect the spatial distribution of system properties (cf. Sect. 3.5) most often some empirical corrections (e.g. in [75]) are introduced to fit the result to reality. An approach trying to circumvent this problem is proposed in [78], basing on a mathematical description regarding the most important qualitative dependences between the relative changes of manipulated and controlled variables during growth. For a certain thermal setup this approach allows to easily calculate reference trajectories for different crystal shapes and growth rates.

In order to overcome such limitations one may describe the system behavior without neglecting the spatial dependence of some of the system properties. Then one is confronted with the problem of numerically solving a set of time dependent 2D/3D partial differential equations with free boundary conditions. Even though powerful finite element methods for solving such problems exist, and computational performance has dramatically

increased in the last years this still is one of the most challenging tasks [79]. The situation gets even worse if feed-forward trajectories need to be rescheduled in real time during growth, for instance in order to react to some perturbations [80]. Extensive studies on this task can be found in [81–84], presented for the examples of growth of large diameter silicon and germanium crystals.

In order to reduce the computational effort one might restrict the problem to the quasi-stationary case. The feed-forward trajectory is then generated piecewise. This very powerful strategy has been presented in detail by Derby and Brown in [18, 19]. An approach using a simplified 2D-model especially designed for control purposes can be found in [85].

*4.3. PID based control using optical diameter estimation*

In Refs. [16, 41] a method for determining an estimate of the crystal radius is presented using optical imaging. The idea is based on the fact that light emitted by the red-hot heaters is reflected in upward direction from the meniscus. These reflections can be seen and detected by an optical camera as a so-called "bright ring". Then, image processing software is able to determine the diameter of the ring in real time. This value, scaled by an empirically determined factor accounting for the difference between measured meniscus and expected crystal radius, is used as the measured variable in the control system. Since silicon has a large Laplace constant (i.e., high surface tension and low density resulting in large meniscus heights) and because of its metallic reflectivity this material is an obvious candidate for this technique. Hence, although the crystal radius itself is not measured, this technique is widely and successfully used especially in silicon Cz growth [65, 86].

When designing a control system which tracks crystal diameter and growth rate (cf. Sect. 1) one has to reflect the different time constants the available control inputs have on the system: (i) Changes in pulling speed are affecting the system quite quickly; (ii) changes in heater power need some time depending on the thermal conditions occurring in the system [17, 43]. Therefore, most often a cascaded control structure is chosen, assuming that pulling speed $v_\mathrm{p}$ is more or less equal to the growth rate (cf. Fig. 5) [87].

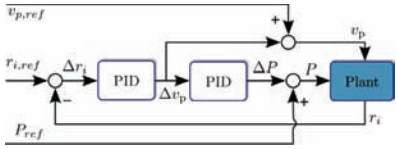


Fig. 5. Cascaded PID based control scheme utilizing pulling speed and heater power for diameter control (according to [87]).

Deviations $\Delta r_\mathrm{i}$ from the reference value $r_\mathrm{i,ref}$ of the crystal radius $r_\mathrm{i}$ are fed into a PID controller manipulating the reference value $v_\mathrm{p,ref}$ of the pulling speed by an amount of $\Delta v_\mathrm{p}$. This value, indicating a deviation of the real pulling speed trajectory from its pre-calculated reference value, is also fed into a second PID controller manipulating the reference value $P_\mathrm{ref}$ of the heater power by an amount $\Delta P$. By this strategy it is ensured that the system is able to react quite quickly on perturbations occurring in crystal diameter. Accumulated deviations in the pulling speed trajectory lead to a change of the heater power trajectory, ensuring that the system is kept on its reference state in a long term manner. Especially the pulling speed is brought back to its reference.

This control approach requires very careful planning of the feed-forward trajectories, especially for the pulling speed needed to obtain a certain growth rate trajectory.

*4.4. PID based control using weight measurement*

If one does not have the possibility to capture the diameter of the bright meniscus ring, the usual control strategy is to use the crystal or the crucible "weight" as measured variable [15, 88]. The basic idea is to measure the force acting on the pulling or crucible rod and to compare it with the required force resulting from the reference shape of the crystal [32]. The deviation between both values is used to drive a PID controller manipulating the heater power. Crystal weighing is preferred due to problems of evaporation of material from the charge and the crucible in case of crucible weighing. When using rf-heaters additional vertical forces induced in the susceptor come into play also [86].

*4.4.1. Control system design*

In Fig. 6 the structure of a weight based control system is sketched. One has to distinguish between two modes of operation [86]:

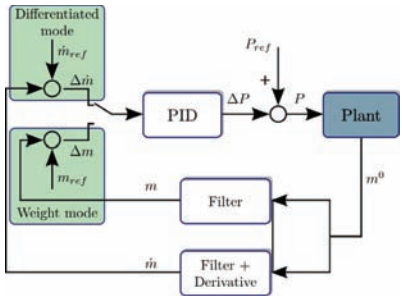


Fig. 6. Weight based PID control scheme utilizing heater power for diameter control.

*Weight mode.* The weight measured by the load cell is compared to the reference value and the difference is used as an error signal for the PID controller. Hence, in this mode the controller tries to keep the weight on its reference value, meaning that a previous error in crystal radius later results in an error of opposite sign. Thus, oscillations may occur. However, this mode circumvents

noise generation by numerical differentiation of the force raw signal as required in differentiated weight mode.

*Differentiated weight mode.* The force raw signal is differentiated with respect to time and then compared to the reference value resulting from the predefined shape of the crystal. If one neglects the dynamics of the meniscus this signal is proportional to the crystal radius, i.e., this mode tries to keep the radius on its reference value without being influenced from the past. The differentiation of the raw signal leads to a phase advance in the control system which tends to make the system "more stable". On the other hand, sophisticated signal processing and filtering methods as well as high resolution load cells are required.

The most crucial part in this technique is the *anomalous* behavior of the signal, cf. Sect. 2.2. The consequence of this anomaly is that the performance of the control system is fundamentally limited. The controller "is only allowed to respond carefully" to any sort of perturbation since they could be of opposite direction not indicating what really goes on at the interface. For example, if the radius of the crystal increases, the controller would have to increase heater power in order to counteract this perturbation (i.e., the parameters $K_\mathrm{P}, K_\mathrm{I}, K_\mathrm{D}$ of the controller (5) must be chosen positive). However, what is first detected in this case is a decrease of the differentiated weight gain signal leading the controller to decrease heater power, thus countenancing the increase of the crystal radius.

*4.4.2. Improvements and optimizations*

In this section some approaches trying to compensate the problems mentioned above are sketched.

In Refs. [35, 36] Bardsley et al. present a sophisticated control algorithm containing a method trying to overcome the problems resulting from the anomalous behavior. They try to estimate the anomalous components in the measured weight gain signal and subtract them from the signal. The estimation is done using a linear model calculating the radius change $\delta r_\mathrm{i}$ induced by changes in heater power. This value can be used for calculating an estimate of the anomalous component of the signal. Experimental results presented in [33] demonstrate the performance of this approach. However, it is restricted to the knowledge of a sufficiently precise model of the process, especially of the thermal conditions in the furnace.

A challenging task in this control approach is the choice of the parameters of the PID controller. Most often this is done by trial and error. However, there exist some interesting approaches trying to determine optimal parameters of the PID controller on the basis of the model knowledge available. Satunkin et al. [20, 44] proposes an approach based on a cost functional for adjusting parameters in a single as well as in a multi-loop control system utilizing heater power and pulling speed as manipulated variables. The same authors present in [44] a modeling approach focusing on inaccuracies of the weight sensor and the consideration of these in the control system. Another model based approach can be found in [89].

As already mentioned the dynamic characteristic of the process changes during crystal growth. As a consequence parameters of the PID controller determined for one setpoint may not produce acceptable results as the process proceeds. The strategy to overcome this problem is to change the parameters on relevant intervals. This strategy is commonly known as *parameter* or *gain scheduling* in the field of adaptive control [90, 91]. An approach for Cz growth can be found in [89].

### *4.5. Model based control*

*4.5.1. Lumped parameter model based control*

In Refs. [17, 43, 56, 57] Gevelber et al. propose a model based multi-loop control system. The first two publications of this series are based on a 7th order model of the process, while the latter ones make use of a more refined model of order 34. In these publications a multi--loop control system is proposed in order not only to ensure a correct diameter during the process, but also in order that identifiable disturbances are compensated before they affect the growth dynamics. Two main disturbances are identified, both related to the melt drop: the thermal state of the melt, which changes the heat flux entering the interface, and the thermal environment that the crystal sees, affecting the heat flux from the interface and thus the growth dynamics.

By adding, for instance, a closed loop around the melt temperature, the impact of this disturbance is significantly reduced, enabling tighter control of diameter and thus minimizing growth rate variations in a robust manner (e.g. not sensitive to model error or process variations). Additionally, this work analyzes the importance of controlling interface shape in addition to crystal diameter, in terms of meeting additional control objectives such as keeping thermal stress below a limit in order to minimize dislocation defects. Controlling interface shape in addition to diameter, requires the use of additional actuators, and an important part of the design task is to select an actuator set that can control both degrees of freedom relatively independently. To further obtain design insight Gevelber et al. derive a model which especially reflects the influence of radiation heat transfer within the furnace as exactly as possible within a lumped parameter model.

Another approach is presented in [21, 22]. There, the fact that it is easy to derive a sufficiently precise model of the pure meniscus dynamics in contrast to the fact that such a model of the thermal behavior is not available is utilized. Using a model of the meniscus dynamics a model based controller calculates desired values $v_{\mathrm{z,ref}}$ of the ratio between pulling speed and growth rate quite similar to the approach presented in Sect. 3.3. Since one lacks a model of the thermal behavior, PID controllers are placed around this model based controller transforming this intermediate value into the inputs pulling speed $v_\mathrm{p}$ and heater power $P$ available at the process. This approach is sketched in Fig. 7. By this strategy a large amount of lumped parameter model knowledge is introduced into the control system.

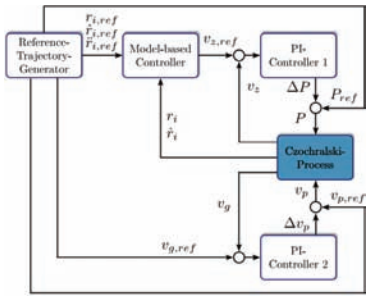


Fig. 7. Combination of model based and PID control according to [21, 22].

Further model based approaches can be found in [31] (using a linear state space controller), in [85] (using a 2D-approximation), and in [92] (combining heuristic and deterministic techniques in the 4″ growth of GaAs crystals using the LEC method).

In all cases discussed in this section the overall closed loop performance is considerably enhanced, however, because of the lumped parameter character, some more or less strict constraints exist with respect to process setup, model validation or trajectory planning.

*4.5.2. Distributed parameter model based control*

Some publications try to overcome the limitations resulting from the lumped parameter approach by directly working on the partial differential equations of the distributed parameter models. Such approaches are for example presented by James Ng et al. in [93–95] and Wang in [96] and are fundamentally important for understanding the dynamics of the process, especially when focusing on the effects related to heat transport phenomena or variable phase boundary problems. However, for an implementation under real world conditions and controller parameterization they are not suitable. The reason for this is that in these models the manipulated variables are also spatially distributed, e.g. a temperature distribution on the heater surface. But: what the controller actually manipulates is the current entering the heater which is a lumped quantity which is in an unknown way connected to the temperature distribution on the heater surface.

*4.5.3. Model predictive control*

A third model based approach is the so-called model predictive control which is often used in process technology. Roughly speaking, model predictive control makes use of a dynamic model of the process, too. However, the way of calculating values for the manipulated variable is based on optimization methods, cf. Fig. 8. The solution of such optimization problems is well known and widely used in mathematics. For this purpose, in each time step the set of control activities recorded so far is evaluated in order to predict the values of the manipulated variable over a finite prediction horizon — based on the mathematical model and using optimization criteria. The optimization criteria, in some sense the "parameters" of a model predictive controller, reflect, for example, the dynamics of the deviation between desired and real values [97, 98]. The advantage compared to the approaches presented in the previous section is that the underlying models can be arbitrarily complex. The disadvantage is the enormous computational effort. One has to keep in mind that for computing a new setpoint value of the manipulated variable several time dependent solutions of the model are required.

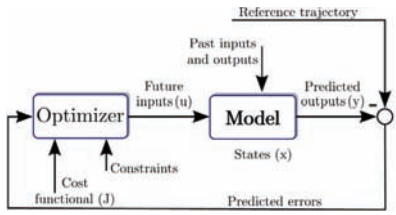


Fig. 8. Model predictive control.

An interesting approach based on this strategy can be found in [99, 100]. The model used in this approach is of lumped parameter type. It includes melt convection, which requires very strict assumptions to be fulfilled in order to make the model applicable. Another approach to establish such a model based control on the basis of a lumped parameter model has been published by Voronkov et al. [12, 87]. It is closely related to the $v_g/G$ theory [7, 10] which requires very precise tracking of the growth rate $v_g$.

### *4.6. Further references*

So far, the challenges and some of the fundamental strategies for controlling the Czochralski crystal growth process have been presented. Unfortunately, because of the limited space available in this special issue, many details had to be skipped in the discussion. For this reason the reader is referred to much more exhaustive presentations of these subjects in [31, 73, 101–103].

## 5. Conclusion

The contribution gives a brief overview of selected strategies for the control of the Czochralski process. Although a large variety of approaches exist, the control of this process continues to be a challenging task employing scientists and engineers all around the world. By the very nature of the process, model based control is required to further improve yield and quality of the crystals. However, the choice of an appropriate model is crucial in this respect. These models must be simple enough and should yet cover the main dynamics. For the meniscus dynamics existing lumped parameter models are sufficient for very good control results. However, further progress may be

expected from improved models of the thermal dynamics. These models should to a sufficient extent account for the spatially distributed nature of the heat transport phenomena, but they must still be simple enough to be useful for on-line control and estimation under industrial conditions.

## References


[1] M. Cole, R. Ware, M. Whitaker, in: *Proc. 5th Int. Conf. on Cryst. Growth, Boston 1977*, 1977, Abstract 132.

[2] D. Hurle, G. Joyce, M. Ghassempoory, A. Crowley, E. Stern, *J. Cryst. Growth* **100**, 11 (1990).

[3] M. Neubert, P. Rudolph, *Prog. Cryst. Growth Charact. Mater.* **43**, 119 (2001).

[4] S. Motakef, K. Kelly, K. Koai, *J. Cryst. Growth* **113**, 279 (1991).

[5] A. Jordan, R. Caruso, A. von Neida, J. Nielsen, *J. Appl. Phys.* **52**, 3331 (1981).

[6] A. Jordan, A. von Neida, R. Caruso, *J. Cryst. Growth* **70**, 555 (1984).

[7] V.V. Voronkov, *J. Cryst. Growth* **59**, 625 (1982).

[8] M. Gevelber, G. Stephanopoulos, *J. Cryst. Growth* **84**, 647 (1987).

[9] D. Hurle, in: *Sir Charles Frank, OBE, FRS: An 80th Birthday Tribute*, Eds. R. Chambers, J. Enderby, A. Keller, A. Lang, J. Steeds, Adam Hilger, Bristol 1991, p. 188.

[10] R. Falster, V. Voronkov, *Mater. Res. Soc. Bull.* **73**, 28 (2000).

[11] M. Gevelber, D. Wilson, N. Duanmu, *J. Cryst. Growth* **230**, 217 (2001).

[12] V. Voronkov, P. Mutti, US patent No's US 2002043206 and US 6726764 (2004).

[13] G. Teal, J. Little, *Phys. Rev.* **78**, 647 (1950).

[14] L. Roth, W. Taylor, *Proc. Inst. Radio Eng.* **40**, 1338 (1952).

[15] J. Levinson, US Patent No. 2,908,004, October 6th 1959 (1959).

[16] E. Patzner, R. Dessauer, M. Poponiak, *Solid State Technol.* **10**, 25 (1967).

[17] M. Gevelber, M. Wargo, G. Stephanopoulos, *J. Cryst. Growth* **85**, 256 (1987).

[18] J. Derby, R. Brown, *J. Cryst. Growth* **74**, 605 (1986).

[19] J. Derby, R. Brown, *J. Cryst. Growth* **75**, 227 (1986).

[20] G. Satunkin, S. Rossolenko, *Cryst. Res. Technol.* **21**, 1125 (1986).

[21] J. Winkler, M. Neubert, J. Rudolph, *J. Cryst. Growth* **312**, 1005 (2010).

[22] J. Winkler, M. Neubert, J. Rudolph, *J. Cryst. Growth* **312**, 1019 (2010).

[23] J. Mullin, B. Straughan, W. Brickell, *J. Phys. Chem. Solids* **26**, 782 (1965).

[24] D. Looze, A. Farzin, B. Bernstein, *J. Cryst. Growth* **148**, 79 (1995).

[25] A. Jordan, R. Caruso, A. von Neida, *Bell System Tech. J.* **62**, 477 (1983).

[26] T. Johansen, *J. Cryst. Growth* **80**, 343 (1987).

[27] K. Azuma, Jap. Patent No. 60-11299 (1983).

[28] P. Rudolph, M. Neubert, S. Arulkumaran, M. Seifert, *Cryst. Res. Technol.* **32**, 35 (1997).

[29] M. Neubert, P. Rudolph, *Mitteilungsblatt der DGKK* **69**, 11 (1999) (in German).

[30] *Crystal Growth Techniques Based on Capillary: Czochralski, Floating Zone, Shaping and Crucible Process*, Ed. T. Duffar, Wiley, Hoboken 2010.

[31] G. Satunkin, *Prog. Cryst. Growth Character. Mater.* **56**, 1 (2010).

[32] W. Bardsley, G. Green, C. Holliday, D. Hurle, *J. Cryst. Growth* **16**, 277 (1972).

[33] W. Bardsley, F. Frank, G. Green, D. Hurle, *J. Cryst. Growth* **23**, 341 (1974).

[34] W. Bardsley, B. Cockayne, G. Green, D. Hurle, G. Joyce, J. Roslington, P. Tufton, H. Weber, *J. Cryst. Growth* **24/25**, 369 (1974).

[35] W. Bardsley, D. Hurle, G. Joyce, *J. Cryst. Growth* **40**, 13 (1977).

[36] W. Bardsley, D. Hurle, G. Joyce, G. Wilson, *J. Cryst. Growth* **40**, 21 (1977).

[37] E. Boucher, T. Jones, *J. Chem. Soc. Faraday Trans.* **176**, 1419 (1980).

[38] K. Mika, W. Uelhoff, *J. Cryst. Growth* **30**, 9 (1975).

[39] T. Surek, S. Coriell, B. Chalmers, *J. Cryst. Growth* **50**, 21 (1980).

[40] J. Brice, *J. Cryst. Growth* **2**, 393 (1968).

[41] T. Digges, R. Hopkins, R. Seidensticker, *J. Cryst. Growth* **29**, 326 (1975).

[42] T. Johansen, *J. Cryst. Growth* **118**, 353 (1992).

[43] M. Gevelber, G. Stephanopoulos, M. Wargo, *J. Cryst. Growth* **91**, 199 (1988).

[44] G. Satunkin, A. Leonov, *J. Cryst. Growth* **102**, 592 (1990).

[45] K. Kim, A. Kran, P. Smetana, G. Schwuttke, *J. Electrochem. Soc.* **130**, 1156 (1983).

[46] N. Duanmu, Ph.D. Thesis, College of Engineering, Boston University, 2006.

[47] T. Johansen, *J. Cryst. Growth* **84**, 609 (1987).

[48] T. Johansen, *J. Cryst. Growth* **123**, 188 (1992).

[49] T. Surek, *J. Appl. Phys.* **47**, 4384 (1976).

[50] V. Tatarchenko, E. Brener, *J. Cryst. Growth* **50**, 33 (1980).

[51] G. Babkin, E. Brener, V. Tatarchenko, *J. Cryst. Growth* **50**, 45 (1980).

[52] D. Hurle, *J. Cryst. Growth* **128**, 15 (1993).

[53] J. Derby, R. Brown, *J. Cryst. Growth* **83**, 137 (1987).

[54] A. Crowley, *IMA J. Appl. Math.* **30**, 173 (1983).

[55] T. Johansen, *J. Cryst. Growth* **114**, 27 (1991).

[56] M. Gevelber, *J. Cryst. Growth* **139**, 286 (1994).

[57] M. Gevelber, *J. Cryst. Growth* **139**, 271 (1994).

[58] D.G. Luenberger, *IEEE Trans. Milit. Elec.* **8**, 74 (1964).

[59] G. Steel, M. Hill, *J. Cryst. Growth* **30**, 45 (1975).

[60] G. Satunkin, *J. Cryst. Growth* **154**, 172 (1995).

[61] G. Satunkin, S. Rossolenko, V. Kurlov, B. Reg'kin, V. Tatarchenko, A. Avrutik, *Cryst. Res. Technol.* **21**, 1257 (1986).

[62] J. Derby, R. Brown, *J. Electrochem. Soc.* **132**, 470 (1985).

[63] P. Thomas, J. Derby, L. Atherton, R. Brown, *J. Cryst. Growth* **96**, 135 (1989).

[64] U. Gross, R. Kersten, *J. Cryst. Growth* **15**, 85 (1972).

[65] R. Lorenzini, F. Nuff, D. Blair, *Solid State Technol.* **2**, 33 (1974).

[66] A. Zinnes, B. Nevis, *J. Cryst. Growth* **19**, 187 (1973).

[67] A. Valentino, C. Brandle, *J. Cryst. Growth* **26**, 1 (1974).

[68] H. van Dijk, C. Jochem, G. Scholl, P. van der Werf, *J. Cryst. Growth* **21**, 310 (1974).

[69] K. Bachmann, H. Kirsch, K. Vetter, *J. Cryst. Growth* **7**, 290 (1970).

[70] S. Kimbel, Ph.D. Thesis, Washington University, 2000.

[71] S. Kimbel, J. O'Sullivan, *Proc. SPIE* **4188**, 45 (2001).

[72] S. Rossolenko, I. Pet'kov, V. Kurlov, B. Red'kin, *J. Cryst. Growth* **116**, 185 (1992).

[73] N. Abrosimov, V. Kurlov, S. Rossolenko, *Prog. Cryst. Growth Charact. Mater.* **46**, 1 (2003).

[74] E. Kubota, *Cryst. Res. Technol.* **34**, 539 (1999).

[75] M. Masi, S. Carra, M. Polli, M. Ratti, G. Guadalupi, *Mater. Chem. Phys.* **66**, 236 (2000).

[76] G. Joyce, D. Hurle, Q. Vaughan, *J. Cryst. Growth* **132**, 1 (1993).

[77] H. Nalbandyan, *J. Cryst. Growth* **67**, 115 (1984).

[78] M. Neubert, J. Winkler, "Nonlinear Model-Based Control of the Czochralski Process IV: Feedforward Control", *J. Cryst. Growth*, submitted for publication.

[79] G. Brown, T. Kinney, P. Sackinger, D. Bornside, *J. Cryst. Growth* **97**, 99 (1989).

[80] A. Voigt, M. Metzger, "Numerical Simulation and Control of Industrial Crystal Growth by the Czochralski and Vertical Gradient Freeze Method", Caesar Preprint, August 2000.

[81] E. Dornberger, W. von Ammon, N. van den Bogaert, F. Dupret, *J. Cryst. Growth* **166**, 452 (1996).

[82] N. van den Bogaert, F. Dupret, *J. Cryst. Growth* **171**, 65 (1997).

[83] N. van den Bogaert, F. Dupret, *J. Cryst. Growth* **171**, 77 (1997).

[84] E. Olivari, P. Jacmin, N. van den Bogaert, V. Wertz, F. Dupret, *J. Cryst. Growth* **180**, 627 (1997).

[85] A. Sabanskis, K. Bergfelds, A. Muiznieks, T. Schröck, A. Krauze, *J. Cryst. Growth* **337**, 9 (2013).

[86] D. Hurle, *J. Cryst. Growth* **42**, 473 (1977).

[87] V. Voronkov, P. Mutti, U.S. Patent No. US 2002/0043208 A1 (2002).

[88] T. Rummel, Apparatus for pulling rod-shaped crystals of semiconductor material from a melt in a crucible, US Patent No. 3,259,467, July 5th 1966.

[89] M. Neubert, J. Winkler, *J. Cryst. Growth* **360**, 3 (2012).

[90] K.J. Åström, B. Wittenmark, *Adaptive Control*, Prentice Hall, Upper Saddle River (NJ) 1994, Ch. 9.

[91] *Industrial Digital Control Systems*, Vol. 37 of *IEEE Control Engineering Solutions*, Eds. K. Warwick, D. Rees, Peter Peregrinus Ltd., Stevenage 1988, Ch. 14.7.

[92] K. Riedling, *J. Cryst. Growth* **89**, 435 (1988).

[93] J. Ng, S. Dubljevic, *J. Proc. Contr.* **21**, 1369 (2011).

[94] J. Ng, S. Dubljevic, *Chem. Eng. Sci.* **67**, 111 (2012).

[95] J. Ng, I. Aksikas, S. Dubljevic, *Int. J. Contr.*, 1 (2013).

[96] P. Wang, *Optim. Contr. Appl. Meth.* **16**, 305 (1995).

[97] *Nonlinear Model Predictive Control*, Vol. 26 of *Progress in Systems and Control Theory*, Eds. F. Allgöwer, A. Zheng, Birkhäuser Verlag, Basel 2007.

[98] E. Camacho, C. Bordons, *Model Predictive Control*, *Advanced Textbooks in Control and Signal Processing*, Springer, Berlin 2004.

[99] R. Irizarry-Rivera, W.D. Seider, *J. Cryst. Growth* **178**, 593 (1997).

[100] R. Irizarry-Rivera, W.D. Seider, *J. Cryst. Growth* **178**, 612 (1997).

[101] J. Winkler, M. Neubert, J. Rudolph, N. Duanmu, M. Gevelber, *Crystal Growth Processes Based on Capillarity*, Wiley, 2010, p. 115.

[102] V.A. Tatarchenko, *Shaped Crystal Growth*, Vol. 20 of *Fluid Mechanics and its Applications*, Kluwer Academic, Dordrecht 1994.

[103] *Handbook of Crystal Growth*, Vol. 2: *Bulk Crystal Growth*, Ed. D.T.J. Hurle, North Holland Elsevier, Amsterdam 1994.

Special Anniversary Issue: Professor Jan Czochralski Year 2013 — Invited Paper

# Czochralski Growth and Properties of Scintillating Crystals

A. Yoshikawa[a,b,*], V. Chani[a] and M. Nikl[c]

[a]Institute for Materials Research, Tohoku University, 2-1-1 Katahira, Aoba-ku, Sendai 980-8577, Japan

[b]NICHe, Tohoku University, 6-6-10 Aoba, Aramaki, Aoba-ku, Sendai 980-8579, Japan

[c]Institute of Physics ASCR, Cukrovarnicka 10, 162 53 Prague, Czech Republic

The Czochralski method is one of the very few melt growth techniques that are industry friendly when considering the combination of quality, dimensions, and cost of the produced crystals suitable for their commercialization in scintillation detectors. This method is one of the oldest and most developed crystal growth processes regarding an adequate understanding the physical phenomena observed during solidification process and its practical expansion especially in the industrial scale production. It allows controllable formation of single-crystalline cylindrical ingots of various inorganic scintillation materials. The review summarizes recent progress on the Czochralski growth of a number of scintillation materials. The oxide crystals are mainly considered including the Ce and Pr--doped $RE_3Al_5O_{12}$, RE = Y, Lu, aluminum garnets and newly discovered ultraefficient Ce-doped $Gd_3(Ga,Al)_5O_{12}$ multicomponent garnet, high density $PbWO_4$ and $CdWO_4$ tungstates, Ce-doped $RE_2SiO_5$, RE = Y, Gd, Lu, oxyorthosilicates and $(Y,Lu)AlO_3$ aluminum perovskites and finally the classical $Bi_4Ge_3O_{12}$ scintillator. Additionally, the details of the growth of other practically important non-oxide crystals, namely the Ce and Eu-doped $LiCaAlF_6$ neutron and ultraefficient Ce-doped $LaBr_3$ scintillators, are discussed. The potential of novel micro-pulling down growth method is briefly described in the combinatorial search for new scintillator materials. Selected luminescence and scintillation characteristics including the spectra and decay kinetics, light yield and radiation resistance are also illustrated and overviewed.

DOI: 10.12693/APhysPolA.124.250

PACS: 81.10.Fq, 78.70.Ps, 29.40.Mc, 78.55.Hx

## 1. Introduction

Inorganic scintillating crystals are solid-state materials of high structural perfection that demonstrate scintillation (luminescence) after their excitation by some kind of ionizing radiation (vacuum ultraviolet (VUV), X-ray, or $\gamma$-ray), accelerated particles (electrons, alpha-particles, protons, or ions), or even neutrons. Absorbed energy of the incoming radiation and/or particles is transformed into the flash of light in near UV-visible spectral region. The ratio between the total emitted energy and energy of incoming high energy photon or particle defines the overall scintillation efficiency and can be at the best few tenths, but typically much less, see [1, 2]. The luminescent characteristics of the scintillating crystals are defined by (1) intrinsic centers in the material, i.e. that of undoped crystals or (2) extrinsic centers that are due to impurities or defects formed in the crystal structure. Generally, the dopants are foreign ions that substitute for the cations or anions of the host [3].

Single-crystalline scintillators coupled with photodetectors are used in many high-tech fields that include high-energy particle physics, medical imaging (positron emission tomography, PET and related systems that help to visualize parts of the human body), border security, astrophysics, geophysical resource examination, etc. [4]. Depending on the application, various combinations of physical and scintillation characteristics of the crystals are considered. However, generally the scintillating crystals have to possess high structural perfection, low content of non-desired impurities, reasonably uniform dopant distribution, and be produced with reasonable cost. Furthermore, high density (presence of heavy atoms in the structure) and maximum stopping power (high effective atomic number) are always desired to reduce dimensions of the detection elements and sensors. These requirements allow miniaturization of the devices and reduce the necessary size of the crystals to be grown.

Application of the crystal growth techniques that allow realistically fast growth of massive bulk crystals is always preferable in the industrial scale manufacturing process. The Czochralski (CZ) melt crystal growth is one of such techniques. However, this method cannot be used for any crystal. Congruent melting of the target material is one of the requirements that make application of this method possible and efficient. Table I illustrates list of selected scintillating crystals that are currently produced by the CZ method.

TABLE I

List of selected scintillating crystals.

| Crystal | Density | Melting point | Hygroscopicity | References |
|---|---|---|---|---|
| $Pr:Lu_3Al_5O_{12}$ | 6.71 | 1980 | no | [5, 6] |
| $Ce:Gd_3(Ga,Al)_5O_{12}$ | variable | | no | [7–9] |
| $PbWO_4$ | 8.28 | 1160 | no | [10–13] |
| $CdWO_4$ | 7.90 | 1325 | no | [14–15] |
| $Ce:Lu_2SiO_5$ | 7.4 | 2150 | no | [16–19] |
| $Ce:Y_2SiO_5$ | 4.45 | 2070 | no | [19] |
| $Ce:Gd_2SiO_5$ | 6.71 | 1900 | no | [19] |
| $Bi_4G_3O_{12}$ | 7.13 | 1050 | no | [20–22] |
| $Ce:LuAlO_3$ | 8.34 | ≈1900 | no | [1, 23, 24] |
| $Ce,Eu:LiCaAlF_6$ | 4.88 | 820 | no | [25–29] |
| $Ce:LaBr_3$ | 5.30 | 783 | yes, very high | [30–34] |

*corresponding author; e-mail: yoshikawa@imr.tohoku.ac.jp

The purpose of this review is to summarize recent success in CZ growth, details of the growth processes, and physical appearance and performance of number of important inorganic scintillating crystals of oxides and halides that have already been practically applied and used in the applications, particularly those listed above.

## 2. Inorganic scintillating crystals

Number of alkali metal halides, including most classical Tl:NaI and very recent Ce:$LaBr_3$ single crystals, together with other binary and complex halides demonstrate excellent scintillation performance. However, most of these materials are highly hygroscopic. Therefore, their practical application requires hermetic sealing to ensure their isolation from moisture in the surrounding. From this point of view the oxide crystals are more preferable considering the design of radiation detectors. Some of the prospective non-hygroscopic crystals are listed as follows: $CdWO_4$, $PbWO_4$, $Bi_4Ge_3O_{12}$, Ce:$Gd_2SiO_5$, Ce:$Lu_2SiO_5$, Ce:$Y_2SiO_5$, Ce:$LuAlO_3$, Pr(Ce):$Lu_3Al_5O_{12}$, Ce:$Gd_3(Ga,Al)_5O_{12}$, Eu(Ce):$LiCaAlF_6$, and $BaF_2$.

## 3. Czochralski crystal growth

The Czochralski crystal growth process, developed formerly for the growth of crystals of metals, is about a century old [35], but it is still one of the leading crystal growth methods. It is well recognized in academic research and industry. This technique allows controllable formation of single-crystal cylindrical ingots of various inorganic scintillating crystals. It can be also applied to the growth of organic crystals. The process is well established for the growth of semiconductors, oxides, fluorides, and other halide crystals as well as metals. In spite of its relative simplicity (Fig. 1), the process requires precise control of considerable number of factors that in different degree affect the crystal quality and commercial potential.

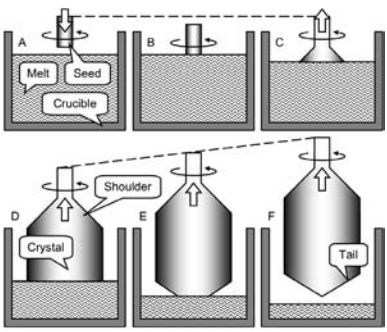


Fig. 1. Phases of typical Czochralski process including (A) approximation of the seed to the overheated melt, (B) immersion of the seed into the melt and their thermal equilibration, (C) pulling of the seed in upward direction with continuous increase of the crystal diameter and shoulder formation, (D) steady state of the pulling of the crystal of constant diameter, (E) ending the growth with continuous diameter decrease, and (F) separation of the crystal from the melt and its following cooling to room temperature.

TABLE II

Czochralski growth parameters.

| Item for control | Some factors to control |
|---|---|
| crucible | material composition, corrosion, melting point, shape and dimensions, contaminations, rotation, displacement, etc. |
| atmosphere | composition, pressure, flow rate, etc. |
| melt | composition, starting material treatment, evaporation of constituents, meniscus, corrosion, etc. |
| seed | structure, composition, orientation, dimensions, shape, etc. |
| pulling | pulling rate, rotation (rate, acceleration, direction) etc. |
| thermal aspect | heating source and its power, hot zone design and insulation materials, temperature gradients, automatic diameter control, etc. |
| cost efficiency | melt solidification fraction, cost of the crucible and the melt ingredients, cost of apparatus, time consumption for the preparation of starting materials, total time of the growth process, etc. |

List of such factors is demonstrated in Table II. Unfortunately, most of the reports on the Czochralski growth of scintillating crystals do not portray details of the process reflecting all of these factors. Thus, summary of the growth results presented below could not be considered as complete description of the technology. Nevertheless, many features of the crystal growth process are quite common and can be anticipated in the preparation of a new material, based on growth experience obtained before with other crystals.

## 4. Oxide crystals

In this section, growth of oxide scintillating crystals is summarized. In most cases, oxides have higher melting point than halides. Therefore, the growth apparatus must be designed to manage high power supply and to work at temperatures up to 2000 °C or even more. In the following sections, the growth of selected types of oxide crystals is outlined.

### *4.1. Garnets*

Growth of artificial garnet crystals is well established for decades [36], and it is commonly accepted that growth of yttrium-aluminum garnet $Y_3Al_5O_{12}$ (YAG) from the melt can be successfully performed practically by any

melt growth technique. From the point of view of crystal growth, YAG may be considered as typical crystalline substance that can play role of reference material. Its higher density analog, the $Lu_3Al_5O_{12}$ (LuAG) has the same crystallographic structure and physicochemical properties that makes its growth also comparatively simple. On the other hand, LuAG is formed with much heavier rare-earth oxide Lu instead of Y that makes LuAG more attractive for scintillating applications [37].

As an example, the growth of Pr-doped LuAG was recently reported in [38–40]. The growth system was equipped with inductive radio-frequency (RF) heating. The 2 inches in diameter bulk single crystals were produced at pulling rate of 1 mm/h and seed (Pr:LuAG) rotation of 8–12 rpm [5]. The growth apparatus used automatic diameter control system that was operated using signal received from the weight sensor. The Ir crucible was $Ø100 \times 100\ mm^2$ in dimensions, and it was protected from oxidation by Ar atmosphere.

The Pr:LuAG crystals of common shape (Fig. 2, left) contained many cracks at the shoulder and tail parts. This shortcoming was associated with high thermal stress acting in the upper portion of the crystal following from large cone angle and the stress in the tail part caused from concave shape of the solid/liquid interface. The problem was resolved by reducing the shoulder cone angle and flattening the solid–liquid interface, and as a result growth of crack-free crystals (Fig. 2, right) was established [5]. The length of the crystal was 110 mm, and total solidification fraction for this process was about 40% with respect to the volume of the starting melt.

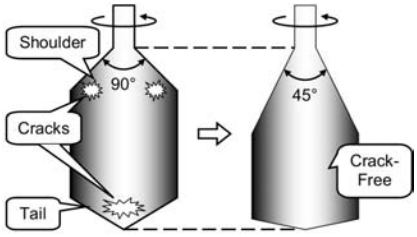


Fig. 2. Avoiding crack formation in 2-inch Pr:$Lu_3Al_5O_{12}$ crystals grown by Czochralski method by modification of the crystal shape (shoulder angle) and modification of temperature gradients according to [5].

Another problem of the Pr-doped $Lu_3Al_5O_{12}$ crystals is uniformity of the dopant distribution. From the chemical point of view, behavior of the host $Lu^{3+}$ and guest $Pr^{3+}$ cations in the garnet structure is comparable. However, dimensions of these cations are very different. Therefore, substitution of $Lu^{3+}$ with $Pr^{3+}$ is generally difficult. This was proven experimentally when composition of the grown Pr:LuAG and the dopant distribution along the growth axis were evaluated. The fraction of $Pr^{3+}$ (with respect to $Lu^{3+}$) in the starting melt composition was 2.5%, however, that in the crystal was 0.18–0.25 or less with corresponding segregation coefficient of Pr to be about 0.07. Nevertheless, the crystals demonstrated acceptable uniformity regarding dopant content and the samples cut from different part of the crystal had practically the same light yield that was about three times greater than that of $Bi_4Ge_3O_{12}$ (BGO) that is often considered as reference material regarding its scintillating performance. Optical properties and gamma-ray response of Pr:LuAG crystal including those containing different dopant content of 0.10, 0.18, and 0.22% are reported in [6].

Ce:$Gd_3(Ga,Al)_5O_{12}$ (Ce:GAGG) garnet is the most recent multi-component garnet type crystal that demonstrates very high light yield with moderately fast scintillation response [41]. Growth of undoped and activated GAGG was well established by different melt growth techniques including Czochralski [8, 9], floating zone (FZ) [7], and micro-pulling-down ($\mu$-PD) [42, 43]. In the past [8], undoped GAGG were grown considering their applications as material for the magnetic refrigerator. However, very recently the Ce-doped GAGG attracted much attention as a scintillating material.

In [8], the undoped GAGG crystals were produced in $N_2$+2%$O_2$ atmosphere from relatively small inductively heated Ir crucible of $Ø50 \times 50\ mm^2$ in dimensions. The growth was performed without automatic diameter control. The starting mixtures had excess of $Gd_2O_3$ of 0.02–0.15 per garnet formula unit with respect to ideal $Gd_3(Ga,Al)_5O_{12}$ composition. This was necessary to perform the process from the Gd-enriched melt corresponding to congruently melting composition of GAGG. The steady state pulling rate for the step of constant diameter growth (Fig. 1D) was 2 mm/h with crystal rotation rate of 35 rpm that established flat solid–liquid interface. At faster rotation, the interface became convex resulting undesired crystal faceting. The crystal obtained from the $Gd_{3.02}(Ga_{0.7}Al_{0.3})_{4.98}O_{12}$ melt was about 30 mm in diameter and 60 mm long, and it demonstrated reasonable optical quality and had no visible defects.

The quality of the $Gd_3(Ga_{1-x}Al_x)_5O_{12}$ crystals decreased considerably when concentration of Al was equal or exceeding 0.4 [8]. It was also noted that crack formation in the crystals was most probably associated with the strain induced in the crystal because of difference in ionic radii of $R(Al^{3+}) = 53.5$ pm and $R(Ga^{3+}) = 62.0$ pm [44]. Increased content of $Gd^{3+}$ in the crystal reduced probability of crack formation as a result of its probable incorporation into octahedral sites of the garnet structure and its greater size of $R(Gd^{3+}) = 93.8$ pm. In addition, it was detected that the crack formation was more intense when the crystals were faceted that was result of convex shape of the solid–liquid interface. The lattice parameters and the composition measurements demonstrated that the distribution coefficients of $Al^{3+}$ was $K(Al^{3+}) = 1.14$ for $x = 0.1$ and $K(Al^{3+}) = 1.07$ for $x = 0.4$ considering $Gd_3(Ga_{1-x}Al_x)_5O_{12}$ garnet formula. Based on these val-

ues, the existence of congruently melting composition of $Gd_3Ga_3Al_2O_{12}$ was predicted in [8].

CZ growth of the $Gd_3Ga_3Al_2O_{12}$ crystals modified with corresponding Ce-doping was also reported in [9]. Similar to [8], the crystals were grown using reduced pulling rate (1 mm/min) and rotation of 4–12 rpm from Ir crucible of about the same dimensions also heated inductively. The growth atmosphere was $Ar_2$+1.5%$O_2$. This atmosphere was selected to prevent oxidation of the crucible ($Ar_2$) and to reduce evaporation of $Ga_2O_3$ from the surface of the melt ($O_2$) at the same time. $Lu_3Al_5O_{12}$ crystal oriented along (100) axis was used as a seed. The crystals with diameter of 25 mm and length of 80–120 mm were produced with concentration of the Ce-dopant of 1.0, 2.0, and 3.0%. The solidification fractions for these growths were 0.50, 0.9, and 0.48, respectively, that exceeded prototype process reported in [8]. The interior parts of the crystals had perfect optical quality. However surface of the crystals was not transparent and irregular as a result of gallium oxide evaporation, thermal etching, and/or deposition of Ir particles originating from oxidation of the crucible material. According to composition analysis, the crystals were not perfectly uniform demonstrating moderate segregation for the host cations of $K(Al^{3+}) = 1.12$ and $K(Ga^{3+}) = 0.92$ and considerable segregation for the Ce-dopant of $K(Ce^{3+}) = 0.36$. This demonstrated that GAGG cannot be considered as true congruently melting compound at least at the compositional range reported.

Regarding dopant incorporation, it was noted in [9] that segregation coefficient $K(Ce^{3+})$ in GAGG was considerably greater than $K(Ce^{3+}) = 0.082$ reported for the YAG crystal grown by temperature gradient technique (TGT) in [45]. Also, according to [46], the Ce content in the YAG crystals produced by CZ method was 8.4 times less compared to the Ce-content in the melt, that also corresponds to $K(Ce^{3+})$ of about 0.1. Thus, all observations demonstrated that GAGG crystals accept Ce-dopant much more easily than YAG that is very reasonable conclusion considering greater lattice parameter of GAGG compared to YAG and large size of $Ce^{3+}$ cation.

Luminescence and scintillation characteristics and all the development of the LuAG-based scintillators including the discovery of ultra-efficient multi-component Ce:GAGG scintillators has been recently reviewed [37].

TABLE III

Optical, luminescence and scintillation characteristics of single crystals reported in this paper. Number in parenthesis in the scintillation decay time column represent the percentage of total intensity governed by the indicated decay time. Times in parenthesis in the LY column represent the time gates with which the LY was evaluated. See also web sites http://scintillator.lbl.gov/, http://crystalclear.web.cern.ch/crystalclear/ for scintillation parameters.

| Crystal | Band gap [eV] | Ce(Pr,Eu) $5d$–$4f$ em. [nm] | Ce(Pr,Eu) $4f$–$5d$ abs. [nm] | Ce(Pr,Eu) conc. [mol.%] | Main scint. decay time [ns] | LY (Ph/MeV) | Energy res. at 662 keV [%] |
|---|---|---|---|---|---|---|---|
| LuAG:Ce [37] | $\approx 8$ | 505, 555 | 202, 215, 227, 346, 448 | 0.15 | 55–65 (20–40%) | 18,000–26,000 | 5.5–7 |
| LuAG:Pr [37] | $\approx 8$ | 308 | Below 190, 239, 284 | 0.15 | 20 (20–40%) | 16,000–20,000 | 4.5–6.5 |
| GAGG:Ce [37] | 6–6.2 | 528, 565 | 235, 342, 439 | 0.1 | 88 (90%) | 46,000–51,000 | 4.9–5.5 |
| $CdWO_4$ [50] | $4.4 \pm 0.3$ [51] | 495 | n/a | n/a | 5000 | 27,000 | 6.6 |
| $PbWO_4$ [52, 53] | 4.4 [54] | 420 | n/a | n/a | 3–6 | 200 | 30–40 |
| LSO:Ce [55] | 6.3–6.5 | 395 | Ce1:205–235, 267, 296, 356 | 0.05–0.1 | 35 | 26,000 | 7.9 |
| GSO:Ce [56] | 6.2 | 430 | Ce1:250, 284, 345 | 0.1 | 60 | 12, 500 | 7.8 |
| YSO:Ce | 6.4–6.7 | 410 | Ce1:205–235, 264, 297, 356 | 0.1 | 50 | 24,000 | 9.3 |
| LYSO:Ce, Ca [57] | 6.3–6.5 | 395 | Ce1:205–235, 267, 296, 356 | 0.05–0.1 | 39 | 32,000 | 8.1 |
| $(Lu_{0.6}Gd_{0.4})_2SiO_5$:Ce [58] | $\approx 6.6$ | 415 | Ce1:269, 304, 339, 357, 378 | 0.44 | 30 (90%) | 29,000 | 6.7 |
| $Bi_4Ge_3O_{12}$ | 4.96 [59] | 480 | n/a | n/a | 300 | 8,500 | 9.0 |
| YAP:Ce | 8.8 | 360 | 219, 237, 275, 291, 304 [60] | 0.15 | 20–30 | 21,600 | 4.6 |
| LuAP:Ce | 8.44 [61] | 365 | 216, 231, 278, 294, 308 [60] | 0.05 | 16–20 | 11,400 | 9.0 |
| $LiCaAlF_6$:Ce [62] | $\approx 12$ | 285 | 160–174, 227, 244, 271 | $< 0.01$ | 35 | 5,000 (ph./neutron) | |
| $LiCaAlF_6$:Eu [62] | $\approx 12$ | 370 | 200–220, 290–350 | $< 0.01$ | 1670 | 40,000 (ph./neutron) | |
| $LaCl_3$:Ce [63, 64] | 7 | 337, 358 | 243, 250, 263, 274, 280 | 10 | 24(60%) | 50,000 | 3.1 |
| $LaBr_3$:Ce [63, 65] | 5.6 | 355, 390 | 260, 270, 284, 299, 308 | 5 | 16(100%) | 70,000 | 2.6 |
| $LuI_3$:Ce [66, 67] | | 475, 520 | $\approx 300, 390, 419$ | 0.5 | $< 50$ ns (50%) | 42,000(0.5 $\mu$s) | 4.7 |
| | | | | 2 | | 51,000(10 $\mu$s) | – |
| | | | | | | 58,000(0.5 $\mu$s) | |
| | | | | | | 71,000(10 $\mu$s) | |

Optical, luminescence, and scintillation characteristics of Ce and Pr-doped LuAG and Ce-doped GAGG are summarized in Table III. $Ce^{3+}$ center at the dodecahedral site of LuAG structure shows fast $5d$–$4f$ luminescence centered at about 510 nm (see Fig. 3) with the decay time of nearly 60 ns and the onset of thermal quenching above 700 K [47]. The same transition of $Pr^{3+}$ is situated at 308 nm (see Fig. 3) with the room temperature decay

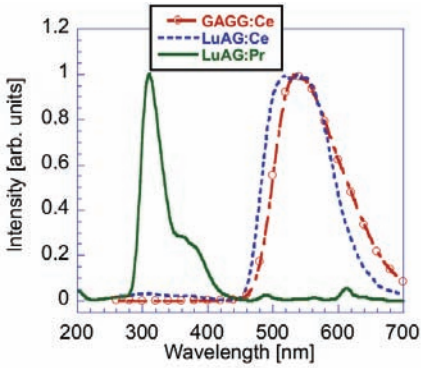


Fig. 3. Normalized radioluminescence spectra of Ce--doped LuAG and GAGG and Pr-doped LuAG (excitation X-ray, 40 kV).

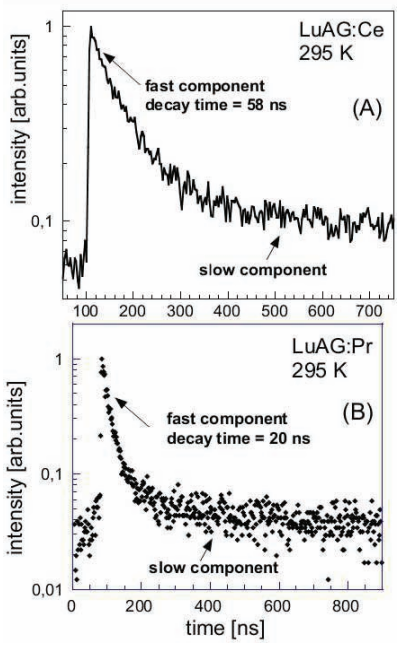


Fig. 4. Scintillation decays of Ce-doped (A) and Pr--doped (B) LuAG. Excitation source was $^{22}$Na radioisotope (511 keV).

time of 20 ns which makes it more suitable for fast scintillator. Moreover, energy resolution of Pr-doped LuAG was found excellent, below 5% at 662 keV [48]. Scintillation response is in both cases troubled by slow components due to electron re-trapping at shallow traps in LuAG host [49] (Fig. 4) and elimination of these traps by the balanced admixture of Gd and Ga cations in multicomponent garnet host resulted in the enormous light yield increase [41].

### *4.2. Tungstates: $PbWO_4$, $CdWO_4$*

Tungstate crystals including cadmium tungstate, $CdWO_4$, lead tungstate, $PbWO_4$, and others are high--density materials that show excellent stopping power for the X- and gamma-rays. They are chemically resistant and non-hygroscopic that makes them suitable for operation in number of device applications [68].

Because of the low melting point, the $PbWO_4$ single crystals can be grown by the Czochralski method using platinum (Pt) crucibles in air because the Pt is chemically resistant to normal atmospheric conditions (air). Particularly, the $PbWO_4$ crystals reported in [10] were pulled from the melt with rate of 2 mm/h and rotation of 20–40 rpm from Pt crucible of 35 mm in diameter. In these growths, the crystal diameter control was performed by monitoring the weight of the crucible with residual melt. The seed was oriented along *c*-axis direction. More detailed information about crystal growth details are available from [11]. The $PbWO_4$ starting materials were produced by double heat treatment of initial mixtures at 850 °C for 20 h in air and at 900 °C for 25 h after additional remixing. The resulting solid was inspected by X-ray diffraction (XRD) to ensure complete reaction of the initial oxides of PbO and $WO_3$ and absence of foreign phases of PbO, $WO_3$ or $Pb_2WO_5$. About 150 g of as produced starting solid was charged into the $Ø50 \times 50$ mm$^2$ Pt crucible that was lately heated resistively in the hot zone unit with axial temperature gradient of 10–15 °C/cm above the melt level.

The authors of [11] paid special attention to the crack formation in $PbWO_4$ crystals and the maneuvers that may decrease number of these defects. This problem was associated with significant difference in thermal expansion that occurred along (100) and (001) crystallographic directions. It was observed that quality of the crystals was improved by slow cooling the crystal to room temperature after its annealing. Also, the cracking was induced from asymmetry of the temperature distribution around the crystal and high axial temperature gradient above the melt. In addition, the seed misalignment caused non-uniform growth of the crystal in radial direction. Thereafter, the shape control of the conical shoulder part (Fig. 1C) was not possible and the growth was terminated.

In addition, the $PbWO_4$ had tendency to crack when the diameter was increased very fast (Fig. 1C, wide cone angle). This was associated with formation of convex solid/liquid interface and high temperature gradient occurring in the crystal because of the wide cone angle.

This phenomenon was suppressed by adjusting the seed rotation to some appropriate value to avoid uncontrollable melt super-cooling. Finally, the best seed rotation rate observed in [11] was 25–30 rpm. The crack-free crystal reported had cone angle of about 90 similar to that illustrated in Fig. 1F, and it was grown with almost flat solid/liquid interface. The diameter of the crystal on its cylindrical part (Fig. 1D) was controlled by modification of the temperature of the melt. The pulling-up rate did not exceed 3 mm/h because its increase to 4–5 mm/h resulted in reduction of the crystal transmission partially due to unavoidable incorporation of the foreign phase inclusions. To reduce the crystal stresses and the crack formation, the as grown crystals were annealed at 1000 °C for 5 h and then cooled down to room temperature at the rate of about 10 °C/h.

The optical transmission spectra of the 3 mm thick specimens cut perpendicular to the growth axis from the top and middle parts of the $PbWO_4$ crystals grown in [11] did not demonstrate any absorption around 430 nm (yellow coloration). However, those cut from the bottom part of the crystal had some absorption in this spectral region. This absorption was reduced when the crystals were grown from the melts obtained by re-melting of the crystals grown in previous experiments. For such crystals, the uniformity of the transmittance along the growth axis was considerably better.

Mass production of $PbWO_4$ crystals was well established quite some years ago. Fabrication and delivery of more than one thousand of certified scintillation elements per month was reported back in 2005 [12]. It was also noted in [13] that most of parameters of the crystals were well reproducible, and significantly less than 10% of the crystals were rejected as not satisfying the standards of quality control for their usage in calorimetric detectors in new high-energy physics accelerators.

Cadmium tungstate, $CdWO_4$ is another scintillating crystal of great importance particularly to be used in computed tomography and radiation monitoring systems [14]. It crystallizes in the wolframite structure with Cd and W cations sited in octahedral positions of the crystalline lattice. In [14], the $CdWO_4$ were produced by the CZ method on the seeds oriented along (010) cleavage plane. The crystals were grown from Pt crucibles heated inductively and surrounded with alumina ceramic for thermal insulation. The diameter of the crystals was monitored with weight sensors, and the growths were performed in oxidizing or inert atmosphere. The crystals produced were $\varnothing 50 \times 150$ mm$^2$ in dimensions. The crystals were generally colorless and free of visible inclusions when solidification fraction did not exceed one-third part of the starting melt and when the diameter of the crystals was not greater than 50% of crucible diameter. However, larger crystals exceeding 60 mm in diameter contained macrodefects in the core part and at the bottom fraction of the crystals. The $CdWO_4$ crystals reported contained pores with dimensions varied from 20 to 150 $\mu$m. According to [14], the growth was performed at 1350 °C, and at this temperature range the melt lost part of CdO as a result of its decomposition and evaporation. Therefore, the CdO solid particles were always found on the walls of the furnace and the remained melt was always enriched with $WO_3$ as compared with stoichiometric composition of $CdWO_4$. This melt composition instability was responsible for formation of secondary phase greenish inclusions of solid $WO_3$ particles incorporated into bottom (tail) part of the crystals. Formation of cracks parallel to the (010) cleavage plane is another type of imperfections found in the $CdWO_4$ crystals produced by conventional CZ method [15].

Growth of the $CdWO_4$ crystals by low thermal gradient (0.1–1 °C/cm) CZ method was reported in [15]. In this method, the growth was performed from Pt crucible of $\varnothing 70 \times 200$ mm$^2$ in dimensions placed inside three-zone furnace heated resistively and providing temperature gradient of about 1 °C/cm. The progress of the process was controlled by weight sensor, and the growth atmosphere was air. Two practices were applied to suppress undesired evaporation of CdO leading to progressed non-stoichiometry of the melt. Firstly, the crystal diameter was set to be relatively close to the crucible diameter leaving about 30–40% of the free surface of the melt at direct contact with air above the melt. Secondly, the top of the crucible was covered with conical lid equipped with small opening in the center providing pass for the seed holder rod. In such conditions (Fig. 5), the total amount of evaporated material was less than 0.2–0.5 wt% because the melt was not overheated regarding the melting point (the melt temperature was almost constant and equal to the melting temperature). As a result, 90% of the starting melt could be transformed into high-quality single-crystalline product with dimensions of $\varnothing 45 \times 150$ mm$^2$. It was demonstrated in [15] that growth results were not affected very much by changing the rotation rate within the range of 5–20 rpm or practicing the reverse rotation.

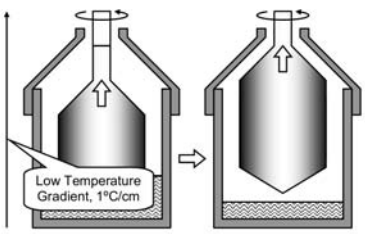


Fig. 5. Growth of the $CdWO_4$ [15] and $Bi_4Ge_3O_{12}$ [22] crystals by low thermal gradient (0.1–1 °C/cm) CZ method.

Intense study of the $PbWO_4$ single crystals in 1990's was initiated due to selection of this material for the new generation of calorimetric detectors in Large Hadron Collider in CERN, see reviews [52, 53]. Later on, various electron trapping and hole trapping centers were system-

atically characterized [69, 70] and their role in scintillation mechanism clarified. Luminescence of $PbWO_4$, $CdWO_4$ and other scheelite or wolframite structure tungstates are of self-trapped or trapped exciton nature and determined by the transition in the oxyanion group which results in violet–blue (420 nm) and blue–green (480 nm) emission bands in $PbWO_4$ and $CdWO_4$ single crystals, respectively. Essential difference between the decay time and quantum efficiency of excitonic luminescence around room temperature in $PbWO_4$ (few nanosecond decay time and few percent efficiency) and $CdWO_4$ (ten microsecond decay time and 100% efficiency) are due to different temperature stability of the exciton states. In $PbWO_4$, rather low binding energy of exciton of about 0.075 eV [71] results in its thermal disintegration already around 150–180 K, while an onset of thermally induced ionization and/or quenching of luminescence in $CdWO_4$ occurs well above room temperature [72].

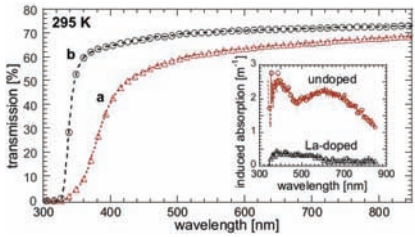


Fig. 6. Initial transmission and irradiation ($^{60}$Co radioisotope, 10 Gy dose) induced absorption in the inset of the couple of equivalently grown undoped (a) and La-doped (100 at. ppm in the crystal) (b) $PbWO_4$ single crystals. Reprinted from [52].

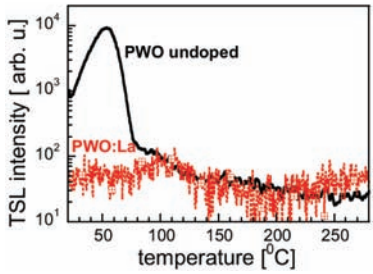


Fig. 7. Spectrally unresolved thermo-luminescence glow curve above room temperature after X-ray irradiation at room temperature, reprinted from [52].

Optimization of the $PbWO_4$ and $CdWO_4$ scintillation characteristics was focused mainly on their radiation hardness [52, 53] and afterglow [73], respectively, and has been achieved by the aliovalent doping. While in the former case the stable trivalent impurities (La, Gd, Y, Lu) increased the radiation hardness even several times compared to the high-purity and high-quality undoped crystal, in the latter case the monovalent dopants (Li, Na) have been most successful choice. The magnitude of this effect in the $PbWO_4$ is demonstrated in Figs. 6 and 7 where the $\gamma$-ray irradiation induced absorption and thermoluminescence glow curve are displayed. Trivalent doping at $Pb^{2+}$ site dramatically decreased the energy storage and color centers creation in the lattice due to the excess charge provided. Optical, luminescence and scintillation characteristics of $CdWO_4$ and $PbWO_4$ are summarized in Table III.

### *4.3. Oxyorthosilicates: $RE_2SiO_5$ (RE = rare earths)*

Cerium-doped oxyorthosilicates of rare-earth metals is another class of important scintillating oxide crystals. $Ce:Lu_2SiO_5$, $Ce:Y_2SiO_5$, and $Ce:Gd_2SiO_5$ are widely used for gamma-ray detection and other applications [18, 19]. These materials are represented by general formula of $Ce:RE_2SiO_5$, where RE is lanthanide metal. Growth of such crystals by the Czochralski method is well established for decades due to their congruent melting [16–19]. Regarding the structure, the crystals formed by large rare-earth cations from $Tb^{3+}$ to $La^{3+}$ solidify in monoclinic structure with space group $P2_1/c$. However, those based on small cations from $Lu^{3+}$ to $Dy^{3+}$ form monoclinic structure with space group $C2/c$ [16]. In the first case of $Gd_2SiO_5$ type structure ($P2_1/c$), the rare-earth sites have coordination numbers CN = 7 and CN = 9. However, in the case of $Lu_2SiO_5$ type crystals, the corresponding numbers are CN = 6 and CN = 7. As a result, higher coordination numbers allow easier incorporation of the large $Ce^{3+}$ dopant. Therefore, the segregation coefficients of $Ce^{3+}$ are about 0.6 [16] or 0.56 [19] for $Gd_2SiO_5$, 0.34 [19] for $Y_2SiO_5$, and 0.2 [16] or 0.22 [19] for $Lu_2SiO_5$.

Growth of $Lu_2SiO_5$ from standard iridium crucibles is comparatively difficult because the melting point of $Lu_2SiO_5$ (2150 °C) is relatively close to the melting point of Ir. However, the melting temperature may be noticeably reduced (2100 °C) by partial and isomorphic substitution of Lu with Gd as it was reported in [16]. Alternatively, $Gd_2SiO_5$ melts at lower temperature of about 1900 °C that is well acceptable for Ir crucibles because it is even less than that of YAG crystals produced commercially for decades. On the other hand, $Gd_2SiO_5$ cleaves, and it has not as good scintillating performance as that of $Lu_2SiO_5$ [16].

The CZ growth of $Lu_2SiO_5$ crystals of 40–80 mm in diameter was reported in [17]. The crucibles were made of Ir and were of 60–120 mm diameter. The growths were performed in gas flow, closed atmosphere, or in vacuum. The crystals were doped with Ce, Ce+Tb, Ce+Mg, and Ce+Ca, and the melting points for corresponding starting materials were referred in [17] to be in the range of 1970–1980 °C. Depending on the growth process, the pulling rate was 0.7–2.0 mm/h, and the rotation rate was

8–15 rpm. The crystal diameter was 30–78 mm, and the crystal length was in the range of 70–170 mm.

$Lu_2SiO_5$ is usually doped with 0.05–0.5% of Ce [18]. However, in some cases [17, 18] co-doping supports better scintillating performance. For example, incorporation of $Ca^{2+}$ into Ce:$Lu_2SiO_5$ may improve the light yield and the decay time, and effect of the co-dopant depends on its content in the crystal. On the other hand, this co-doping may reduce growth stability (acentric growth) even when the process conditions including temperature gradients in the hot zone remain unchanged. This phenomenon was particularly associated in [18] with reduction of the surface tension of the melt when it was enriched with $Ca^{2+}$. This shortcoming was suppressed by incorporation of additional compensating co-dopant of Zn into the structure. As a result, the acceptable surface tension was restored, stabilizing the growth process without reduction of scintillation performance of the crystal. The experiments demonstrated that amount of the Zn in the melt should be greater than that of Ce and Ca.

In [18], the Ø32 × 100 $mm^2$ crystals were grown by CZ method from the melts of $Ce_{0.02}Lu_{1.98}SiO_5$ composition undoped and co-doped with Ca and Ca–Zn. The co-dopant contents in the melt varied in the range of 0.1–0.4 at.% (relative to content of lutetium in the melt) for Ca and 0.1–0.6 at.% for Zn. It is evident that actual Ce and co-dopant contents in the crystals were different compared to the melt composition as a result of segregation. The growths were performed on (100)-oriented seed from the Ø60 × 60 $mm^2$ cylindrical Ir crucibles heated inductively, and the surrounding atmosphere was $N_2$+0.7%$O_2$. The pulling rate was 1.5 mm/h, and the rotation rate was 10 rpm. The 25% increase of the light output was detected for the crystal with 0.1% Ca-co-doping concentration as compared to the Ce-only doped reference specimens. Following increase of the Ca-content in the Ce--doped $Lu_2SiO_5$ was accompanied by continued decrease of the light yield. Regarding the decay time, the fastest decay (28–31 ns) was observed in the crystals containing maximal Ca content of 0.4 at.%. As for the $Zn^{2+}$ co--doping made for stabilization of the growth, it did not affect the light yield and the decay process considerably. Also, both co-dopants of Ca and Zn did not influence the peak emission wavelength of 416 nm [18].

Growth of the Ce:$Y_2SiO_5$ crystals from the melts of $Ce_{0.02}Y_{1.98}SiO_5$ and $Ce_{0.02}Ca_{0.02}Y_{1.96}SiO_5$ nominal compositions in the conditions similar to those described in the above paragraphs was reported in [19]. The crystals had no cracks and demonstrated reasonably good shape that was almost as good as that of the Ce:$Lu_2SiO_5$ produced at comparable conditions. However, in the case of co-doping of Ce:$Y_2SiO_5$ with Ca, the increase of the scintillation light yield was negligible (around 5% only) that was much less relatively to Ce:$Lu_2SiO_5$ (over 20%).

The crystals of Ce:$Gd_2SiO_5$ grown from the melts of $Ce_{0.02}Gd_{1.98}SiO_5$ and $Ce_{0.02}Ca_{0.02}Gd_{1.96}SiO_5$ [19] compositions had cracks. This was associated with using of iridium rod as a seed and with easy cleaving of $Gd_2SiO_5$ as compared with $Lu_2SiO_5$ and $Y_2SiO_5$. Similar observations were reported in [16] for the crystal grown on iridium rods as a seed from the melts of $Gd_2SiO_5$ and $Gd_{1.8}Lu_{0.2}SiO_5$ compositions with the cracks progressed along (100) and (010) planes. Formation of these cracks was successfully eliminated when the growth was performed on the $Gd_2SiO_5$ seeds oriented along cleavage planes. As for the light yield of Ce-doped $Gd_2SiO_5$, it was several times less than that of Ce-doped $Lu_2SiO_5$ and $Y_2SiO_5$ [19]. Moreover, doping of the Ce:$Gd_2SiO_5$ with 0.1% Ca further decreased the light yield for about three times.

The attempt to grow solid solution (or mixed) crystals corresponding to $(Gd_xLu_{1-x})_2SiO_5$ composition was reported in [16] assuming that in some range of the Gd-content the crystals will form the structure similar to that of non-admixed $Lu_2SiO_5$. Ce-doped crystals of $x = 0$, 0.2, 0.5, 0.9 and 1.0 were grown from inductively heated Ir crucibles in $N_2$+1–2%$O_2$ atmosphere. The crystals containing up to 50 mol.% of Gd had $Lu_2SiO_5$ structure. However, that with $x = 0.9$ was isomorphic to $Gd_2SiO_5$ ($x = 1$). As it was expected, the lattice parameters of the both type crystals ($Lu_2SiO_5$ and $Gd_2SiO_5$) changed according to average ionic radius of the rare--earth metals participating in formation of the crystals. In both type crystals, the segregation coefficient of the main rare-earth (such as Lu for $Lu_2SiO_5$) exceeds unity, but that of other rare-earths was less than 1. The segregation coefficient of Ce increased almost linearly with crystal composition from $Lu_2SiO_5$ to $Gd_2SiO_5$, and it was almost independent on the type of the crystal structure that was formed [16].

More detailed study of the Ce-doped mixed LSO–GSO crystals regarding the growth process and relation between the structure and scintillation characteristics has been published recently [58]. The occurrence of two $Ce^{3+}$ luminescent centers in LSO, YSO, and GSO has been established in the early 1990's [56] given to two Lu or Gd sites in the structure mentioned above. EPR study determined [74] that about 95% of $Ce^{3+}$ centers is located at bigger 7-coordinated site in LSO. The onset of excited state ionization of $Ce^{3+}$ centers around room temperature was found by classical photoconductivity studies [75] and further described in detail by purely optical methods [76].

Large effort has been devoted to the study of afterglow of LSO:Ce which was an obstacle for its practical applications [77] and is related to the dominant TSL peak at about 350 K, always observed in Ce-doped LSO or LYSO [78] (Fig. 8). The most recent models point to the agglomeration of $Ce^{3+}$ centers with electron traps based on the oxygen vacancies where tunneling driven radiative recombination exists [79, 80]. The above mentioned Ca or Mg co-doping in Ce-doped LSO or LYSO enabled its optimization regarding the minimization of afterglow (see Fig. 9), where older generation LYSO:Ce sample from [78] and latest commercial samples of LYSO:Ce,Ca and YSO:Ce from Proteus, see also [57], are compared. The

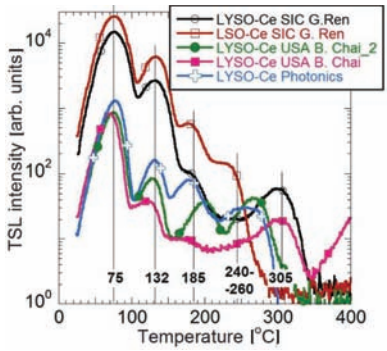


Fig. 8. TSL glow curves after X-irradiation at RT at LSO:Ce and LYSO:Ce. Reprinted from [78] with permission.

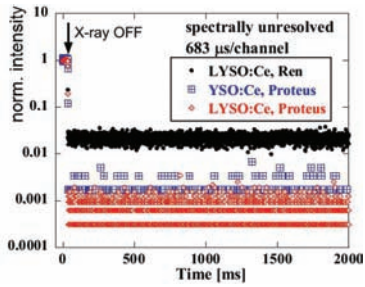


Fig. 9. Afterglow of LYSO:Ce (sample studied in [78]), LYSO:Ce,Ca and YSO:Ce (samples studied in [57]) after X-ray irradiation (40 kV, 10 mA) switch-off at room temperature.

Ca co-doping of LSO:Ce resulted also in increase of LY and speed-up of scintillation decay [81, 82]. Optical, luminescence and scintillation characteristics of Ce-doped LSO, LYSO, YSO, GSO and LGSO are summarized in Table III.

*4.4. Bismuth germanate, $Bi_4Ge_3O_{12}$ (BGO)*

Bismuth germanate, $Bi_4Ge_3O_{12}$ (BGO) is another popular scintillating crystal that is produced by various melt growth techniques for a long time [20]. It is one of the most commercialized scintillating materials due to its congruent melting and relatively low melting point. As a result, it is produced in relatively simple conditions including ordinary open-air atmosphere. Therefore, the $Bi_4Ge_3O_{12}$ crystals are fabricated by various melt growth methods including CZ [20–22], Bridgman [83], micro-pulling-down [42, 84], and other techniques.

In the melt of $Bi_4Ge_3O_{12}$ composition heated just above the melting point, the $Bi_2O_3$ is more volatile [20, 84]. Therefore, some non-stoichiometry may be induced in the melt when the CZ growth of BGO is progressed. This can be compensated with application of some excess of $Bi_2O_3$ in the starting melt. Moreover, in Bi-containing melts the $Bi_2O_3$ may be reduced to metallic Bi [20]. In such circumstances, the metallic Bi particles interact with crucible material of platinum forming a low melting-point alloy. This reduces lifetime of the crucible considerably. Nevertheless, the platinum remains material of choice for such growths because any other candidate materials were not found. The effect of the corrosion can be somehow suppressed using $O_2$-rich atmosphere or pure oxygen. However, in most cases the growth is performed in air. Both resistive and inductive heatings are applied.

The BGO crystals reported in [21] were grown for research purposes from the inductively heated Pt crucibles of $\varnothing 34 \times 36$ mm$^2$ or $\varnothing 52 \times 54$ mm$^2$ in dimensions. The crystals were 14.3 and 22.1 mm in diameter. In both these cases the predetermined ratio between the diameters of the crystal and the crucible was adjusted to be constant (0.42). The crystals were grown on (111)-oriented seed with pulling rate of 6 mm/h.

The BGO growth process analyzed in [22] was mostly developed for commercialization of the crystals. The method is based on the low thermal gradient (0.1–1 °C/cm) conception described above for the growth of the $CdWO_4$ crystals [15] and illustrated in Fig. 5, right. Application of such growth system allowed authors of [22] to produce transparent high-quality crystals of BGO with dimensions achieving $\varnothing 150 \times 400$ mm$^2$. In the growth conditions applied (Fig. 5, right), the visual control of the meniscus and the growth interface was not possible, because the lid sited on the top of the crucible disturbed the view. Therefore, the seeding and the growth were controlled with precise weight sensing system. The platinum lid on the top reflected the thermal radiation making the radial and axial temperature gradients as low as 0.05–0.10 °C/cm. This was positive factor with respect to protection of the melt from local overheating. Also, this lid played some role in suppressing evaporation of volatile constituents from the surface of the melt.

Because of low temperature gradients, it was possible to set crystal to crucible diameters ratio as high as 0.8. Therefore, similarity of the growth system setup illustrated in Fig. 5 (right) and the Bridgman growth was noticed in [22]. However, compared to the Bridgman method, the low temperature gradient CZ system was able to perform growth of crystals with their rotation that provided better mixing of the melt.

Luminescence properties of the $Bi_4Ge_3O_{12}$ were described for the first time in 1973 by Weber and Monchamp [85]. Broadband emission peaking around 480 nm (see inset in Fig. 10) with large Stokes shift of 14 000 cm$^{-1}$ was ascribed to $^3P_1$–$^1S_0$ transition at $Bi^{3+}$. The onset of thermal quenching was found around 250 K, see Fig. 10, so that quantum efficiency of the luminescence center around room temperature is of about 0.13

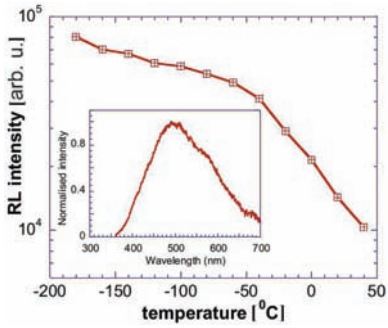


Fig. 10. Temperature dependence of radioluminescence intensity of BGO at room temperature excited by X-rays, 40 kV. Spectrum shape is in the inset.

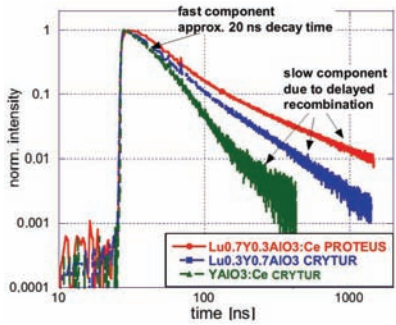


Fig. 11. Normalized scintillation decays of aluminum perovskites, composition in legend, excitation by 662 keV ($^{137}$Cs radioisotope), the data are from [96].

and is strongly temperature dependent. Later detailed luminescence study ascribed this emission to self-trapped exciton around $Bi(GeO_4)_6$ structural unit [86]. Optical, luminescence and scintillation characteristics of BGO are summarized in Table III.

### *4.5. Lutetium–aluminum perovskite, $LuAlO_3$ (LuAP)*

Behavior of $LuAlO_3$ perovskite phase at high temperatures approaching its melting point is complicated and difficult to resolve [4, 87]. Compared to its analog of Ce:$YAlO_3$, the Ce:$LuAlO_3$ scintillating crystals attract much attention as a result of its greater density and greater stopping power following from the substitution of relatively light Y with heavy Lu. On the other hand, increased content of yttrium in the (Y,Lu)$AlO_3$ solid solution improves stability of the growth [4].

One of the successful growth of the Ce:$LuAlO_3$ perovskite crystals was reported in [23]. The crystals were grown from Ø50 × 50 mm$^2$ iridium crucible in the $N_2$ atmosphere. The pulling and rotation rates were 1 mm/min and 15 rpm, respectively. High quality macro-defect-free crystal of Ø20 × 50 mm$^2$ in dimensions was produced with a well-established shape resulting from application of diameter control system that considered lowering level of the melt in the crucible. The Lu-rich $LuAlO_3$ crystals reported in [23] were activated with Ce and co-activated with Ce+Mo. Formation of (Y,Lu)$AlO_3$ crystals was also discussed in some detail. The growth of Ce:$LuAlO_3$ from the melts containing 0.5–2.0% of Ce (with respect to Lu content as a host cation) in molybdenum crucibles was reported in [24], and the segregation coefficient of Ce for such process was reported to be about 0.4. As a result, the content of Ce in the crystal was approximately 0.2–0.8%. Some of the crystals were "contaminated" with secondary garnet phase of $Lu_3Al_5O_{12}$.

Luminescence of Ce-doped $YAlO_3$ crystal was described by Weber [88], and favorable scintillation characteristics were reported somewhat later by several groups [89–91]. Research activity in the field of aluminum perovskites was reviewed in [52, 69]. Emission peak in near ultraviolet at 360–370 nm, photoluminescence decay time of 18 ns, and thermal stability of luminescence and scintillation parameters to 500 K, together with excellent energy resolution around 4.5% at 662 kV make this material very attractive for various applications. Nevertheless, complicated growth of LuAP or Lu-rich (Lu,Y)$AlO_3$ makes its manufacturing cost very high and only few industrial scale producers appeared and for limited time only [92]. Moreover, with increasing Lu content light yield of the material drops down almost to 50% of YAP:Ce. Similarly to garnets, shallow electron trap exists in the materials that are well visible in thermo-luminescence, and the origin of some of them was determined by EPR measurements [93, 94]. In fact, increasing amount of Lu in (Lu,Y)$AlO_3$:Ce makes the depth of traps bigger [78, 95]; the amount of slow components in scintillation decay strongly increases (Fig. 11) which is probably the main cause of LY decrease [96]. Optical, luminescence and scintillation characteristics of Ce-doped YAP and LuAP are summarized in Table III.

## 5. Important non-oxide crystals

The growth aspects of two non-oxide crystals are overviewed below. One of the problems of the growth of such crystals is associated with starting materials because of their hygroscopic nature. Therefore their initial treatment and preparation for the growth procedure need considerable technically complicated precautions when compared with the oxide crystals discussed above.

### *5.1. Ce-doped and Eu-doped $LiCaAlF_6$*

Initially the Ce-doped lithium-calcium-aluminum fluorite (LiCAF) with colquirite-type structure was considered as excellent material for UV solid-state lasers [26]. However, lately it was proposed to be used as scintillating substance [25, 97, 98]. This crystal melts congruently. It is normally grown by CZ method from Pt or carbon

crucibles under $CF_4$ atmosphere to avoid contamination of the melt and the solid with oxygen. Both resistive [28] and inductive [27] heating methods are applied to produce the melts used for the growths.

The typical procedure for the growth of undoped $LiCaAlF_6$ is described in [28]. The crystals were grown by CZ method in a vacuum tight chamber from the resistively heated Pt crucibles with crystal diameter control system. The powders of high-purity starting materials were mixed together and charged into the crucible. The pre-growth treatment of starting materials involved several steps described below, see also [28, 29]:

1. The growth chamber with starting materials in the crucible is evacuated ($10^{-3}$ Pa) to remove moisture and oxygen traces from the starting materials and the interior surfaces of the chamber. At the same time, the crucible is heated from room temperature to 700 °C for 12 h.
2. The high-purity (99.99%) [28] or (99.9999%) [29] $CF_4$ gas is slowly injected into the chamber.
3. Thereafter, heating of the starting materials is performed until their complete melting at approximately 820 °C.

The growth in [28] was performed using typical process similar to that illustrated in Fig. 1. The crystals were grown along *a*-axis following orientation of undoped $LiCaAlF_6$ seed pulled with the rate of 0.8–1.0 mm/h. The seed rotation rate was 8–15 rpm.

The LiCAF crystals of 76 mm (3 inches) in diameter reported in [28] contained inclusions. This was associated with instability of the solid/liquid interface. Improvement of the interface behavior can be made through adjustment of the rotation rate to its optimal magnitude. Also, changing the melt level in the crucible could uncontrollably modify the temperature gradients established around the crystal and especially at the vicinity of the growth front. Partial stabilization of these thermal conditions can be made by displacing the crucible in vertical (upward) direction. After such maneuvers the number of the inclusions was reduced [28]. However, this positive result was accompanied with intense crack formation that was most probably result of high temperature gradient and increased thermal stresses acting in the crystal at the cooling stage. To avoid crack formation, the as grown crystal and the crucible with rest of the melt were displaced in downward direction after the crystal was separated from the melt and the growth was completed. This way, the cooling of both was performed in low temperature gradient environment. As a result, the as treated crystal was free of both the inclusions and cracks. It was noted in [28] that surface of the crystal shoulder was coated with some particles of LiF and $AlF_3$, however, interior part of the crystal was transparent. Vaporization of LiF and $AlF_3$ from the surface of the melt was also noticed in [26].

Growth of Ce-doped $LiCaAlF_6$ is generally similar to that of described above. The Ce-doped LiCAF crystals of 25 and 50 mm in diameter and up to 100 mm in length were grown in [25] from Pt crucible also in $CF_4$ atmosphere. The melt contained 0.5 mol.% of $CeF_3$ and NaF was used as a charge compensator.

The growth of Ce-doped LiCAF reported in [29] was performed from the melts enriched with 1 mol.% of LiF and $AlF_3$ to compensate their vaporization from the melt. Also 1 mol.% of $CeF_3$ and NaF were charged into the starting mixture to maintain presence of the Ce-dopant and its charge compensation. The crystals were grown from Pt crucible on *a*-axis oriented LiCAF seed with pulling rate of 1 mm/h and the rotation rate of 10 rpm. The $\varnothing 18 \times 60$ mm$^2$ crystals produced in such conditions were visually defect-free, and they did not contain any cracks, bubbles, inclusions, and/or other substances as LiF and $AlF_3$ on the surface. The segregation coefficient of $Ce^{3+}$ was calculated based on the results of composition measurements, and its value was determined to be $K(Ce^{3+}) = 0.021$. In spite of low segregation coefficient, the distribution of the Ce-dopant along growth axis was reasonably uniform probably due to the low solidification fraction realized in these processes (about 25% only). Nevertheless, noticeable increase of the Ce content with solidification fraction was detected [29]. On the other hand, this did not affect uniformity of the lattice parameters.

In the $LiCaAlF_6$ structure, the $Ca^{2+}$ host cation is substituted by the $Ce^{3+}$ dopant. This substitution was very low (considerably less than 1%). That is why the crystals demonstrated perfect uniformity regarding the lattice parameters measured along the growth axis. The crystal of greater diameter (25 mm) had tendency to form inclusions, cracks, and impurity phase (at the bottom part of the crystal). It was noted that when the inclusions were formed in the shoulder part they were observed along the whole crystal length. To avoid this problem, more careful and "smooth" increase of the crystal diameter at the beginning of the growth was recommended [29]. The crystals produced at solidification fractions exceeding 70% contained inclusions of $CaF_2$. This was result of enrichment of the melt with $CaF_2$ following progressed evaporation of LiF and $AlF_3$ from the melt surface. Therefore, the crystals of acceptable quality were produced at total solidification fractions not exceeding 60%. Enrichment of the melt with $CeF_3$ and NaF could be another source of changing the composition of the residual melt because of low segregation coefficient of Ce.

For the growth of the 2 mol.% Eu-doped $LiCaAlF_6$ crystals, the system equipped with inductive heating and automatic diameter control was applied [27]. $EuF_3$ was used as a source of Eu-dopant. The crucible and the fragments of thermal insulation were produced from high-purity graphite. The crystal produced using *c*-axis oriented $LiCaAlF_6$ crystal as a seed was about 50 mm in diameter and had no visible defects.

Radio-luminescence spectra in Fig. 12 show the peak positions at about 285 nm and 368 nm for the Ce- and Eu-doped LiCAF, respectively, and provide a quantita-

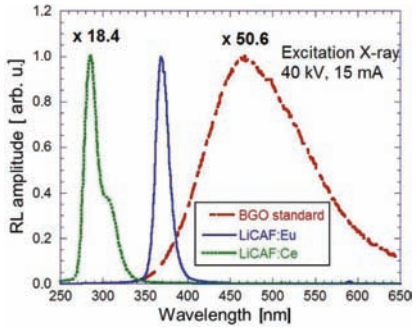


Fig. 12. Radio-luminescence spectra of the Ce- and Eu-doped LiCAF compared with the BGO standard scintillator, see also [62]. Spectra can be compared in an absolute scale.

tive comparison of scintillation efficiency of the Ce- and Eu-doped LiCAF and standard BGO scintillator under X-ray excitation. After integration of the spectra (spectra considered in appropriate units as radiation flux vs. energy) the ratio of emission intensities is 0.8:9:1, respectively. The difference of more than one order of magnitude between the Ce and Eu-doped LiCAF points to significant efficiency loss in the former.

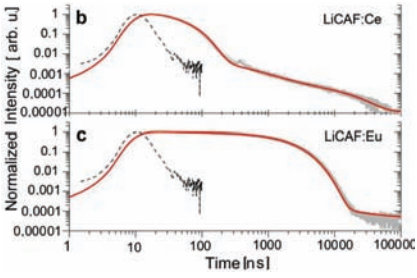


Fig. 13. Scintillation decay of (a) Ce-doped LiCAF, and (b) Eu-doped LiCAF under nanosecond soft X-ray excitation at RT. The fit by function $I(t)$ is given by solid line. The dashed line is the instrumental response, see [62] for further details.

Scintillation decays shown in Fig. 13 are approximated by the model function $I(t)$:

$$I(t) = a_0 + a_1 \mathrm{e}^{-t/\tau_1} + a_2 \mathrm{e}^{-t/\tau_2} + (bt + c)^{-p} \qquad (1)$$

and has been chosen to include two excited state levels or one excited state and one shallow trap levels given by exponential terms, and an additional tunneling and/or other recombination process coming from the transfer stage of scintillation mechanism given by the inverse power term, see [62] for further details. Leading exponential decay components with decay times of 34.7 ns and 1.67 $\mu$s are due to $5d$–$4f$ transition of $Ce^{3+}$ and $Eu^{2+}$ emission centers, respectively. Optical, luminescence and scintillation characteristics of Ce and Eu-doped LiCAF are summarized in Table III.

### *5.2. Ce-doped lanthanum bromide, Ce:$LaBr_3$*

Ce-doped lanthanum bromide ($LaBr_3$) is another non-oxide inorganic scintillator that is produced commercially in last years. It demonstrates very high light yield, excellent energy resolution, and fast decay [30]. $LaBr_3$ crystals have hexagonal structure that is isomorphic with $UCl_3$ [31]; it belongs to the space group of $P63/m$. The density of this crystal is comparatively high (5.3 g/cm$^3$). It melts congruently at temperature of 783 °C that is typically low for this type of materials. Therefore, according to [30, 34], these crystals can be grown using the Bridgman and Czochralski techniques from the melt. Actual Bridgman processes were performed for the growth of $LaBr_3$ [30] using ultra-dry forms of $LaBr_3$ and $CeBr_3$ of 99.99% purity. The crystals were produced with 0.2%, 0.5%, 1.3%, and 5% of dopant content.

No considerable details available for the growth process itself, and most reports on characterization of $LaBr_3$ are based on the examinations of the crystals produced by Saint Gobain Ceramics and Plastics Inc. [32, 33]. This company reported growth of the crystals of 127 mm (5 inches) in diameter back in 2006 [32] and growth procedure and/or parameters of the process are not disclosed.

During last 15 years the research on fast and efficient scintillators focused also on the new family of rare-earth (mostly La, Lu) halides where some of them showed extremely high light yield and excellent energy resolution. The Ce-doped $LaCl_3$, $LaBr_3$ and $LuI_3$ appeared as the most promising compositions and their characteristics are listed in Table III where also scintillation time decay, LY and energy resolution are given for a specific Ce concentrations. Further information about their luminescence and scintillation characteristics can be found for $LaCl_3$:Ce in [63, 64], $LaBr_3$:Ce [63, 65] and $LuI_3$:Ce [66, 67].

## 6. Search for new materials through combinatorial growth of micro-scale crystals

Development of new scintillating crystals is always resource- and time-consuming. Therefore, preliminary testing of small crystals obtained with alternative melt growth techniques that are generally transferable to the Czochralski process is sometimes practiced. Particularly, the crystals of few mm in dimensions available from the micro-pulling-down ($\mu$-PD) process are often (but not always) sufficient for the first round characterization of their physical properties. This was proven experimentally when studies of hundreds of new oxides, fluorides, and other non-fluoride halide crystals including chlorides, bromides, and iodides were performed especially in the past two decades. Many types of optical characterizations of the materials do not require massive ingots of

the substance of interest, and few millimeter specimens produced after appropriate cutting and polishing are acceptable for preliminary inspection. In normal practice, when the as grown crystals have macro-dimensions, the millimeter-scale specimens required for the inspection are cut from the bulk material. When these dimensions are acceptable, the $\mu$-PD process becomes method of choice.

Regarding the structural quality, the perfection of the $\mu$-PD crystals in some cases is comparable to that of the crystals produced by conventional melt growth methods. For example, the quality of the $\mu$-PD rare-earth sesquioxide crystals was similar to those grown by the CZ method. According to the rocking curve measurements reported in [99], the full width at half maximum (FWHM) were 90 arcsec, 100 arcsec, and 217 arcsec for the Tm:$Y_2O_3$, Tm:$Sc_2O_3$, and Tm:$Lu_2O_3$ $\mu$-PD crystals. Some of the $\mu$-PD crystals may have macroscale dimensions with cross-section exceeding 5 mm. Such materials can be certainly considered as macrocrystals ready for complete characterization.

## 7. Summary

The Czochralski method is one of the oldest and most developed crystal growth techniques regarding either an adequate understanding of the physical phenomena observed during solidification process or its practical expansion especially in the industrial scale production. It is widely used for the growth of large-size and high-quality single-crystalline cylindrical ingots of various chemical natures for a range of technical applications. Mass production of scintillating detectors is one of such applications that require application of well-established growth procedure because of large amount of crystalline material necessary. For example, traditional PET scanners require several thousands of high-quality single crystalline detectors that assembled into ring-shaped array [100] with dimensions comparable to that of human body and appropriate for millimeter-scale accuracy of image reconstruction. The Czochralski crystal growth technology is one of very few melt growth method that in a high degree satisfy optimal combination of crystal quality, crystal dimensions, and reasonable cost of produced crystals considering price of individual scintillating detector. The growth processes and material characteristics overviewed above illustrate applicability of the Czochralski method for the growth of single crystals having outstanding scintillating properties.

## Acknowledgments

This work is partially supported by (i) Japan Society for the Promotion of Science (JSPS) Grant-in-Aid for Exploratory Research (AY), (ii) the funding program for next generation world-leading researchers, JSPS, (iii) Development of Systems and Technology for Advanced Measurement and Analysis, Japan Science and Technology Agency (JST), (iv) Adaptable & Seamless Technology Transfer Program through Target-driven R&D (A-STEP) and JST, (v) Supporting Industry program, Ministry of Economy, Trade and Industry (METI). In addition, we would like to thank following persons for their support: Mr. Yoshihiro Nakamura in Institute of Multidisciplinary Research for Advanced Materials (IMRAM), Tohoku University and Mr. Hiroshi Uemura, Ms. Keiko Toguchi and Ms. Megumi Sasaki, Ms. Yumiko Saijo in IMR. Some part of this work was carried out under the collaboration program of Cooperative Research and Development Center for Advanced Materials, IMR, Tohoku University. Authors thanks to Mr. Sugawara, Ms. Nomura in Cryst. Growth & Design. Partial support of the Czech project supporting the Czech Japan collaboration, MEYS, KONTAKT II, no. 12150 is gratefully acknowledged. Thanks are due to A. Beitlerova and V. Jary for radioluminescence and afterglow measurements and W. Chewpraditkul for providing the data for Fig. 11.

## References

[1] D.J. Robbins, *J. Electrochem. Soc.* **127**, 2694 (1980).

[2] A. Lempicki, A.J. Wojtowicz, E. Berman, *Nucl. Instrum. Methods Phys. Res. A* **333**, 304 (1993).

[3] M.J. Weber, *J. Lumin.* **100**, 35 (2002).

[4] M. Nikl, *Meas. Sci. Technol.* **17**, R37 (2006).

[5] K. Kamada, K. Tsutsumi, Y. Usuki, H. Ogino, T. Yanagida, A. Yoshikawa, *IEEE Trans. Nucl. Sci.* **55**, 1488 (2008).

[6] T. Yanagida, M. Sato, K. Kamada, Y. Fujimoto, Y. Yokota, A. Yoshikawa, V. Chani, *Opt. Mater.* **33**, 413 (2011).

[7] A. Yoshikawa, Y. Fujimoto, A. Yamaji, S. Kurosawa, J. Pejchal, M. Sugiyama, S. Wakahara, Y. Futami, Y. Yokota, K. Kamada, K. Yubuta, T. Shishido, M. Nikl, *Opt. Mater.* (2013).

[8] H. Kimura, H. Maeda, M. Sato, *J. Cryst. Growth* **74**, 187 (1986).

[9] K. Kamada, T. Yanagida, J. Pejchal, M. Nikl, T. Endo, K. Tsutsumi, Y. Fujimoto, A. Fukabori, A. Yoshikawa, *IEEE Trans. Nucl. Sci.* **59**, 2112 (2012).

[10] K. Nitsch, M. Nikl, S. Ganschow, P. Reiche, R. Uecker, *J. Cryst. Growth* **165**, 163 (1996).

[11] N. Senguttuvan, Premila Mohan, S. Moorthy Babu, C. Subramanian, *J. Cryst. Growth* **183**, 391 (1998).

[12] A. Annenkov, E. Auffray, G. Drobychev, M. Korzhik, V. Kostylev, O. Kovalev, P. Lecoq, V. Ligoun, O. Missevitch, R. Zouevski, *Nucl. Instrum. Methods Phys. Res. A* **537**, 173 (2005).

[13] T. Eissner, D.A. Bremer, V. Dormenev, P. Drexler, M. Moritz, R.W. Novotny, R. Schubert, *Nucl. Sci. Symp. Med. Imag. Conf.* **N47-1**, 2095 (2011).

[14] B.P. Nazarenko, V.N. Baumer, E.F. Dolzhenkova, M.B. Kosmyna, *Inorg. Mater.* **41**, 1114 (2005)) (Translated from *Neorganicheskie Materialy* **41**, 1261 (2005).

[15] E.N. Galashov, V.A. Gusev, V.N. Shlegel, Ya.V. Vasiliev, *Crystallogr. Rep.* **54**, 689 (2009).

[16] G.B. Loutts, A.I. Zagumennyi, S.V. Lavrishchev, Yu.D. Zavartsev, P.A. Studenikin, *J. Cryst. Growth* **174**, 331 (1997).

[17] Y.D. Zavartsev, S.A. Koutovoi, A.I. Zagumennyi, *J. Cryst. Growth* **275**, e2167 (2005).

[18] M.A. Spurrier, P. Szupryczynski, H. Rothfuss, K. Yang, A.A. Carey, C.L. Melcher, *J. Cryst. Growth* **310**, 2110 (2008).

[19] M. Koschan, K. Yang, M. Zhuravleva, C.L. Melcher, *J. Cryst. Growth* **352**, 133 (2012).

[20] G. Gevay, *Prog. Cryst. Growth Charact.* **15**, 145 (1987).

[21] M. Berkowski, K. Iliev, V. Nikolov, P. Peshev, W. Piekarczyk, *J. Cryst. Growth* **108**, 225 (1991).

[22] Ya.V. Vasiliev, R.R. Akhmetshin, Yu.A. Borovliev, D.N. Grigoriev, V.A. Gusev, V.N. Shlegel, V.P. Smakhtin, *Nucl. Instrum. Methods Phys. Res. A* **379**, 533 (1996).

[23] W. Drozdowski, A.J. Wojtowicz, T. Łukasiewicz, J. Kisielewski, *Nucl. Instrum. Methods Phys. Res. A* **562**, 254 (2006).

[24] W.W. Moses, S.E. Derenzo, A. Fyodorov, M. Korzhik, A. Gektin, B. Minkov, V. Aslanov, *IEEE Trans. Nucl. Sci.* **NS-42**, 275 (1995).

[25] A. Gektin, N. Shiran, S. Neicheva, V. Gavrilyuk, A. Bensalah, T. Fukuda, K. Shimamura, *Nucl. Instrum. Methods Phys. Res. A* **486**, 274 (2002).

[26] K. Shimamura, S.L. Baldochi, I.M. Ranieri, H. Sato, T. Fujita, V.L. Mazzocchi, C.B.R. Parente, C.O. Paiva-Santos, C.V. Santilli, N. Sarukura, T. Fukuda, *J. Cryst. Growth* **223**, 383 (2001).

[27] T. Yanagida, N. Kawaguchi, Y. Fujimoto, K. Fukuda, Y. Yokota, A. Yamazaki, K. Watanabe, J. Pejchal, A. Uritani, T. Iguchi, A. Yoshikawa, *Opt. Mater.* **33**, 1243 (2011).

[28] H. Sato, A. Bensalah, A. Yoshikawa, M. Nikl, H. Machida, T. Fukuda, *Opt. Mater.* **24**, 123 (2003).

[29] K. Shimamura, S.L. Baldochi, Na Mujilatu, K. Nakano, Z. Liu, N. Sarukura, T. Fukuda, *J. Cryst. Growth* **211**, 302 (2000).

[30] K.S. Shah, J. Glodo, M. Klugerman, W.W. Moses, S.E. Derenzo, M.J. Weber, *LBNL-51793*, University of California, Oakland 2002.

[31] W.H. Zachariasen, *J. Chem. Phys.* **16**, 254 (1948).

[32] P.R. Menge, *Performance of Large BrilLanCe 380 (Lanthanum Bromide) Scintillators, SORMA XI, Ann Arbor (MI, USA), 2006.*

[33] F. Quarati, A.J.J. Bos, S. Brandenburg, C. Dathy, P. Dorenbos, S. Kraft, R.W. Ostendorf, V. Ouspenski, A. Owens, *Nucl. Instrum. Methods Phys. Res. A* **574**, 115 (2007).

[34] W.M. Higgins, A. Churilov, E. van Loef, J. Glodo, M. Squillante, K. Shah, *J. Cryst. Growth* **310**, 2085 (2008).

[35] J. Czochralski, *J. Phys. Chem.* **91**, 219 (1918).

[36] C.D. Brandle, *J. Cryst. Growth* **264**, 593 (2004).

[37] M. Nikl, A. Yoshikawa, K. Kamada, K. Nejezchleb, C.R. Stanek, J.A. Mares, K. Blazek, *Prog. Cryst. Growth Charact. Mater.* **59**, 47 (2013).

[38] M. Nikl, H. Ogino, A. Krasnikov, A. Beitlerova, A. Yoshikawa, T. Fukuda, *Phys. Status Solidi A* **202**, R4 (2005).

[39] H. Ogino, A. Yoshikawa, M. Nikl, A. Krasnikov, K. Kamada, T. Fukuda, *J. Cryst. Growth* **287**, 335 (2006).

[40] A. Yoshikawa, K. Kamada, F. Saito, H. Ogino, M. Itoh, T. Katagiri, D. Iri, M. Fujita, *IEEE Trans. Nucl. Sci.* **55**, 1372 (2008).

[41] K. Kamada, T. Yanagida, T. Endo, K. Tsutumi, Y. Fujimoto, A. Fukabori, A. Yoshikawa, J. Pejchal, M. Nikl, *Crystal Growth Des.* **11**, 4484 (2011).

[42] K. Kamada, T. Yanagida, J. Pejchal, M. Nikl, T. Endo, K. Tsutumi, Y. Usuki, Y. Fujimoto, A. Fukabori, A. Yoshikawa, *J. Cryst. Growth* **352**, 84 (2012).

[43] *Shaped Crystals: Growth by Micro-Pulling-Down Technique*, Eds. T. Fukuda, V.I. Chani, Springer, Berlin 2007.

[44] R.D. Shannon, C.T. Prewitt, *Acta Crystallogr. B* **25**, 925 (1969).

[45] G. Zhao, X. Zeng, J. Xu, Y. Xu, Y. Zhou, *J. Cryst. Growth* **253**, 290 (2003).

[46] Ji. Kvapil, Jo. Kvapil, B. Manek, B. Perner, R. Autrata, P. Schauer, *J. Cryst. Growth* **52**, 542 (1981).

[47] V. Bachmann, C. Ronda, A. Meijerink, *Chem. Mater.* **21**, 2077 (2009).

[48] K. Kamada, T. Yanagida, T. Endo, K. Tsutumi, M. Yoshino, J. Kataoka, Y. Usuki, Y. Fujimoto, A. Fukabori, A. Yoshikawa, *J. Cryst. Growth* **352**, 91 (2012).

[49] M. Nikl, A. Vedda, M. Fasoli, I. Fontana, V.V. Laguta, E. Mihokova, J. Pejchal, J. Rosa, *Phys. Rev. B* **76**, 195121 (2007).

[50] M. Moszynski, M. Balcerzyk, M. Kapusta, A. Syntfeld, D. Wolski, G. Pausch, J. Stein, P. Schotanus, *IEEE Trans. Nucl. Sci.* **52**, 3124 (2005).

[51] Y. Abraham, N.A.W. Holzwarth, R.T. Williams, *Phys. Rev. B* **62**, 1733 (2000).

[52] M. Nikl, *Phys. Status Solidi A* **178**, 595 (2000).

[53] A.A. Annenkov, M.V. Korzhik, P. Lecoq, *Nucl. Instrum. Methods Phys. Res. A* **490**, 30 (2002).

[54] M. Itoh, H. Yokota, M. Horimoto, M. Fujita, Y. Usuki, *Phys. Status Solidi B* **231**, 595 (2002).

[55] J.A. Mares, M. Nikl, E. Mihokova, A. Beitlerova, A. Vedda, C. D'Ambrosio, *IEEE Trans. Nucl. Sci.* **55**, 1142 (2008).

[56] H. Suzuki, T.A. Tombrello, C.L. Melcher, J.S. Schweizer, *Nucl. Instrum. Methods Phys. Res. A* **320**, 263 (1992).

[57] W. Chewpraditkul, C. Wanarak, T. Szczesniak, M. Moszynski, V. Jary, A. Beitlerova, M. Nikl, *Opt. Mater.* **35**, 1679 (2013).

[58] O. Sidletskiy, A. Belsky, A. Gektin, S. Neicheva, D. Kurtsev, V. Kononets, C. Dujardin, K. Lebbou, O. Zelenskaya, V. Tarasov, K. Belikov, B. Grinyov, *Cryst. Growth Des.* **12**, 4411 (2012).

[59] F. Antonangeli, N. Zema, M. Piacentini, *Phys. Rev. B* **37**, 9036 (1988).

[60] E. Mihóková, M. Nikl, M. Bacci, M. Dušek, V. Petříček, *Phys. Rev. B* **79**, 195130 (2009).

[61] V. Kolobanov, V. Mikhailin, N. Petrovnin, D. Spassky, Yu. Zorenko, *Phys. Status Solidi B* **243**, R60 (2006).

[62] M. Nikl, P. Bruza, D. Panek, M. Vrbova, E. Mihokova, J.A. Mares, A. Beitlerova, N. Kawaguchi, K. Fukuda, A. Yoshikawa, *Appl. Phys. Lett.* **102**, 161907 (2013).

[63] K.W. Krämer, P. Dorenbos, H.U. Güdel, C.W.E. van Eijk, *J. Mater. Chem.* **16**, 2773 (2006).

[64] O. Guillot-Noël, J.T.M. De Haas, P. Dorenbos, C.W.E. Van Eijk, K. Krämer, H.U. Güdel, *J. Lumin.* **85**, 21 (1999).

[65] E.V.D. Van Loef, P. Dorenbos, C.W.E. van Eijk, K. Kramer, H.U. Gudel, *Phys. Rev. B* **68**, 045108 (2003).

[66] J. Glodo, K.S. Shah, M. Klugerman, P. Wong, B. Higgins, P. Dorenbos, *Nucl. Instrum. Methods Phys. Res. A* **537**, 279 (2005).

[67] M.D. Birowosuto, P. Dorenbos, C.W.E. van Eijk, *IEEE Trans. Nucl. Sci.* **52**, 1114 (2005).

[68] S.Ph. Burachas, F.A. Danevich, A.Sh. Georgadze, H.V. Klapdor-Kleingrothaus, V. Kobychev, B.N. Kropivyansky, V.N. Kuts, A. Muller, V.N. Muzalevsky, A.S. Nikolaiko, O.A. Ponkratenko, V.D. Ryzhikov, A.S. Sai, I.M. Solsky, V.I. Tretyak, Yu.G. Zdesenko, *Nucl. Instrum. Methods Phys. Res. A* **369**, 164 (1996).

[69] M. Nikl, V.V. Laguta, A. Vedda, *Phys. Status. Solidi B* **245**, 1701 (2008).

[70] V.V. Laguta, M. Burvi, M. Nikl, J. Rosa, S. Zazubovich, *Phys. Rev. B* **83**, 094123 (2011).

[71] A. Krasnikov, M. Nikl, S. Zazubovich, *Phys. Status Solidi B* **243**, 1727 (2006).

[72] M.M. Chirila, K.T. Stevens, H.J. Murphy, N.C. Giles, *J. Phys. Chem. Solids* **61**, 675 (2000).

[73] L. Nagornaya, G. Onyshchenko, E. Pirogov, N. Starzhinskiy, I. Tupitsyna, V. Ryzhikov, Yu. Galich, Yu. Vostretsov, S. Galkin, E. Voronkin, *Nucl. Instrum. Methods Phys. Res. A* **537**, 163 (2005).

[74] L. Pidol, O. Guillot-Noel, A. Kahn-Harari, B. Viana, D. Pelenc, D. Gourier, *J. Phys. Chem. Solids* **67**, 643 (2006).

[75] E. van der Kolk, S.A. Basun, G.F. Imbusch, W.M. Yen, *Appl. Phys. Lett.* **83**, 1740 (2003).

[76] H. Feng, V. Jary, E. Mihokova, D. Ding, M. Nikl, G. Ren, H. Li, S. Pan, A. Beitlerova, R. Kucerkova, *J. Appl. Phys.* **108**, 033519 (2010).

[77] P. Dorenbos, C.W.W. van Eijk, A.J.J. Bos, C.L. Melcher, *J. Phys. Condens. Matter* **6**, 4167 (1994).

[78] M. Nikl, E. Mihokova, J. Pejchal, A. Vedda, M. Fasoli, I. Fontana, V.V. Laguta, V. Babin, K. Nejezchleb, A. Yoshikawa, H. Ogino, G. Ren, *IEEE Trans. Nucl. Sci.* **55**, 1035 (2008).

[79] A. Vedda, M. Nikl, M. Fasoli, E. Mihokova, J. Pejchal, M. Dusek, G. Ren, C.R. Stanek, K.J. McClellan, D.D. Byler, *Phys. Rev. B* **78**, 195123 (2008).

[80] S. Blahuta, A. Bessière, B. Viana, V. Ouspenski, E. Mattmann, J. Lejay, D. Gourier, *Materials* **4**, 1224 (2011).

[81] M.A. Spurrier, P. Szupryczynski, K. Yang, A.A. Carey, C.L. Melcher, *IEEE Trans. Nucl. Sci.* **55**, 1178 (2008).

[82] B. Viana, T.H. Maldiney, S. Blahuta, A. Béssi?re, D. Gourier, C. Richard, D. Scherman, V. Ouspenski, *Proc. SPIE* **8626**, 86260R (2013).

[83] M. Kobayashi, K. Harada, Y. Hirose, M. Ishii, I. Yamaga, *Nucl. Instrum. Methods Phys. Res. A* **400**, 392 (1997).

[84] V. Chani, K. Lebbou, B. Hautefeuille, O. Tillement, J.-M. Fourmigue, *Cryst. Res. Technol* **41**, 972 (2006).

[85] M.J. Weber, R.R. Monchamp, *J. Appl. Phys.* **44**, 5495 (1973).

[86] R. Moncorge, B. Jacquier, G. Boulon, *J. Lumin.* **14**, 337 (1976).

[87] D. Klimm, *J. Cryst. Growth* **312**, 730 (2010).

[88] M.J. Weber, *J. Appl. Phys.* **44**, 3205 (1973).

[89] T. Takeda, T. Miyata, F. Muramatsu, T. Tomiki, *J. Electrochem. Soc.* **127**, 438 (1980).

[90] E. Autrata, P. Schauer, J. Kvapil, Jos. Kvapil, *Scanning* **5**, 91 (1983).

[91] V.G. Baryshevsky, M.V. Korzhik, V.I. Moroz, V.B. Pavlenko, A.A. Fyodorov, S.A. Smirnova, O.A. Egorycheva, V.A. Kachanov, *Nucl. Instrum. Methods Phys. Res.* **58**, 291 (1991).

[92] J. Trummer, E. Auffray, P. Lecoq, A. Petrosyan, P. Sempere-Roldan, *Nucl. Instrum. Methods Phys. Res. A* **551**, 339 (2005).

[93] A. Vedda, M. Fasoli, M. Nikl, V.V. Laguta, E. Mihokova, J. Pejchal, A. Yoshikawa, M. Zhuravleva, *Phys. Rev. B* **80**, 045113 (2009).

[94] V.V. Laguta, M. Nikl, A. Vedda, E. Mihokova, J. Rosa, K. Blazek, *Phys. Rev. B* **80**, 045114 (2009).

[95] A.N. Belsky, E. Auffray, P. Lecoq, C. Dujardin, N. Garnier, H. Canibano, C. Pedrini, A.G. Petrosyan, *IEEE Trans. Nucl. Sci.* **48**, 1095 (2001).

[96] W. Chewpraditkul, A. Phunpueok, T. Szczesniak, M. Moszynski, V. Babin, M. Nikl, *Phys. Status Solidi A* (2013).

[97] M. Nikl, N. Solovieva, E. Mihokova, M. Dusek, A. Vedda, M. Martini, K. Shimamura, T. Fukuda, *Phys. Status Solidi A* **187**, R1 (2001).

[98] A. Yoshikawa, T. Yanagida, Y. Yokota, N. Kawaguchi, S. Ishizu, K. Fukuda, T. Suyama, K.J. Kim, J. Pejchal, M. Nikl, K. Watanabe, M. Miyake, M. Baba, K. Kamada, *IEEE Trans. Nucl. Sci.* **56**, 3796 (2009).

[99] A. Fukabori, V. Chani, K. Kamada, F. Moretti, A. Yoshikawa, *Cryst. Growth Des.* **11**, 2404 (2011).

[100] J.A.K. Blokland, P. Trindev, M.P.M. Stokkel, E.K.J. Pauwels, *Europ. J. Radiol.* **44**, 70 (2002).

# Abstract

*Zeszyty Historyczne*, Volumes 15 and 16, edited by prof. Miroslaw Wladyslaw Nader, published by the Publishing House of the Warsaw University of Technology (series *Prace Naukowe*), titled: ”Jan Czochralski Year”, to commemorate the life and scientific heritage of an outstanding Polish scientist, inventor, crystallographer, chemist, metallurgist, creator of the basics of the electronics industry. This special edition is a tribute to the eminent Polish scholar, professor of the Warsaw University of Technology and an Honorary Doctor of the University. The aim of the publication is to present the most important events preceding the Polish Parliament’s resolution which declared the year 2013 as the Year of Professor Jan Czochralski. The publication includes the calendar of main events, archives, selected publications and other materials related to the commemoration.

The edition consists of two print volumes, with a digital and multimedia Appendix. **Volume 1,** titled ***Outline of biography and historical documentation*** contains documents referring to the proclamation of the Jan Czochralski Year. Numerous archival documents show involvement of the Warsaw University of Technology in the process of restoring the memory of Professor Jan Czochralski. The papers describe the personality of Professor and his achievements in different areas of research. For archiving purposes, a chronicle of Jan Czochralski Year was added, with particular emphasis on activities undertaken by the Warsaw University of Technology and Professor’s hometown Kcynia.

**Appendix** to Volume 1 includes fuller compendium of events (seminars, exhibitions) from all over the country and a number of presentations given on seminars and conferences. The complete bibliography of the Professor's publications, linked with full texts, is recorded on a CD. A DVD includes an archive of films produced in memory of Professor Jan Czochralski.

**Volume 2,** titled ***In Memory of Professor Jan Czochralski: Selected papers,*** contains a number of scientific publications (reprints from leading journals and original papers), which reflect the idea of continuation and development of Professor Czochralski achievements. In order to acknowledge that the methods and ideas developed by Jan Czochralski are still valuable, there is a special issue of *Acta Physica Polonica A* dedicated entirely to Professor. The issue includes a number of articles written by a group of honorable scholars from all over the world. Some of these papers have been reprinted in Volume 2. Among other authors are winners of the first edition of the Jan Czochralski Prize, organized by the Warsaw University of Technology and granted by the Ministry of Science and Higher Education.

*Zeszyty Historyczne*, prepared by the Main Library of the Warsaw University of Technology, published with a subsidy of the Ministry of Science and Higher Education, are disseminated free of charge.